

## University of Southampton Research Repository

Copyright © and Moral Rights for this thesis and, where applicable, any accompanying data are retained by the author and/or other copyright owners. A copy can be downloaded for personal non-commercial research or study, without prior permission or charge. This thesis and the accompanying data cannot be reproduced or quoted extensively from without first obtaining permission in writing from the copyright holder/s. The content of the thesis and accompanying research data (where applicable) must not be changed in any way or sold commercially in any format or medium without the formal permission of the copyright holder/s.

When referring to this thesis and any accompanying data, full bibliographic details must be given, e.g.

Thesis: Author (Year of Submission) "Full thesis title", University of Southampton, name of the University Faculty or School or Department, PhD Thesis, pagination.

Data: Author (Year) Title. URI [dataset]



# **University of Southampton**

Faculty of Engineering and Physical Science

School of Chemistry

## **Flexible Thermoelectric Energy Generators for E-textiles**

by

**Aran Amin**

ORCID ID [<https://orcid.org/0000-0003-4266-8132>]

Thesis for the degree of Doctor of Philosophy

September 2022



# University of Southampton

## Abstract

Faculty of Engineering and Physical Sciences

School of Chemistry

Thesis for the degree of Doctor of Philosophy

### **Flexible Thermoelectric Energy Generators for E-textiles**

by

Aran Amin

Thermoelectric generators are a solid-state energy harvesting technology that utilises thermal gradients to generate useable electricity. However, the applicable uses for thermoelectric generators remain in niche fields, due to their low efficiency as well as their bulky and rigid nature. To expand the applicable uses of thermoelectric generators it is vital to improve their flexibility as well as ensure the simplicity and scalability of their fabrication to incorporate them into future electronic textiles and internet of things applications. This thesis describes an investigation into the combination of polyol synthesis chemistry with screen-printing to develop a procedure for the fabrication of scalable and flexible thermoelectric generators. Promising material candidates examined in this thesis are n-type nanowires of Bismuth telluride and Bismuth telluride selenide, as well as p-type Tellurium nanorods and Bismuth antimony telluride nanoplatelets. These nanomaterials were then screen-printed onto flexible substrates such as Kapton and a polyurethane-based interface layer on polyester-cotton. The paste used to print these nanomaterials was formulated using a solvent-binder system of N-Methyl-2-pyrrolidone as the solvent and polyvinylidene fluoride as the binder. For the first time, such a solvent-binder system was systematically studied, where the binder content was varied with respect to the amount of Bismuth telluride nanowires in the paste. This was done to optimise the binder content with respect to the thermoelectric material in post-annealed screen-printed films. The annealed Bismuth telluride films achieved a maximum Seebeck coefficient of  $-192 \pm 10 \mu\text{V K}^{-1}$  with a Power factor of  $36 \pm 7 \mu\text{W m}^{-1} \text{K}^{-2}$  at 225 K. Additionally, a novel systematic study into the content of Tellurium nanorods in screen-printed Bismuth antimony telluride nanoplatelet films was carried out to identify an optimal concentration for improved thermoelectric performance. The ideal content of Tellurium nanorods in the p-type films was shown to be 12 % of the film's weight with a room temperature Seebeck coefficient of  $210 \pm 10 \mu\text{V K}^{-1}$  and a Power factor of  $54 \pm 6 \mu\text{Wm}^{-1} \text{K}^{-2}$ . Further testing in the form of bending studies was performed on the screen-printed films to observe their suitability for flexible applications. Finally, the screen-printed films were used to fabricate flexible thermoelectric generator devices where their power outputs were measured with respect to the thermal gradient across the devices using a thermal camera. It was discovered that the p-type polyvinylidene fluoride-Tellurium nanorod composite films were compatible with electronic textile applications achieving a power output of 50 nW at a temperature gradient of 29.8 K. This was because the composite films could generate a power output after being printed onto a polyurethane-based interface layer on polyester-cotton without the composite films being annealed.

## **Disruptions to research as a result of COVID-19**

It should be stated that during the research stage of this PhD project, all experimental research work had to cease for a period of 8 months out of the 3.5 years of funded laboratory time at the onset of the COVID-19 pandemic. Additionally, more time was lost due to the restrictions in place in the multitude of laboratories and facilities used during this project, which limited access to vital pieces of equipment needed for the development and analyses of the materials studied in this project. This includes equipment related to annealing the materials, analysing the materials' morphology as well as their thermoelectric properties at different temperature ranges and finally measuring prototype devices' power outputs. Furthermore, regaining access to these facilities took more time and as a result, delayed the publication and communications of the project's research output. The project's main focus was on developing novel screen-printable flexible nanostructured films as such the devices fabricated were a secondary priority that was conducted towards the latter stages of the project which were the most affected by covid disruptions. These restriction-based delays as well as unforeseen Covid infections within the research team and project collaborators affected the measuring and analysis of many films and devices. This resulted in causing these films and devices to be oxidised despite putting in place protective measures such as storing samples inside a vacuum desiccator in a dry nitrogen glovebox. As such we observed lower than expected thermoelectric properties and power outputs, without the necessary time to repeat the fabrication and analysis of more samples during the allotted time of the research project.

## Novelty statement

This thesis presents novel research not seen previously in the literature. The primary novelty of this research was the discovery and investigation of annealed interconnected nanostructured networks formed from annealed Bismuth telluride nanowires. Followed by screen-printing Bismuth telluride nanowires using a paste formulation of N-Methyl-2-pyrrolidone as the solvent and polyvinylidene fluoride as the binder on to flexible substrates. As well as demonstrating how varying the binder content in the pastes with respect to the content of Bismuth telluride nanowires can affect the screen-printed films' post-annealed material and thermoelectric properties.

Other minor points of novelty were:

- Comparing the post-annealed thermoelectric properties between screen-printed films of Bismuth telluride and Bismuth telluride selenide nanowires.
- Studied the changes in the material and thermoelectric properties of screen-printed Bismuth antimony telluride nanoplatelet films with the addition of Tellurium nanorod additives.
- Developed two prototype flexible thermoelectric generators. The first on Kapton was a 3-thermocouple generator using screen-printed annealed n-type Bismuth telluride nanowires and screen-printed annealed p-type Bismuth antimony telluride nanoplatelets containing Tellurium nanorods which acted as a thermoelectric additive. While the second single-leg flexible thermoelectric generator was based on 5 nanocomposite films of polyvinylidene fluoride-Tellurium nanorods. The nanocomposites were screen-printed onto a polyurethane-based interface layer on a polyester-cotton substrate. This demonstrates the suitability of these nanocomposite-based flexible thermoelectric generators for electronic textile applications.

## Table of Contents

Disruptions to research as a result of COVID-19.....	ii
Novelty statement.....	iii
<b>Table of Contents .....</b>	<b>iv</b>
<b>Table of Tables .....</b>	<b>ix</b>
<b>Table of Figures .....</b>	<b>xi</b>
<b>List of Accompanying Materials .....</b>	<b>xxiii</b>
<b>Research Thesis: Declaration of Authorship .....</b>	<b>xxv</b>
<b>Acknowledgements .....</b>	<b>xxvii</b>
<b>Definitions, Abbreviations and Symbols .....</b>	<b>xxix</b>
<b>Chapter 1 Introduction.....</b>	<b>1</b>
1.1 Aims, Objectives and Project motivations .....	1
1.1.1 Project motivations.....	1
1.2 Introduction to thermoelectric theory .....	3
1.2.1 Initial discovery and research on thermoelectric generators .....	3
1.2.2 Semiconductor theory .....	3
1.2.3 Current semiconductor-based thermoelectric generator devices .....	5
1.2.4 Thermoelectric properties .....	7
1.3 The properties of Bismuth telluride-based thermoelectric generators .....	9
1.3.1 Crystal structure of Bismuth telluride-based alloys .....	10
1.4 Nanostructuring of Bismuth telluride-based alloys.....	11
1.4.1 Nanomaterial synthesis techniques.....	13
1.5 Polyol reflux synthesis of nanostructures.....	14
1.6 Screen-printing.....	16
1.7 State-of-the-art of polyol reflux synthesis and screen-printing procedures for the fabrication of flexible thermoelectric Tellurium and Bismuth telluride-based materials .....	19
1.7.1 Polyol reflux synthesised Bismuth telluride-based nanostructures .....	19
1.7.2 Tellurium-based nanocomposites .....	23

1.7.3	Bismuth telluride-based screen-printed films and devices .....	25
1.7.4	Wearable electronic textile compatible thermoelectric generators .....	28
1.8	Conclusions.....	30
<b>Chapter 2</b>	<b>Experimental methodology .....</b>	<b>31</b>
2.1	Polyol reflux synthesis methodology .....	31
2.1.1	Synthesis of $\text{Bi}_2\text{Te}_3$ and $\text{Bi}_2\text{Te}_x\text{Se}_{x-3}$ nanowires .....	32
2.1.2	Synthesis of $\text{Bi}_{0.4}\text{Sb}_{1.6}\text{Te}_3$ nanoplatelets .....	33
2.1.3	Synthesis of Tellurium nanorods.....	33
2.2	Paste formulations .....	34
2.2.1	Initial paste formulation.....	34
2.2.2	N-Methyl-2-pyrrolidone/Polyvinylidene fluoride thermoelectric paste formulation.....	35
2.2.3	Paste formulation with Dimethyl sulfoxide .....	35
2.3	Material characterisation techniques .....	36
2.3.1	Scanning electron microscope .....	36
2.3.2	Energy-dispersive X-ray spectroscopy .....	37
2.3.3	Grazing incidence X-ray diffraction .....	38
2.4	Thermoelectric characterisation techniques .....	40
2.4.1	Seebeck coefficient characterisation .....	40
2.4.1.1	Room temperature Seebeck coefficient measurement.....	40
2.4.1.2	Variable temperature Seebeck coefficient characterisation .....	41
2.4.2	Hall probe measurements.....	42
2.5	Flexibility characterisation .....	45
2.6	Power output characterisation .....	46
<b>Chapter 3</b>	<b>Screen-printed polyol reflux synthesised Bismuth telluride nanowire films</b>	<b>48</b>
3.1	Characterisation analysis of drop-casted films of $\text{Bi}_2\text{Te}_3$ nanowires .....	48
3.1.1	Material characterisation .....	48
3.1.2	Thermoelectric characterisation .....	50

## Table of Contents

3.2	Characterisation analysis of Screen-printed films for a variety of PVDF concentrations .....	54
3.2.1	Material characterisation .....	54
3.2.2	Thermoelectric characterisation.....	58
3.2.3	Flexibility characterisation .....	62
3.3	Single-leg flexible thermoelectric generator device and power output measurements .....	64
3.4	Conclusions .....	67
<b>Chapter 4</b>	<b>Selenium alloying of polyol reflux synthesised Bismuth telluride selenide nanowires.....</b>	<b>69</b>
4.1	Characterisation of Se alloyed nanowires .....	69
4.1.1	One-step addition of Se and Bi precursor into the polyol reflux synthesis.....	69
4.1.2	Two-step addition of Se and Bi precursor into the polyol reflux synthesis.....	72
4.2	Screen-printed PVDF-Bi <sub>2</sub> Te <sub>2.5</sub> Se <sub>0.5</sub> nanowire composite films.....	76
4.2.1	Morphological comparison between Bi <sub>2</sub> Te <sub>2.5</sub> Se <sub>0.5</sub> & Bi <sub>2</sub> Te <sub>3</sub> films.....	76
4.2.2	Thermoelectric analysis comparing post-annealed Bi <sub>2</sub> Te <sub>2.5</sub> Se <sub>0.5</sub> & Bi <sub>2</sub> Te <sub>3</sub> films 83	
4.2.3	Bending analysis for screen-printed Bi <sub>2</sub> Te <sub>2.5</sub> Se <sub>0.5</sub> & Bi <sub>2</sub> Te <sub>3</sub> films .....	85
4.3	Conclusions .....	87
<b>Chapter 5</b>	<b>Screen-printed reflux synthesised Bismuth antimony telluride nanoplatelet films .....</b>	<b>89</b>
5.1	Characterisation analysis of drop-casted films polyol synthesised Bi <sub>0.4</sub> Sb <sub>1.6</sub> Te <sub>3</sub> nanoplatelets .....	89
5.1.1	Material characterisation .....	89
5.1.2	Thermoelectric analysis of drop-casted Bi <sub>0.4</sub> Sb <sub>1.6</sub> Te <sub>3</sub> nanoplatelet films .....	92
5.2	Characterisation analysis of Screen-printed PVDF-Bi <sub>0.4</sub> Sb <sub>1.6</sub> Te <sub>3</sub> nanoplatelets composite films.....	93
5.2.1	Characterisation analysis of scaled-up polyol synthesised Bi <sub>0.4</sub> Sb <sub>1.6</sub> Te <sub>3</sub> nanoplatelets .....	93
5.2.2	Screen-printed PVDF-Bi <sub>0.4</sub> Sb <sub>1.6</sub> Te <sub>3</sub> nanoplatelet films .....	95

5.3	Tellurium nanorod additive study .....	98
5.3.1	Characterisation analysis of drop-casted Tellurium nanorods .....	98
5.3.2	Characterisation analysis of screen-printed Tellurium nanorods.....	100
5.3.3	Characterisation of screen-printed PVDF-Bi <sub>0.4</sub> Sb <sub>1.6</sub> Te <sub>3</sub> -Te films .....	101
5.3.3.1	Material characterisation .....	102
5.3.3.2	Thermoelectric characterisation .....	108
5.3.3.3	Flexibility characterisation .....	110
5.4	Device fabrication and power output measurements.....	111
5.4.1	Single-leg flexible thermoelectric generator device .....	112
5.4.2	P-N thermocouple flexible thermoelectric generator device .....	114
5.5	Conclusions.....	117
<b>Chapter 6</b>	<b>Screen-printed Tellurium-Polyvinylidene fluoride composite-based flexible thermoelectric generators for E-textiles .....</b>	<b>121</b>
6.1	Scaled-up polyol reflux synthesis of Tellurium nanorods .....	121
6.2	Bending analysis of Screen-printed Tellurium-Polyvinylidene fluoride composite .....	123
6.3	Device fabrication and power output measurements.....	125
6.4	Conclusions.....	128
<b>Chapter 7</b>	<b>Conclusions and Future work .....</b>	<b>129</b>
7.1	Summary of results .....	129
7.2	Future work .....	134
<b>Appendix A</b>	<b>[Optimising post-printing annealing process for screen-printed 20 % PVDF-Bi<sub>2</sub>Te<sub>3</sub> nanowire films].....</b>	<b>137</b>
<b>Appendix B</b>	<b>[Screen-printing annealed Bi<sub>2</sub>Te<sub>3</sub> nanowire powders] .....</b>	<b>143</b>
<b>Appendix C</b>	<b>[Screen-printed Bi<sub>0.4</sub>Sb<sub>1.6</sub>Te<sub>3</sub> nanoplatelets using a DMSO-PVDF paste formulation] .....</b>	<b>146</b>
<b>Appendix D</b>	<b>[SEM images of screen-printed 5 % PVDF-Bi<sub>0.4</sub>Sb<sub>1.6</sub>Te<sub>3</sub>+ Te nanorods] .....</b>	<b>147</b>
<b>Appendix E</b>	<b>[Viscosity measurements] .....</b>	<b>149</b>
	<b>List of References .....</b>	<b>151</b>



## Table of Tables

<b>Table 1.1-</b> Potential electrical power output from different parts of the human body based on how active the person is between low and high activity <sup>[6,7]</sup> .....	2
<b>Table 1.2-</b> The summary of thermopower at a given temperature and output power for a given heat flux for PRS $\text{Bi}_x\text{Sb}_{2-x}\text{Te}_{3-y}\text{Se}_y$ nanomaterials along with their bulk values.....	22
<b>Table 1.3-</b> Summary of the room temperature TE performance of the Te nanostructure-polymer composites.....	24
<b>Table 1.4-</b> Summary of thermopower at a given temperature and output power for a given heat flux for screen-printed $\text{Bi}_x\text{Sb}_{2-x}\text{Te}_{3-y}\text{Se}_y$ materials along with their bulk values.....	27
<b>Table 5.1-</b> The TE properties of annealed PVDF- $\text{Bi}_{0.4}\text{Sb}_{1.6}\text{Te}_3$ nanoplatelets films on Kapton at room temperature. The Seebeck coefficient was taken with the portable Seebeck probe. The results are an average of multiple measurements with the error being the standard deviation of the average. ....	95
<b>Table 5.2-</b> The TE properties of annealed PVDF-Te nanorod films on Kapton at room temperature. The Seebeck coefficient was taken with the portable S probe, while the electrical properties were measured with a Hall probe. The results are an average of multiple measurements with the error being the standard deviation of the average. ....	101
<b>Table 5.3-</b> The average thickness measurements for the PVDF- $\text{Bi}_{0.4}\text{Sb}_{1.6}\text{Te}_3$ nanoplatelets + Te nanorod films.....	102
<b>Table A.1-</b> The TE properties of annealed $\text{Bi}_2\text{Te}_3$ films on Kapton at room temperature. The Seebeck coefficient was measured with the portable Seebeck probe. The results are an average of multiple measurements with the error being the standard deviation of the average for the Hall probe results and the 7 % error of the portable Seebeck probe.....	140
<b>Table A.2-</b> The TE properties of annealed 20% PVDF- $\text{Bi}_2\text{Te}_3$ films on Si and $\text{SiO}_2/\text{Si}$ at room temperature. The Seebeck coefficient was measured with the portable Seebeck probe. The results are an average of multiple measurements with the error being	

the standard deviation of the average for the Hall probe results and the 7 % error  
of the portable Seebeck probe..... 142

## Table of Figures

- Fig.1.1-** The diagram shows the basic electronic band structure of conductors, semiconductors and insulators. The CB and VB of the conductors overlap through the Fermi level, while semiconductors and insulators have a band gap. ....4
- Fig. 1.2-** The diagram shows the band structure for n-type and p-type semiconductors with the Fermi level shifted towards either the CB or VB depending on the type of doping, with filled circles representing extra electron energy levels and empty circles representing extra hole energy levels. ....5
- Fig.1.3-** TEG illustration displaying the TEG set-up for a single pair of p-type and n-type legs connected electrically in series via a metal contact and thermally in parallel (top), while the other image shows the TEG device as a series of TEG pairs with heat passing through the device producing a current as an output (bottom) from Snyder et al <sup>[11]</sup>. ....6
- Fig. 1.4-** The graph shows the optimised figure of merit ZT for carrier concentration tuning is a balance between thermal conductivity (K) (y-axis range between  $0 \text{ Wm}^{-1}\text{K}^{-1}$  and  $10 \text{ Wm}^{-1}\text{K}^{-1}$ ), electrical conductivity ( $\sigma$ ) (y-axis range between  $0 \text{ S cm}^{-1}$  and  $5000 \text{ S cm}^{-1}$ ) and Seebeck coefficient ( $\alpha$ , y-axis between  $0 \text{ } \mu\text{VK}^{-1}$  and  $500 \text{ } \mu\text{VK}^{-1}$ ). Graph from Snyder et al <sup>[11]</sup>. ....9
- Fig.1.5-** The graphs above show the ZT ranges for the best TE materials for a temperature range between 300 K and 900 K. Graphs taken from Beretta et al <sup>[26]</sup>. ....9
- Fig. 1.6-** Diagram of  $\text{Bi}_2\text{Te}_3$  rhombohedral structure divided into 3 quintuple layers separated by a van der Waals gap. Alongside the octahedral coordination between the  $\text{Te}^{(1)} - \text{Bi} - \text{Te}^{(2)} - \text{Bi} - \text{Te}^{(1)}$  sites. The image is taken from Witting et al <sup>[27]</sup>. ....10
- Fig.1.7-** Graph of different mechanical heat engine technology efficiencies for a temperature range from 300 K to 1300 K compared with TE ambitions for ZT. Graph taken from Vining et al <sup>[25]</sup>. ....11
- Fig.1.8-** Graphs of the theoretical predictions of ZT for a  $\text{Bi}_2\text{Te}_3$  quantum well for the x-y plane (1) and x-z plane (2) with respect to the thicknesses of the quantum well in that plane (left), as well as  $\text{Bi}_2\text{Te}_3$  nanowire with respect to the nanowire orientation and thickness at that orientation in the x,y and z plane (right). The graphs are taken from Hicks et al and Dresselhaus et al <sup>[23,31]</sup>. ....12

## Table of Figures

- Fig.1.9-** Graphs show the change in the electronic density of states (DOS) vs energy for a 3D bulk semiconductor (a), 2D quantum well (b), 1D quantum wire (c) and 0D quantum dot (d). The graphs are taken from Mao et al <sup>[33]</sup>. ..... 13
- Fig. 1.10-** Schematic of a PRS reaction to synthesis nanowires; (a) metal precursor dissolution and complex formation with solvent (yellow), (b) metal atoms reduction in solvent (black), (c) nucleation at crystal phases, (d) particle growth and (e) formulation of metal nanowires..... 15
- Fig.1.11-** Illustration of the screen-printing process. .... 17
- Fig. 1.12-** Illustration shows the synthesis process steps in forming Metal-Tellurium-Selenium nanowires. The image is taken from Zhou et al <sup>[45]</sup>. ..... 20
- Fig.1.13-** Image of the process for inkjet printed FTEG device. (a–c) Synthesis process for the  $\text{Bi}_2\text{Te}_3$  and  $\text{Bi}_{0.5}\text{Sb}_{1.5}\text{Te}_3$  nanowires and subsequent ink formulation for inkjet printing, (d–f) inkjet printing onto flexible polyimide film, (g) thermal annealing of the films, and (h–i) spray printing of liquid metal contacts and doctor blade coating of silicone sealant. Image from Chen et al <sup>[53]</sup>. ..... 21
- Fig. 1.14-** Illustration of the formation of the self-assembled Te nanorod-PVDF composite. Image from Dun et al <sup>[67]</sup>. ..... 23
- Fig. 1.15-** Graphs of normalised resistance as a function of the radius of bending (left) and bending cycles for a radius of 50 mm (right). Graphs from Kim et al <sup>[75]</sup>. ..... 25
- Fig. 1.16-** Screen-printed  $\text{Bi}_{1.8}\text{Te}_{3.2}$  on (a) polyester/cotton with polyurethane interface, (b) Valmiera 1032/9682, (c) Valmiera 440-AL, (d) ATEX 3000, (e) ATEX 3200-2-sp, (f) PAR GC409SG, (g) PAR GC16 and (h) ATEX 03321-2-WN. Images from Cao et al <sup>[74]</sup>.26
- Fig. 1.17-** Wearable medical systems powered by bulk  $\text{Bi}_2\text{Te}_3$ -based TEGs with (a) pulse oximeters wristwatch system, (b) a headband electroencephalography device and (c) an electrocardiography device shirt with (1) highlighting the TEGs while (2) shows the amorphous Si solar cells. Images from Leonov et al <sup>[5]</sup>. ..... 29
- Fig.2.1-**Image of the set-up used to run the polyol reflux synthesis..... 31
- Fig. 2.2-** Schematic of an SEM. The electron beam (blue) passes through condensing and focusing lenses and hits the sample to produce many different signals picked up by various detectors (BSE= Backscatter electrons detector, SE= Secondary electrons detector and X= X-ray photons detector) <sup>[15,89]</sup>. ..... 36

- Fig.2.3-** Schematic diagram SEM beam electrons interacting with sample atom's electrons forming characteristic x-ray photons and Bremsstrahlung radiation. Initially (a&b) beam electron (dark blue) knocks out an inner orbital electron leaving a vacancy (c) which is filled by an outer electron (d) which generates a characteristic x-ray photon. (e) Beam electrons decelerate when interacting with sample atom's electrons releasing Bremsstrahlung radiation <sup>[15]</sup>.....38
- Fig. 2.4-** Schematic diagram of X-rays scattering on an array of atoms in a crystal lattice to demonstrate Bragg's law. With the x-rays obeying the Bragg's condition and adding constructively after scattering.....39
- Fig.2.5-** Image of the PTM-3 Seebeck coefficient 2-probe measuring test system.....40
- Fig. 2.6-** Picture (left) of the Seebeck measuring test system used to measure the Seebeck coefficient over a temperature range using a vacuum chamber and liquid nitrogen to modify the temperature. With red arrows, indicating the relevant parts to the machine with the diagram (right) illustrating the 4-probe set up for measuring the Seebeck coefficient and electrical conductivity with  $T_H$  (hot probe),  $T_C$  (cold probe) and V1 and V2 measuring the Seebeck voltage. All 4 probes were used to measure the electrical conductivity by having an induced current passed from the outer probes  $T_H$  and  $T_C$  through the sample with voltage measured by V1 and V2. 41
- Fig. 2.7-** Schematic of the basic set-up for Hall probe analysis with 4-probes (R1, R2, R3, R4) on a sample which is placed on a board on top of a magnet, as well as (red arrows) the magnetic field, induced current (blue arrows) with the voltage  $V_{14}$  being measured between probes R1 and R4.....43
- Fig. 2.8-** Schematic of the linear 4-point probe set-up used by the commercial test system and the Van der Pauw method used by the Hall probe. The blue arrows represent the current accounted for by the techniques, while the green arrows represent the unaccounted current. ....44
- Fig.2.9-** Image of custom bending rig used for flexibility studies.....46
- Fig. 2.10-** Sketch of the electrical circuit of a TEG with a load resistor, where  $V_{TEG}$  and  $R_{TEG}$  are the total Seebeck voltage and resistance of the TEG respectively. ....46
- Fig.2.11-** Sketch of a single-leg FTEG device with 5 TE legs between a heat source and a heat sink, with a red and black arrow showing the direction of heat and current respectively. ....47

## Table of Figures

- Fig.3.1-** SEM images (a&b) of a top-down view of PRS  $\text{Bi}_2\text{Te}_3$  nanowires on an Au-coated Si substrate and (c) an EDX spectrum of the drop-casted PRS  $\text{Bi}_2\text{Te}_3$  nanowires film..... 48
- Fig. 3.2-** GIXRD diffraction patterns obtained for (a) reference XRD of tellurobismuthite ( $\text{Bi}_2\text{Te}_3$ ) mineral from the International Centre of Diffraction Data (ICDD) database (PDF 00-015-0863) and (b) drop-casted film of PRS  $\text{Bi}_2\text{Te}_3$  nanowires on an Au-coated Si substrate..... 49
- Fig. 3.3-** SEM of a top-down view of drop-casted  $\text{Bi}_2\text{Te}_3$  nanowire film on a Si substrate (a) before annealing and (b) post-annealing, alongside EDX spectres for (c) before annealing and (d) post-annealing. .... 50
- Fig. 3.4-** GIXRD diffraction patterns obtained for (a) reference XRD of tellurobismuthite ( $\text{Bi}_2\text{Te}_3$ ) mineral from the International Centre of Diffraction Data (ICDD) database (PDF 00-015-0863) and (b)  $\text{Bi}_2\text{Te}_3$  INNs on an Au-coated Si substrate after being annealed in an Ar atmosphere at 400°C for 2 hr. .... 52
- Fig.3.5-** The (a) Seebeck coefficient, (b) electrical conductivity and (c) power factor between temperatures of 250 K and 450 K for a drop-casted  $\text{Bi}_2\text{Te}_3$  nanowire film annealed at 400 °C for 2 hr in an Ar inert atmosphere on a glass substrate. The error bars in the graphs are a result of the uncertainty of the measuring tool as stated in section 2.412..... 53
- Fig.3.6-** SEM micrographs of a) PRS  $\text{Bi}_2\text{Te}_3$  nanowires with dimensions and b) PRS scaled up by a factor of two  $\text{Bi}_2\text{Te}_3$  nanowires with dimensions. .... 55
- Fig.3.7-** SEM micrographs of (a) annealed screen-printed 20% PVDF- $\text{Bi}_2\text{Te}_3$  nanowires, (b) 10% PVDF- $\text{Bi}_2\text{Te}_3$  nanowires, (c) fully formed 10% PVDF- $\text{Bi}_2\text{Te}_3$  INNs, (d) annealed screen-printed 5% PVDF- $\text{Bi}_2\text{Te}_3$  nanowires and EDX spectra of the screen-printed 10% PVDF- $\text{Bi}_2\text{Te}_3$  nanowires films (e) before and (f) after annealing to represent the drop in oxygen and fluorine..... 56
- Fig.3.8-** GIXRD diffraction patterns obtained for (a) reference XRD of tellurobismuthite ( $\text{Bi}_2\text{Te}_3$ ) mineral from International Centre of Diffraction Data (ICDD) database (PDF 01-085-0439) (b) unannealed drop-casted  $\text{Bi}_2\text{Te}_3$  nanowires, (c) annealed drop-casted  $\text{Bi}_2\text{Te}_3$  nanowires, (d) unannealed 10 % PVDF- $\text{Bi}_2\text{Te}_3$  nanowires composite film and (e) annealed 10 % PVDF- $\text{Bi}_2\text{Te}_3$  nanowires composite film and (f) annealed 10 % PVDF- $\text{Bi}_2\text{Te}_3$  INNs composite film. All films were annealed in an inert Ar atmosphere at 400 °C for 2 hr..... 58

<b>Fig.3.9-</b> Temperature-dependent TE properties measured over a temperature range of 150 K to 425 K for (a) Seebeck coefficient, (b) electrical conductivity (c) charge carrier mobility, (d) $\log_{10}$ scale charge carrier concentration and (e) power factor of the post-annealed screen-printed film composites containing 20%, 10% and 5% PVDF with respect to the $\text{Bi}_2\text{Te}_3$ nanowires as well as the 10% PVDF- $\text{Bi}_2\text{Te}_3$ INNs composite. The error bars in the graphs are a result of the uncertainty of the measuring tool as stated in section 2.412 and the standard deviations from the average Hall probe results at different temperatures. ....	59
<b>Fig.3.10-</b> EDX spectrum of the annealed screen-printed 5 % PVDF- $\text{Bi}_2\text{Te}_3$ nanowire film after measuring its TE measurements in Fig. 3.9. ....	62
<b>Fig. 3.11-</b> (a) Resistance normalized to initial resistance of 5% PVDF-NW and an annealed drop-casted films for 1000 bending cycles, with a bending radius of 10 mm, (b) photograph insert of curved composite nanowire film, 5% PVDF-NW and an annealed drop-casted films before (c) and after (d) bending. ....	63
<b>Fig. 3.12-</b> Image of single-leg 5% PVDF- $\text{Bi}_2\text{Te}_3$ nanowire FTEG device. ....	64
<b>Fig.3.13-</b> Graphs showing (a) the voltage vs current response for different temperature differences, (b) the open-circuit voltage with respect to the temperature difference, (c) the output power vs current and (d) the maximum output power with respect to the temperature difference of the single-leg 5% PVDF- $\text{Bi}_2\text{Te}_3$ nanowire FTEG device. ....	65
<b>Fig.3.14-</b> The thermal images are taken of the single-leg 5% PVDF- $\text{Bi}_2\text{Te}_3$ nanowire FTEG device during measuring with a normalised temperature range with (a) 9.4 K, (b) 12.9 K, (c) 17.1 K,(d) 20.8 K, (e) 25.1 K, (f) 28.5 K and (g) 31.9 K. ....	66
<b>Fig. 4.1-</b> SEM images (a) of a top-down view of $\text{Bi}_2\text{Te}_{3-x}\text{Se}_x$ nanowires on a Si substrate, (b) showing the nanowire lengths and (c) EDX spectrum of the drop-casted PRS $\text{Bi}_2\text{Te}_{3-x}\text{Se}_x$ nanowires film. ....	70
<b>Fig.4.2-</b> GIXRD diffraction patterns obtained for (a) reference XRD of Bismuth Selenide Telluride ( $\text{Bi}_2\text{SeTe}_2$ ) mineral from the International Centre of Diffraction Data (ICDD) database (PDF 01-089-2006) and (b) drop-casted film of PRS $\text{Bi}_2\text{Te}_{3-x}\text{Se}_x$ nanowires on a Si substrate. ....	71

## Table of Figures

- Fig.4.3-** GIXRD diffraction patterns for the (black) drop-casted film of  $\text{Bi}_2\text{Te}_3$  nanowires on a Si substrate (red) for the drop-casted film of  $\text{Bi}_2\text{Te}_{3-x}\text{Se}_x$  nanowires between  $26^\circ$  and  $40^\circ$ ..... 72
- Fig.4.4-** SEM images (a) of a top-down view of PRS  $\text{Bi}_2\text{Te}_{3-x}\text{Se}_x$  nanowires on a Si substrate, with (b) showing the nanowires lengths and (c) an EDX spectrum of the drop-casted PRS  $\text{Bi}_2\text{Te}_{3-x}\text{Se}_x$  nanowires film..... 73
- Fig. 4.5-** GIXRD diffraction patterns obtained for (a) reference XRD of Bismuth Telluride Selenide ( $\text{Bi}_2\text{Te}_{2.5}\text{Se}_{0.5}$ ) mineral from the International Centre of Diffraction Data (ICDD) database (PDF 00-051-0643) and (b) drop-casted film of PRS  $\text{Bi}_2\text{Te}_{3-x}\text{Se}_x$  nanowires on a Si substrate. .... 74
- Fig.4.6-** GIXRD diffraction patterns obtained for (black line) drop-casted film of  $\text{Bi}_2\text{Te}_3$  nanowires and (red line) drop-casted film of  $\text{Bi}_2\text{Te}_{2.5}\text{Se}_{0.5}$  on a Si substrate for the range of (a)  $36^\circ - 40^\circ$  and (b)  $60^\circ - 70^\circ$  ..... 76
- Fig.4.7-** Photograph of single pass screen-printed (a) PVDF- $\text{Bi}_2\text{Te}_3$  and (b) PVDF- $\text{Bi}_2\text{Te}_{2.5}\text{Se}_{0.5}$  nanowire films..... 77
- Fig.4.8-** SEM images (a) of a top-down view of annealed PVDF- $\text{Bi}_2\text{Te}_3$  and (b) annealed PVDF- $\text{Bi}_2\text{Te}_{2.5}\text{Se}_{0.5}$  and screen-printed films, with an EDX spectrum of the (c) annealed PVDF- $\text{Bi}_2\text{Te}_3$  and (d) the annealed PVDF- $\text{Bi}_2\text{Te}_{2.5}\text{Se}_{0.5}$  films..... 78
- Fig.4.9-** GIXRD diffraction patterns obtained for (a) reference XRD of Bismuth Telluride Selenide ( $\text{Bi}_2\text{Te}_{2.5}\text{Se}_{0.5}$ ) mineral from the International Centre of Diffraction Data (ICDD) database (PDF 00-051-0643) and (b) screen-printed PRS  $\text{Bi}_2\text{Te}_{2.5}\text{Se}_{0.5}$  nanowire film annealed at  $400^\circ\text{C}$  for 2 hr in an Ar atmosphere on a Kapton substrate. .... 79
- Fig.4.10-**GIXRD diffraction patterns obtained for (a) reference XRD of tellurobismuthite ( $\text{Bi}_2\text{Te}_3$ ) mineral from the International Centre of Diffraction Data (ICDD) database (PDF 00-082-0358) (b) screen-printed PRS  $\text{Bi}_2\text{Te}_3$  nanowire film annealed at  $400^\circ\text{C}$  for 2 hr in an Ar atmosphere on a Kapton substrate..... 80
- Fig. 4.11-** GIXRD diffraction patterns obtained for (black line) screen-printed  $\text{Bi}_2\text{Te}_3$  nanowires annealed in an inert Ar atmosphere and (red line) screen-printed PRS  $\text{Bi}_2\text{Te}_{2.5}\text{Se}_{0.5}$  nanowire film annealed at  $400^\circ\text{C}$  for 2 hr in an inert Ar atmosphere on a Kapton substrate for the range of (a)  $10^\circ - 70^\circ$  and (b) zoomed in for  $66^\circ - 69^\circ$  ..... 81

- Fig. 4.12-** GIXRD diffraction patterns obtained for (black line) drop-casted film of PRS  $\text{Bi}_2\text{Te}_{2.5}\text{Se}_{0.5}$  nanowires on Si substrate and (red line) screen-printed PRS  $\text{Bi}_2\text{Te}_{2.5}\text{Se}_{0.5}$  nanowire film annealed at 400 °C for 2 hr in an inert Ar atmosphere on a Kapton substrate for the range of (a) 10 °-70 °, (b) zoomed in for 37 °- 40 ° and (c) zoomed in for 62 °- 64 °. ....82
- Fig. 4.13-** Room temperature TE properties of (a) Seebeck coefficient, (b) electrical conductivity and (c) power factor for 1 printing pass and 3 printing pass films of PVDF- $\text{Bi}_2\text{Te}_3$  and PVDF- $\text{Bi}_2\text{Te}_{2.5}\text{Se}_{0.5}$  films annealed at 400 °C for 2 hr in an inert Ar atmosphere. The uncertainty is based on the standard deviation of the results and the measured thickness of the films. ....83
- Fig.4.14-** Room temperature (a) charge carrier mobility and (b) charge carrier concentration for 1 printing pass and 3 printing pass films of PVDF- $\text{Bi}_2\text{Te}_3$  and PVDF- $\text{Bi}_2\text{Te}_{2.5}\text{Se}_{0.5}$  films annealed at 400 °C for 2 hr in an inert Ar atmosphere. The uncertainty is based on the standard deviation of the results and the measured thickness of the films.84
- Fig. 4.15-** The resistance normalized to the initial resistance of the single printing pass PVDF- $\text{Bi}_2\text{Te}_3$  and PVDF- $\text{Bi}_2\text{Te}_{2.5}\text{Se}_{0.5}$  for 1000 bending cycles, with a bending radius of 10 mm. ....86
- Fig.5.1-** SEM images (a) of a top-down view of the drop-casted  $\text{Bi}_x\text{Sb}_{1-x}\text{Te}_3$  nanoplatelets on a Si substrate, with (b) showing the nanoplatelet's lengths and thicknesses. (c) EDX spectrum of the drop-casted nanoplatelets film.....90
- Fig. 5.2-** GIXRD diffraction patterns obtained for (a) reference of Bismuth Antimony Telluride ( $\text{Bi}_{0.4}\text{Sb}_{1.6}\text{Te}_3$ ) mineral from ICDD database (PDF 01-072-1836) and (b) for the drop-casted film of  $\text{Bi}_{0.4}\text{Sb}_{1.6}\text{Te}_3$  nanoplatelets on a Si substrate. ....91
- Fig.5.3-** Comparison between the GIXRD diffraction patterns for the (black) drop-casted film of  $\text{Bi}_2\text{Te}_3$  nanowires and (red) for the drop-casted film of  $\text{Bi}_{0.4}\text{Sb}_{1.6}\text{Te}_3$  nanoplatelets between 25 ° and 45 °. ....92
- Fig. 5.4-** SEM images (a) of a top-down view of scaled-up PRS  $\text{Bi}_{0.4}\text{Sb}_{1.6}\text{Te}_3$  nanoplatelets on a Si substrate, with (b) showing the nanoplatelet's lengths and thicknesses. While (c) an EDX spectrum of the drop-casted PRS  $\text{Bi}_{0.4}\text{Sb}_{1.6}\text{Te}_3$  nanoplatelets film.....93
- Fig. 5.5-** GIXRD diffraction patterns obtained for (a) reference of Bismuth Antimony Telluride ( $\text{Bi}_{0.4}\text{Sb}_{1.6}\text{Te}_3$ ) mineral from ICDD database (PDF 01-072-1836) and (b) for the drop-casted film of scaled-up PRS  $\text{Bi}_{0.4}\text{Sb}_{1.6}\text{Te}_3$  nanoplatelets on a Si substrate. ....94

## Table of Figures

- Fig. 5.6-** Image of 5 x 50 mm PVDF-Bi<sub>0.4</sub>Sb<sub>1.6</sub>Te<sub>3</sub> nanoplatelet film for 4 printing pass. .... 95
- Fig. 5.7-** SEM images of annealed PVDF-Bi<sub>0.4</sub>Sb<sub>1.6</sub>Te<sub>3</sub> nanoplatelet films at (a&b) low and (c&d) high magnifications. While (e) the EDX spectrum for an annealed PVDF-Bi<sub>0.4</sub>Sb<sub>1.6</sub>Te<sub>3</sub> nanoplatelet film of 1 printed pass. .... 96
- Fig.5.8-** SEM images (a&b) of a top-down view of PRS Te nanorods on a Si substrate. While (c) an EDX spectrum of the drop-casted PRS Te nanorods film. .... 99
- Fig. 5.9-** GIXRD diffraction patterns obtained for (a) reference of Tellurium (Te) mineral from ICDD database (PDF 00-086-2268) and (b) for the drop-casted film of PRS Te nanorods on a Si substrate. .... 99
- Fig. 5.10-** Images of the (a) 2 and (b) 4 printed pass PVDF-Te nanorod films. While (c) shows the films before and after annealing at 450 °C for 1 hr in an Ar inert atmosphere. 100
- Fig. 5.11-** Image of (a) PVDF-Bi<sub>0.4</sub>Sb<sub>1.6</sub>Te<sub>3</sub> nanoplatelets and (b) PVDF-Bi<sub>0.4</sub>Sb<sub>1.6</sub>Te<sub>3</sub> + 8 % Te. ... 102
- Fig.5.12-** SEM images of PVDF-Bi<sub>0.4</sub>Sb<sub>1.6</sub>Te<sub>3</sub> nanoplatelet with 0 % (a,c,e & g) and 12 % (b,d,f & h) Te nanorods films annealed at 450 °C for 1 hr in an inert Ar atmosphere. While (i) the EDX spectrum for an annealed PVDF-Bi<sub>0.4</sub>Sb<sub>1.6</sub>Te<sub>3</sub> nanoplatelet with 0 % Te nanorods and (j) the EDX spectrum for the film with 12 % Te nanorods. .... 105
- Fig.5.13-** GIXRD diffraction patterns obtained for (a) reference of Bismuth Antimony Telluride (Bi<sub>0.4</sub>Sb<sub>1.6</sub>Te<sub>3</sub>) mineral from ICDD database (PDF 01-072-1836) and (b) PVDF-Bi<sub>0.4</sub>Sb<sub>1.6</sub>Te<sub>3</sub> nanoplatelet containing (b) 0 %, (c) 4 %, (d) 8 %, (e) 12 %, (f) 16 % and (g) 20 % Te nanorods films annealed at 450 °C for 1 hr in an inert Ar atmosphere. .... 106
- Fig. 5.14-** GIXRD diffraction patterns obtained between 24 ° and 33 ° for (a) reference of Bismuth Antimony Telluride (Bi<sub>0.4</sub>Sb<sub>1.6</sub>Te<sub>3</sub>) mineral from ICDD database (PDF 01-072-1836) and (b) 5% PVDF-Bi<sub>0.4</sub>Sb<sub>1.6</sub>Te<sub>3</sub> nanoplatelet containing (b) 0 %, (c) 4 %, (d) 8 %, (e) 12 %, (f) 16 % and (g) 20 % Te nanorods films annealed at 450 °C for 1 hr in an inert Ar atmosphere. With the lattice orientations identified for (1 0 1) for Te ICDD database (PDF 00-086-2268), (0 1 5) Bi<sub>0.4</sub>Sb<sub>1.6</sub>Te<sub>3</sub> ICDD database (PDF 01-072-1836) and in red the (0 1 5) (Bi<sub>0.5</sub>Sb<sub>0.5</sub>)<sub>4</sub>Te<sub>3</sub> ICDD database (PDF 01-072-1838). 107
- Fig. 5.15-** Room temperature TE properties of (a) Seebeck coefficient, (b) electrical conductivity, (c) charge carrier mobility, (d) log<sub>10</sub> scale charge carrier concentration and (e) power factor for Bi<sub>0.4</sub>Sb<sub>1.6</sub>Te<sub>3</sub> nanoplatelet + Te nanorod films annealed at 450 °C for 1 hr

- in an inert Ar atmosphere. The uncertainty is based on the standard deviation of the results and the measured thickness of the films. ....109
- Fig. 5.16-** The resistance normalized to the initial resistance of the single printing pass PVDF-Bi<sub>0.4</sub>Sb<sub>1.6</sub>Te<sub>3</sub>+12 % Te nanorod film on Kapton for 1000 bending cycles, with a bending radius of 10 mm.....111
- Fig.5.17-** Image of single-leg PVDF-Bi<sub>0.4</sub>Sb<sub>1.6</sub>Te<sub>3</sub> nanoplatelet + 12 % Te nanorod FTEG device.112
- Fig.5.18-** Graphs show (a) the voltage vs current response for different temperature differences, (b) the open-circuit voltage with respect to the temperature difference, (c) the output power vs current and (d) the maximum output power with respect to the temperature difference of the single-leg 5% PVDF-Bi<sub>0.4</sub>Sb<sub>1.6</sub>Te<sub>3</sub> nanoplatelet + 12 % Te nanorod FTEG device. ....113
- Fig.5.19-** The thermal images are taken of the single-leg PVDF- Bi<sub>0.4</sub>Sb<sub>1.6</sub>Te<sub>3</sub> nanoplatelet + 12 % Te nanorod FTEG device during measuring with a normalised temperature range of (a) 9.1 K, (b) 15.9 K, (c) 21.1 K,(d) 27.6 K, (e) 34.3 K, (f) 39.7 K and (g) 46.4 K.113
- Fig.5.20-** Image of a 3 thermocouple FTEG device on Kapton made of p-type PVDF-Bi<sub>0.4</sub>Sb<sub>1.6</sub>Te<sub>3</sub> nanoplatelet + 12 % Te nanorod films and n-type PVDF-Bi<sub>2</sub>Te<sub>3</sub> nanowire films. The thermocouples are connected via silver metal contacts.....114
- Fig. 5.21-** Graphs show (a) the voltage vs current response for different temperature differences, (b) the open-circuit voltage with respect to the temperature difference, (c) the output power vs current and (d) the maximum output power with respect to the temperature difference of a 3 thermocouple FTEG device on Kapton. ....115
- Fig. 5.22-** The thermal images are taken of the 3 thermocouple FTEG device on Kapton during measuring with a normalised temperature range of (a) 7.9 K, (b) 13.5 K, (c) 18.2 K, (d) 22.1 K, (e) 26.9 K, (f) 30.7 K and (g) 35.9 K.....116
- Fig. 6.1-** SEM images (a&b) of a top-down view of scaled-up Te nanorods on a Si substrate, with red circles indicating areas where the nanorods are growing out of the dice-shaped nanoparticles. While (c) an EDX spectrum of the drop-casted scaled-up Te nanorods film.....122
- Fig.6.2-** GIXRD diffraction patterns obtained for reference of Tellurium (Te) mineral from ICDD database (a) (PDF 00-086-2268) and (b) (PDF 00-085-0554). With the black and red indexes associated for (a) and (b) respectively. As well as the drop-casted films

## Table of Figures

- on Si substrates for (c) PRS Te nanorods and (d) the scaled-up PRS Te nanorods. .... 123
- Fig.6.3-** The (a) resistance normalized to the initial resistance of the single printing pass PVDF- Te nanorod film on polyurethane-based interface layer on polyester-cotton for 1000 bending cycles, with a bending radius of 10 mm and (b) photograph insert of curved composite PVDF-Te nanorod film. .... 124
- Fig. 6.4-** Image of the single-leg p-type PVDF-Te nanorod FTEG device. .... 125
- Fig.6.5-** Graphs showing (a) the voltage vs current response for different temperature differences, (b) the open-circuit voltage with respect to the temperature difference, (c) the output power vs current and (d) the maximum output power with respect to the temperature difference of a single-leg PVDF-Te nanorod FTEG device..... 126
- Fig.6.6-** The thermal images are taken of the single-leg PVDF-Te nanorod FTEG device during measuring with a normalised temperature range of (a) 8.0 K, (b) 10.3 K, (c) 13.8 K, (d) 18.2 K, (e) 21.5 K, (f) 26.0 K and (g) 29.8 K..... 127
- Fig.A.1-** Photograph (a) of screen-printed 20% PVDF-Bi<sub>2</sub>Te<sub>3</sub> nanowire film on polyester cotton ~200 μm with (b) an SEM image of one of the polyester-cotton fibres coated by the composite and (c) an image of the screen-printed 20% PVDF-Bi<sub>2</sub>Te<sub>3</sub> nanowire film on a Kapton substrate with (d) an SEM image of the Bi<sub>2</sub>Te<sub>3</sub> nanowire film on a Kapton annealed at 300 °C for 1 hr in an inert Ar atmosphere. .... 137
- Fig.A.2-** GIXRD diffraction patterns obtained for (a) reference XRD of tellurobismuthite (Bi<sub>2</sub>Te<sub>3</sub>) mineral from International Centre of Diffraction Data (ICDD) database (PDF 01-082-0358) (b) unannealed screen-printed 20% PVDF-Bi<sub>2</sub>Te<sub>3</sub> nanowires, (c) screen-printed Bi<sub>2</sub>Te<sub>3</sub> nanowires annealed in an inert Ar atmosphere at (c) 200 °C, (d) 250 °C and (e) 300 °C for 1 hr..... 139
- Fig.A.3-** TGA of PVDF powder from the range of 30 °C to 900 °C in a nitrogen inert environment. .... 139
- Fig.A.4-** Image of 20% PVDF-Bi<sub>2</sub>Te<sub>3</sub> films printed onto (left) SiO<sub>2</sub>/Si and (right) Si wafer pieces.140
- Fig.A.5-** GIXRD diffraction patterns obtained for (a) the SiO<sub>2</sub>/Si substrate, (b) reference XRD of tellurobismuthite (Bi<sub>2</sub>Te<sub>3</sub>) mineral from International Centre of Diffraction Data (ICDD) database (PDF 01-082-0358), screen-printed 20% PVDF-Bi<sub>2</sub>Te<sub>3</sub> nanowires

annealed in an inert Ar atmosphere at (c) 300 °C, (d) 350 °C, (e) 400 °C, (f) 450 °C and (g) 500 °C for 1 hr.....141

**Fig.B.1-** An (a) SEM image of drop-casted annealed  $\text{Bi}_2\text{Te}_3$  nanowires on a Si substrate. Images of the nanowire powder before (b) and after (c) annealing at 400 °C for 2 hr in an inert Ar atmosphere. ....143

**Fig.B.2-** Image (a) of annealed drop-casted  $\text{Bi}_2\text{Te}_3$  nanowire films, with (b-c) SEM images. ....144

**Fig.C.1-** Images of the screen-printed PVDF- $\text{Bi}_{0.4}\text{Sb}_{1.6}\text{Te}_3$  nanoplatelet film before (a) and after (b) the Kapton substrate had been peeled off the alumina plate. ....146

**Fig.D.1-** SEM images of PVDF- $\text{Bi}_{0.4}\text{Sb}_{1.6}\text{Te}_3$  nanoplatelet with a Te nanorod content of (a) 4 %, (b) 8 % and (c) 12 %.....148

**Fig.E.1-** Graph of the viscosity of the 5 % PVDF- $\text{Bi}_2\text{Te}_3$  nanowire paste with respect to the number of readings taken. ....149



## List of Accompanying Materials

### Journal article

“Screen-printed Bismuth telluride nanostructured composites for flexible thermoelectric applications” A. Amin, R. Huang, D. W. Newbrook, V. Sethi, S. P. Beeby and I. S. Nandhakumar, *J. Phys. Energy*, , DOI:10.1088/2515-7655/ac572e.

### Conference presentations

Southampton Electrochemistry Conference – May 2022

Virtual Conference on Thermoelectrics –July 2022



## Research Thesis: Declaration of Authorship

Print name: Aran Amin

Title of thesis: Flexible Thermoelectric Energy Generators for E-textiles

I declare that this thesis and the work presented in it are my own and has been generated by me as the result of my own original research.

I confirm that:

1. This work was done wholly or mainly while in candidature for a research degree at this University;
2. Where any part of this thesis has previously been submitted for a degree or any other qualification at this University or any other institution, this has been clearly stated;
3. Where I have consulted the published work of others, this is always clearly attributed;
4. Where I have quoted from the work of others, the source is always given. With the exception of such quotations, this thesis is entirely my own work;
5. I have acknowledged all main sources of help;
6. Where the thesis is based on work done by myself jointly with others, I have made clear exactly what was done by others and what I have contributed myself;
7. Parts of this work have been published as:

“Screen-printed Bismuth telluride nanostructured composites for flexible thermoelectric applications” A. Amin, R. Huang, D. W. Newbrook, V. Sethi, S. P. Beeby and I. S. Nandhakumar, *J. Phys. Energy*, , DOI:10.1088/2515-7655/ac572e.

Signature: ..... Date:23/09/22



## Acknowledgements

I'd like to thank my supervisor Dr. Iris Nandhakumar whose support, guidance and encouragement have allowed my research to come to the point where it is today and without which I would not be at the final stage of my PhD candidacy. I'd like to further thank my co-supervisor Prof. Stephan Beeby whose insights have been a huge help in the direction of my PhD project.

I must also acknowledge my funding sources, my project's industrial sponsor Carrington textiles, and the Engineering and Physical Sciences Research Council (EPSRC). In addition, I'd like to acknowledge the Royal Society of Chemistry for their Experimental Research Grant.

Additionally, I want to thank the members of the SET group Dr. Ruomeng Huang, Dr. Daniel Newbrook and Vikesh Sethi for the access to and measuring of my samples' thermoelectric properties at different temperature ranges as well as for measuring the device power outputs.

I would like to thank my colleagues and friends in the Nandhakumar group and in particular want to thank Samuel Beddoe, Josh White and Dr. Samuel Perry, it was fun both in and out of the lab with you guys. I also want to say that I enjoyed learning about your projects and trying to help you guys with your issues while you helped me with mine. I also want to thank my colleagues in the SEMS Group especially Dr. Shang Yong and Dr. Abiodun Komolafe for lending me their experience and teaching me how to screen-print and test the flexibility of my samples. My sincere best wishes for the future careers of all my colleagues who I've had the pleasure of working with.

I also want to thank my family and friends for supporting me during these trying times and for always being willing to listen to me rambling on about my work, as well as, for asking questions and giving me the opportunity to explain my work at different technical levels, which allowed me to see research outside the bubble of academia.

Finally, I want to thank the person who has become my world during these 4 years, mi Lulú who has been my rock and supported me during the bad times as well as being my partner in celebrating with me during the good. I will never forget our times together in the labs and office corridors as well as around Southampton and beyond. You've helped make this PhD such a special time in my life, which has shaped the person I am today. Gracias, zor spas and thank you for putting up with my utter nonsense and crazy ideas mi pandita.



## Definitions, Abbreviations and Symbols

IoT .....	Internet of things
E-textiles.....	Electronic textiles
TEG .....	Thermoelectric generators
FTEG .....	Flexible thermoelectric generators
GPS .....	Global positioning system
$\text{Bi}_2\text{Te}_3$ .....	Bismuth telluride
TE.....	Thermoelectric
VB .....	Valence band
CB .....	Conduction band
Si.....	Silicon
$\Delta T$ .....	Thermal gradient
$\Delta V$ .....	Electrostatic potential or Seebeck voltage
S.....	Seebeck coefficient
ZT.....	Figure of merit
$\sigma$ .....	Electrical conductivity
$\kappa$ .....	Thermal conductivity
PF.....	Power factor
$\eta$ .....	Efficiency
$\kappa_e$ .....	Electronic thermal conductivity
$\kappa_l$ .....	Lattice thermal conductivity
$n(E)$ .....	Charge carrier density at energy E
$\mu(E)$ .....	Charge carrier mobility at energy E
n .....	Charge carrier concentration
$\mu$ .....	Charge carrier mobility
$\text{Sb}_2\text{Te}_3$ .....	Antimony telluride
$\text{Bi}_2\text{Te}_{2.7}\text{Se}_{0.3}$ .....	Bismuth telluride selenide

## Definitions, Abbreviations and Symbols

$\text{Bi}_{0.5}\text{Sb}_{1.5}\text{Te}_3$ .....	Bismuth antimony telluride
Bi .....	Bismuth
Te .....	Tellurium
Se .....	Selenium
Sb .....	Antimony
DOS .....	Electronic density of states
$g(E)$ .....	Density of states per unit volume and energy
MOCVD .....	Metalorganic chemical vapour deposition
EG.....	Ethylene glycol
PRS .....	Polyol reflux synthesis
SPS .....	Spark plasma sintering
PVP.....	Polyvinylpyrrolidone
$\text{TeO}_2$ .....	Tellurium dioxide
$\text{Bi}(\text{NO}_3)_3 \cdot 5\text{H}_2\text{O}$ .....	Bismuth nitrate pentahydrate
FGA .....	Forming gas atmosphere
PEDOT:PSS .....	Poly(3,4-ethylenedioxythiophene)polystyrene sulfonate
PANI .....	Polyaniline
PVDF .....	Polyvinylidene fluoride
DMSO.....	Dimethyl sulfoxide
RBF.....	Round bottom flask
KOH.....	Sodium hydroxide
SeO.....	Selenium oxide
Te solution .....	A solution of Ethylene glycol containing dissolved Tellurium dioxide, Sodium hydroxide and Polyvinylpyrrolidone
Bi solution .....	A solution of Ethylene glycol containing dissolved Bismuth nitrate pentahydrate
Au.....	Gold
$\text{Sb}(\text{CH}_3\text{CO}_2)_3$ .....	Antimony acetate

BiSb solution .....	A solution of Ethylene glycol containing dissolved Bismuth nitrate pentahydrate and Antimony acetate
NMP .....	N-Methyl-2-pyrrolidone
SEM .....	Scanning electron microscope
BSE .....	Backscatter electrons (BSE)
SE.....	Secondary electrons
EDX.....	Energy-dispersive x-ray spectroscopy
GIXRD .....	Grazing incidence X-ray diffraction
ICDD .....	International Centre for Diffraction Data
$\rho$ .....	Resistivity
Single-leg.....	A thermoelectric generator which only uses one material
Ar.....	Argon
INN .....	Interconnected nanostructured network
TGA.....	Thermogravimetric analysis
20 % PVDF-Bi <sub>2</sub> Te <sub>3</sub> .....	Composite film made from 20 % PVDF and 80 % Bismuth telluride
10 % PVDF-Bi <sub>2</sub> Te <sub>3</sub> .....	Composite film made from 10 % PVDF and 90 % Bismuth telluride
5 % PVDF-Bi <sub>2</sub> Te <sub>3</sub> .....	Composite film made from 5 % PVDF and 95 % Bismuth telluride
PVDF-Bi <sub>2</sub> Te <sub>3</sub> .....	Composite film of PVDF and Bismuth telluride
PVDF-Bi <sub>2</sub> Te <sub>2.5</sub> Se <sub>0.5</sub> .....	Composite film of PVDF and Bismuth telluride selenide
BTP1 .....	One printing pass of screen-printed bismuth telluride nanowires
BTP1-INNs .....	One printing pass of screen-printed bismuth telluride INNs
BTP3 .....	Three printing passes of screen-printed bismuth telluride nanowires
BTSP1 .....	One printing pass of screen-printed Bismuth telluride selenide nanowires
BTSP3 .....	Three printing passes of screen-printed Bismuth telluride selenide nanowires
PVDF-Bi <sub>0.4</sub> Sb <sub>1.6</sub> Te <sub>3</sub> .....	Composite film of PVDF and Bismuth antimony telluride
PVDF-Te.....	Composite film of PVDF and Tellurium



# Chapter 1 Introduction

## 1.1 Aims, Objectives and Project motivations

This project aimed to establish an industrially scalable procedure for the development of printed nanostructured Tellurium and Bismuth telluride-based flexible thermoelectric generators (FTEGs) for low-temperature applications in electronic textiles (E-textiles) and the internet of things (IoT).

The objectives to reach this overarching aim were to, identify and optimise a procedure to synthesise large batches of Tellurium and Bismuth telluride-based nanostructures. Once that was achieved the next stage was to identify a printing technique for the deposition of large-area thermoelectric films. Following that inks/pastes would be formulated and optimised depending on the requirements needed for the printing technique. Finally, post-printing annealing procedures are performed on the printed films and optimised for the highest thermoelectric properties, as well as conducting bending tests on the printed films to examine their flexibility, and to assess whether they meet the project aims.

### 1.1.1 Project motivations

Research in the field of devices for the internet of things (IoT) to be integrated into wearable electronic textile (E-textile) systems has expanded over the years, with the development of low-power-consuming sensors, displays and communication devices <sup>[1-4]</sup>. To ensure the fully autonomous nature of such wearable systems, they need a constant power source which is not possible with batteries alone, since they need to be recharged which restricts the functionality of these wearable systems <sup>[4]</sup>. One potential route to obtaining a constant power source is to harvest the thermal energy output of the human body. As a useful side-effect of metabolism, the human body constantly emits heat between  $50 \text{ Wm}^{-2}$  and  $150 \text{ Wm}^{-2}$  <sup>[5,6]</sup>. This body heat can be utilised to generate electricity via the use of thermoelectric generators (TEG) <sup>[7,8]</sup>. Table 1.1 shows the potential electrical power generation for different parts of the human body. The advantage of TEGs is that they are solid-state devices with long life spans, with no required internal maintenance as they have no moving parts <sup>[8]</sup>. Additionally, they can be scaled-up or miniaturized to generate a power output at different temperature ranges for a variety of situations: e.g. using bulk TEGs for industrial heat recovery potentially producing a power output at the  $\sim 10 \text{ kW}$  scale or to power wristwatches using human body heat to generate a power output of  $\sim 1 \mu\text{W}$  <sup>[7,8]</sup>.

However, current commercial TEGs are limited in their application due to being bulky, rigid and having low efficiencies. As such they have remained in niche fields e.g. TEGs being used as a power source in deep-space satellites <sup>[9]</sup>.

**Table 1.1**-Potential electrical power output from different parts of the human body based on how active the person is between low and high activity <sup>[6,7]</sup>.

Body part	Power generation (mW)
Forehead	2.3-27.6
Chest	3.1-36.6
Arm	1.7-20.2
Forearm	1.3-16.1
Abdomen	3.1-36.6
Thigh	2.4-28.8
Foot	2.1-25.2

To expand the applications of TEGs into wearable systems they need to be developed with greater mechanical flexibility to more effectively harvest the thermal energy from the curved surfaces of the human body. An example of the potential use of wearable flexible thermoelectric generators (FTEGs) is in preventive healthcare, where wearable FTEGs and sensors could be integrated into patient gowns, where the FTEGs could power said sensors (<1.5 mW) to measure patient's blood pressure and respiration rate <sup>[6,7,10]</sup>. In cases such as this, so long as the thermal gradient between the body and ambient environment is sufficient, FTEGs could replace batteries in providing electricity to low power consumption devices so long as there is a constant thermal gradient through the FTEGs. This would allow the integrated wearable systems in the patient gowns to be fully autonomous, while constantly monitoring the patient's physiology, biochemistry and motion <sup>[3]</sup>. Additionally, given the need for a higher temperature gradient for higher energy harvesting output, more attainable application routes could be found in extreme environmental situations where FTEGs could be integrated into wearable systems for arctic and desert conditions. FTEGs could play a role by acting as a power source for a wearable E-textile system on arctic and desert clothing, potentially powering GPS and other sensors. To ensure that FTEGs can play a role in these future applications, they need to be efficient enough to meet the energy demands of these various potential devices (GPS, biosensors and other IoTs).

As such the main materials that will be used to fabricate the FTEG devices in this project are bismuth telluride ( $\text{Bi}_2\text{Te}_3$ )-based, as they have the highest thermoelectric (TE) properties for the low-temperature gradients between the human body and the ambient environment <sup>[10,11]</sup>.

## 1.2 Introduction to thermoelectric theory

### 1.2.1 Initial discovery and research on thermoelectric generators

The ability of TEGs to harvest energy is based on the Seebeck effect, discovered by Thomas Johann Seebeck in 1821 <sup>[7,8]</sup>. He observed that a potential difference could be generated between a temperature gradient of two dissimilar metals. The phenomenon was further investigated by Gustav Magnus in 1851 to reveal that the potential difference produced between the two junctions of two dissimilar metals was directly proportional to the applied temperature difference <sup>[12]</sup>. Modern-day TE research is based on the work of Abram Loffe and his collaborators in the 1950-1970s. During this time they introduced the concept of TE energy conversion where semiconductors were identified as a promising TE material owing to their higher TE energy conversion efficiencies <sup>[12,13]</sup>.

### 1.2.2 Semiconductor theory

Semiconductors are a class of material between conductors and insulators. The division of materials between these classes is based on the material's electronic properties. For bulk materials, their electronic structure can be thought of as bands which are described by band theory. In band theory, the material's electronic structure has a valence band (VB) filled with valence electrons and a conduction band (CB) with few electrons, split between the Fermi level, which can be seen in Fig. 1.1 <sup>[14]</sup>. In the case of conductors, their bands overlap allowing for free electrons to move through the material. As the overlap of CB and VB bands forms one band which is partly filled and empty, this gives conductors high electrical conductivity <sup>[15]</sup>. Insulators have a large band gap between their VB and CB which makes it difficult for electrons to move freely. Although semiconductors also exhibit band gaps, theirs are much smaller than insulators. An example of the size difference is that the band gap for a semiconductor such as Silicon (Si) is 1.1 eV while for an insulator like Diamond its 5 eV <sup>[14]</sup>.

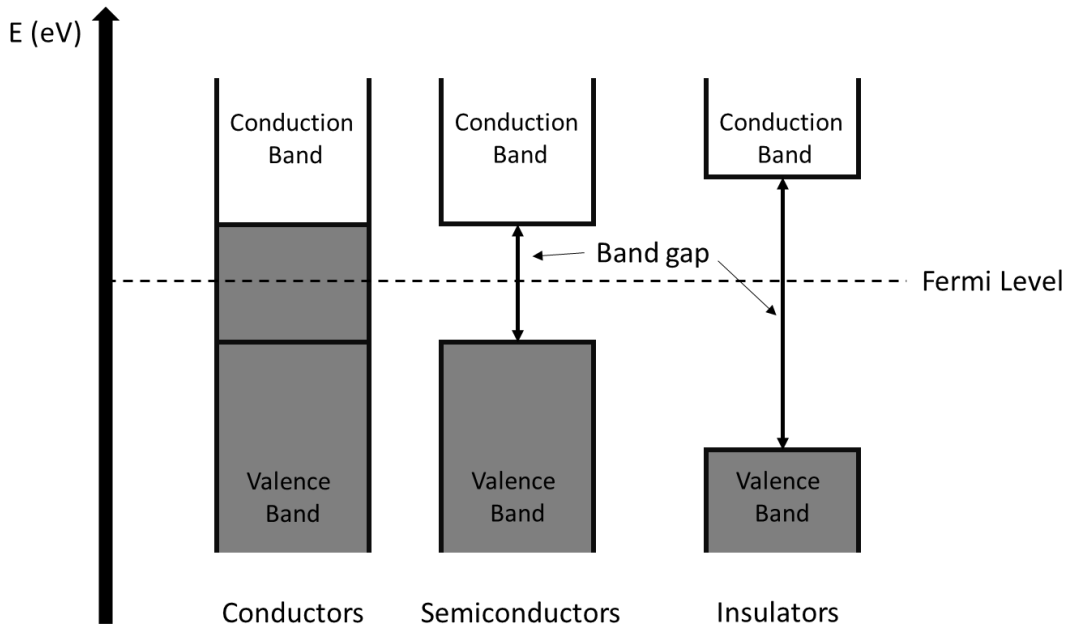


**Fig.1.1-** The diagram shows the basic electronic band structure of conductors, semiconductors and insulators. The CB and VB of the conductors overlap through the Fermi level, while semiconductors and insulators have a band gap.

As mentioned above free electrons in conductors can move between the overlapping bands, however, this is not the case for semiconductors. Due to their small band gaps, valence electrons can be excited via thermal energy from the VB to the CB, allowing a current to flow in the material [14,16]. When an electron is excited to the CB it leaves a vacant position or hole in the VB where it once was. This hole is a quasi-particle that is treated as having an equal but opposite charge to the excited electron [16].

Semiconductors are further split into undoped/intrinsic and doped/extrinsic semiconductors. Intrinsic semiconductors such as Si and  $\text{Bi}_2\text{Te}_3$  are perfect crystals with no defects and no free electrons as all their atoms' outer electron shells are filled. As such intrinsic semiconductors behave similarly to insulators, as at 0 K they have a filled VB and an empty CB [14-17]. Extrinsic semiconductors have defects/impurities in their crystal structure where some atoms' outer electron shells contain extra electrons or holes. These defects are due to foreign atoms being added to the crystal, the process of which is known as doping. Depending on the type of dopant a semiconductor can be doped to contain extra electrons and become an n-type semiconductor or extra holes and become a p-type semiconductor. These extra charge carriers are loosely bound to their atoms, while their atoms are rigidly held within the semiconductor crystal. The atoms used for n-type doping are known as donor atoms as they give electrons while the p-type is known as acceptor atoms.

By doping the semiconductor, the Fermi level shifts accordingly as shown in Fig. 1.2. For n-type doping, extra electron energy levels are formed closer to the CB and an increase in the concentration of the electrons in the CB compared to the holes in the VB causes the Fermi level to shift towards the CB. While in the case of p-type doping extra holes in the band gap allow for the excitation of the VB electrons leaving holes in the VB. The resulting higher concentration of holes in the VB compared to electrons in the CB causes the Fermi level to shift towards the VB <sup>[14-17]</sup>.

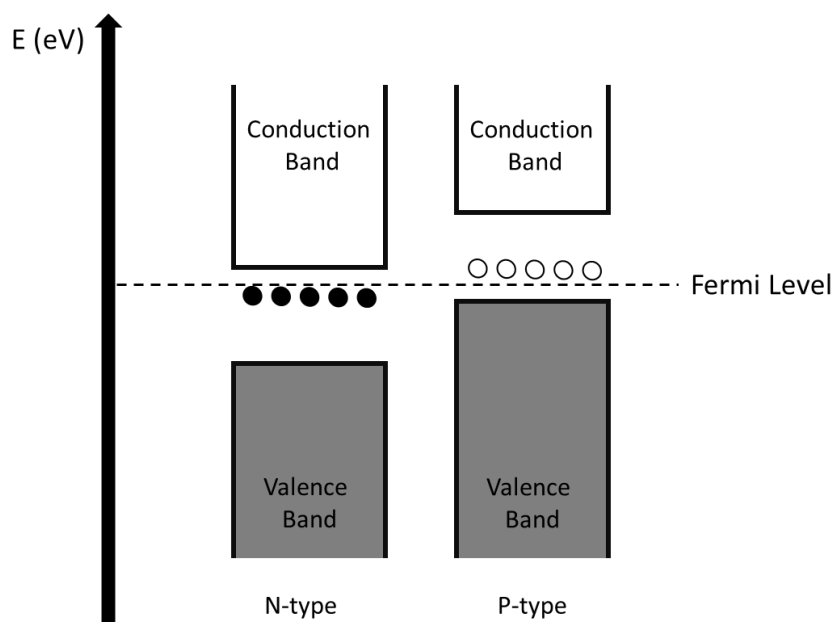


**Fig. 1.2-** The diagram shows the band structure for n-type and p-type semiconductors with the Fermi level shifted towards either the CB or VB depending on the type of doping, with filled circles representing extra electron energy levels and empty circles representing extra hole energy levels.

### 1.2.3 Current semiconductor-based thermoelectric generator devices

The current TEG device's architecture uses p-type and n-type semiconductors as TE legs, which are connected in series electrically, with heat moving in parallel through the device <sup>[7]</sup>. To generate a useable output power, TEG devices use multiple pairs of TE legs <sup>[11]</sup> as shown in Fig.1.3.

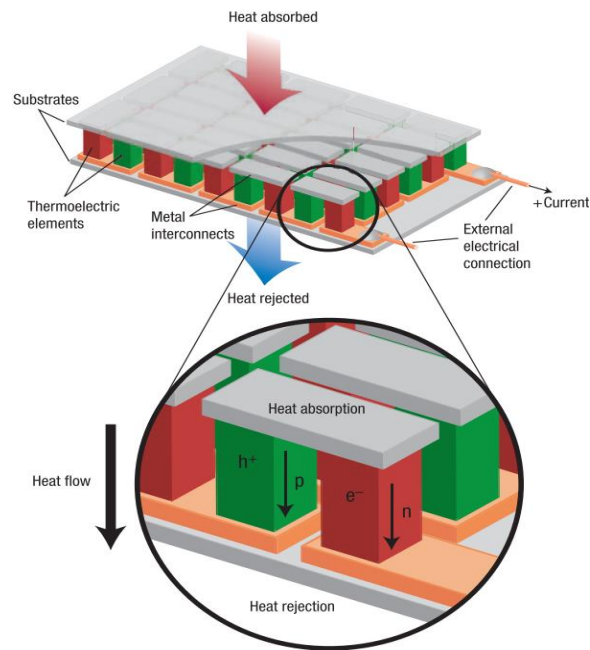
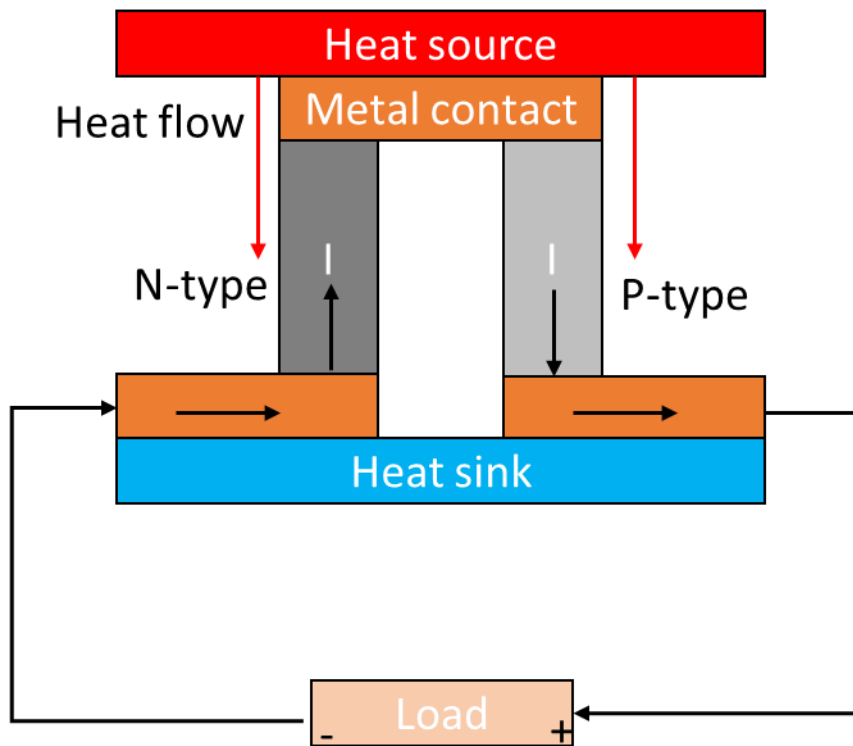


**Fig.1.3-** TEG illustration displaying the TEG set-up for a single pair of p-type and n-type legs connected electrically in series via a metal contact and thermally in parallel (top), while the other image shows the TEG device as a series of TEG pairs with heat passing through the device producing a current as an output (bottom) from Snyder et al <sup>[11]</sup>.

The TEG uses the thermal gradient ( $\Delta T$ ) between the heat flow from the hot side/heat source to the cold side/heat sink, to generate an electrostatic potential or Seebeck voltage ( $\Delta V$ )<sup>[12]</sup>. In the TEG device, the phonons migrate from the heat source to the heat sink of the p and n-type semiconductors as the heat flow, shown in Fig. 1.3. The Seebeck voltage arises from the diffusion of both electron and hole charge carriers in the semiconductors in the direction of the heat flow until the heterogeneous charge distribution equilibrates<sup>[18]</sup>. This occurs when there is a build-up of the majority and minority charge carriers on the cold and hot sides respectively, forming an electric potential difference across the material. This phenomenon is known as the Seebeck effect and when both p and n-type semiconductors are connected by a metal contact a current is produced.

#### 1.2.4 Thermoelectric properties

The Seebeck effect is measured by using the Seebeck coefficient ( $S$ ), which is a fundamental property of TE materials, that is calculated as:

$$S = -\frac{\Delta V}{\Delta T} \quad (1.1)$$

$S$  has the units of  $\mu\text{VK}^{-1}$  and can be negative or positive depending on the charge carrier concentration of the material i.e. more electrons (n-type,  $S < 0$ ) or more holes (p-type,  $S > 0$ )<sup>[7,8]</sup>.

In the literature, the figure of merit ( $ZT$ ) is related to the efficiency of the TEG. This is calculated using the equation below:

$$ZT = \frac{S^2 \sigma T}{\kappa} \quad (1.2)$$

Where  $S$  is the Seebeck coefficient,  $\sigma$  is the electrical conductivity with units  $\text{S m}^{-1}$  and  $\kappa$  is the thermal conductivity with units  $\text{Wm}^{-1}\text{K}^{-1}$  of the TE materials that make up the TEG respectively.  $\kappa$  is the total sum of the contributions of electronic and lattice thermal conductivities of the material seen in equation 1.5. While  $T$  is the absolute temperature and  $ZT$  is the dimensionless figure of merit<sup>[8]</sup>. To achieve the highest performance in TEG devices,  $S$  and  $\sigma$  need to be as high as possible, whilst  $\kappa$  needs to be as low as possible. Additionally, the numerator of the  $ZT$  is also often cited in the literature as the power factor (PF):

$$PF = S^2 \sigma \quad (1.3)$$

The PF with units  $\mu\text{Wm}^{-1}\text{K}^{-2}$  states the material's thermopower output<sup>[19-22]</sup>. The equation for the overall efficiency of a TEG is described as:

$$\eta = \frac{\Delta T}{T_H} \frac{\sqrt{1+ZT}-1}{\sqrt{1+ZT}+\frac{T_C}{T_H}} \quad (1.4)$$

## Chapter 1

The efficiency  $\eta$ , is determined by the thermal gradient  $\Delta T$  between the two ends of the TE material, where  $T_H$  and  $T_C$  denote the hot and cold ends of the material respectively <sup>[12]</sup>. Thus, determining the overall efficiency is quite difficult as it would change depending on the external temperature of the TE material's environment and the  $\Delta T$  at any one time.

Issues arise with the physical nature of the conductivity of TE materials, as the Wiedemann-Franz law states that by increasing  $\sigma$ ,  $\kappa$  also increases, due to the increase in the electrons' contribution to  $\kappa$  as shown in equation 1.8 <sup>[12,23]</sup>:

$$\kappa = \kappa_e + \kappa_l \quad (1.5)$$

Equation 1.5 relates to how the total thermal conductivity of a material is the sum of the electronic thermal conductivity  $\kappa_e$  from free charge carriers in the material and  $\kappa_l$  the lattice thermal conductivity contributions via vibrations in the lattice of the material <sup>[24]</sup>. Additionally, increasing either  $S$  or  $\sigma$  will decrease the other <sup>[8]</sup>. This can be shown with the Mott relation equation for  $S$  and the dependency equation of  $\sigma$  on carrier concentration and mobility that states:

$$S = \frac{\pi^2 k_B}{3 q} k_B T \left( \frac{1}{n} \frac{dn(E)}{dE} + \frac{1}{\mu} \frac{d\mu(E)}{dE} \right)_{E=E_F} \quad (1.6)$$

$$\sigma = q(\mu_e n + \mu_h p) \quad (1.7)$$

$$\kappa_e = L\sigma T \quad (1.8)$$

$$\eta_c = \frac{T_H - T_C}{T_H} \quad (1.9)$$

Where in equation 1.6 the Mott relation  $S$  is equated to the temperature  $T$ ,  $n(E)$  the carrier density at energy  $E$ ,  $\mu(E)$  the mobility at energy  $E$ ,  $E_F$  the Fermi energy,  $n$  the charge carrier concentration,  $\mu$  charge mobility as well as  $q$  and  $k_B$  the electronic charge and the Boltzmann constant. In equation 1.7 the electrical conductivity is equal to  $\mu_e$ ,  $\mu_h$  the electron and hole mobilities and  $n$ ,  $p$  the number densities of the electrons and holes respectively <sup>[12]</sup>. Finally, equation 1.8 describes the Wiedemann-Franz law as the electronic thermal conductivity  $\kappa_e$  being equal to the  $L$  the Lorenz factor for a material ( $2.45 \times 10^{-8} \text{ V}^2 \text{ K}^{-2}$  for metals and  $1.5 \times 10^{-8} \text{ V}^2 \text{ K}^{-2}$  for undoped semiconductors), the electrical conductivity  $\sigma$  and the material's temperature  $T$  <sup>[12]</sup>. This leads to a balancing act between the 3 TE parameters as shown in Fig. 1.4 to optimise the  $ZT$ . The optimal TE figure of merit ( $ZT$ ) calculated in equation 1.2, lies in the highly doped semiconductor range for charge carrier concentrations of  $10^{19}$ - $10^{20} \text{ cm}^{-3}$  as shown in Fig. 1.4 <sup>[8,11,12,18]</sup>. Finally, equation 1.9 represents the Carnot efficiency which is depended on the hot and cold sides of the TEG denoted as  $T_H$  and  $T_C$  respectively. This represents the thermodynamic limit for TEGs when  $ZT$  is infinite as can be seen in Fig. 1.7 <sup>[25]</sup>.

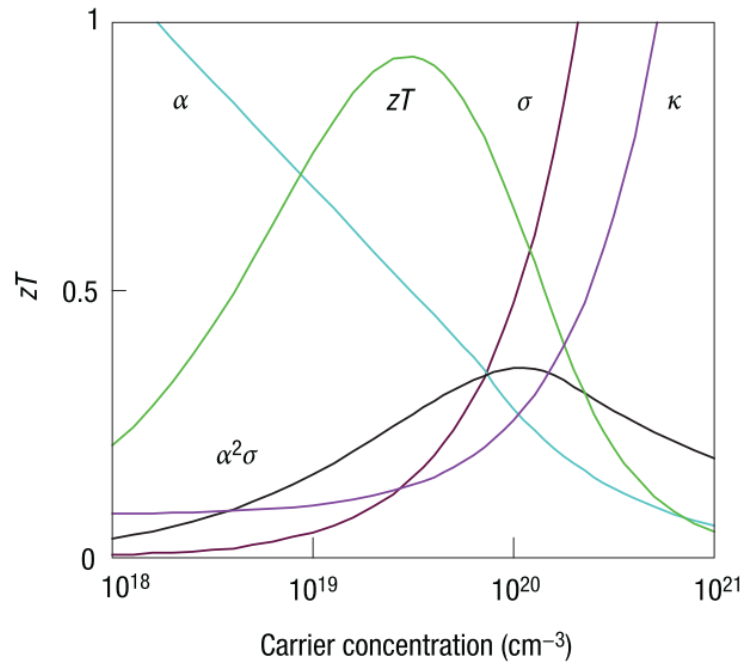


**Fig. 1.4-** The graph shows the optimised figure of merit  $zT$  for carrier concentration tuning is a balance between thermal conductivity ( $\kappa$ ) (y-axis range between 0  $\text{Wm}^{-1}\text{K}^{-1}$  and 10  $\text{Wm}^{-1}\text{K}^{-1}$ ), electrical conductivity ( $\sigma$ ) (y-axis range between 0  $\text{S cm}^{-1}$  and 5000  $\text{S cm}^{-1}$ ) and Seebeck coefficient ( $\alpha$ , y-axis between 0  $\mu\text{VK}^{-1}$  and 500  $\mu\text{VK}^{-1}$ ). Graph from Snyder et al <sup>[11]</sup>.

### 1.3 The properties of Bismuth telluride-based thermoelectric generators

The most efficient TE performing n-type and p-type semiconductors for different temperature ranges have been studied extensively with materials with the highest  $zT$  shown in Fig. 1.5.

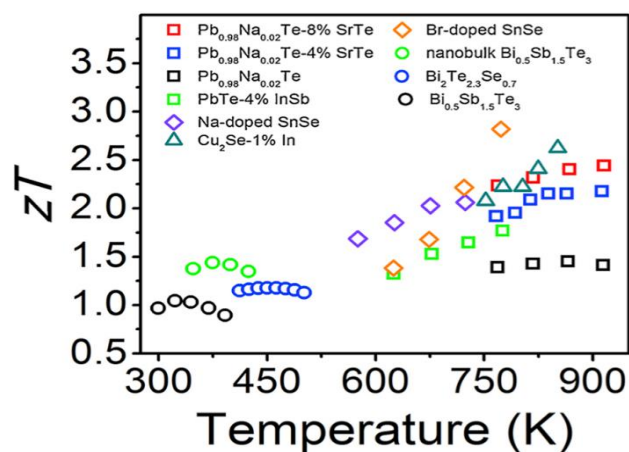


**Fig.1.5-** The graphs above show the  $zT$  ranges for the best TE materials for a temperature range between 300 K and 900 K. Graphs taken from Beretta et al <sup>[26]</sup>.

From the graph, it can be shown that Bismuth telluride ( $\text{Bi}_2\text{Te}_3$ ) based alloys' Bismuth telluride selenide ( $\text{Bi}_2\text{Te}_{2.7}\text{Se}_{0.3}$ ) and Bismuth antimony telluride ( $\text{Bi}_{0.5}\text{Sb}_{1.5}\text{Te}_3$ ) are the most efficient TE materials for a temperature range between 300 and 500 K. As a result, these alloys have been the most researched and are currently embedded in commercial TEGs.

**1.3.1 Crystal structure of Bismuth telluride-based alloys**

$\text{Bi}_2\text{Te}_3$  along with its ternary alloys' are chalcogenides partly comprising elements from group 16 of the periodic table.  $\text{Bi}_2\text{Te}_3$  is a narrow band gap (0.16 eV) semiconductor [15] which allows for valence electrons to be more easily excited to the CB.  $\text{Bi}_2\text{Te}_3$  has a tetradymite crystal structure where the Bismuth (Bi) atoms and Tellurium (Te) atoms are octahedrally coordinated with  $\text{Te}^{(1)} - \text{Bi} - \text{Te}^{(2)} - \text{Bi} - \text{Te}^{(1)}$ , where the numbers in the paraphrasis relate to inequivalent Te sites [27,28]. Each Te site has a different number of Bi sites neighbouring it with  $\text{Te}^{(1)}$  having six Bi sites and  $\text{Te}^{(2)}$  having three [29]. The bonds between the  $\text{Bi} - \text{Te}^{(1)}$  sites are comparable to the distance in a covalent bond, while the  $\text{Bi} - \text{Te}^{(2)}$  bond lengths are longer and closer to the expended value for ionic bonding [28]. These form crystal lattices which are hexagonally close placed. The crystal structure is separated into quintuple atomic layers, as each fifth atomic layer of the quintuple is connected to the next by weak van der Waals forces forming a rhombohedral structure [15,27,28]. This can be seen in Fig. 1.6:

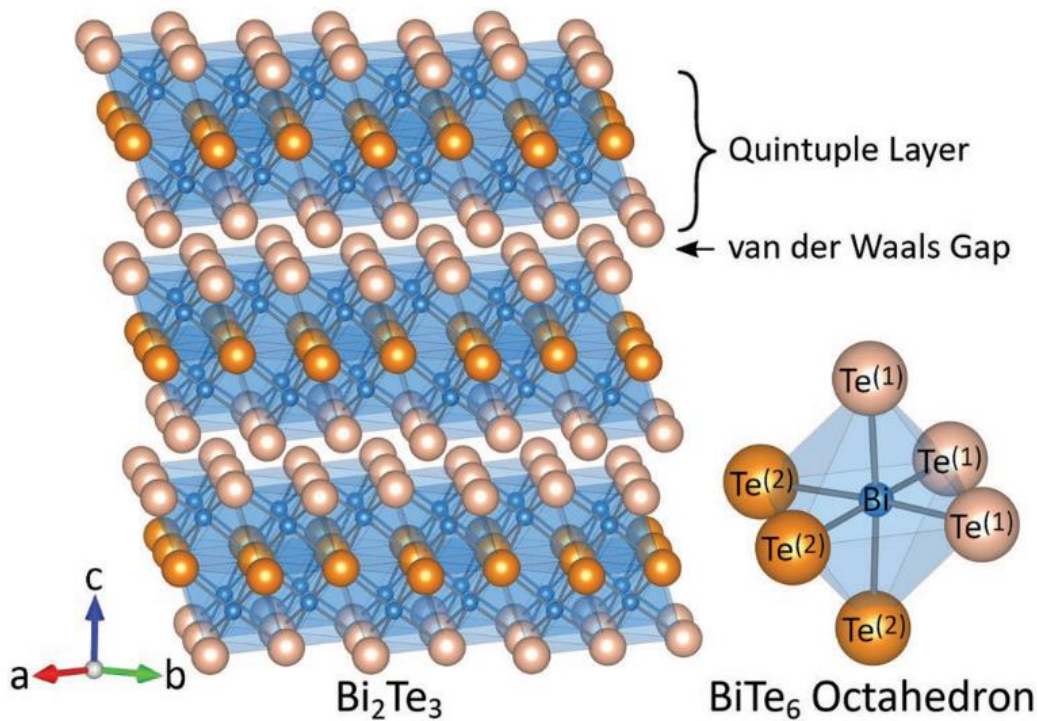


**Fig. 1.6-** Diagram of  $\text{Bi}_2\text{Te}_3$  rhombohedral structure divided into 3 quintuple layers separated by a van der Waals gap. Alongside the octahedral coordination between the  $\text{Te}^{(1)} - \text{Bi} - \text{Te}^{(2)} - \text{Bi} - \text{Te}^{(1)}$  sites. The image is taken from Witting et al [27].

As the  $\text{Te}^{(1)} - \text{Te}^{(1)}$  sites of neighbouring quintuple layers are connected by a weak van der Waals bond, this causes their lattice thermal and electrical conductivities along the basal plane (a & b-axis) to be two and six times higher respectively than along the perpendicular of the basal plane (c-axis). This also causes the mechanical strength of the structure to be weaker and more susceptible to mechanical cleavage along the perpendicular of the basal plane, similar to the case of graphite [27].

For the  $\text{Bi}_2\text{Te}_{2.7}\text{Se}_{0.3}$  and  $\text{Bi}_{0.5}\text{Sb}_{1.5}\text{Te}_3$  cases, they also follow the same crystal structure as  $\text{Bi}_2\text{Te}_3$ . The difference between the ternary and binary alloys is that with  $\text{Bi}_2\text{Te}_{2.7}\text{Se}_{0.3}$  the Selenium (Se) prefers to reside at the  $\text{Te}^{(2)}$  site, while for  $\text{Bi}_{0.5}\text{Sb}_{1.5}\text{Te}_3$  the Antimony (Sb) can occupy Bi sites [28].

## 1.4 Nanostructuring of Bismuth telluride-based alloys

As seen in Fig. 1.5 the ZT for  $\text{Bi}_2\text{Te}_3$ -based materials have remained at or below a ZT of 1.5, and have been for the past few decades [8,11,23]. Even though TEGs are commercially available, in order to have a high-performing TEG device it is stated in the literature that the research community needs to push for  $\text{ZT} > 4$  to compete with other heat engine technologies such as geothermal energy [25]. Fig. 1.7 compares the efficiencies of other thermal energy harvesting technologies with respect to the TE efficiencies at different ZTs.

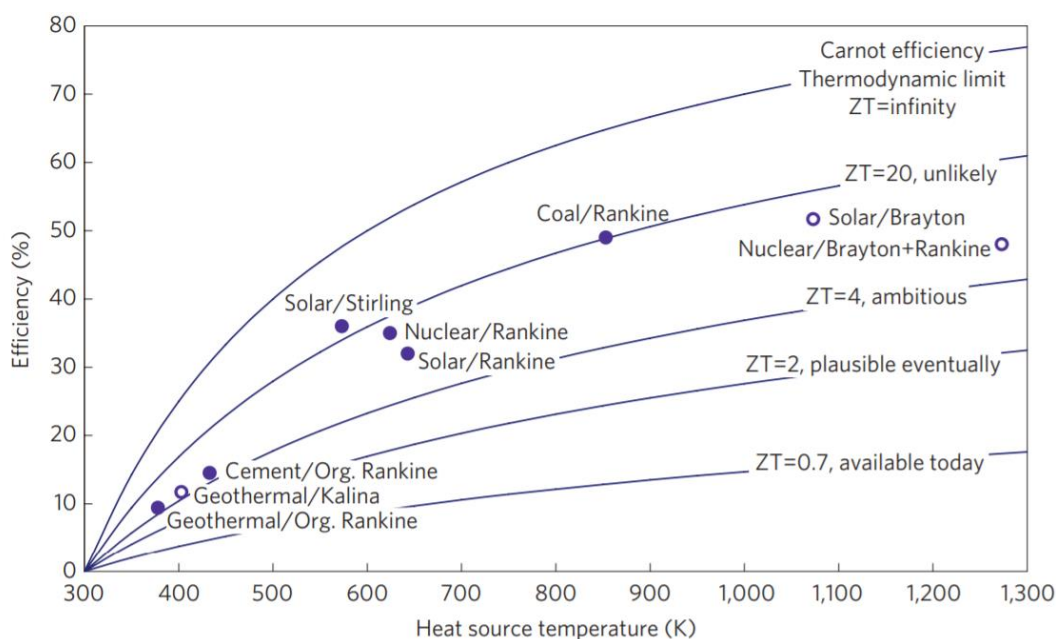


**Fig.1.7-** Graph of different mechanical heat engine technology efficiencies for a temperature range from 300 K to 1300 K compared with TE ambitions for ZT. Graph taken from Vining et al [25].

These high ZT TEGs would achieve efficiencies that would make them viable for commercial applications in waste energy recovery, as well as powering wearable IoT devices [7,8,25,30]. However, without some breakthrough in the research, this seemed unlikely to be achieved due to the low efficiencies of current TE materials. To improve the efficiency of TEGs it was shown that nanostructuring could be a viable route in a theoretical study that modelled  $\text{Bi}_2\text{Te}_3$  by Hicks et al and Dresselhaus et al [23,31]. They found that for  $\text{Bi}_2\text{Te}_3$  1D nanowires a ZT=14 can be obtained when the diameters of the nanowires were 0.5 nm. While the same conditions for 2D quantum wells can achieve ZT=5 for the same thickness of 0.5 nm [23,31]. This is seen in Fig. 1.8 for different directional orientations of the nanowires and quantum wells.

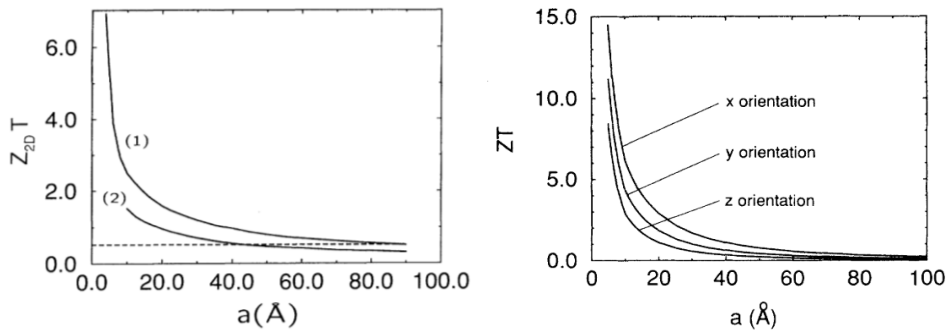


**Fig.1.8-** Graphs of the theoretical predictions of ZT for a  $\text{Bi}_2\text{Te}_3$  quantum well for the x-y plane (1) and x-z plane (2) with respect to the thicknesses of the quantum well in that plane (left), as well as  $\text{Bi}_2\text{Te}_3$  nanowire with respect to the nanowire orientation and thickness at that orientation in the x,y and z plane (right). The graphs are taken from Hicks et al and Dresselhaus et al [23,31].

This improvement in ZT is a result of a decrease in the  $\kappa_l$  contribution to  $\kappa$ , as phonons, either scatter at the boundaries of the nanowires, or from the nanowire surface as well as the interface between nanowires [12]. However, unlike in the bulk regime, this decrease in  $\kappa$  should not drastically reduce  $\sigma$ , due to it mainly resulting from a decrease in the  $\kappa_l$  contribution to  $\kappa$  [9]. However, the charge carriers can still be affected by these scattering mechanisms of the nanowires, as they interact with the boundaries of the nanowire surfaces. Additionally,  $\sigma$  can also be reduced via an increase in trap states and defects which are more likely to be found in nanowires, resulting in lower carrier mobility [32].

Another contributing factor to a higher ZT is an increase in  $S$ , due to the quantum confinement of charge carriers to only 1D and 2D movement [23,31]. This quantum confinement effect causes a change in the electronic density of states (DOS) of the material, as the motion of charge carriers is restricted by infinite potential walls. These changes in the DOS are shown in Fig. 1.9.

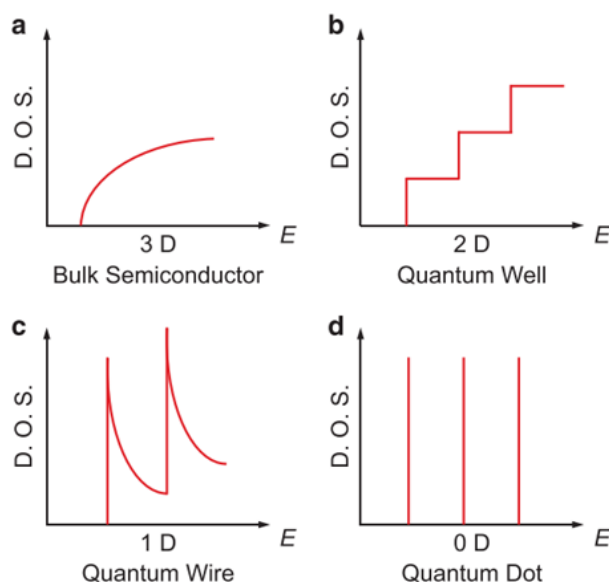


**Fig.1.9-** Graphs show the change in the electronic density of states (DOS) vs energy for a 3D bulk semiconductor (a), 2D quantum well (b), 1D quantum wire (c) and 0D quantum dot (d). The graphs are taken from Mao et al <sup>[33]</sup>.

This change in the DOS leads to increases in the DOS per unit volume and energy ( $g(E)$ ) which causes an increased energy dependence of the charge carrier concentration ( $n(E)$ ). As a consequence of this proportional relationship between  $g(E)$  and  $n(E)$ , as well as the energy derivative of  $n(E)$  contributing to  $S$  through the Mott relation seen in equation 1.6, this change in DOS leads to a higher  $S$  <sup>[32–34]</sup>.

#### 1.4.1 Nanomaterial synthesis techniques

Initial nanostructuring studies have shown an improvement in  $ZT$  through the reduction of  $\kappa$ , for example, a study by Venkatasubramanian et al obtained a  $ZT$  of  $\sim 2$  at 300 K for a 2D superlattices of  $\text{Bi}_2\text{Te}_3\text{-Sb}_2\text{Te}_3$  <sup>[19,35–37]</sup>. Venkatasubramanian et al <sup>[37]</sup> fabricated these 2D superlattices using metalorganic chemical vapour deposition (MOCVD) a process that involves using a vacuum chamber and gaseous procurers to form the desired material. The use of a high vacuum environment limits the scalability of such procedures and would not be viable in industry despite the high TE performance of their produced nanomaterials. Other techniques such as templated electrodeposition have been used to generate thin (diameter  $< 30$  nm) 1D nanowires of  $\text{Bi}_2\text{Te}_3$  in anode aluminium oxide templates. However, these templates are brittle and can not be used for FTEG devices <sup>[19,38]</sup>. Additionally, to liberate these nanowires from the anode aluminium oxide templates a sodium hydroxide solution must be used which has been observed to cause an amorphous shell to surround the nanowires which could affect their  $\sigma$  <sup>[38]</sup>.

For nanostructured FTEGs to be commercially viable the TE nanomaterials must be able to be produced at scale with a separation process that does not hinder TE performance. With those criteria in mind, we believe polyol synthesis is the ideal route to produce high-performing TE nanomaterials at scale. The following section describes how polyol synthesis can be used to synthesise a variety of nanostructures.

### 1.5 Polyol reflux synthesis of nanostructures

Polyol synthesis is a method that was first used in the 1980s and further developed in the 1990s that showed a promising route to synthesising nanostructures at an industrial scale <sup>[39,40]</sup>. The basic premise is that of a liquid-phase bottom-up approach where metal precursors are dissolved in polyalcohols or polyols and ether glycols such as Ethylene glycol (EG) and its derivatives. These polyols act as the reaction solvent, as well as the reducing and stabilising agent <sup>[39-41]</sup>. The benefits of Polyol synthesis are; the high boiling point of the solvents allowing for high crystallisation of the end product, the protection of the end product from oxidation while it is still in the solvent, the minimisation of aggregation of particles via the solvent's coordination with the particles surfaces and the high solvent viscosity allowing for diffusion-controlled nanostructure growth <sup>[39]</sup>.

Polyol synthesis can be modified under reflux conditions with the addition of a condenser which allows for a constant solvent concentration in the reaction, as the solvent vapours released at high temperatures are cooled in the condenser and are returned to the reaction. As reflux conditions are commonly used in the polyol synthesis of TE nanomaterials the term polyol reflux synthesis (PRS) will be used to describe this technique <sup>[39-41]</sup>.

The steps of the PRS process as stated by Fievet et al <sup>[39]</sup> seen in Fig. 1.10 are; dissolving the metal precursor into the PRS solvent which can occur at room or greater than room temperature, the nucleation step of specific crystal orientations and the growth step leading to the formation of the metal nanoparticles.

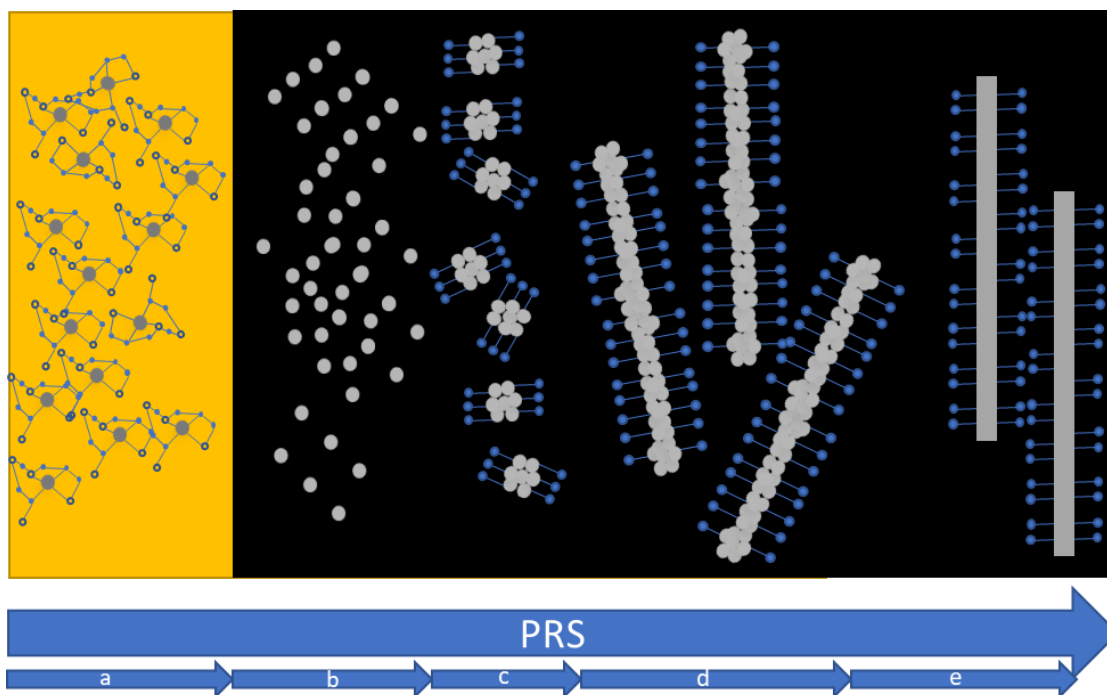


**Fig. 1.10-** Schematic of a PRS reaction to synthesis nanowires; (a) metal precursor dissolution and complex formation with solvent (yellow), (b) metal atoms reduction in solvent (black), (c) nucleation at crystal phases, (d) particle growth and (e) formulation of metal nanowires.

The precursors used in PRS are usually metal salts that contain counter-anions such as nitrate, chloride, acetate, hydroxide and sulfate. The formation of complexes between the metal ions and the solvent improves the solubility of the precursor<sup>[39]</sup>. PRS occurs at high temperatures as that is when the polyols can act as a reducing agent. However, using EG as an example it has an oxidation level of 1.65 eV which causes the reduction process to be much slower than other reducing agents such as sodium borohydride or hydrazine. As such these or other reducing agents are used alongside the PRS solvent to expedite the reduction step in the PRS reaction<sup>[39–41]</sup>. The reducing of the metal precursors is a necessary step in the PRS reaction as they have a higher oxidation state than the atomic species needed in the synthesis<sup>[42]</sup>.

Once the reaction commences the precursors are decomposed due to the heat of the reaction, which is then followed by the nucleation and growth stages based on the mechanism proposed by LaMer et al<sup>[42,43]</sup>. As stated by Xia et al<sup>[42]</sup> during this step the concentration of metal atoms reaches a point of supersaturation where the atoms start to aggregate into small clusters or nuclei via homogeneous nucleation. These nuclei grow and the metal atom's concentration in the solvent drops, however, if this concentration drops below superstation the nucleation is halted.

## Chapter 1

So long as there is an adequate supply of metal atoms from the decomposition of the precursor, the nuclei will grow into nanocrystals of ever-larger sizes until an equilibrium state is reached between the atoms on the surface of the nanocrystal and the atoms in the solution <sup>[42]</sup>. The next step in the reaction is the growth step where the nanocrystals can agglomerate into seed particles which in turn form the desired nanostructures <sup>[42]</sup>.

To control the morphology of the final nanomaterial product, PRS uses growth direction or capping agents to modify the shape of the nanostructures. Additionally, the capping agents keep the nanostructures suspended in the PRS solvent. These capping agents adsorb onto particular crystal orientations of the seed particles, which modifies the thermodynamic and kinetic factors and presents a physical barrier to atomic deposition and diffusion <sup>[44]</sup>. So far, a variety of different morphologies of metal nanomaterials have been achieved such as cubes, spheres and pyramids, however, for the interest of nanostructuring TE material, the focus has been on 2D nanoplatelets and 1D nanowires and nanorods.

The use of PRS in the literature is often coupled with spark plasma sintering (SPS) to turn the as-synthesised nanomaterial powder into bulk pellets <sup>[35,45]</sup>. For our aims of fabricating FTEGs, such a procedure would not be possible, as such we've aimed to couple PRS with screen-printing. This is to take advantage of the scalability that screen-printing offers to produce large-area flexible films at high volumes, screen-printing is discussed more in the following section.

### 1.6 Screen-printing

Screen-printing is a heavily used deposition technique in the clothing industry for its ease and scalability. Furthermore, screen-printing can produce a variety of patterns with different colours over a wide area on different substrates such as fabrics. However, over the last few years, it has been widely used in the tech industry for printing OLEDs, solar cells and general circuits onto wide-area flexible substrates <sup>[46]</sup>. Screen-printing uses thixotropic pastes, which according to Steffe et al <sup>[47]</sup> refers to the paste's time-dependent decrease in viscosity, due to shearing, and the subsequent recovery of viscosity when the shearing is removed <sup>[48]</sup>. Screen-printing is a form of stencilling where the shape of the printed deposits is determined by a patterned image on a porous mesh (screen). The screen is patterned by photolithography where the mesh pores are blocked with a photopolymer emulsion material. The emulsion is then cured under UV light with a photomask of the desired image <sup>[46,49]</sup>. The uncured emulsion is then washed off leaving behind the patterned image on the screen.

The initial step in screen-printing is to forcefully spread a thixotropic paste across the patterned mesh on the screen via a blade. The shearing from the blade reduces the paste's viscosity allowing it to flood the mesh pores. However, the viscosity increase after the shearing force is removed allowing the paste to be viscous enough not to leak out of the mesh. Afterwards, a shearing force is applied to the paste using a squeegee to press the paste through the mesh and onto the substrate. During this second shearing of the paste, its viscosity once again reduces allowing the paste droplets to deposit onto the substrate. As the shearing force is removed the paste droplets coalesce and increase in viscosity, allowing the deposit to maintain the shape of the patterned image on the screen. The substrate is placed at a small distance away from the screen known as the printing gap<sup>[46,48,50,51]</sup>. This process results in a patterned wet deposit on the substrate, which can be seen in Fig. 1.11 below.

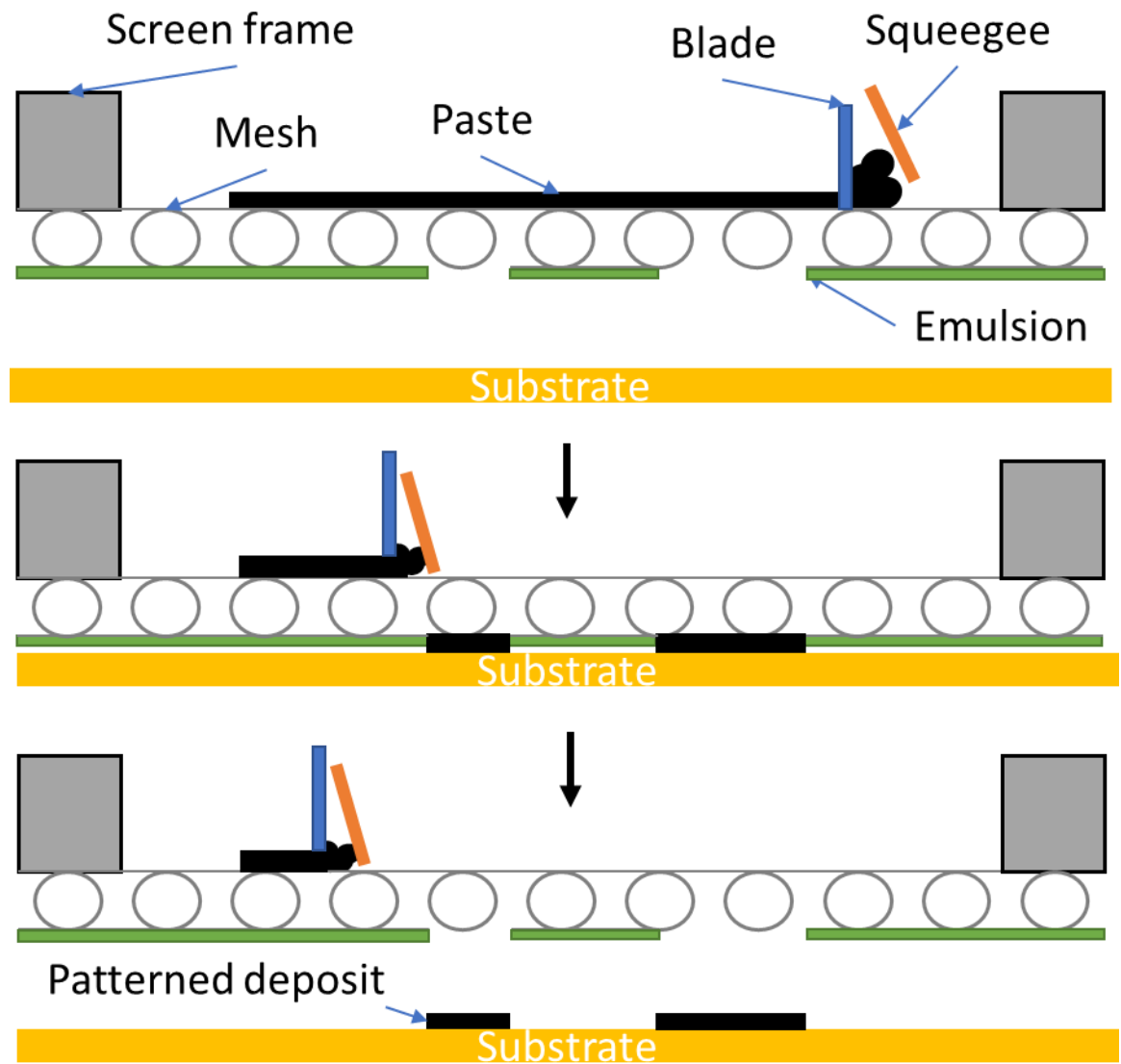


Fig.1.11- Illustration of the screen-printing process.

## Chapter 1

The printed wet deposit is then processed via drying/curing, which results in the formation of a thick film (film thickness  $> 1 \mu\text{m}$ )<sup>[46]</sup>. In screen-printing, two factors need to be considered which can affect the pattern resolution of the printed deposit as a result of the paste's thixotropic nature. The first is how fast the paste is printed through the screen (shear rate), while the second is how much pressure is applied to the paste (shear stress). This is because the paste needs to be viscous enough, to maintain its form during the printing process, to produce a deposit with a high resolution. Separately if the paste is too viscous no amount of sheer-thinning will print the paste through the mesh pores, as such the paste's viscosity with no shearing force applied needs to be considered as well<sup>[48,51]</sup>.

Additionally, the paste's viscosity needs to be matched with the type of screen that the paste will be printed on. This is because the screen's mesh is typically made from either polyester, nylon, silk or stainless steel threads<sup>[48,49]</sup>. These threads affect the thickness and resolution of the printed film, depending on the thread frequency as well as the individual thread's thickness and roughness<sup>[46]</sup>. Additionally, the thickness of the emulsion used to pattern the screen can affect the thickness of the printed films. Furthermore, the printed film's image resolution's reproducibility is depended on how good of a gasket-like seal the emulsion can make with the substrate as the paste is printed through the screen by the squeegee<sup>[48]</sup>. The mesh pores also affect the size of the pigments that are to be printed to avoid clogging the screen, with Deganello et al<sup>[46]</sup> stating a maximum size ratio of particle:pore is 1:10.

For the TE research field, screen-printing allows for commercially viable FTEGs by modifying the process via the use of cylindrical screens for roll-to-roll printing<sup>[51]</sup>. This allows for the FTEGs to be printed onto a wide range of substrates for a variety of applications such as onto fabrics for E-textiles. In the case of FTEGs, the pastes are made from TE (nano/micro) particles dispersed in a solvent with a binding agent to give the formulated paste the necessary viscosity to screen-print thick planar films. These films then require annealing to burn off the binder and give the TE film its functionality.

Nonetheless, some challenges remain, as TEGs are vertically designed as shown in section 1.1, while screen-printing produces planar films. Attempting to alleviate this issue by printing multiple films on top of one another, leads to less overall  $\sigma$ , due to the surface roughness of each layer<sup>[51]</sup>. Additionally, structural defects in the mesh can be imaged onto the deposited film, this can result in voids in the film which can reduce the overall  $\sigma$ . Voids can also be produced during the annealing process and are found in the locations where the binder gets burned off. Finally, any residue binder left after the annealing process will reduce the film's overall  $\sigma$ <sup>[51]</sup>.

## 1.7 State-of-the-art of polyol reflux synthesis and screen-printing procedures for the fabrication of flexible thermoelectric Tellurium and Bismuth telluride-based materials

A significant effort has been made by the TE research community to produce devices made from inorganic nanostructures via a multitude of different procedures such as MOCVD and templated electrodeposition as seen in section 1.41 [19,52–55]. However, to ensure a possible route to industry for these TE nanostructures, their synthesis procedure needs to be simple and scalable. With these requirements in mind, we propose the use of PRS coupled with screen-printing. This is because PRS can produce high yields of nanostructures that can be scaled up from a lab-based setup to industry. Another advantage to PRS is that it can be used to synthesise nanoparticles with vastly different morphologies.

However, the drawbacks of PRS can be the use of highly toxic substances at high temperatures while maintaining an inert atmosphere [35,56,57]. Screen-printing harmonises well with PRS as a scalable deposition technique that has been used in a future scaled FTEG device fabrication procedure via the use of a roll-to-roll process with cylindrical screens [51]. Here we review the current literature for screen-printed and PRS  $\text{Bi}_2\text{Te}_3$ -based  $\text{Bi}_x\text{Sb}_{2-x}\text{Te}_{3-y}\text{Se}_y$  nanostructures. Additionally, we also examine the state of current wearable prototype TE-powered systems and textile-compatible PRS Te nanostructure polymer composites.

### 1.7.1 Polyol reflux synthesised Bismuth telluride-based nanostructures

One polyol solvent-capping agent system used in the literature that has shown promising results in producing scalable highly efficient nanostructures is EG and Polyvinylpyrrolidone (PVP). In 2012, Zhang et al [35] synthesised ultrathin  $\text{Bi}_2\text{Te}_3$  nanowires with an average diameter of 8 nm, in a two-stage one-pot synthesis with a product yield of 93 %. They initially synthesised Te nanowires using Tellurium dioxide ( $\text{TeO}_2$ ) as the metal precursor and coupled the EG-PVP system with hydrazine hydrate to act as the reducing agent. In the second stage, a Bi precursor of Bismuth nitrate pentahydrate ( $\text{Bi}(\text{NO}_3)_3 \cdot 5\text{H}_2\text{O}$ ) dissolved in EG was added to the mixture.

Following the synthesis, the nanowires were cleaned in ethanol with diluted hydrazine hydrate (10 % volume ratio) and stirred till the nanowires precipitated to remove the PVP. Then the nanowires were washed in ethanol 3 times to remove the other chemicals used in the synthesis especially hydrazine hydrate due to its toxic and hazardous nature [35,58]. These nanowires were then dried in a vacuum and were formed into bulk pellets by SPS. The pellets' geometry was 2.54 cm in diameter and 0.25 cm in thickness with a relative density of ~80 %. Their highest reported

values were at 380 K with  $S$ ,  $\sigma$ ,  $PF$ ,  $\kappa$  and  $ZT$  of  $\sim 240 \mu\text{V K}^{-1}$ ,  $4.3 \times 10^4 \text{ S m}^{-1}$ ,  $2400 \mu\text{Wm}^{-1}\text{K}^{-2}$ ,  $1.0 \text{ Wm}^{-1} \text{K}^{-1}$  and 0.96 respectively [35].

The applications of this EG-PVP system were expanded later on by Zhou et al [45] in 2016 who synthesised a number of different metal-tellurium-selenium-based ternary nanowire alloys using lead, cadmium, copper, silver and bismuth. For our review, we will only be focusing on the bismuth telluride selenide nanowires they synthesised. The difference between this synthesis and the one demonstrated by Zhang et al [35], is that a Se precursor (selenous acid,  $\text{H}_2\text{SeO}_3$ ) was dissolved in EG and injected into the reaction system after they had synthesised Te nanowires forming  $\text{Te}_x\text{Se}_{1-x}$  nanowires. They then inject the Bi into the reaction system forming  $\text{Bi}_2(\text{Te}_x\text{Se}_{1-x})_3$  nanowires. They found these nanowires had a diameter to be 11 nm. The three main steps of Zhou et al [45] reaction are shown in Fig.1.12.

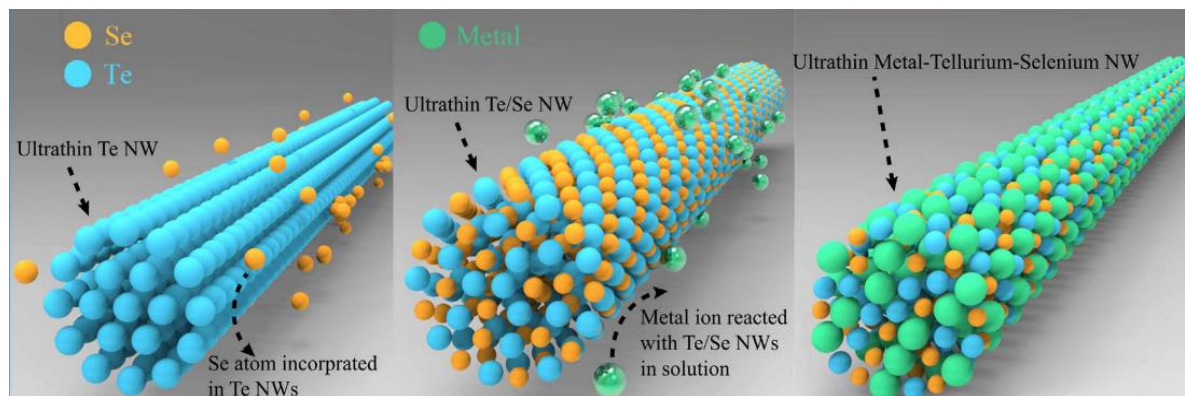


**Fig. 1.12-** Illustration shows the synthesis process steps in forming Metal-Tellurium-Selenium nanowires. The image is taken from Zhou et al [45].

Zhou et al [45] used SPS to fabricate pellets of  $\text{Bi}_2\text{Te}_{2.7}\text{Se}_{0.3}$  nanowires and observed peak TE performance at 320 K an  $S$ ,  $\sigma$ ,  $PF$ ,  $\kappa$  and  $ZT$  of  $\sim 160 \mu\text{V K}^{-1}$ ,  $4.8 \times 10^4 \text{ S m}^{-1}$ ,  $1023 \mu\text{Wm}^{-1}\text{K}^{-2}$ ,  $0.45 \text{ Wm}^{-1} \text{K}^{-1}$  and 0.75 respectively.

In both 2017 and 2019, the  $\text{Bi}_2\text{Te}_3$  synthesis process of Zhang et al [35] was coupled with inkjet printing by Chen et al [53,57]. Unlike previous papers they synthesised  $\text{Bi}_2\text{Te}_3$  and  $\text{Bi}_{0.5}\text{Sb}_{1.5}\text{Te}_3$  nanowires, however, instead of forming pellets, Chen et al [53,57] formulated inks to inkjet print thin films. The as-synthesised nanowires were cleaned and dispersed in Di-water. These dispersions were bath sonicated to formulate the ink. They ranged the thickness of the inkjet-printed films depending on how many passes the printer nozzle made over the films. The films were annealed in a forming gas atmosphere (FGA) (95% hydrogen, 5% argon) for both 400 °C for 2 hr in their 2017 paper for  $\text{Bi}_2\text{Te}_3$  and 450 °C for 10 mins for both  $\text{Bi}_2\text{Te}_3$  and  $\text{Bi}_{0.5}\text{Sb}_{1.5}\text{Te}_3$  films for their 2019 paper [53,57]. This alteration in the annealing process was due to the poor performance of the p-type  $\text{Bi}_{0.5}\text{Sb}_{1.5}\text{Te}_3$  nanowire films resulting from a lack of nanowire-nanowire sintering leading to low  $\sigma$ .

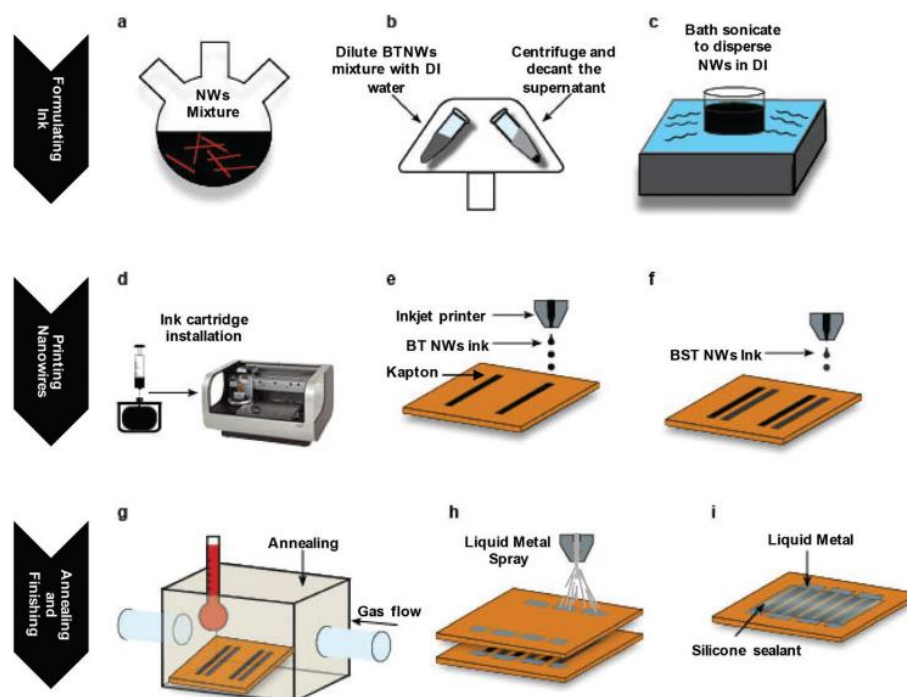


**Fig.1.13-** Image of the process for inkjet printed FTEG device. (a–c) Synthesis process for the  $\text{Bi}_2\text{Te}_3$  and  $\text{Bi}_{0.5}\text{Sb}_{1.5}\text{Te}_3$  nanowires and subsequent ink formulation for inkjet printing, (d–f) inkjet printing onto flexible polyimide film, (g) thermal annealing of the films, and (h–i) spray printing of liquid metal contacts and doctor blade coating of silicone sealant. Image from Chen et al [53].

The optimal thickness Chen et al [53] reported in 2019 for  $\text{Bi}_2\text{Te}_3$  at 100 passes ( $0.89 \pm 0.06 \mu\text{m}$ ) with an  $S, \sigma, \text{PF}, \kappa$  and  $ZT$  of  $\sim 120 \mu\text{V K}^{-1}, 8000 \text{ S m}^{-1}$  and  $110 \mu\text{Wm}^{-1} \text{ K}^{-2}, 1.19 \text{ Wm}^{-1} \text{ K}^{-1}$  and 0.04. While for  $\text{Bi}_{0.5}\text{Sb}_{1.5}\text{Te}_3$  at 50 passes ( $0.62 \mu\text{m} \pm 0.08$ ) the  $S, \sigma, \text{PF}, \kappa$  and  $ZT$  were  $85 \mu\text{V K}^{-1}, 2.4 \times 10^4 \text{ S m}^{-1}$  and  $180 \mu\text{Wm}^{-1} \text{ K}^{-2}, 0.55 \text{ Wm}^{-1} \text{ K}^{-1}$  and 0.13. These TE values for both materials were measured at a temperature of 400 K. Finally, eutectic gallium–indium liquid metal contacts were spray-coated onto the films, connecting them electrically and forming an FTEG device made of 5 couples. Chen et al [53] were then able to report an output power of 127 nW with a  $\Delta T = 32.5 \text{ K}$ . So far, the work from Chen et al [53] is the only work on printing  $\text{Bi}_2\text{Te}_3$ -based nanowires.

**Table 1.2-** The summary of thermopower at a given temperature and output power for a given heat flux for PRS  $\text{Bi}_x\text{Sb}_{2-x}\text{Te}_{3-y}\text{Se}_y$  nanomaterials along with their bulk values.

Ref	Material (n/p)	Temperature/ Heat flux (K)	Fabrication process	Seebeck coefficient ( $\mu\text{V K}^{-1}$ )	Electrical conductivity ( $\times 10^4 \text{ S m}^{-1}$ )	Power factor ( $\mu\text{Wm}^{-1}\text{K}^{-2}$ )	Output Power
[59]	Bulk $\text{Bi}_2\text{Te}_3$	N/A	Mechanical alloying/ SPS	-150	8.0	1800	N/A
[60]	Bulk $\text{Bi}_{0.5}\text{Sb}_{1.5}\text{Te}_3$	373.15	Hot pressing	210	8.5	3700	N/A
[35]	$\text{Bi}_2\text{Te}_3$	380	SPS	-240	4.3	2400	N/A
[61]	$\text{Bi}_2\text{Te}_3$ -PEDOT:PSS	300/80	Dip coated	24.5	1.24	7.45	130 $\mu\text{W}$
[62]	$\text{Bi}_{0.5}\text{Sb}_{1.5}\text{Te}_3$	375	SPS	180	2.0	1500	N/A
[45]	$\text{Bi}_2\text{Te}_{2.7}\text{Se}_{0.3}$	320	SPS	-160	4.8	1023	N/A
[53]	$\text{Bi}_2\text{Te}_3/\text{Bi}_{0.5}\text{Sb}_{1.5}\text{Te}_3$	400/32.5	Inkjet printing	-120/85	0.8/ 2.4	110/180	127 nW
[63]	$\text{Sb}_2\text{Te}_3$	318.15	Cold compaction	105	14	1580	N/A
[64]	$\text{Bi}_2\text{Te}_3$	433	Spin coated	-116	2.6	350	N/A
[65]	$\text{Bi}_{0.5}\text{Sb}_{1.5}\text{Te}_3$ +Te	450	SPS	150	1.8	4000	N/A
[66]	$\text{Bi}_2\text{Te}_3$ -PEDOT:PSS/ $\text{Sb}_2\text{Te}_3$ -PEDOT:PSS	300	Aerosol jet printing	20/32	0.35/0.25	18/30	N/A

So far, we have seen rigid nanostructured pellets that have PFs that surpass their bulk counterparts for n-type  $\text{Bi}_2\text{Te}_3$ , however, more work needs to be done to improve the PFs of the flexible nanostructured  $\text{Bi}_2\text{Te}_3$ -based films in order to incorporate them into high-performing FTEG devices.

### 1.7.2 Tellurium-based nanocomposites

In parallel to the research conducted on  $\text{Bi}_2\text{Te}_3$ -based nanomaterials, there has been a considerable effort in literature to couple Te nanostructures with organic polymers to fabricate flexible TE composite. These composites would take advantage of the high  $S$  ( $>250 \mu\text{V K}^{-1}$ ) that the Te nanostructures possess, as well as improve the poor electrical properties of Te with electrically conductive flexible polymers [67–71]. The most studied polymers for these composites have been poly(3,4-ethylenedioxythiophene)polystyrene sulfonate (PEDOT:PSS) as well as polyaniline (PANI). Researchers have also investigated fabricating composites with non-conductive polyvinylidene fluoride (PVDF) for its mechanical flexibility and low thermal conductivity [67–71].

A study by Yee et al [69] fabricated a composite by adding a PEDOT:PSS solution into the Te nanowire synthesis and drop-casting the resulting product onto sapphire substrates and drying them under a heat lamp and annealed at  $140^\circ\text{C}$  for 5 mins. They found the optimal ratio of Te nanowires to PEDOT:PSS in the composite to be 84:16 respectively. They further enhanced their composite by doping the PEDOT:PSS solution with a 5 % volume of Dimethyl sulfoxide (DMSO). This gave them a maximum room temperature PF of  $100 \mu\text{Wm}^{-1}\text{K}^{-2}$  which was considerably higher than the PF of their Te nanowires ( $<3 \mu\text{Wm}^{-1}\text{K}^{-2}$ ) [69]. While Dun et al [67] fabricated what they called a flexible TE fabric by formulating a dispersion with Te nanorods and PVDF with dimethyl-formamide as the solvent. The dispersion was drop-casted onto a glass substrate on a hotplate at  $80^\circ\text{C}$  and left overnight, after which the resulting composite was peeled off the glass substrate. They observed that the composite consisted of a thin layer of a self-assembled Te nanorod network beneath a layer of PVDF, which was attributed to the heavy element nature of Te, as illustrated in Fig.1.14 [67]. The ratio between the Te nanorods and PVDF in the composite was 66:34 respectively. The composite achieved a room temperature  $S$ ,  $\sigma$ , and PF of  $288 \mu\text{V K}^{-1}$ ,  $551.6 \text{ S m}^{-1}$  and  $45.8 \mu\text{Wm}^{-1}\text{K}^{-2}$  respectively [67], which is higher than the TE performance recorded in the literature for drop-casted films of Te nanorods ( $< 3 \mu\text{Wm}^{-1}\text{K}^{-2}$ ) [68]. The improvement in TE performance was due to the large sizes of the nanorods with the PVDF acting as the support structure allowing the composite to be a flexible free-standing film.

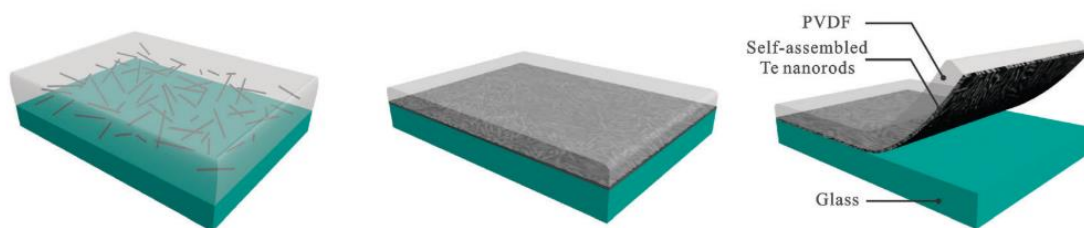


**Fig. 1.14-** Illustration of the formation of the self-assembled Te nanorod-PVDF composite. Image from Dun et al [67].

Screen-printable composites of Te nanowires and PANI were fabricated by Wang et al <sup>[71]</sup> at a ratio of 70:30 respectively. The screen-printable paste was formulated by first doping the PANI using camphorsulfonic acid and dissolving it in m-cresol which acted as the paste solvent. Afterwards, the synthesised Te nanorods are dispersed in m-cresol and added to the paste. They observed a room temperature TE performance for  $S$ ,  $\sigma$ , PF,  $\kappa$  and ZT of  $102 \mu\text{V K}^{-1}$ ,  $1.02 \times 10^4 \text{ S m}^{-1}$ ,  $105 \mu\text{Wm}^{-1}\text{K}^{-2}$ ,  $0.21 \text{ Wm}^{-1}\text{K}^{-1}$  and 0.156 respectively for the screen-printed composite film. Wang et al <sup>[71]</sup> also screen-printed an FTEG device with 10 composite films acting as the TE legs with a silver screen-printed electrode. They achieved maximum output voltage and output power of 29.9 mV and  $0.73 \mu\text{W}$ , respectively at a temperature gradient of 40 K.

**Table 1.3-** Summary of the room temperature TE performance of the Te nanostructure-polymer composites.

Ref	Material	Seebeck coefficient ( $\mu\text{V K}^{-1}$ )	Electrical conductivity ( $\text{S m}^{-1}$ )	Power factor ( $\mu\text{Wm}^{-1}\text{K}^{-2}$ )
[68]	Te nanowires	408	8	2.7
[72]	Te nanowires	551	1.29	0.39
[68]	Te nanowires-PEDOT:PSS	163	1930	70.9
[71]	Te nanorods-PANI	102	10200	105
[69]	Te nanowires-PEDOT:PSS	72	20000	103
[67]	Te nanorods-PVDF	288	551.6	45.8
[72]	Te nanorods-PVDF	469	0.32	0.07
[73]	Te nanowires-PEDOT:PSS	75	25200	141.9

Despite the impressive headway seen in the literature these composites still have a long way to go in terms of overall TE performance and device fabrication. Though the research by Wang et al <sup>[71]</sup> has shown the potential viability to incorporate these composites into wearable E-textile systems, as they can generate TE power outputs without the need to be annealed. This makes them suitable for standard fabrics such as polyester-cotton which has a maximum processing temperature of  $180 \text{ }^\circ\text{C}$  <sup>[74]</sup>. However, to our knowledge, there has not been any research investigating the possibility of such incorporation into wearables using scalable fabrication processes such as screen-printing.

### 1.7.3 Bismuth telluride-based screen-printed films and devices

Alongside the work done by Wang et al [71], many research groups have utilised screen-printing as a means of developing commercially scalable  $\text{Bi}_2\text{Te}_3$ -based FTEG devices. Kim et al [75] screen-printed  $\text{Bi}_2\text{Te}_3$  and  $\text{Sb}_2\text{Te}_3$  films onto glass fabric to test their capacity as FTEGs. They observed room temperature  $S$ ,  $\sigma$ ,  $\text{PF}$ ,  $\kappa$  and  $\text{ZT}$  of  $\sim 141/98 \mu\text{V K}^{-1}$ ,  $0.67/1.5 \times 10^5 \text{ S m}^{-1}$ ,  $1330/1440 \mu\text{Wm}^{-1}\text{K}^{-2}$ ,  $1.1/1.45 \text{ Wm}^{-1}\text{K}^{-1}$  and  $0.35/0.3$  for the  $\text{Bi}_2\text{Te}_3$  and  $\text{Sb}_2\text{Te}_3$  films respectively after the films had been annealed at  $530^\circ\text{C}$  for 10 mins in nitrogen atmosphere [75]. They fabricated electrodes by screen-printing copper films onto nickel/silicon dioxide/silicon wafer substrates. The electrodes were fabricated in this manner to avoid delamination during bending. These electrodes were then attached to the TE films using silver paste. The resulting FTEG was coated in Polydimethylsiloxane for better interconnection. Kim et al [75] then tested the bendability of the FTEGs by observing the change in normalised resistance per radius of bending and per bending cycles as shown in Fig. 1.15.

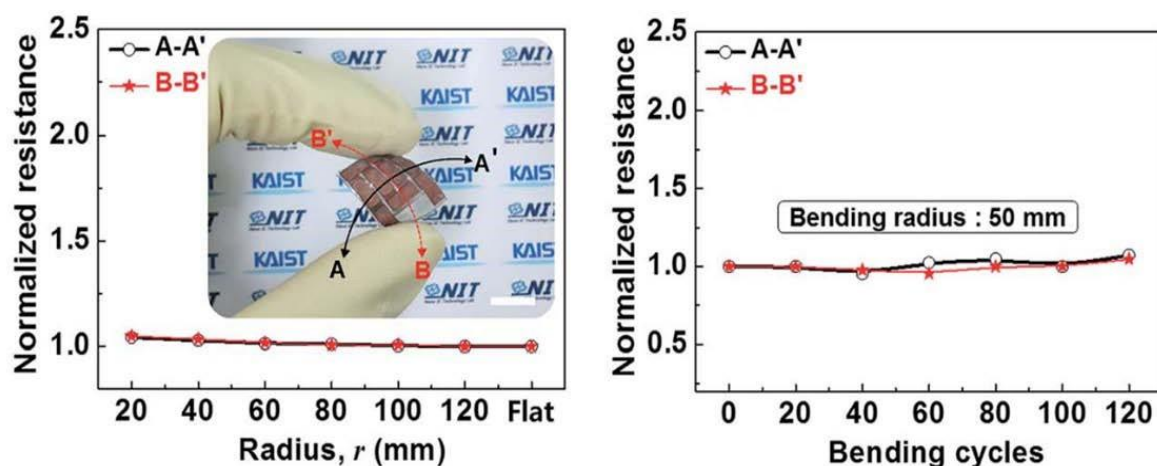


**Fig. 1.15-** Graphs of normalised resistance as a function of the radius of bending (left) and bending cycles for a radius of 50 mm (right). Graphs from Kim et al [75].

From the data in Fig. 1.15, it was shown that the internal resistance changes were less than 7 %, showcasing how viable these materials would be as part of a wearable FTEG device. Additionally, Kim et al [75] also fabricated a small band shape FTEG device with 11 TE couples that were placed onto a human wrist, which generated a power output of  $3 \mu\text{W}$  on a matched external load at an air temperature of  $15^\circ\text{C}$ . They further stated that the output power per unit weight was  $28 \text{ mW g}^{-1}$  at  $\Delta T = 50 \text{ K}$  [75]. Kim et al [76] also worked on screen-printing the ternary versions of  $\text{Bi}_2\text{Te}_3/\text{Sb}_2\text{Te}_3$ ,  $\text{Bi}_2\text{Te}_{2.7}\text{Se}_{0.3}/\text{Bi}_{0.5}\text{Sb}_{1.5}\text{Te}_3$ . Initially, they looked to optimise the annealing conditions (temperature, time) and improve the performance of  $\text{Bi}_2\text{Te}_{2.7}\text{Se}_{0.3}$ . The  $\text{Bi}_2\text{Te}_{2.7}\text{Se}_{0.3}$  was annealed in an FGA similar to Chen et al (96% Hydrogen, 4% Argon) with the optimal conditions being for an annealing time of 4 hr at  $450^\circ\text{C}$ . This resulted in the TE properties for  $S$ ,  $\sigma$ ,  $\text{PF}$ ,  $\kappa$  and  $\text{ZT}$  being  $-210 \mu\text{VK}^{-1}$ ,  $4 \times 10^4 \text{ S m}^{-1}$ ,  $1764 \mu\text{Wm}^{-1}\text{K}^{-2}$ ,  $0.65 \text{ Wm}^{-1}\text{K}^{-1}$  and  $0.9$  at  $300 \text{ K}$  [76].

## Chapter 1

Kim et al then fabricated an FTEG device made from 72 pairs of screen-printed  $\text{Bi}_2\text{Te}_{2.7}\text{Se}_{0.3}/\text{Bi}_{0.5}\text{Sb}_{1.5}\text{Te}_3$  legs, using the same electrodes as in their earlier work. They were able to measure a power density output of  $6.32 \text{ mWcm}^{-2}$  for a  $\Delta T = 25.6 \text{ K}$  [76].

In further developments in the literature towards FTEGs for E-textiles, Cao et al [74,77] screen-printed  $\text{Bi}_{1.8}\text{Te}_{3.2}$  and  $\text{Sb}_2\text{Te}_3$  onto Kapton substrates. Different pastes were formulated using two different epoxy binders, 4,4'- Isopropylidenediphenol-epichlorohydrin and epichlorohydrin-polyglycol based epoxy denoted as epoxy A & B respectively and  $\text{Bi}_{1.8}\text{Te}_{3.2}$  and  $\text{Sb}_2\text{Te}_3$  powders as active material [74,77]. To fabricate the FTEG more SbTe was used as the contacting electrode. Screen-printed films were cured at  $250 \text{ }^\circ\text{C}$  for 3 hr in an inert nitrogen atmosphere. The TE properties at room temperature obtained for  $S$ ,  $\sigma$ , and PF for epoxy A were  $-143.5/103.67 \text{ } \mu\text{V K}^{-1}$ ,  $684.93/19960 \text{ S m}^{-1}$ ,  $14/215 \text{ } \mu\text{Wm}^{-1}\text{K}^{-2}$  and for epoxy B were  $-134.38/110.2 \text{ } \mu\text{V K}^{-1}$ ,  $7812.5/7299.3 \text{ S m}^{-1}$ ,  $141/86 \text{ } \mu\text{Wm}^{-1}\text{K}^{-1}$  for  $\text{Bi}_{1.8}\text{Te}_{3.2}$  and  $\text{Sb}_2\text{Te}_3$  respectively [74,77]. The highest power output then recorded by Cao et al [74,77] was  $444 \text{ nW}$  at a  $\Delta T = 20 \text{ K}$ , using the epoxy B binder-based pastes. They further worked on screen-printing  $\text{Bi}_{1.8}\text{Te}_{3.2}$  and  $\text{Sb}_2\text{Te}_3$  onto a variety of textiles. Using epoxy B-based pastes they fabricated an FTEG device on Valmiera 1032/9628 glass fibre textiles with a reported maximum power output of  $2 \text{ } \mu\text{W}$  at a  $\Delta T = 20 \text{ K}$ . The screen-printed films used in the FTEG device at room temperature had an  $S$ ,  $\sigma$ , PF,  $\kappa$  and ZT of  $-138.4/108.5 \text{ } \mu\text{V K}^{-1}$ ,  $10030/27778 \text{ Sm}^{-1}$  and  $192/327 \text{ } \mu\text{Wm}^{-1}\text{K}^{-2}$ ,  $0.426/1.036 \text{ Wm}^{-1}\text{K}^{-1}$  and  $0.135/0.095$  for  $\text{Bi}_{1.8}\text{Te}_{3.2}$  and  $\text{Sb}_2\text{Te}_3$  respectively [74,77]. Fig 1.16 shows the screen-printed films on different textiles.

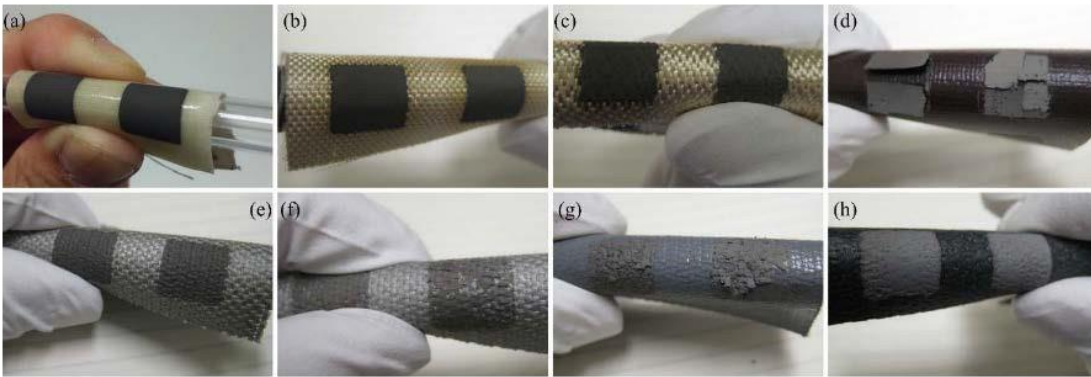


**Fig. 1.16-** Screen-printed  $\text{Bi}_{1.8}\text{Te}_{3.2}$  on (a) polyester/cotton with polyurethane interface, (b) Valmiera 1032/9682, (c) Valmiera 440-AL, (d) ATEX 3000, (e) ATEX 3200-2-sp, (f) PAR GC409SG, (g) PAR GC16 and (h) ATEX 03321-2-WN. Images from Cao et al [74].

**Table 1.4-** Summary of thermopower at a given temperature and output power for a given heat flux for screen-printed  $\text{Bi}_x\text{Sb}_{2-x}\text{Te}_{3-y}\text{Se}_y$  materials along with their bulk values.

Ref	Material (n-type/p-type)	Temperature/Heat flux (K)	Seebeck coefficient ( $\mu\text{V K}^{-1}$ )	Electrical conductivity ( $\times 10^4 \text{ S m}^{-1}$ )	Power factor ( $\mu\text{Wm}^{-1}\text{K}^{-2}$ )	Output Power
[59]	Bulk $\text{Bi}_2\text{Te}_3$	N/A	-150	8.0	1800	N/A
[60]	Bulk $\text{Bi}_{0.5}\text{Sb}_{1.5}\text{Te}_3$	373.15	210	8.5	3700	N/A
[78]	$\text{Bi}_2\text{Te}_3$	300	-130	2.6	2100	N/A
[75]	$\text{Bi}_2\text{Te}_3/\text{Sb}_2\text{Te}_3$	288.15	-141/98	6.7 / 15.0	1330/1440	3 $\mu\text{W}$
[76]	$\text{Bi}_2\text{Te}_{2.7}\text{Se}_{0.3}/\text{Bi}_{0.5}\text{Sb}_{1.5}\text{Te}_3$	300	-210	4.0	1764	N/A
[77]	$\text{Bi}_{1.8}\text{Te}_{3.2}/\text{Sb}_2\text{Te}_3$	300/20	-134.38/110.2	0.78125/0.72993	141/86	444 nW
[74]	$\text{Bi}_{1.8}\text{Te}_{3.2}/\text{Sb}_2\text{Te}_3$	300/20	-138.4/108.5	1.0/2.8	192/327	2 $\mu\text{W}$
[79]	$\text{Bi}_2\text{Te}_{2.8}\text{Se}_{0.2}$	448.15/60	-143	2.7	560	6.1 $\mu\text{W}$
[80]	$\text{Bi}_2\text{Te}_{2.7}\text{Se}_{0.3}/\text{Bi}_{0.5}\text{Sb}_{1.5}\text{Te}_3$	300	-165/209	7.63 / 6.39	2077/2791	N/A
[81]	$\text{Bi}_{0.5}\text{Sb}_{1.5}\text{Te}_3$	318.15/80	204	7.2	3000	54 $\mu\text{W}$

Screen-printing so far has been the most promising technology for scalable fabrication of FTEGs with some papers showing PF values close to or surpassing bulk  $\text{Bi}_2\text{Te}_3$ . Even for the ones that do not surpass the bulk PF, their flexibility and lack of notable increase in resistance from repeated bending cycles show they still can be used as part of an FTEG device. As such, work by Kim et al [75,76] and Cao et al [74,77] is a step toward integrating screen-printable FTEGs into wearable E-textile systems. However, they were only able to record TE performances and device power outputs for high-temperature glass fabrics that are not comfortable for the user. In the case of Cao et al [74] this was because polyester-cotton had a maximum processing temperature of 180 °C. The insufficient annealing caused their printed films on polyester-cotton to be highly resistive. As such, there is a gap in the literature for developing a procedure to fabricate inorganic FTEGs on standard fabrics used in apparel such as polyester-cotton.

#### 1.7.4 Wearable electronic textile compatible thermoelectric generators

For all the work done in the literature, there have been no studies to our knowledge that have integrated these novel FTEGs (based on flexible TE materials) into a wearable E-textile system to power an actual IoT device. The most prominent research into TE-powered wearable E-textile systems has been pioneered by Leonov et al <sup>[5]</sup>. In their research, they demonstrated that bulk  $\text{Bi}_2\text{Te}_3$ -based TEGs can act as a power source for medical devices seen in Fig. 1.17. They initially fabricated a wearable wristwatch-sized TEG that had a power output ranging from 100  $\mu\text{W}$  to 600  $\mu\text{W}$  which powered a pulse oximeter, as shown in Fig. 1.17a <sup>[5,82,83]</sup>. However, pulse oximeters on the market require 10 mW, as such the power consumption of the electronics was reduced to 62  $\mu\text{W}$ . The system was also equipped with a small capacitor that was used to store charge between radio transmission bursts from the system. Additionally, Leonov et al <sup>[5,84]</sup> also fabricated a wearable headband that had an electroencephalography device that was powered by bulk TEGs as seen in Fig.1.17b. Just as with the pulse oximeter, the electroencephalography device's power consumption was reduced by designing a low-power biopotential readout application-specific integrated circuit for the device. Despite the reduction in power consumption, a total area greater than 50  $\text{cm}^2$  was still needed for the TEGs to produce the necessary power. The TEGs were able to produce a power output of 3.7 mW at 19 °C <sup>[5,84]</sup>. Finally, Leonov et al <sup>[5]</sup> integrated a wearable E-textile system into a shirt that contained an electrocardiography device which used a hybrid power source of 14 TEGs with each TEG taking up an area of 3 x 4  $\text{cm}^2$  and 2 amorphous Si solar cells on the shoulders seen in Fig.1.17c. The system's hybrid power source fed into a battery which was mainly powered by the TEGs when the E-textile is worn, while the solar cells act as a backup power source when the shirt was not in use. The TEGs were able to provide a power of 1 mW at 22 °C while the E-textile system consumed 0.6 mW <sup>[5]</sup>. However, despite the achievements made by Leonov et al <sup>[5]</sup>, there are still drawbacks to using bulk TEGs. The first is the difficulty in achieving good thermal contact between the rigid TEG and the curved surfaces of the human body, as such, there is a limited area where rigid TEGs could harvest energy <sup>[85]</sup>. The second is the user discomfort from wearing bulky and rigid TEGs on their clothing. While the third drawback is the difficulty of scaling up the production of these E-textile systems beyond the prototype stage.

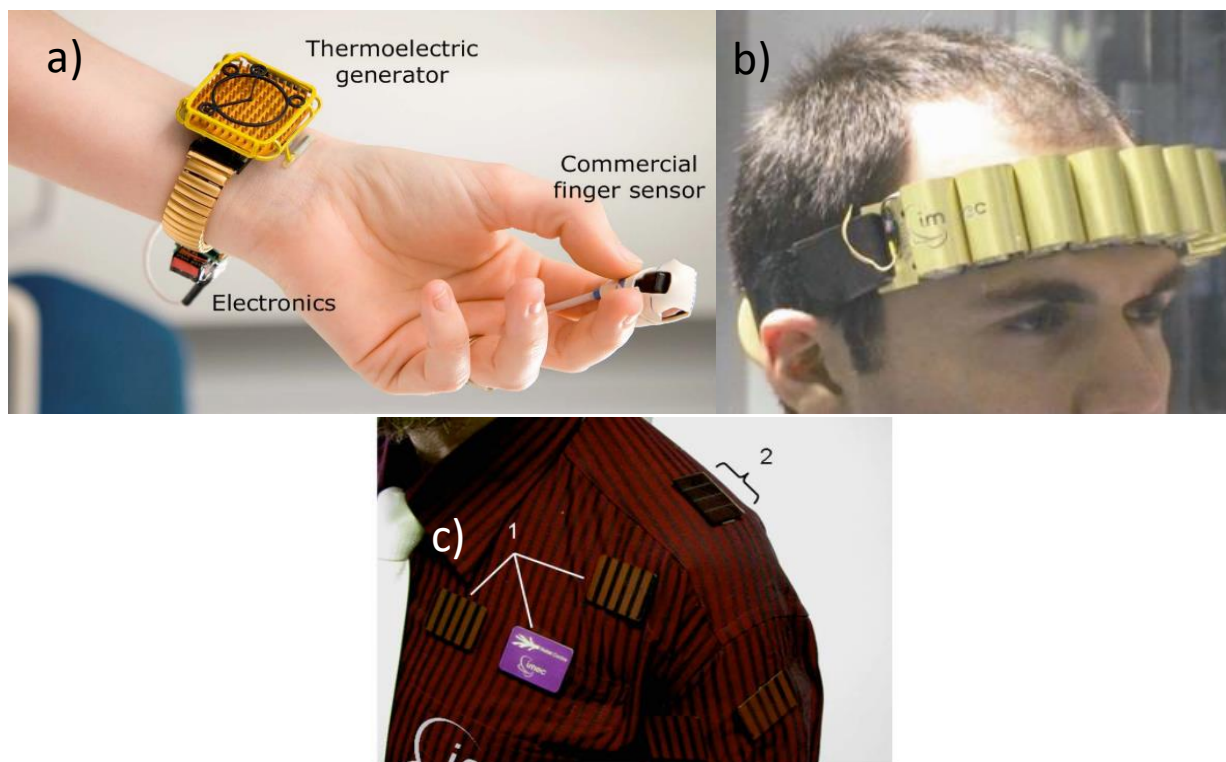


**Fig. 1.17-** Wearable medical systems powered by bulk  $\text{Bi}_2\text{Te}_3$ -based TEGs with (a) pulse oximeters wristwatch system, (b) a headband electroencephalography device and (c) an electrocardiography device shirt with (1) highlighting the TEGs while (2) shows the amorphous Si solar cells. Images from Leonov et al <sup>[5]</sup>.

## 1.8 Conclusions

In conclusion, despite TEGs current niche uses <sup>[9]</sup>, they still have the potential for further development to expand their applicable uses into areas such as powering medical sensors on wearable E-textile systems as demonstrated by Leonov et al <sup>[5]</sup>. However, the disparity between the curved surface of the human body and the bulky and rigid Bi<sub>2</sub>Te<sub>3</sub>-based TEGs limits the areas of energy harvesting in such wearables <sup>[85]</sup>. Additionally, such bulky devices on clothing would be noticeable and uncomfortable to the user. These drawbacks have been attempted to be addressed in the literature with the fabrication of lightweight screen-printed FTEG devices, with considerations put into the flexibility of all components of the FTEG such as the metal contact electrodes in the case of Kim et al <sup>[75,76]</sup> FTEG device. Additionally, through the work of Cao et al <sup>[74]</sup>, Bi<sub>2</sub>Te<sub>3</sub>-based FTEGs are capable of being screen-printed onto a variety of different fabrics and cured at temperatures between 150 °C and 250 °C. Both works highlight the potential of screen-printed Bi<sub>2</sub>Te<sub>3</sub>-based FTEGs to be incorporated into an E-textile system. However, the textiles printed onto so far have been high-temperature glass fabrics that are not comfortable for the user. This shows there is still a gap in the literature for developing a procedure to fabricate inorganic screen-printable FTEGs on standard fabrics used in apparel such as polyester-cotton. Additionally, as well as improving the flexibility of the TEGs their TE performance must also be improved for TEGs to be competitive with other heat engine technologies <sup>[25]</sup>. The most optimal roadmap for this is to synthesise nanostructures of the Bi<sub>2</sub>Te<sub>3</sub>-based materials used in current commercial TEGs as shown by the theoretical studies of Hick et al <sup>[23,31]</sup> and Dresselhaus et al <sup>[23,31]</sup>. When comparing different nanomaterial synthesis routes, PRS as shown by Zhang et al <sup>[35]</sup> stands out as a simple and scalable procedure for synthesising nanomaterials, that could be incorporated into the fabrication of FTEG devices as demonstrated by Chen et al <sup>[53]</sup>. However, more research needs to be conducted as there is still a large gap in the literature for FTEGs fabricated from printed Bi<sub>2</sub>Te<sub>3</sub>-based nanowires as Chen et al <sup>[53]</sup> is the only study on this topic, despite the real potential printing has for producing commercial nanostructured FTEGs devices. We believe that coupling nanomaterials synthesised via PRS with screen-printing could result in a viable procedure to scalably produce high-power outputting FTEG devices. Furthermore, along with Bi<sub>2</sub>Te<sub>3</sub>-based nanostructures, the literature has shown Te-polymer nanostructured composites as a potential flexible lightweight TE material without the need for high temperature annealing as shown by Wang et al <sup>[71]</sup>. This would mean these composites are compatible with standard fabrics such as polyester-cotton, however, to our knowledge no research investigating this has not been identified. This project aims to fill these gaps in the literature, by fabricating wearable FTEG devices via screen-printing PRS Te and Bi<sub>2</sub>Te<sub>3</sub>-based nanostructured composite films on Kapton and polyester-cotton.

## Chapter 2 Experimental methodology

In this chapter, we explore the experimental methodology used to conduct the research in this thesis. This includes the procedures related to the synthesis of the various nanomaterials examined as well as the paste formulation process utilised to screen-print said nanomaterials. Finally, the characterisation techniques used to quantify the samples' material and TE properties as well as the theory behind how these techniques work are also reviewed.

### 2.1 Polyol reflux synthesis methodology

The experimental set-up for PRS is shown in Fig. 2.1 and comprises a Schlenk line, condenser and a round bottom flask (RBF) which contain the reaction mixture. The RBF is purged of oxygen by using a vacuum pump through the Schlenk line for 5-10 mins then nitrogen gas flows into the Schlenk line and RBF for 2-5 mins. This process is repeated 3 times to remove as much oxygen as possible before running the PRS.

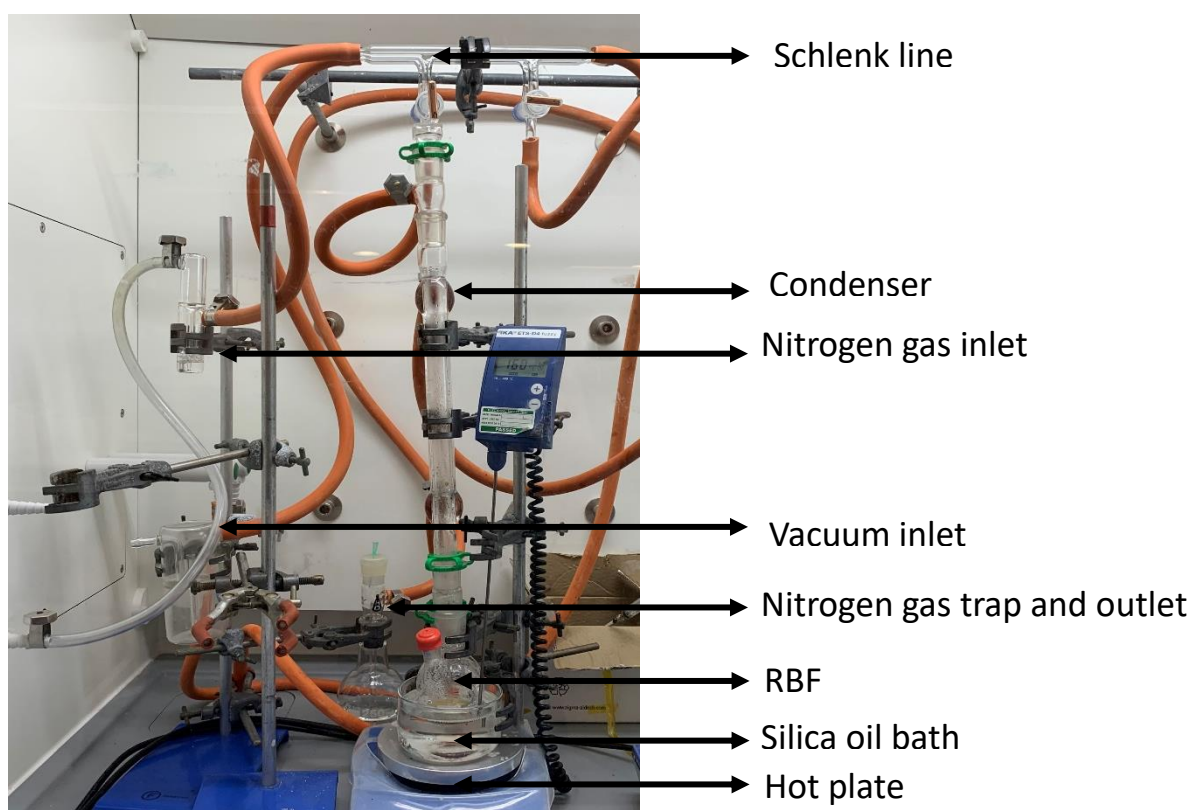


**Fig.2.1**-Image of the set-up used to run the polyol reflux synthesis.

### 2.1.1 Synthesis of $\text{Bi}_2\text{Te}_3$ and $\text{Bi}_2\text{Te}_x\text{Se}_{x-3}$ nanowires

To synthesise  $\text{Bi}_2\text{Te}_3$  nanowires 25 mL of EG (Sigma-Aldrich) was used as the solvent, 0.2 g of PVP (Fluka) as the growth directing agent, 1 mL of hydrazine hydrate (Sigma-Aldrich) as the reducing agent and 0.6 g of sodium hydroxide (KOH) (Fisher) to provide the basic pH environment need for the reaction. The metal salts used were 0.48 g of  $\text{TeO}_2$  (Aldrich,  $\geq 99.0\%$ ) as the Te precursor and 1.07 g of  $\text{Bi}(\text{NO}_3)_3 \cdot 5\text{H}_2\text{O}$  (Sigma-Aldrich,  $\geq 98.0\%$ ) as the Bi precursor. For the  $\text{Bi}_2\text{Te}_{3-x}\text{Se}_x$  38 mg of selenium oxide ( $\text{SeO}$ ) (Sigma-Aldrich,  $\geq 99.0\%$ ) is used as the Se precursor, and the amount of Bi precursor was reduced to 1 g.

The EG was separated into two different solutions of 20 mL and 5 mL. The PVP, KOH and  $\text{TeO}_2$  were dissolved into 20 mL of EG and dubbed the Te solution, while the  $\text{Bi}(\text{NO}_3)_3 \cdot 5\text{H}_2\text{O}$  was dissolved into 5 mL of EG and named the Bi solution. The Te solution was poured into an RBF, which was connected to a condenser with cold water running through it. A magnetic stirrer bar stirring at 600 rpm was used to maintain the uniformity of the reaction in the RBF. The solution temperature was increased to 160 °C using a hot plate and silica oil bath. As the temperature increased the solution colour changed from clear, to dark yellow and then to light black once the solution reached 160 °C, indicating that the EG was reducing the  $\text{TeO}_2$ . After 1 hr at 160 °C, the hydrazine hydrate was added to the RBF causing the light black solution to change into a dark black, indicating a strengthening of the reduction reaction. With this reduction reaction taking place the  $\text{TeO}_2$  reduces to metal Te seed particles. As the seed particles grew the PVP controlled their growth into forming Te nanowires, as described in section 1.6. The mixture was left to stir for 1 hr, afterwards, the Bi solution was added to the RBF, and the mixture was yet again left to stir for 1 hr to complete the reaction. Once the reaction was complete the mixture was centrifuged at 5000 rpm overnight. The resulting supernatant was decanted leaving the nanowire precipitant behind. Following the synthesis, the nanowires were cleaned by dispersing them (via bath sonication), in a cleaning solution made from 3:1 acetone/Di-water respectively. This cleaning solution formulation was chosen as it had been shown in the literature to remove the PVP <sup>[86]</sup>. These dispersions were then centrifuged at 10000 rpm for 20 mins and the resulting supernatant was decanted. This process was repeated 3 times to fully clean the nanowires. Following this, the nanowires were then left to dry overnight using a vacuum pump. Finally, the end product was weighed out and observed to have a mass of ~0.8 g, which was sufficient to formulate screen-printable pastes <sup>[87]</sup>. The nanowires were then dispersed in ethanol and drop-casted onto gold (Au)-coated Si, Si, glass and Kapton substrates for morphology and TE analysis. Dark grey films formed on the substrates after drop-casting. The rest of the dried powder was ground with a mortar and pestle and weighed into a speed mixing pot in order to formulate a screen-printable paste.

### 2.1.2 Synthesis of $\text{Bi}_{0.4}\text{Sb}_{1.6}\text{Te}_3$ nanoplatelets

The chemicals used to fabricate  $\text{Bi}_{0.4}\text{Sb}_{1.6}\text{Te}_3$  nanoplatelets were the same as described in section 2.1.1 but used in different quantities. 35 mL of EG is used as a solvent and the volume is split into 2 solutions. 0.48 g of  $\text{TeO}_2$ , 0.6 g of PVP and 2.24 g of KOH were dissolved in 20 mL of EG, this solution was called the Te solution. Meanwhile, 0.25 g of  $\text{Bi}(\text{NO}_3)_3 \cdot 5\text{H}_2\text{O}$  and 0.44 g of antimony acetate ( $\text{Sb}(\text{CH}_3\text{CO}_2)_3$ , Sigma-Aldrich) as the Sb precursor was dissolved in 15 mL of EG dubbed the BiSb solution. The amount of the reducing agent hydrazine hydrate in this reaction was adjusted to 2.5 mL.

In this reaction, EG's properties as a reducing agent at high temperatures were used to partially reduce the precursors as the hydrazine hydrate alone was insufficient<sup>[63,88]</sup>. This was carried out by heating and stirring the Te and BiSb solutions in their RBFs at 100 °C and 160 °C respectively. As EG is a weak reducing agent more time was needed to reduce the precursors, as such the solutions were left overnight where the BiSb solution had turned dark brown, while the Te solution had turned light black. 0.8 mL of hydrazine hydrate was injected into the Te solution, and the solution was left to stir for 1 hr. The Te solution was then heated to 110 °C, after which the BiSb solution was added. Afterwards, 1.5 mL hydrazine hydrate was injected into the mixture, which was then left to stir for 1 hr. Finally, the mixture was heated to 140 °C and left to stir for 24 hr. The end product was then cleaned and dried using the same process as in section 2.1.1. The nanoplatelet powder was determined to have a mass of ~0.6 g, which was sufficient for screen-printable pastes<sup>[87]</sup>. A portion of the cleaned nanoplatelet powder was then dispersed in ethanol and drop-casted onto Au-coated Si, Si and glass substrates forming grey films. This was done to characterise the nanoplatelets' material and TE properties. The rest of the dried powder was ground with a mortar and pestle and weighed into a speed mixing pot in order to formulate a screen-printable paste.

### 2.1.3 Synthesis of Tellurium nanorods

Compared to the previous synthesis this process is much simpler as 0.48 g of  $\text{TeO}_2$  and 0.6 g of KOH were dissolved in 20 mL of EG and poured into an RBF. The temperature is set to 160 °C and the solution is stirred at 600 rpm. Once that temperature is reached the solution stirs for an additional 1 hr where the EG starts to reduce the  $\text{TeO}_2$ , which is signified when the solution turns from dark yellow to light black. Afterwards, 1 mL of hydrazine hydrate is then added to the solution which is then left to stir for 1 hr. The RBF is then allowed to cool to room temperature and transferred into a glovebox where the solution is poured into a beaker containing 200 mL of methanol. The Te nanorods then precipitate out of the solution overnight, unlike the previous reaction procedures which would need to use a centrifuge.

This is due to the lack of PVP which acts as a stabilising agent as well as a growth direction agent. Once the precipitant is separated from the supernatant, the supernatant is decanted and the wet powder is transferred into centrifuge tubes containing 20 mL of methanol. The cleaning procedure of section 2.11 is used to remove any traces of KOH and hydrazine hydrate, however, the cleaning solution is replaced with methanol. Before the final precipitation to separate the nanorods from the cleaning solution, a portion of the cleaning dispersion was drop-casted onto Si substrates for material and TE analysis. Following this, the nanorods were then left to dry overnight under vacuum. The dried powders were ground with a mortar and pestle and weighed into a speed mixing pot prepped for paste formulation.

## 2.2 Paste formulations

### 2.2.1 Initial paste formulation

Initially, the  $\text{Bi}_2\text{Te}_3$  powder was synthesised and cleaned resulting in  $\sim 0.8$  g of nanowires as stated in section 2.11. This was then dispersed into an N-Methyl-2-pyrrolidone (NMP, >99%, Sigma-Aldrich) solvent and mixed with a lab vortex mixer at 40 kHz for 1 min. The binder polyvinylidene fluoride (PVDF, average molar weight = 534000, Sigma-Aldrich) was added to the solution, which was placed inside the top mixer again at 40 kHz for 1 min. Finally, the solution was placed on a hotplate where it was heated to 100 °C and left to stir at 400 rpm overnight using a magnetic stirrer bar. The subsequent paste was then sonicated for 2 hr before screen-printing. The NMP-PVDF solvent-binder system was chosen, as it is well-known and heavily used in industrial printed lithium-ion batteries <sup>[48,87]</sup>. This is due to PVDF being a very flexible thermoplastic, as it has a very small amount of cross-linking which makes it a suitable binder for screen-printing FTEGs <sup>[48]</sup>. Furthermore, this makes PVDF a good candidate as a binder rather than using epoxy-based binders which tend to produce more brittle screen-printed films, with a higher tendency to delaminate from the substrate as shown by Cao et al <sup>[74]</sup>. Additionally, if purchased commercially the epoxy-based binders may contain chemicals that could have an adverse effect on the nanowires such as oxidising them, without us being able to realise what is going on in our paste system. The amount of NMP and PVDF had been varied between 3 mL and 10 mL for NMP and 10 % and 30 % with respect to the mass of the nanowire powder for PVDF, in order to optimise the viscosity of the final paste.

### 2.2.2 N-Methyl-2-pyrrolidone/Polyvinylidene fluoride thermoelectric paste formulation

The most effective paste formulation process that was determined in this project for a variety of different TE pastes was, to first dissolve the binder into the solvent and then mix the nanowires into that solution via a combination of speed mixing and bath sonication instead of relying on a magnetic stirring. First PVDF is dissolved in NMP to formulate a binder solution at a concentration of 100 mg/mL. This is achieved in a dry nitrogen glovebox by adding the PVDF into the sample bottle and then pouring in the NMP, after which the solution is stirred with a magnetic stirrer bar at 400 rpm at 60 °C overnight until the solution is clear. The initial ground-up TE nanomaterial powder is stored and added to a 10 mL speed mixing pot in a nitrogen-filled glovebox. NMP is then added to the speed mixing pot and sealed with parafilm and speed mixed for 2500 rpm for 5 mins and bath sonicated (bath water temperature < 10°C) for 2 hr in an ice bath. Then in the glovebox, an amount of binder solution which was at 60 °C is added so that the final screen-printed film is made up of 5% to 20% PVDF. The pot is re-sealed with parafilm and speed mixed at the same speed for 20 mins then bath sonicated (bath water temperature < 10°C) for 2 hr. The paste is then speed mixed for a final 5 mins before being ready to print. The paste is left in a fridge at 4 °C but it should be bath sonicated for 1-2 hr and speed mixed for 5 mins before printing.

### 2.2.3 Paste formulation with Dimethyl sulfoxide

Additionally, a less toxic solvent was also examined, in this case, Dimethyl sulfoxide (anhydrous DMSO, >99%, Sigma Aldrich) to make the pastes less hazardous. PVDF is also soluble in DMSO which has a high boiling point. In addition, the freezing point of DMSO is ~18 °C which would potentially allow for long-term paste storage as particle aggregation is hindered by the frozen solvent<sup>[48]</sup>. The paste was investigated in printing Bi<sub>0.4</sub>Sb<sub>1.6</sub>Te<sub>3</sub> nanoplatelets using the formulation of section 2.22 but with the NMP replaced with DMSO. So far to our knowledge, there has been no literature on a potential DMSO-PVDF solvent-binder system for screen-printable pastes.

## 2.3 Material characterisation techniques

### 2.3.1 Scanning electron microscope

In a scanning electron microscope (SEM), electrons are accelerated via thermionic or field emissions between a cathode and anode. This results in the formation of an electron beam, that is then scanned across the surface of a sample [89]. When the electron beam interacts with the atoms of the sample, it causes different electrical signals to be generated. This is due to the inelastic collisions between the beam electrons and the outermost electrons of the sample's atoms causing ionisation [15]. The following signals that can escape from the sample due to these inelastic collisions include Backscatter electrons (BSE) which are produced at up to 1  $\mu\text{m}$  into the sample, Secondary electrons (SE) produced up to 50 nm into the sample surface, Auger electrons produced up to 1 nm into the sample surface and x-ray photons produced up to 10  $\mu\text{m}$  into the sample [15]. These can be used to investigate the morphology of the sample such as the sample's surface topography [90]. Fig. 2.2 showcases the set-up for an SEM below. The SEM used during this project was a field-emission gun SEM (JSM 6500 SEM, JEOL) using accelerating voltages of up to 15 kV were used with a SE detector.

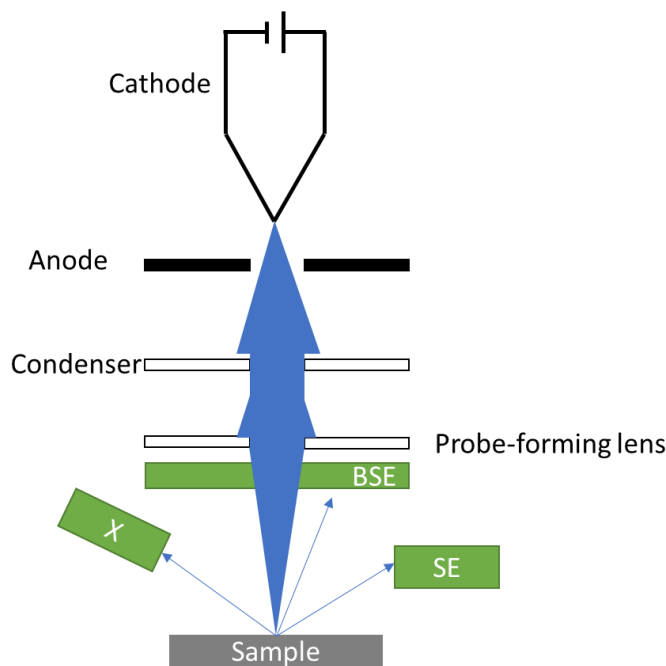


**Fig. 2.2-** Schematic of an SEM. The electron beam (blue) passes through condensing and focusing lenses and hits the sample to produce many different signals picked up by various detectors (BSE= Backscatter electrons detector, SE= Secondary electrons detector and X= X-ray photons detector) [15,89].

The images that the SEM produces are formed from the SE and BSE, which are collected by detectors and converted into data that can be shown as an image on a monitor <sup>[15,89,90]</sup>. The difference between the BSE and SE results in a shadow effect that enhances the 3D appearance of the surface topography of the imaged sample <sup>[90]</sup>.

### 2.3.2 Energy-dispersive X-ray spectroscopy

Energy-dispersive x-ray spectroscopy (EDX) is performed using energy-dispersive lithium-drifted Si detectors with a resolution of  $\Delta E=150-200$  eV placed within the vacuum chamber of an SEM <sup>[89]</sup>. The detectors identify characteristic x-ray photons produced from the interactions between the SEM electron beam and the orbital electrons of the sample's atoms <sup>[15,89]</sup>. This is used for elemental analysis and to identify which elements make up a sample and at what quantities <sup>[89]</sup>. This is due to the unique nature of the characteristic x-ray photons only corresponding to specific wavelengths related to the energies of the electron orbital shells of the atoms. As characteristic x-ray photons are produced when an electron in an inner orbital shell gets knocked out by the electron beam causing an electron from the outer orbital shell to fill the void. To fill the void, the electron emits a discrete x-ray photon due to the quantized nature of the electron orbital shells <sup>[91]</sup>. Additionally, "white" radiation or Bremsstrahlung radiation is produced from decelerating electrons when they're in the sample <sup>[15]</sup>. Both characteristic x-ray photons and Bremsstrahlung radiation make up the EDX spectrum, Fig. 2.3 shows how these x-rays are produced. The EDX detector used during this project was a Thermo Scientific Ultra Dray 10 mm<sup>2</sup> EDS with an uncertainty of 2 %.

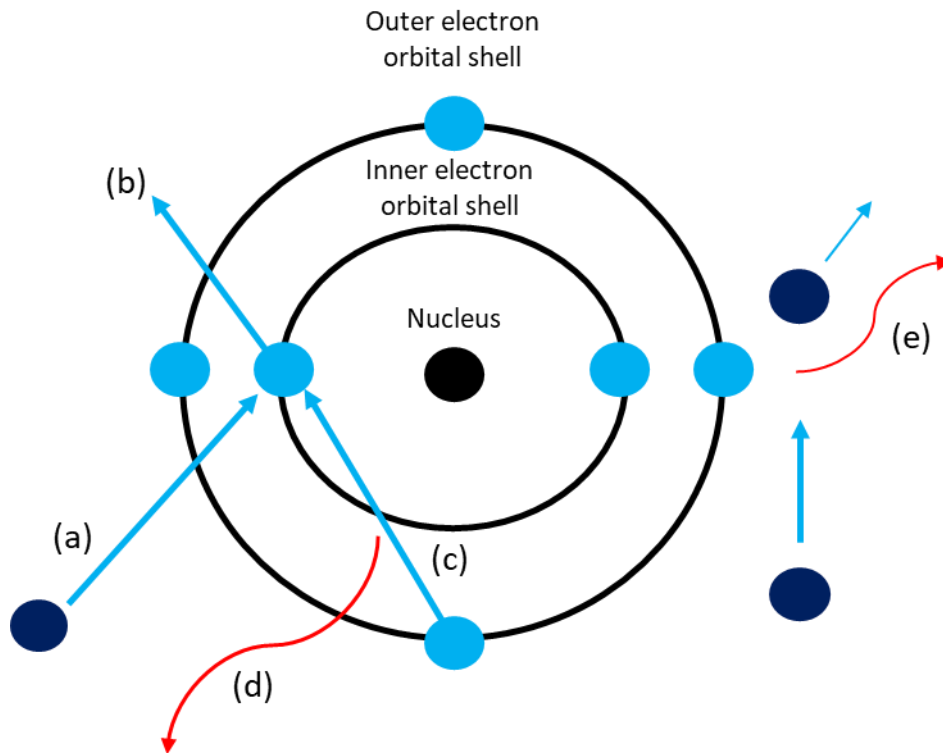


**Fig.2.3-** Schematic diagram SEM beam electrons interacting with sample atom’s electrons forming characteristic x-ray photons and Bremsstrahlung radiation. Initially (a&b) beam electron (dark blue) knocks out an inner orbital electron leaving a vacancy (c) which is filled by an outer electron (d) which generates a characteristic x-ray photon. (e) Beam electrons decelerate when interacting with sample atom’s electrons releasing Bremsstrahlung radiation <sup>[15]</sup>.

### 2.3.3 Grazing incidence X-ray diffraction

Grazing incidence X-ray diffraction (GIXRD) is a widely used material characterisation technique for identifying a sample’s crystal structure, crystallite/grain size and preferred crystal lattice orientation <sup>[15]</sup>. Similarly, to SEM, GIXRD is based on the scattering of x-ray photons by the arrays of a sample’s atoms <sup>[92]</sup>. As the spacing between the planes of atoms and the space between atoms is within the order of the wavelength of x-rays, the Braggs law comes into effect:

$$N\lambda = 2d \sin \theta \tag{2.1}$$

Where in equation 2.1, N is an integer representing an order of the reflection,  $\lambda$  is the wavelength of the X-ray beam (Å), d is the spacing between diffracting planes (Å), and  $\theta$  is the incident angle in degrees <sup>[15]</sup>. Fig. 2.4 shows a diagram of x-ray photons scattering of a crystal lattice.

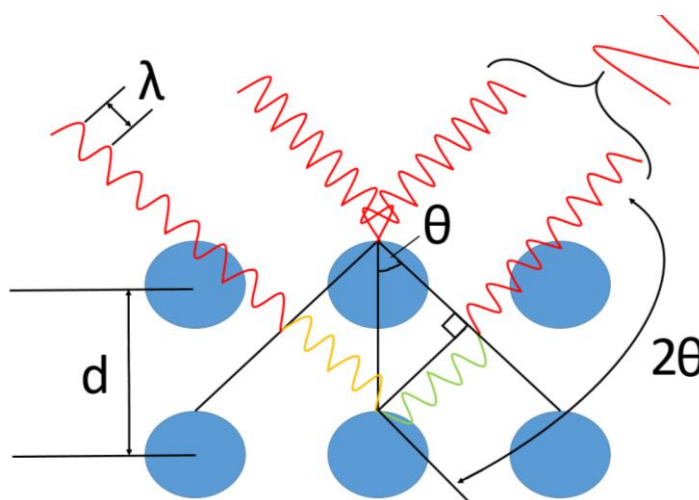


**Fig. 2.4-** Schematic diagram of X-rays scattering on an array of atoms in a crystal lattice to demonstrate Bragg's law. With the x-rays obeying the Bragg's condition and adding constructively after scattering.

Using this principle, as the returning x-rays scatter back, they interfere with each other constructively as they have the same incident angle, where they are collected and analysed forming characteristic peaks on a GIXRD spectrum. This spectrum is then compared to other observed spectra stored in the International Centre for Diffraction Data (ICDD), a database to analyse the sample's crystal structure and match it to a known material. This is done using the data analysis software PDXL, which is connected to the database maintained by the ICDD <sup>[29]</sup>. Additionally, the crystal grain size can be measured from the most intensive diffraction peaks via the PDXL software <sup>[15]</sup>. This is obtained by implementing the Scherer equation onto the diffraction peaks of the GIXRD pattern:

$$D = \frac{K\lambda}{\beta \cos\theta} \quad (2.2)$$

Where  $D$  is the grain size (nm),  $K$  is a constant that refers to the grain shape factor and is approximate to 0.9,  $\lambda$  is the wavelength of the incident X-rays (nm),  $\beta$  is the full width at half maximum (FWHM) intensity of the peak (radians), and,  $\theta$  is the diffraction angle (radians) <sup>[15]</sup>. The grain size is an important quantity, as a smaller grain size leads to more phonon scattering reducing  $\kappa$ , which could improve ZT.

## 2.4 Thermoelectric characterisation techniques

### 2.4.1 Seebeck coefficient characterisation

The machines used to measure the  $S$  of the samples produced during this project were calibrated against a reference nickel foil ( $S \sim 19 \mu\text{V K}^{-1}$ ) from the manufacturer (JouleYacht) which is regularly measured to calibrate these  $S$  measuring systems with the results checked against previous readings to see if they are within the manufacturer’s 7 % relative error <sup>[93]</sup>. As such all  $S$  measurements have an uncertainty of 7 %.

#### 2.4.1.1 Room temperature Seebeck coefficient measurement

The theory behind measuring the  $S$  is to induce a thermal gradient in a material and measure the potential difference across that material. Room temperature  $S$  measurements are conducted with a portable  $S$  probe (PTM-3, MRS, JouleYacht), as shown in Fig. 2.5. One probe with a red band would act as the heat source and reach a temperature of 50 °C, while another with a blue band acted as the heat sink with a temperature of 25 °C. The probes were placed on the sample 2 mm apart and 3 measurements were recorded for 3 different areas of the sample, where the average was taken as  $S$ .

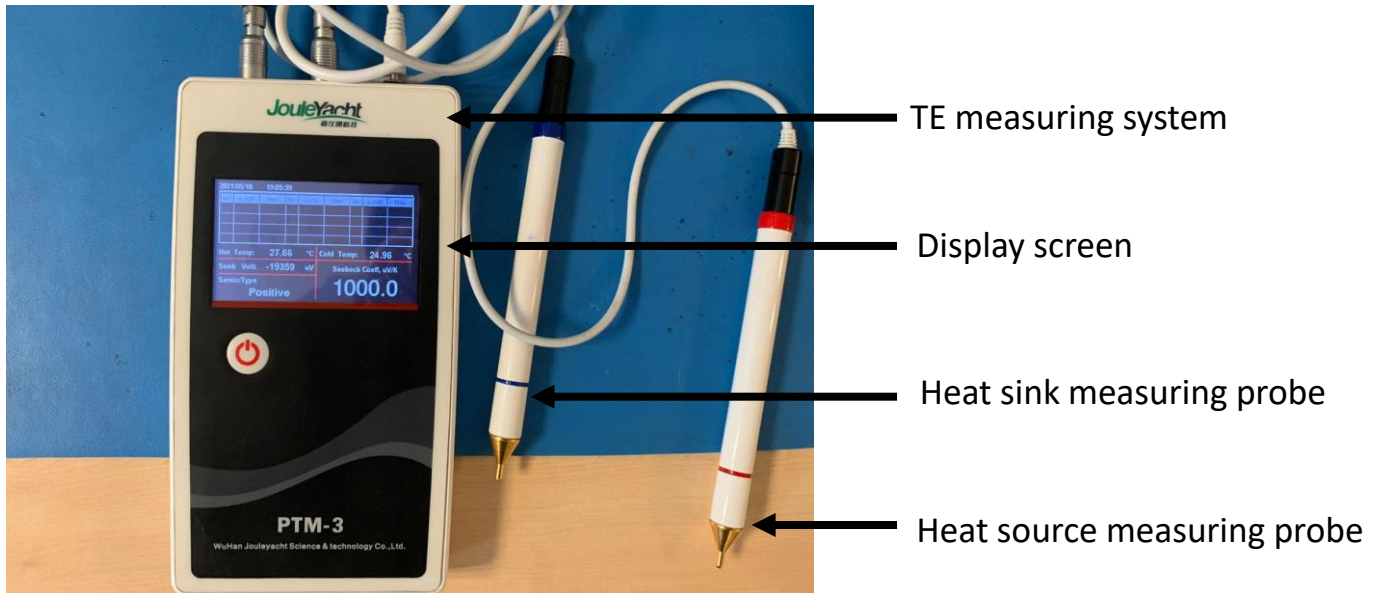
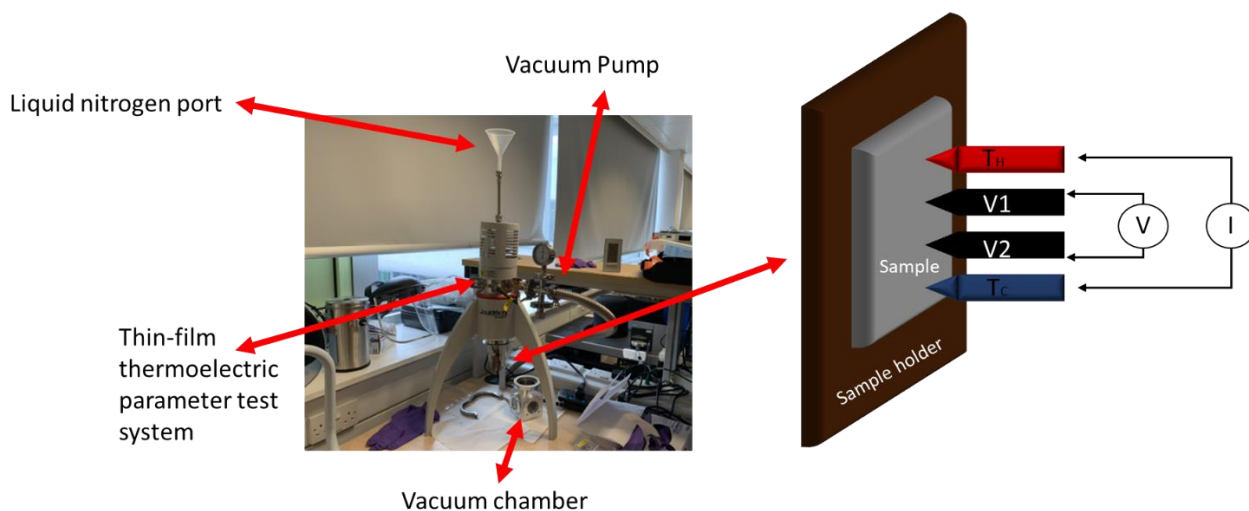


Fig.2.5- Image of the PTM-3 Seebeck coefficient 2-probe measuring test system.

### 2.4.1.2 Variable temperature Seebeck coefficient characterisation

To measure the  $S$  in our samples at different temperatures, thermocouple probes are applied to said samples, with one that acts as a heat source and another as a heat sink to generate a heat flux, whereby the resulting Seebeck voltage is recorded <sup>[15,29]</sup>. The characterisation of the  $S$  and  $\sigma$  over a temperature range, in this project was performed using a commercial Thin-film thermoelectric parameter test system (MRS-3L, JouleYacht), with the ability to record values between the range of 100 K and 600 K seen in Fig. 2.6.



**Fig. 2.6-** Picture (left) of the Seebeck measuring test system used to measure the Seebeck coefficient over a temperature range using a vacuum chamber and liquid nitrogen to modify the temperature. With red arrows, indicating the relevant parts to the machine with the diagram (right) illustrating the 4-probe set up for measuring the Seebeck coefficient and electrical conductivity with  $T_H$  (hot probe),  $T_C$  (cold probe) and  $V1$  and  $V2$  measuring the Seebeck voltage. All 4 probes were used to measure the electrical conductivity by having an induced current passed from the outer probes  $T_H$  and  $T_C$  through the sample with voltage measured by  $V1$  and  $V2$ .

Samples were mounted between two copper heat reservoirs with Au contacts as both heaters and electrical contacts. The  $S$  was measured using the differential method with a maximum temperature difference of 10 K by fixing the temperature of one side of the sample and heating the other side at a constant heating rate and sampling voltage and temperature simultaneously. A linear fitting of the potential difference and the temperature difference is taken, where the gradient is taken as  $S$  according to equation 1.1.

Additionally, the outer thermocouple probes are used alongside the inner probes to conduct 4-point probe measurements to record the  $\sigma$  simultaneously as it records the S with an uncertainty of 5 % for  $\sigma$ . It does this by passing a current through the outer probes onto the sample and recording the voltage induced via the 2 inner probes to obtain a resistivity ( $\rho$ ) value and using the  $\rho$  to obtain the  $\sigma$  as seen in Fig. 2.6.

### 2.4.2 Hall probe measurements

Hall probe measurements are used to characterise a material's Hall electrical conductivity/resistivity as well as the material's charge carrier mobility and charge carrier concentration. Measurements in this project were conducted using a commercial Hall Effect measurement system (Nanometrics, HL5500 Hall system). The equipment works by using 4 probes placed in a square formation on the sample, with each probe at the same distance from the others as seen in Fig. 2.7. Using the van der Pauw technique, a current is passed from one probe to another on one side and the voltage is recorded on the other <sup>[15,29]</sup>. The advantage of this technique is that the only value needed beforehand is the thickness of the material to get the bulk readings <sup>[94]</sup>. The equation list (2.3-2.6) below shows how the bulk  $\sigma$  is calculated from the voltage response:

$$R_{21,34} = \frac{V_{34}}{I_{21}} \quad , \quad R_{12,43} = \frac{V_{43}}{I_{12}} \quad (2.3)$$

$$R_{32,41} = \frac{V_{41}}{I_{32}} \quad , \quad R_{23,14} = \frac{V_{14}}{I_{23}}$$

$$R_{43,12} = \frac{V_{12}}{I_{43}} \quad , \quad R_{34,21} = \frac{V_{21}}{I_{34}}$$

$$R_{14,23} = \frac{V_{23}}{I_{14}} \quad , \quad R_{41,32} = \frac{V_{32}}{I_{41}}$$

$$R_A = \frac{(R_{21,34} + R_{12,43} + R_{43,12} + R_{34,21})}{4} \quad , \quad R_B = \frac{(R_{32,41} + R_{23,14} + R_{14,23} + R_{41,32})}{4} \quad (2.4)$$

$$\exp\left(-\pi \frac{R_A}{R_S}\right) + \exp\left(-\pi \frac{R_B}{R_S}\right) = 1 \quad (2.5)$$

$$\rho = R_S d \quad , \quad \sigma = \frac{1}{\rho} \quad (2.6)$$

Equation 2.3 shows the calculated resistance (R) for each combination of voltage response to current injection <sup>[15,94]</sup>. The probes labelled 1,2,3,4, with an example of  $I_{12}$  represents the positive direct current injected into probe 1 and taken out of probe 2. As well as  $V_{34}$  represents the positive DC voltage measured between probes 3 and 4 ( $V_3 - V_4$ ) <sup>[15]</sup>. Likewise, for all the other combinations.

Equation 2.4 & 2.5 is used to calculate the sheet resistance  $R_s$  with  $R_A$  and  $R_B$  being the characteristic resistances. In Equation 2.6 with  $d$  being the thickness of the sample,  $\rho$  being the bulk resistivity and  $\sigma$  being the bulk electrical conductivity <sup>[15,29]</sup>.

Charge carrier mobility and concentration are calculated from the Hall voltage from equation 2.7. This is obtained by using a magnet underneath the sample in the  $+z$  direction while injecting a current from one probe to another and recording the Hall voltage produced. The polarity of the magnet is switched to the  $-z$ -direction and the process is repeated. This is done for all probe combinations <sup>[94]</sup>. A diagram of the Hall probe setup is shown below in Fig.2.7.

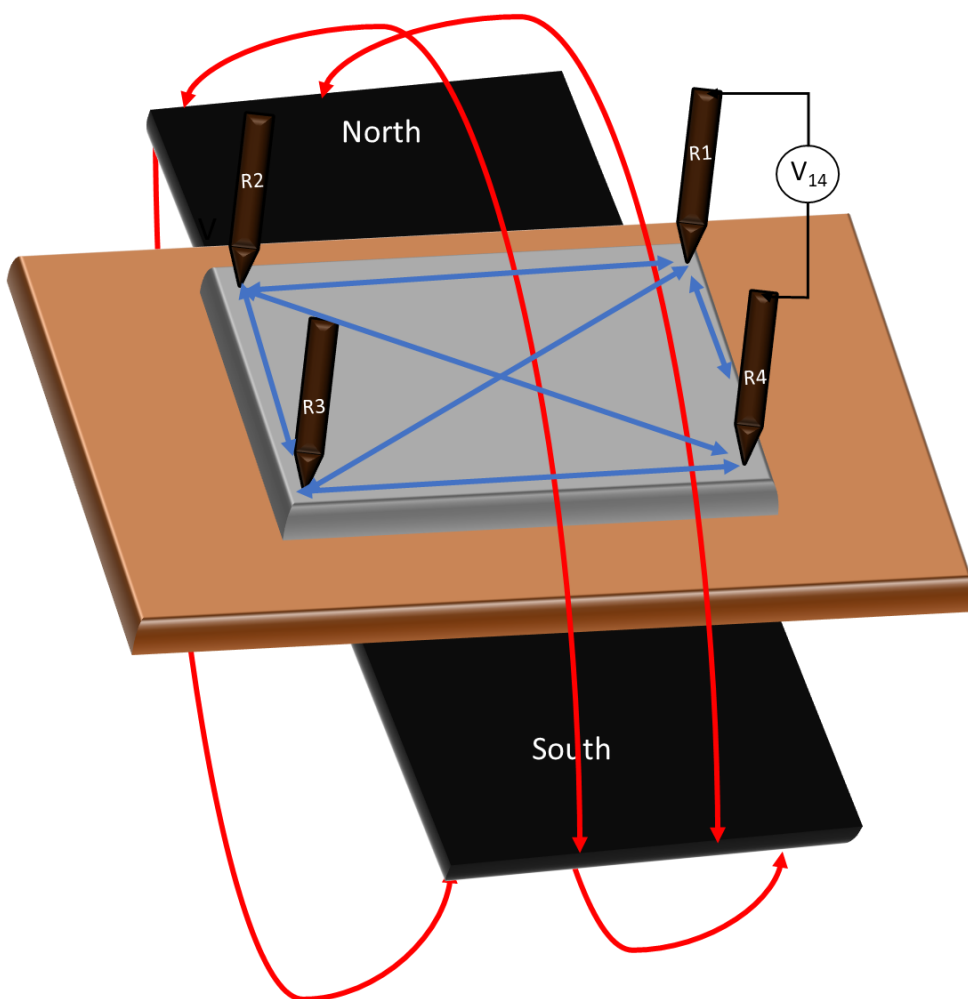


**Fig. 2.7-** Schematic of the basic set-up for Hall probe analysis with 4-probes (R1, R2, R3, R4) on a sample which is placed on a board on top of a magnet, as well as (red arrows) the magnetic field, induced current (blue arrows) with the voltage  $V_{14}$  being measured between probes R1 and R4.

Chapter 2

An example would be to apply a current  $I_{12}$  to probes 1 and 2 and measuring  $V_{34P}$ , then reversing the polarity of the magnet to get  $V_{34N}$ <sup>[15,29]</sup>. This gives 8 different measurements for the Hall voltage, the sum of these depending on if it's positive or negative, determines whether the sample is p or n-type<sup>[15]</sup>. The sum Hall voltage is used to work out the sheet carrier density, which is then used to calculate charge mobility and bulk carrier concentration seen in the equations below:

$$n_s = \frac{8 \times 10^{-8} IB}{q \Sigma V} \quad , \quad \mu_H = \frac{1}{q |n_s| R_s} \quad , \quad n = \frac{n_s}{d} \quad (2.7)$$

Where  $n_s$  is the sheet carrier density,  $\mu_H$  is the charge mobility,  $n$  is the bulk carrier concentration,  $I$  is the applied current,  $B$  is the applied magnetic field in Gauss,  $q$  is the charge of an electron,  $R_s$  is the sheet resistance and  $d$  is the thickness of the sample<sup>[15,29]</sup>.

It should be noted that both the Hall probe and the commercial test system use two different measuring techniques for  $\sigma$ . The Hall probe uses the van der Pauw technique while the commercial test system uses a simple linear 4-point probe set-up. The issue with the linear 4-point probe set-up is that it does not account for alternative pathways for the current outside linear path of the probes as shown in Fig. 2.8.

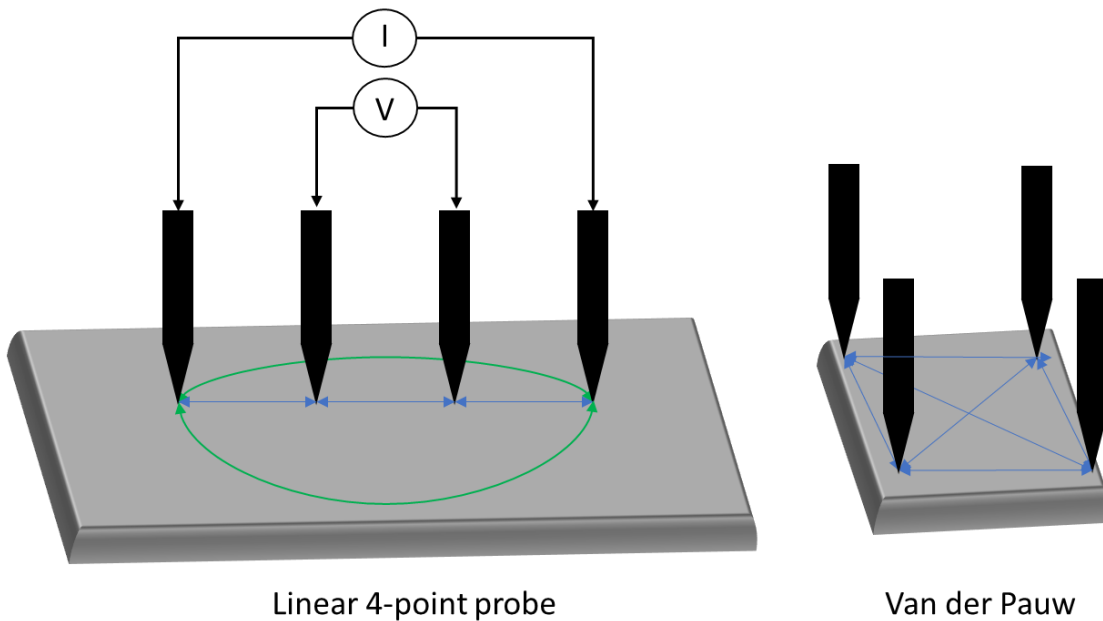


**Fig. 2.8-** Schematic of the linear 4-point probe set-up used by the commercial test system and the Van der Pauw method used by the Hall probe. The blue arrows represent the current accounted for by the techniques, while the green arrows represent the unaccounted current.

To rectify this geometric disparity between the two techniques, the  $\sigma$  results measured using the commercial test system for all temperatures were adjusted by multiplying them by a ratio of the room temperature sheet resistances measured by the Hall probe and commercial test system. This is to achieve more accurate  $\sigma$  values, the equation for which is seen below:

$$\sigma = \sigma_{cts} \frac{R_{shall}}{R_{scts}} \quad (2.8)$$

Where in equation 2.8,  $\sigma_{cts}$  is the electrical conductivity measured by the commercial test system at a given temperature,  $R_{shall}$  is the room temperature sheet resistance measured by the Hall probe,  $R_{scts}$  is the room temperature sheet resistance measured by the commercial test system and  $\sigma$  is the newly adjusted electrical conductivity once this room temperature sheet resistance correction factor is applied to it. Alternatively, the Hall probe has the ability to perform variable temperature measurements by using liquid nitrogen to get to temperatures as low as 125 K and a heater to get to 450 K.

## 2.5 Flexibility characterisation

According to Ou et al <sup>[66]</sup>, the flexibility of TE materials when incorporated into TEGs is severely under-represented in the literature. We address this in our project by conducting bending studies to show our screen-printed films' flexibility. These bending studies were performed using a custom-built rig as shown in Fig. 2.9. The bending rig would move forwards and backwards for a number of bending cycles that could be coded into the electronics via the rig's Arduino program. The samples were placed in the fabric's pocket with the bending radius being determined by the green cylinders which could be swapped. However, the roughness of the fabric pocket would damage some of the films and show a much higher resistance unrelated to the bending, so an additional Kapton pocket was made to counteract this. The movement of the white holders seen in Fig. 2.9 allowed the sample to be bent by the radius of the cylinders. The samples' resistance before and after bending was measured using a 2-point multimeter. The resistance was taken in 100 bending cycle increments for a total of 1000 bending cycles.

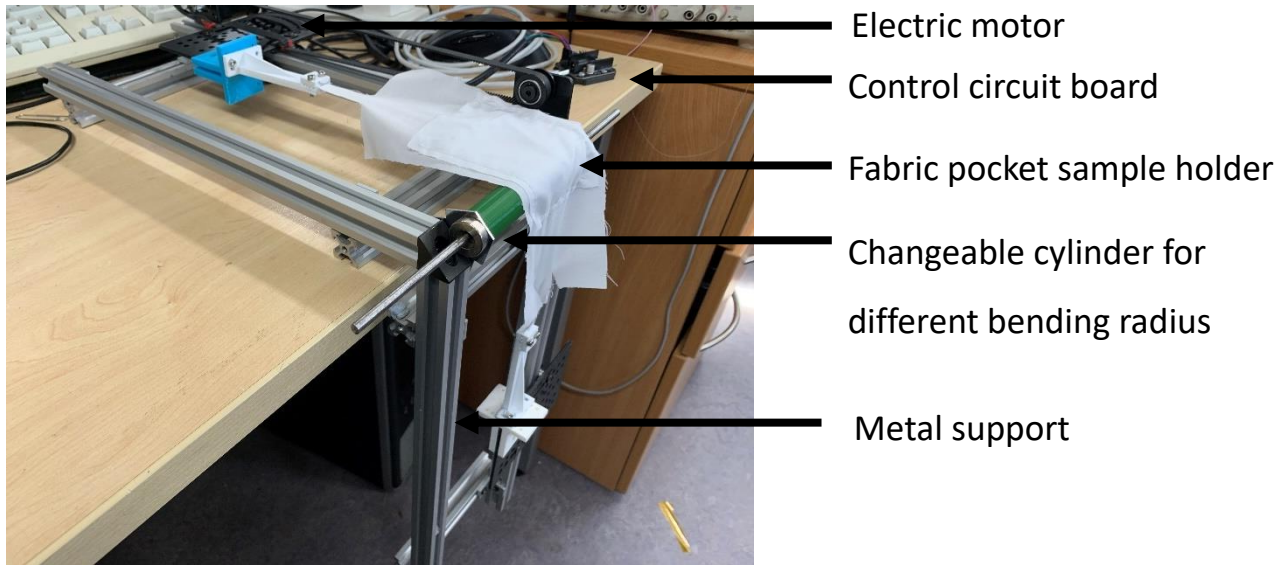


Fig.2.9- Image of custom bending rig used for flexibility studies.

## 2.6 Power output characterisation

The FTEG devices' power outputs were measured by placing the device between two Peltier cells with one acting as the heat source (temperature ranging from 30 °C to 90 °C) and the other as the heat sink (temperature held constant at 20 °C). When the device is connected to a load resistor ( $R_L$ ) (seen in Fig. 2.10) the generated current will deliver electric power to the load resistor <sup>[50]</sup>.

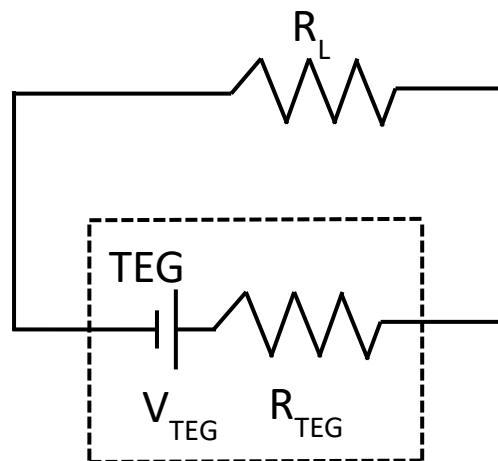


Fig. 2.10- Sketch of the electrical circuit of a TEG with a load resistor, where  $V_{TEG}$  and  $R_{TEG}$  are the total Seebeck voltage and resistance of the TEG respectively.

The device's power output was measured by measuring the voltage and current using 4-point probes. The temperature of the Peltier cells and the thermal gradient across the devices were captured using an infrared camera.

Equation 2.9 shows how the measured voltage and the total resistance across the device can be used to calculate the power output of the device when a temperature gradient is applied to it:

$$P_{TEG} = \frac{V_{TEG}^2}{R_{TEG}} \quad (2.9)$$

Where  $V_{TEG}$ ,  $R_{TEG}$ , and  $P_{TEG}$  are the total output voltage, the resistance across the device and the power output of the TEG. The FTEG prototype devices fabricated during this project had planer geometries with the surface area of the TE legs being 20 x 5 mm. The thickness of the FTEG device depended on the number of printing passes during the FTEG TE legs fabrication. The width of the TE legs was chosen arbitrarily, while their lengths were chosen based on whether the total measured resistance across the device was deemed sufficient to obtain a measurable power output based on equation 2.9. The TEG design from Fig.1.3 was used in our FTEGs that used thermocouples of n-type and p-type TE legs. While the electrical contacts of our single-leg FTEG devices were redesigned into an L shape as all the TE legs would have the same Seebeck voltage. The change in design allows the current to flow through the device instead of getting cancelled out, as would be the case if the single-leg FTEG devices used the design from Fig.1.3. A sketch of a single-leg FTEG device between a heat source and heat sink is shown in Fig.2.11.

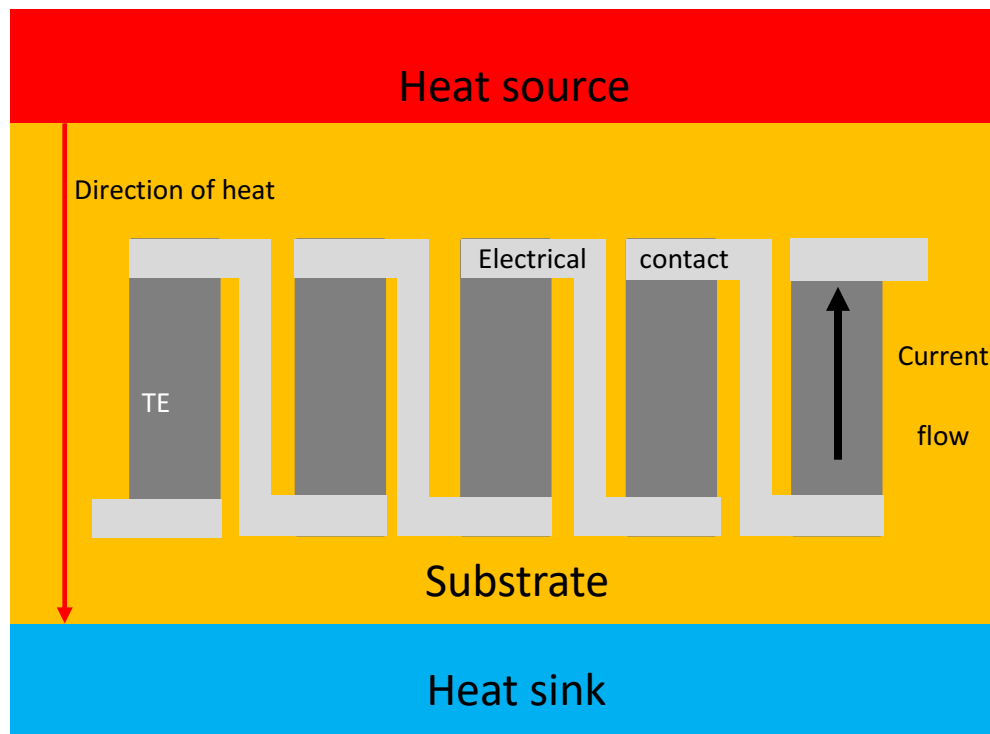


**Fig.2.11-** Sketch of a single-leg FTEG device with 5 TE legs between a heat source and a heat sink, with a red and black arrow showing the direction of heat and current respectively.

## Chapter 3 Screen-printed polyol reflux synthesised Bismuth telluride nanowire films

N-type  $\text{Bi}_2\text{Te}_3$  nanowires were for the first time screen-printed onto flexible Kapton substrates using a paste formulation of polyvinylidene fluoride (PVDF) binder and N-Methyl-2-pyrrolidone (NMP) solvent. We report how annealing can affect the morphology and TE properties of these nanowires as drop-casted and screen-printed films. We also demonstrate the suitability of the screen-printed nanowire composite films for flexible TE applications by performing a detailed bending cycle analysis, as well as fabricating a single-leg FTEG prototype on Kapton with an observable power output below a temperature difference of 32 K.

### 3.1 Characterisation analysis of drop-casted films of $\text{Bi}_2\text{Te}_3$ nanowires

#### 3.1.1 Material characterisation

The  $\text{Bi}_2\text{Te}_3$  nanowires were synthesised as described in section 2.11 and were drop-casted to form films with thicknesses of  $\sim 50 \mu\text{m}$ , which were then characterised by SEM, EDX and GIXRD. SEM revealed the drop-casted films to be made up of nanowires which had average diameters of  $60 \pm 20 \text{ nm}$ , with lengths that ranged from  $0.4 \mu\text{m}$  up to  $5 \mu\text{m}$  as shown in Fig. 3.1.

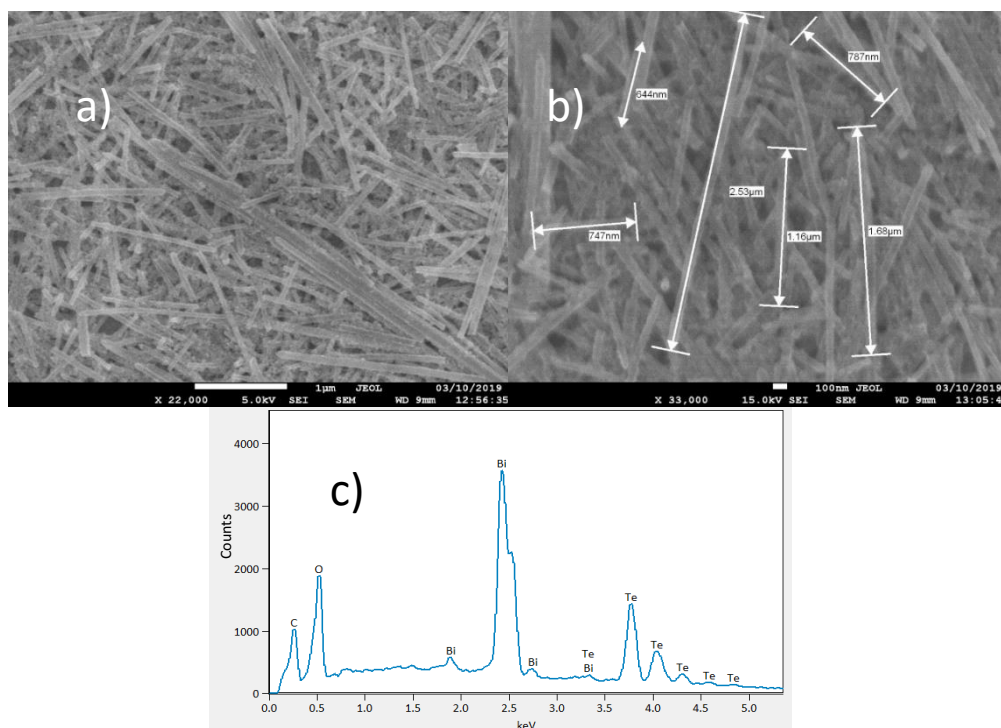


**Fig.3.1-** SEM images (a&b) of a top-down view of PRS  $\text{Bi}_2\text{Te}_3$  nanowires on an Au-coated Si substrate and (c) an EDX spectrum of the drop-casted PRS  $\text{Bi}_2\text{Te}_3$  nanowires film.

The chemical composition of the drop-casted nanowire films was determined by EDX analysis (seen in Fig.3.1(c)) and showed average atomic percentages of 39.6:60.4 for Bi and Te respectively. These percentages are within the 2 % uncertainty of the EDX detector for stoichiometric  $\text{Bi}_2\text{Te}_3$ . We observe a higher Bi content in our nanowires compared to Zhang et al <sup>[35]</sup> as we've increased the mass of the Bi precursor from 0.8185 g to 1.07 g. The drop-casted films had an average oxygen content of 32 % with respect to Bi and Te, revealing that the nanowires had been oxidised during the time taken between removing the PVP capping agent and measuring their chemical composition, which was also observed in the literature by Zhang et al <sup>[35]</sup>.

GIXRD diffraction patterns for the PRS drop-casted  $\text{Bi}_2\text{Te}_3$  nanowires are indexed to the rhombohedral tellurobismuthite crystal structure as shown in Fig.3.2. We observe that the (0 1 5) plane is the dominant  $\text{Bi}_2\text{Te}_3$  crystal lattice orientation which was also observed by Zhang et al <sup>[35]</sup>. From the GIXRD data and using the Scherrer formula (equation 2.2) we observed an average grain size of  $10.4 \pm 0.3$  nm. The material characterisation results for the PRS  $\text{Bi}_2\text{Te}_3$  nanowires were shown to be reproducible with a minimum of 3 syntheses each producing the same results.

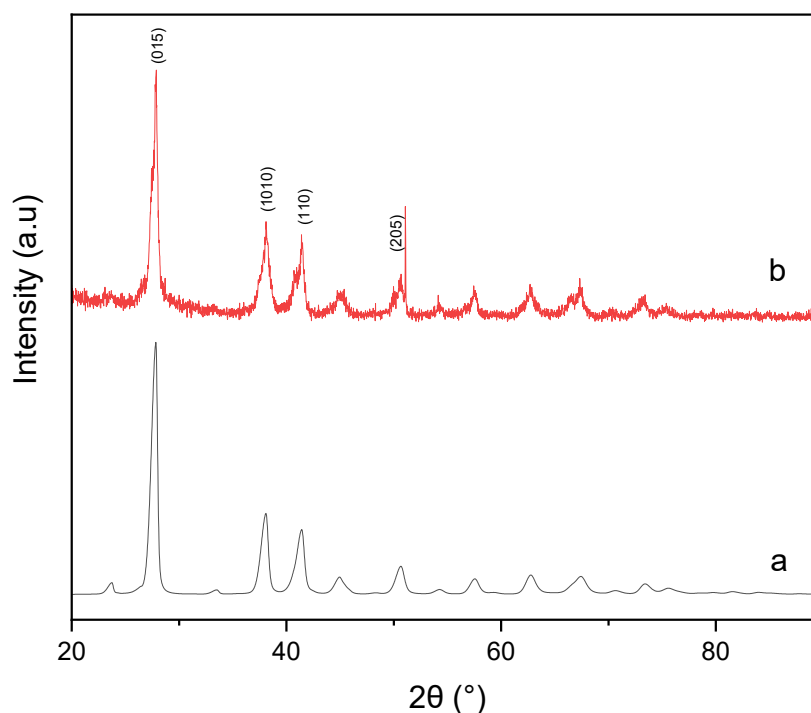


**Fig. 3.2-** GIXRD diffraction patterns obtained for (a) reference XRD of tellurobismuthite ( $\text{Bi}_2\text{Te}_3$ ) mineral from the International Centre of Diffraction Data (ICDD) database (PDF 00-015-0863) and (b) drop-casted film of PRS  $\text{Bi}_2\text{Te}_3$  nanowires on an Au-coated Si substrate.

### 3.1.2 Thermoelectric characterisation

Unfortunately, no TE measurements could be performed on the unannealed drop-casted films, due to their high electrical resistances ( $> 1 \text{ M}\Omega$ ). One possible reason could be the junction resistance between the nanowires. Another reason is the high oxygen content of 32 % observed by the EDX detector, which could be the result of a barrier oxide layer enveloping the nanowires. This would increase the junction resistance between nanowires as described by Thongkham et al <sup>[61]</sup>. This results in the inability to measure the nanowire films' TE properties which is consistent with the lack of such results in the literature.

To improve the films' electrical properties they were annealed inside a tube furnace at  $400 \text{ }^\circ\text{C}$  for 2 hr in an inert argon (Ar) atmosphere <sup>[53]</sup>. After annealing the samples had changed colour, from dark grey to light grey with the films becoming more brittle. The annealed films underwent microstructural analysis by SEM as shown in Fig. 3.3 to observe any morphology changes, due to the annealing process.

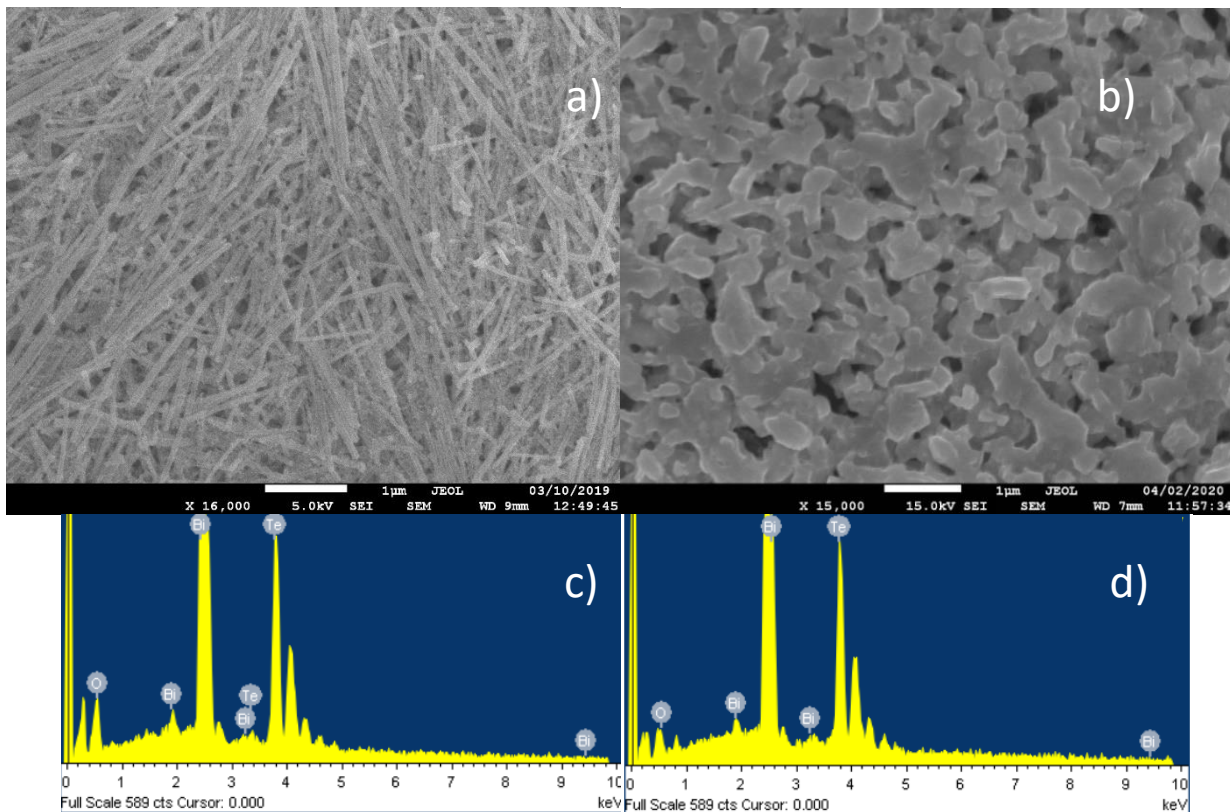


**Fig. 3.3-** SEM of a top-down view of drop-casted  $\text{Bi}_2\text{Te}_3$  nanowire film on a Si substrate (a) before annealing and (b) post-annealing, alongside EDX spectres for (c) before annealing and (d) post-annealing.

Microstructural analysis revealed that the films were no longer a network of individual nanowires but had merged into an interconnected nanostructured network (INN), possibly as a result of the nanowires fusing during annealing. The chemical composition data from the EDX spectrum showed a decrease in the Te with the average atomic ratios being 42.4:57.6 for Bi and Te respectively. This drop is believed to be due to Te sublimation during annealing, as such a decrease in Bi precursor concentration is necessary to achieve stoichiometric  $\text{Bi}_2\text{Te}_3$  for post-annealed PRS  $\text{Bi}_2\text{Te}_3$  nanowires. As such the amount of Bi precursor for the PRS reactions going forward was reduced from 1.07 g to 1 g. When observing the oxygen content, we note a decrease from 32 % to 16 %. This change in atomic percentages between Bi and Te and the halving of the oxygen content could have been the result of residue  $\text{TeO}_2$  and other oxide species being burnt off during annealing.

GIXRD performed on the annealed drop-casted films revealed a similar pattern as seen before with (0 1 5) being the dominant  $\text{Bi}_2\text{Te}_3$  crystal lattice orientation as shown in Fig. 3.4. However, there was a much larger peak present at  $50.7^\circ$  not attributed to any  $\text{Bi}_2\text{Te}_3$  crystal lattice orientation or the glass substrate but instead for Bi (1 1 4) or Te (0 2 1). This has not been observed within the literature previously and is believed to be the Bi (1 1 4) phase, due to the increase in the Bi content in the EDX spectrum. This is believed to be due to excess Bi atoms that had not been incorporated into the Te nanowires and formed metallic Bi among the  $\text{Bi}_2\text{Te}_3$  nanowires. This excess in Bi was the result of a higher mass of Bi precursor in our PRS reaction (1.07 g) compared to Zhang et al <sup>[35]</sup> (0.8185 g) and Chen et al <sup>[57]</sup> (0.82 g). From the GIXRD data, the average grain size quadrupled from  $10.4 \pm 0.3$  nm to  $41.1 \pm 0.7$  nm, which could contribute to a higher charge carrier mobility due to less grain boundary scattering resulting in a higher  $\sigma$ .

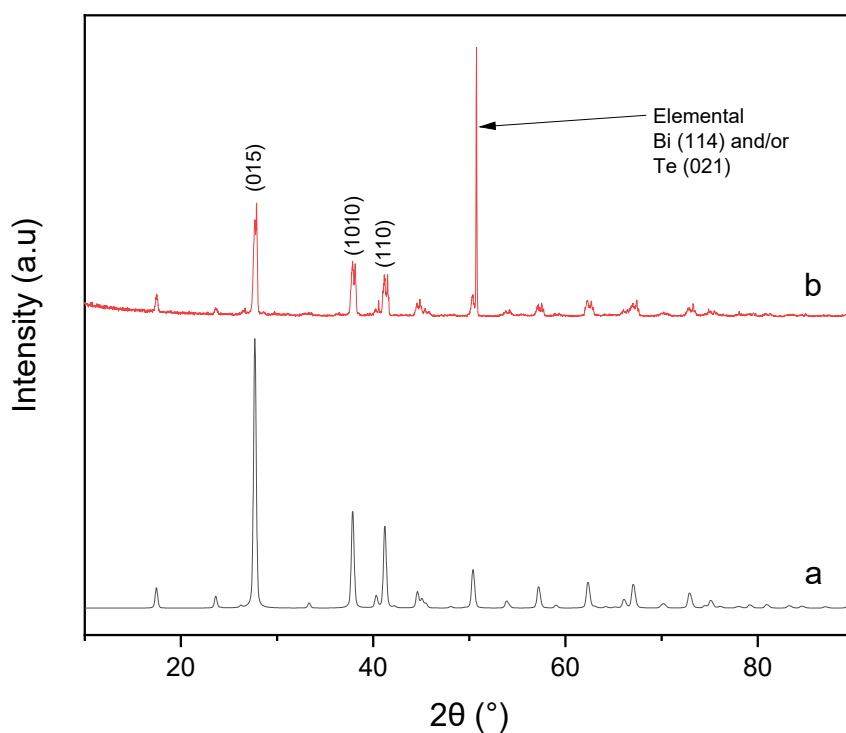


**Fig. 3.4-** GIXRD diffraction patterns obtained for (a) reference XRD of tellurobismuthite ( $\text{Bi}_2\text{Te}_3$ ) mineral from the International Centre of Diffraction Data (ICDD) database (PDF 00-015-0863) and (b)  $\text{Bi}_2\text{Te}_3$  INNs on an Au-coated Si substrate after being annealed in an Ar atmosphere at  $400^\circ\text{C}$  for 2 hr.

The post-annealed drop-casted films were conductive enough to be able to be measured by both the commercial test system and the Hall probe. This can be seen in Fig. 3.5 for a temperature range of 250-450 K. The Hall probe was only used at room temperature, with  $\sigma$  of  $2100 \pm 100 \text{ S m}^{-1}$ , mobility of  $26 \pm 8 \text{ cm}^2\text{V}^{-1}\text{s}^{-1}$  and charge carrier concentration of  $-6.0 \pm 0.4 \times 10^{18} \text{ cm}^{-3}$ . The variable temperature measurements for  $\sigma$  were calculated using equation 2.8 with the room temperature sheet resistances from both the Hall probe and commercial test system producing a correction factor of 0.753. This correction factor was applied to the  $\sigma$  obtained by the commercial test system at different temperatures with the results shown in Fig.3.5b.

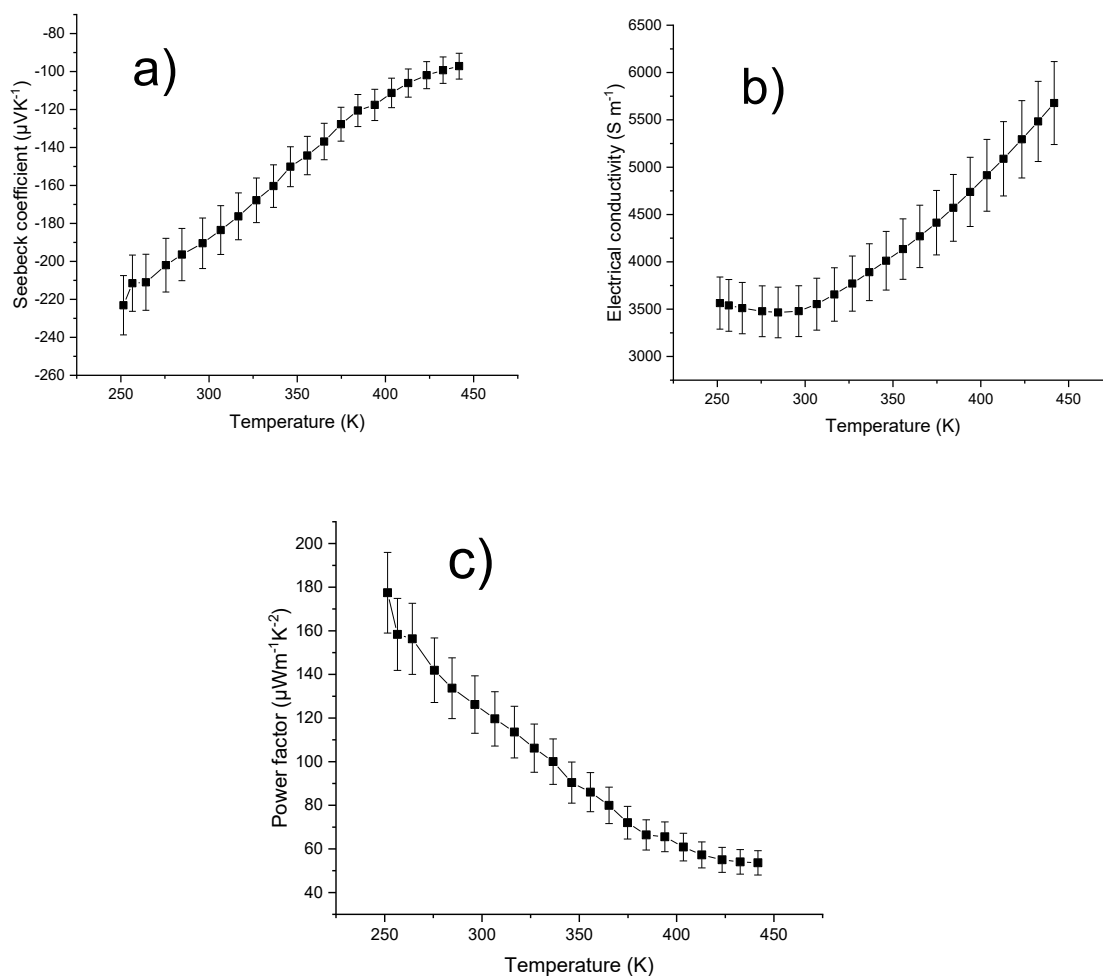


**Fig.3.5-** The (a) Seebeck coefficient, (b) electrical conductivity and (c) power factor between temperatures of 250 K and 450 K for a drop-casted  $\text{Bi}_2\text{Te}_3$  nanowire film annealed at 400 °C for 2 hr in an Ar inert atmosphere on a glass substrate. The error bars in the graphs are a result of the uncertainty of the measuring tool as stated in section 2.412.

From Fig. 3.5 the  $S$  is very large compared to the annealed nanowires from Chen et al <sup>[57]</sup>, as well as bulk  $\text{Bi}_2\text{Te}_3$  with the maximum  $S$  being  $-220 \pm 20 \mu\text{V K}^{-1}$ , which resulted in a PF of  $180 \pm 20 \mu\text{W m}^{-1}\text{K}^{-2}$  at 250 K. This high  $S$  is due to the lower charge carrier concentration measured by the Hall probe compared to bulk  $\text{Bi}_2\text{Te}_3$  <sup>[59]</sup>. As expected from equations 1.6 and 1.7 we observe an inverse relationship between  $S$  and  $\sigma$ . The temperature dependence of both  $S$  and  $\sigma$  is the result of an increase in the number of charge carriers in the material as the temperature increases due to excitation of VB electrons to the CB. As a result, the PF is observed to decline as a function of temperature as it is more affected by  $S$  than  $\sigma$  based on equation 1.3. The main source of the increase in  $\sigma$  of the drop-casted film from its unannealed to annealed state was the increase in mobility. This increased mobility is from the expansion of the average grain size, the change in morphology and the decrease of the oxygen concentration, resulting in the reduction of junction resistance in the film.

The results shown here differ from what was noted by Chen et al <sup>[57]</sup>, as they do not observe this inverse relationship between PF and temperature. This could be explained by our higher Bi content as well as our annealed films' unique INN morphology and the differing annealing environments as they use a forming gas (95 % Ar and 5 % hydrogen) as compared to our inert Ar atmosphere. Though despite this, the maximum PFs are comparable to one another and both fall short of bulk Bi<sub>2</sub>Te<sub>3</sub>. This is due to the drop-casted film's lower charge mobility and carrier concentration by a factor of 5 and 10 respectively compared to bulk Bi<sub>2</sub>Te<sub>3</sub> <sup>[59]</sup>.

### **3.2 Characterisation analysis of Screen-printed films for a variety of PVDF concentrations**

Screen-printable PVDF-Bi<sub>2</sub>Te<sub>3</sub> nanowire pastes were formulated as described in section 2.22. The resulting films' annealing conditions were optimised in Appendix A showing that the ideal annealing temperature and duration was 400 °C for 2 hr in an inert Ar atmosphere. Here we report for the first time how varying the concentration of PVDF in these novel screen-printed composite films between 20 %, 10 % and 5 % can affect the post-annealed films' TE properties. The as-synthesised nanowire PRS reaction precursor chemicals, solvent, capping agent and reducing agent were doubled in mass and volume to double the nanowire product from ~0.8 g to ~1.6 g. This was done to ensure all the pastes used the nanowires from the same batch for this study. It should be noted that the amount of Bi precursor was reduced from 2.14 g to 2 g to avoid the formation of elemental Bi as seen in Fig.3.4. The results shown in this section were verified to be reproducible by repeating the samples and measuring them for a minimum amount of 3 times. This is except for the variable temperature TE measurements for the films containing 5 % PVDF. However, the 5 % PVDF films room temperature TE measurements were verified with 3 separate samples.

#### **3.2.1 Material characterisation**

SEM images as depicted in Fig. 3.6 show the morphology of the as-synthesised Bi<sub>2</sub>Te<sub>3</sub> nanowires. These exhibited diameters ranging from  $90 \pm 20$  nm and a length of between 0.4 and 3  $\mu$ m seen in Fig. 3.6b. These nanowires are shorter and wider than the nanowires observed in Fig. 3.6a as a result of scaling up the reaction by a factor of 2 indicating that the duration of the individual stages of the PRS reaction needed to be increased to achieve the same product as in Fig.3.1.

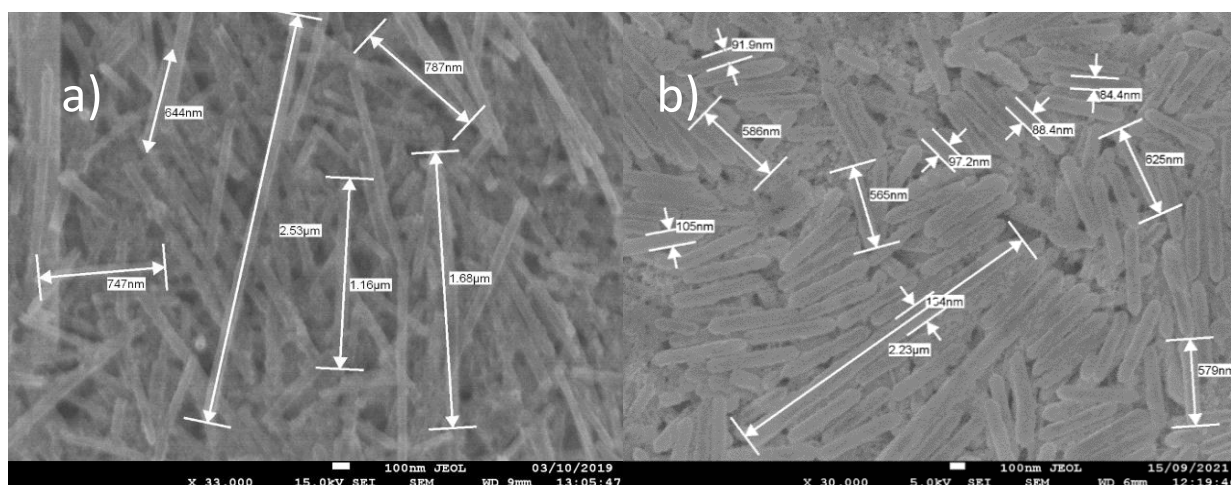


**Fig.3.6-** SEM micrographs of a) PRS  $\text{Bi}_2\text{Te}_3$  nanowires with dimensions and b) PRS scaled up by a factor of two  $\text{Bi}_2\text{Te}_3$  nanowires with dimensions.

The nanowires were formulated into 3 pastes using the procedure described in section 2.22. The films were printed with only a single printing pass onto Kapton at a print gap of 0.4 mm and left to dry in a vacuum oven for 1 hr at 70 °C. Thickness measurements were obtained using a surface profiler where the films had an average thickness of  $5 \pm 1 \mu\text{m}$ . The films had geometries of 50 mm x 5 mm x 0.005 mm. The films were then annealed at 400 °C for 2 hr in an inert Ar atmosphere.

After annealing, we observe differences in the change in morphology of the films. The 20% PVDF- $\text{Bi}_2\text{Te}_3$  nanowire films seen in Fig. 3.7a mostly remain nanowires after annealing, similar to what was seen in Fig. 3.6. While the morphology of the 10 % PVDF- $\text{Bi}_2\text{Te}_3$  nanowire and 5 % PVDF- $\text{Bi}_2\text{Te}_3$  nanowire composite films after annealing as seen in Fig. 3.7b and Fig. 3.7d reveals the presence of both nanowires and INNs, indicating a partial INN formation. We also observed some films of 10 % PVDF- $\text{Bi}_2\text{Te}_3$  forming fully formed INNs seen in Fig. 3.7c referred to as 10% PVDF- $\text{Bi}_2\text{Te}_3$  INNs. The 400 °C annealing temperature is close to the region where PVDF mass loss occurs as can be seen in the thermogravimetric analysis (TGA) plot (seen in Appendix A, Fig. A.3). It can therefore be expected that the PVDF binder can burn off during the annealing process. Before annealing, the nanowires formed loose electrical contacts leading to poor  $\sigma$ . The sintering of the nanowires leads to higher  $\sigma$  and better TE performance which is most likely due to the percolative nature of the INNs. However, this process is still not fully understood as only a handful of 10 % PVDF- $\text{Bi}_2\text{Te}_3$  nanowire films have fully formed INNs denoted by their light grey colour and room temperature portable S probe measurement of  $\sim -220 \mu\text{V K}^{-1}$ . While most 10 % and 5 % PVDF- $\text{Bi}_2\text{Te}_3$  nanowires only form partial INNs differing with darker grey colour and a room temperature portable S probe measurement of  $\sim -140 \mu\text{V K}^{-1}$ . It is believed that the distribution of the PVDF is the main factor that inhibits INN formation in screen-printed films. As the PVDF would act as a thermal barrier shielding the nanowires from the effects of annealing.

### Chapter 3

In the case of the 20% PVDF-Bi<sub>2</sub>Te<sub>3</sub> nanowires films, the concentration of PVDF is too great for any area of the printed film to form INNs, whereas in lower concentrations this is not the case with localised INN formation for 10 % and 5 % PVDF-Bi<sub>2</sub>Te<sub>3</sub> nanowires films. We believe the case of the 10 % PVDF-Bi<sub>2</sub>Te<sub>3</sub> forming fully formed INNs is due to very low localised PVDF concentrations with those film samples, as such more work needs to be done in the future to fully understand these nanostructure formations.

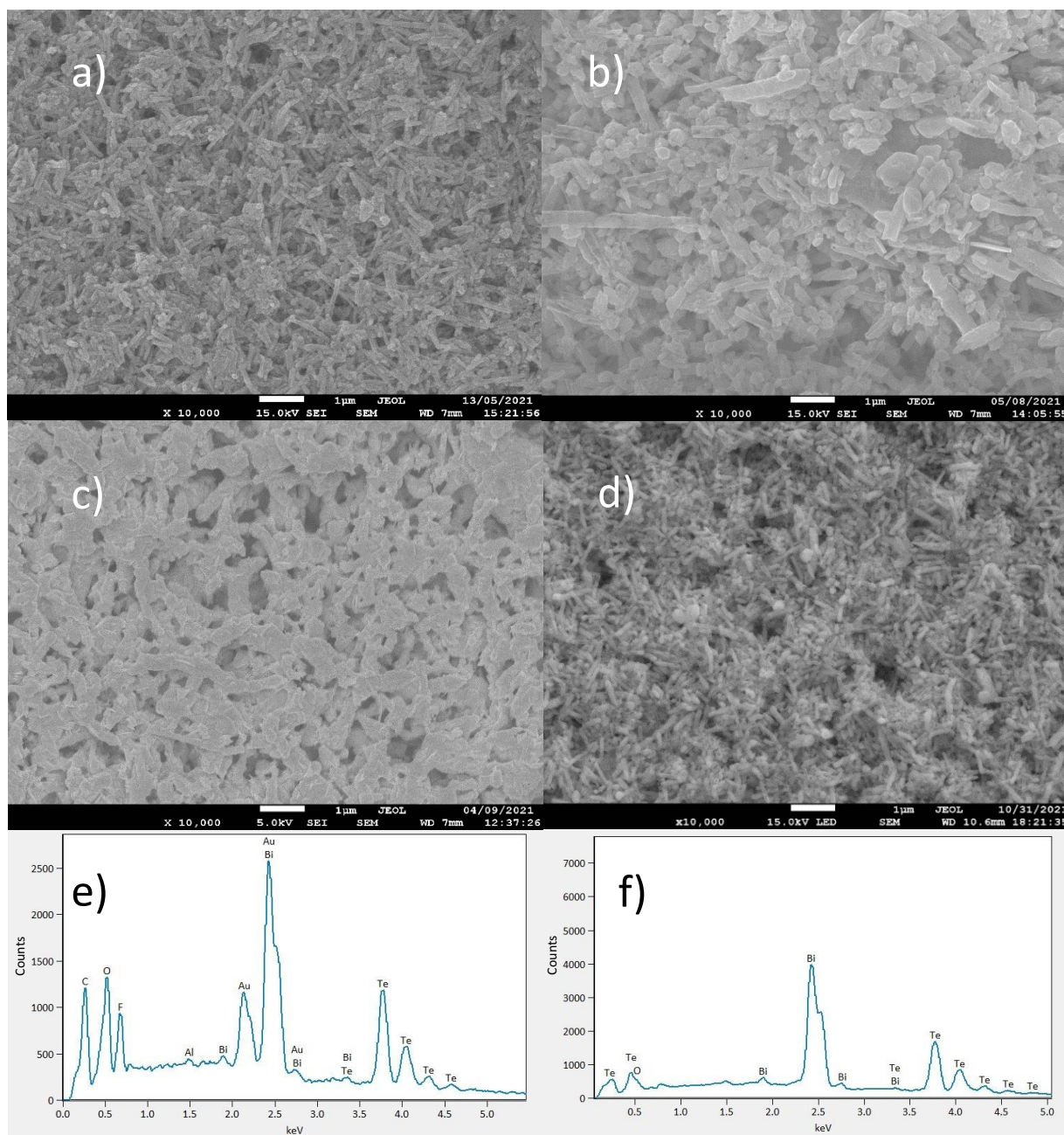


**Fig.3.7-** SEM micrographs of (a) annealed screen-printed 20% PVDF-Bi<sub>2</sub>Te<sub>3</sub> nanowires, (b) 10% PVDF-Bi<sub>2</sub>Te<sub>3</sub> nanowires, (c) fully formed 10% PVDF-Bi<sub>2</sub>Te<sub>3</sub> INNs, (d) annealed screen-printed 5% PVDF-Bi<sub>2</sub>Te<sub>3</sub> nanowires and EDX spectra of the screen-printed 10% PVDF-Bi<sub>2</sub>Te<sub>3</sub> nanowires films (e) before and (f) after annealing to represent the drop in oxygen and fluorine.

The stoichiometry of the screen-printed  $\text{Bi}_2\text{Te}_3$  nanowires before annealing was determined by EDX to be 36:64 for Bi and Te respectively which is close to stoichiometric  $\text{Bi}_2\text{Te}_3$ . The decrease in the Bi content compared to our initial batch in section 3.1 was due to using less Bi precursor as 2 g was used instead of 2.14 g. A strong fluorine peak due to the PVDF binder was also detected in the EDX spectrum (Fig. 3.13e) that significantly reduced in its intensity after annealing (Fig. 3.7f) indicating that the binder has been at least partially removed. We also observed a reduction in the concentration of oxygen with respect to Bi and Te as seen by the peak reduction in Fig. 3.7. On average for all screen-printed films, we observed a reduction from ~30 % to ~15 %.

The GIXRD spectra obtained for the annealed drop-casted as well as screen-printed nanowires in the presence and absence of PVDF are shown in Fig. 3.8 respectively. The GIXRD spectra focus more on how the crystal structure changes with morphology, and since we identified no changes between the 20 %, 10 % and 5% PVDF- $\text{Bi}_2\text{Te}_3$  nanowires crystal structures only the 10 % PVDF- $\text{Bi}_2\text{Te}_3$  nanowires and 10 % PVDF- $\text{Bi}_2\text{Te}_3$  INNs and shown to represent the screen-printed films. The GIXRD spectra reveal a  $\text{Bi}_2\text{Te}_3$  crystal structure with a preferential (0 1 5) orientation which is in agreement with previous reports and what we've observed so far in this chapter <sup>[35]</sup>. The standard ICDD PDF card data (01-085-0439) has been used to identify and index all detected peaks. The crystallinity of the  $\text{Bi}_2\text{Te}_3$  nanowires improves upon annealing giving rise to more pronounced peaks in GIXRD. However, the annealing process did not result in any phase or compositional changes. For the screen-printed films, there is a broad peak visible between  $2\theta$  15 ° and 25 °, which may be attributed to the PVDF binder, as this is not detectable in the drop-casted pristine  $\text{Bi}_2\text{Te}_3$  films. Further, this broad peak notably decreased in intensity after annealing illustrating that the PVDF had only been partially removed. Alternatively the broad peak can also be associated with the Kapton substrate as seen in the literature <sup>[95–97]</sup>. The decrease in the broad peak intensities, in this case, could be the result of more crystalline peaks from the annealed films overshadowing it by contrast. As with the EDX when comparing the GIXRD data to the initial batch of nanowires in Fig. 3.4 we no longer observe a sharp peak after the (2 0 5) lattice orientation, as a result of the reduction of the amount of Bi precursor used in the PRS reaction.

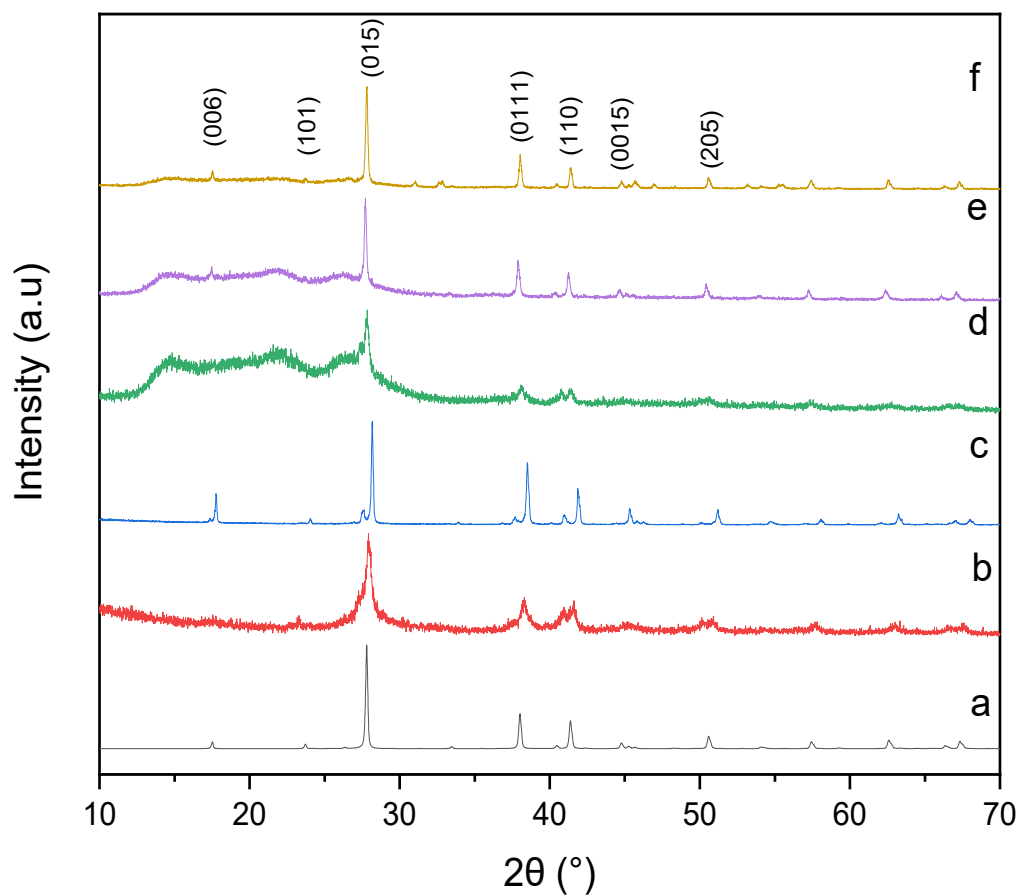


**Fig.3.8-** GIXRD diffraction patterns obtained for (a) reference XRD of tellurobismuthite ( $\text{Bi}_2\text{Te}_3$ ) mineral from International Centre of Diffraction Data (ICDD) database (PDF 01-085-0439) (b) unannealed drop-casted  $\text{Bi}_2\text{Te}_3$  nanowires, (c) annealed drop-casted  $\text{Bi}_2\text{Te}_3$  nanowires, (d) unannealed 10 % PVDF- $\text{Bi}_2\text{Te}_3$  nanowires composite film and (e) annealed 10 % PVDF- $\text{Bi}_2\text{Te}_3$  nanowires composite film and (f) annealed 10 % PVDF- $\text{Bi}_2\text{Te}_3$  INNs composite film. All films were annealed in an inert Ar atmosphere at 400 °C for 2 hr.

### 3.2.2 Thermoelectric characterisation

The in-plane  $S$ ,  $\sigma$  and PF for the screen-printed composite films were collected over a temperature range of 150 K to 425 K and are shown in Fig. 3.9.

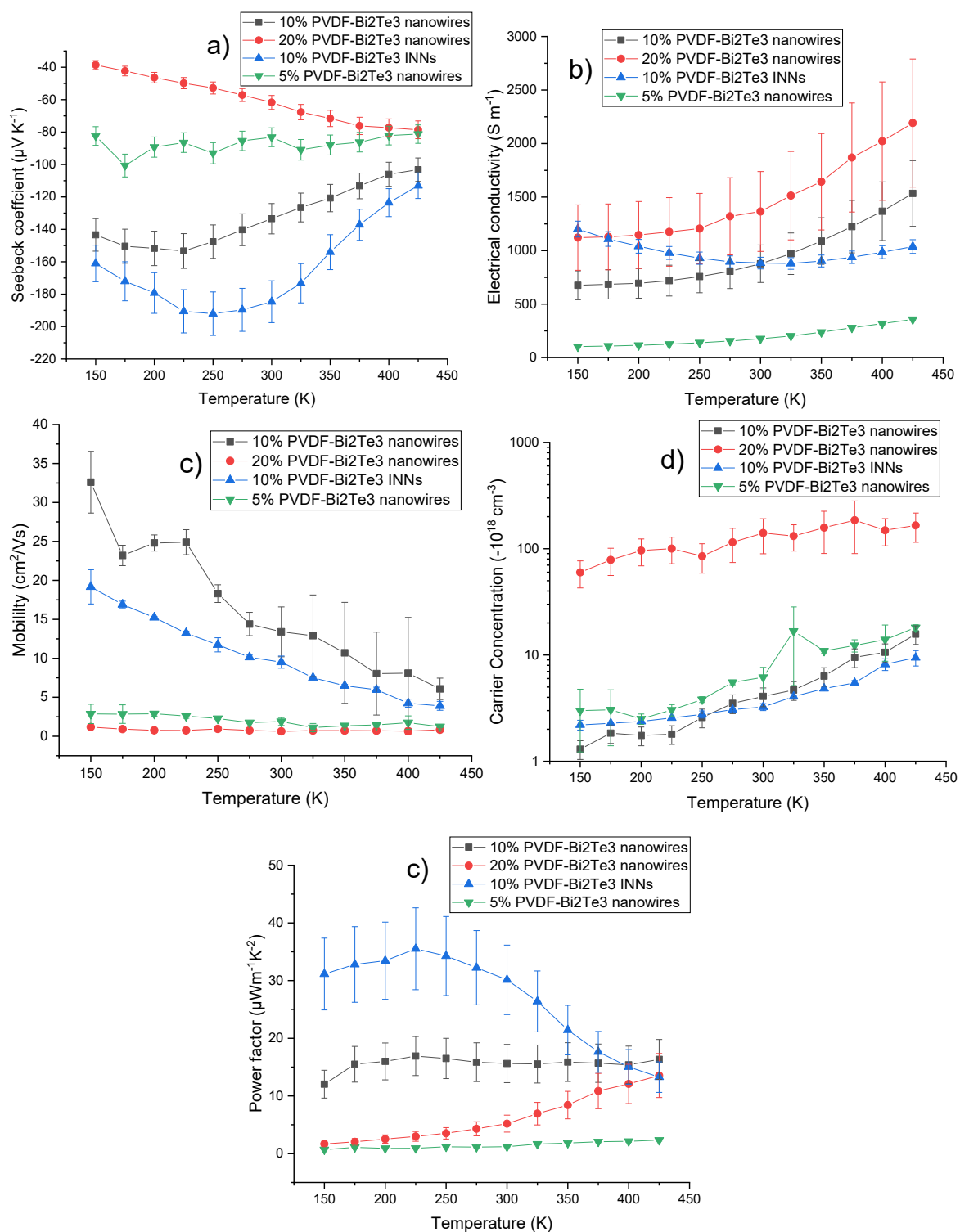


**Fig.3.9-** Temperature-dependent TE properties measured over a temperature range of 150 K to 425 K for (a) Seebeck coefficient, (b) electrical conductivity (c) charge carrier mobility, (d)  $\log_{10}$  scale charge carrier concentration and (e) power factor of the post-annealed screen-printed film composites containing 20%, 10% and 5% PVDF with respect to the Bi<sub>2</sub>Te<sub>3</sub> nanowires as well as the 10% PVDF-Bi<sub>2</sub>Te<sub>3</sub> INNs composite. The error bars in the graphs are a result of the uncertainty of the measuring tool as stated in section 2.412 and the standard deviations from the average Hall probe results at different temperatures.

All films displayed a negative  $S$  and negative charge carrier concentration which is consistent with n-type behaviour. The annealed 10% PVDF- $\text{Bi}_2\text{Te}_3$  INNs displayed a maximum  $S$  of  $-192 \pm 10 \mu\text{V K}^{-1}$  with a PF of  $36 \pm 7 \mu\text{W m}^{-1}\text{K}^{-2}$  at 225 K and a room temperature  $S$  and PF of  $-185 \pm 10 \mu\text{V K}^{-1}$  and  $30 \pm 6 \mu\text{W m}^{-1}\text{K}^{-2}$  respectively. These values are in good agreement with those reported in studies on flexible and printed composite nanomaterials [61,66,98,99]. For example, Ou et al [66] recently reported PFs of  $\sim 18/30 \mu\text{W m}^{-1}\text{K}^{-2}$  for aerosol jet printed nanocrystals of  $\text{Bi}_2\text{Te}_3/\text{Sb}_2\text{Te}_3$  embedded within a flexible PEDOT:PSS matrix respectively. Compared to ball-milled bulk powders of Bi and Te and bulk  $\text{Bi}_2\text{Te}_3$  (as summarised in Table 1.4) our reported  $S$  is higher whilst the PF is lower due to the lower  $\sigma$  measured for our screen-printed composites [59,75,77,78]. If we compare our PFs to the recent studies on inkjet printed nanowires of  $\text{Bi}_2\text{Te}_3$  by Chen et al [53,57] our values appear to be lower. However, their studies report room temperature PFs between  $20 \mu\text{W m}^{-1}\text{K}^{-2}$  and  $30 \mu\text{W m}^{-1}\text{K}^{-2}$  for inkjet printed films annealed in an inert nitrogen atmosphere [57]. Additionally, when their inkjet printed films are annealed in an FGA they obtain a room temperature PF of  $\sim 20 \mu\text{W m}^{-1}\text{K}^{-2}$  for films with 50 and 150 inkjet passes and  $\sim 80 \mu\text{W m}^{-1}\text{K}^{-2}$  for films with 100 inkjet passes [53]. As such our results are comparable to some of the films fabricated by Chen et al [52,56]. However, the difference in our results, when compared to the highest TE performing films by Chen et al [52,56], is due to the addition of PVDF in order to formulate a screen-printable paste, which when burnt off results in voids in the film. This lowers the film's carrier mobility and overall  $\sigma$ . This is the main trade-off between inkjet and screen-printed  $\text{Bi}_2\text{Te}_3$ -based nanostructured films. Additionally, Chen et al [53,57] use of an FGA (95% hydrogen, 5% argon) during annealing which better removes oxygen content in the nanowires. This is due to the hydrogen in the forming gas bonding with the oxygen on the nanowire surface forming water molecules that are then burned off during annealing. This further reduction in oxygen content would reduce inter-nanowire junction resistance and further improve carrier mobility and  $\sigma$ .

When comparing the screen-printed 10% PVDF- $\text{Bi}_2\text{Te}_3$  INNs to the drop-casted  $\text{Bi}_2\text{Te}_3$  INNs on glass (Fig.3.5) two main reasons are believed to be responsible for the disparity in TE performance. The first reason is due to the porosity of the screen-printed films caused by the voids that are created when the PVDF binder is burnt-off [53]. The second reason is that those initial drop-casted  $\text{Bi}_2\text{Te}_3$  INNs were on a rigid glass substrate compared to the screen-printed films which were on Kapton. The flexible Kapton would induce microcracks in the films due to its natural curvature. As a result, the room temperature charge carrier mobility of the drop-casted INNs is  $26 \pm 8 \text{ cm}^2\text{V}^{-1}\text{s}^{-1}$ , while the screen-printed INNs are  $9.5 \pm 0.8 \text{ cm}^2\text{V}^{-1}\text{s}^{-1}$ .

When comparing the screen-printed PVDF-Bi<sub>2</sub>Te<sub>3</sub> composite films with each other we observe different temperature-dependent PFs in Fig. 3.9e. We observe a linear relationship between PF and temperature for the 20 % PVDF-Bi<sub>2</sub>Te<sub>3</sub> nanowire films, while we observe the opposite for the 10 % PVDF-Bi<sub>2</sub>Te<sub>3</sub> INNs. Meanwhile, the 10 % PVDF-Bi<sub>2</sub>Te<sub>3</sub> nanowire films remain relatively flat for the temperature range with an average power factor of  $16 \pm 3 \mu\text{Wm}^{-1}\text{K}^{-2}$ . The linear relationship of the 20 % PVDF-Bi<sub>2</sub>Te<sub>3</sub> nanowire films is due to its highly doped semiconductor nature as seen in Fig.3.9d with carrier concentrations between  $10^{19} \text{ cm}^{-3}$  and  $10^{20} \text{ cm}^{-3}$ . As such it has a similar relation to what would be expected for bulk Bi<sub>2</sub>Te<sub>3</sub>. However, despite the higher  $\sigma$  the much lower S causes the PF to remain lower than for the 10 % PVDF-Bi<sub>2</sub>Te<sub>3</sub> composites. Alternatively, the 10 % PVDF-Bi<sub>2</sub>Te<sub>3</sub> INNs have a much higher S by taking advantage of their lower carrier concentration, while maintaining a reasonable  $\sigma$  to the other films, due to their higher carrier mobilities as a result of the INN's interconnected nature. The INN's inverse relation between PF and temperature is due to its carrier mobility increasing faster than the decrease in its carrier concentration resulting in both  $\sigma$  and S increasing when temperature decreases. The flat relation for the 10 % PVDF-Bi<sub>2</sub>Te<sub>3</sub> nanowire films is due to them having both morphologies of the previously described films with both morphologies counteracting the other at different temperatures. This can be noted by the 10 % PVDF-Bi<sub>2</sub>Te<sub>3</sub> nanowire film's S in Fig. 3.9a and its  $\sigma$  in Fig.3.9b having a similar, however, constraint trend as one of the other films.

While the 5 % PVDF-Bi<sub>2</sub>Te<sub>3</sub> nanowire films, had a very high room temperature PF of  $37 \pm 8 \mu\text{Wm}^{-1}\text{K}^{-2}$  an S of  $\sim 140 \pm 10 \mu\text{V K}^{-1}$  and an  $\sigma$  of  $1900 \pm 400 \text{ S m}^{-1}$  just after annealing, this higher PF is due to the films having carrier concentrations in the highly doped semiconductor range of  $\sim 5 \pm 2 \times 10^{19} \text{ cm}^{-3}$  while still maintaining an S on par with 10 % PVDF-Bi<sub>2</sub>Te<sub>3</sub> nanowire films. Unfortunately, by the time they could be measured with the equipment in section 2.412 they had severely oxidised. The EDX spectrum for the oxygen with respect to the Bi and Te is shown in Fig. 3.10, where the oxygen had increased from  $\sim 15\%$  to  $38.2\%$ . As such the overall PF of the 5 % PVDF-Bi<sub>2</sub>Te<sub>3</sub> nanowire films is quite poor respective to the other films in Fig. 3.9 as both S and  $\sigma$  are reduced by oxidation. As the room temperature results were within the range of uncertainty with the 10 % PVDF-Bi<sub>2</sub>Te<sub>3</sub> INN films, it was decided that 5 % PVDF was the ideal binder concentration with all screen-printed films moving forward. This 5 % binder composition was then used to screen-print annealed Bi<sub>2</sub>Te<sub>3</sub> nanowires which are explored in Appendix B, where it was possible to achieve printed films with moderate S  $\sim 85 \pm 6 \mu\text{V K}^{-1}$ , however, poor  $\sigma$  lead to  $\text{PF} < 0.01 \mu\text{Wm}^{-1}\text{K}^{-2}$ . This was due to a lack of INNs in the annealed Bi<sub>2</sub>Te<sub>3</sub> nanowires and more work is needed to optimise the process.

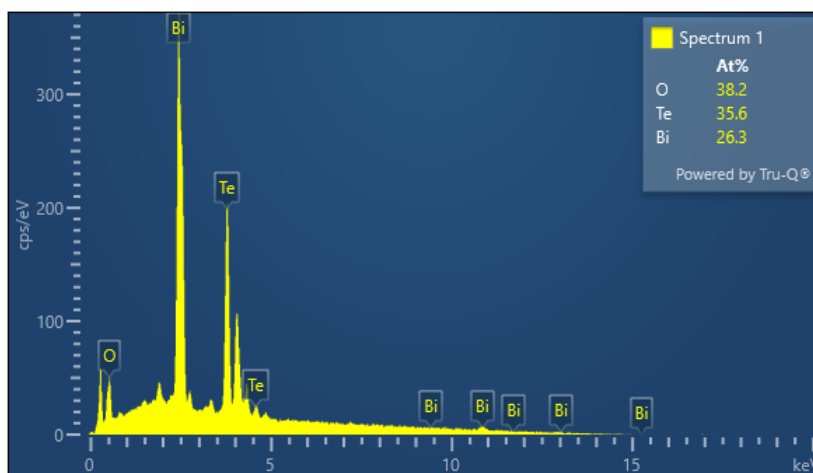


**Fig.3.10-** EDX spectrum of the annealed screen-printed 5 % PVDF-Bi<sub>2</sub>Te<sub>3</sub> nanowire film after measuring its TE measurements in Fig. 3.9.

### 3.2.3 Flexibility characterisation

To evaluate the suitability of the screen-printed films for flexible TE applications a bending test of 1000 bending cycles at a bending radius of 10 mm is performed with the results shown in Fig. 3.11. An annealed screen-printed film of 5 % PVDF-Bi<sub>2</sub>Te<sub>3</sub> nanowires is compared to a drop-casted film of annealed Bi<sub>2</sub>Te<sub>3</sub> nanowires on Kapton. The drop-casted film's cross-sectional SEM revealed the film to have an average thickness of  $\sim 4 \pm 1 \mu\text{m}$ . To account for the roughness of the fabric pocket of the bending apparatus the films are placed in a Kapton pocket, with silver electrodes deposited on both sides of the films to get accurate resistance readings without damaging the films.

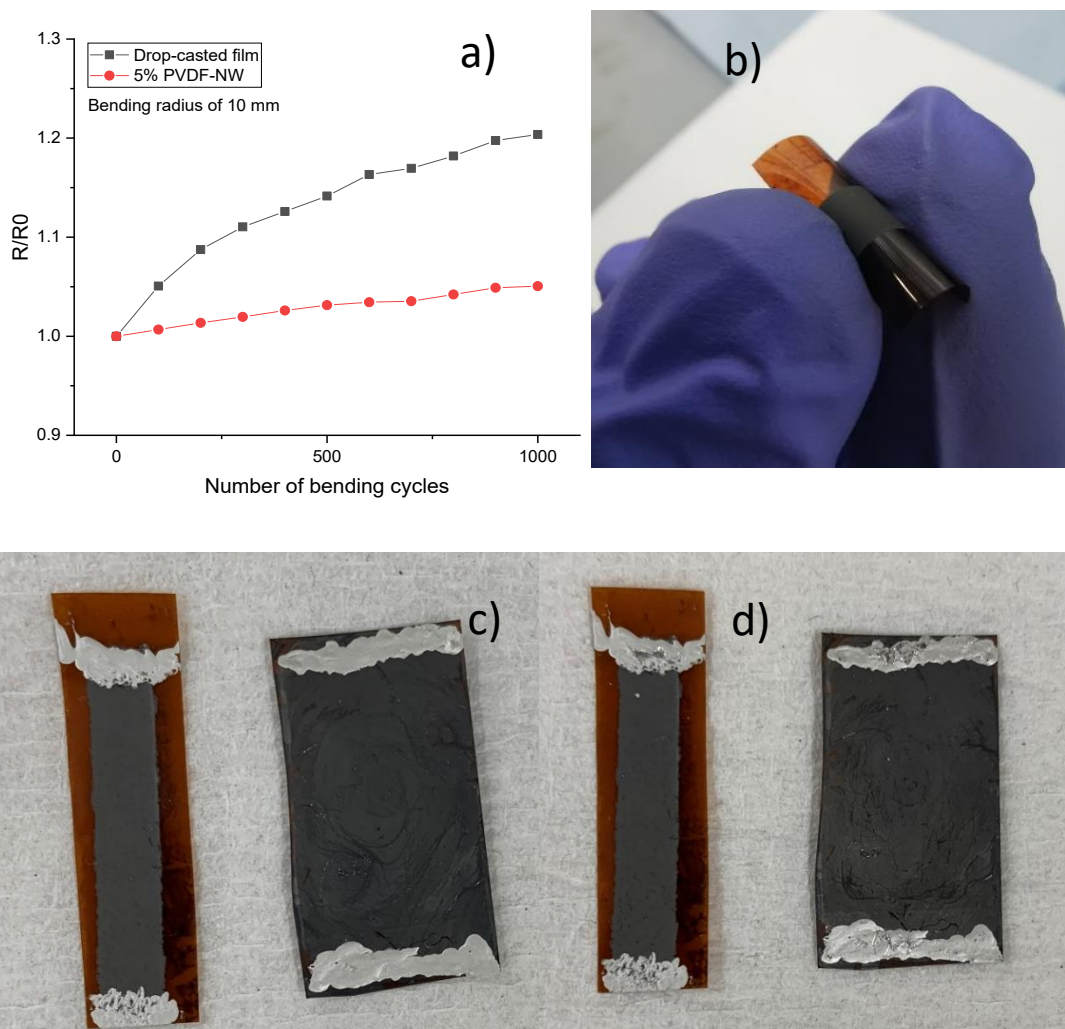


**Fig. 3.11-**(a) Resistance normalized to initial resistance of 5% PVDF-NW and an annealed drop-casted films for 1000 bending cycles, with a bending radius of 10 mm, (b) photograph insert of curved composite nanowire film, 5% PVDF-NW and an annealed drop-casted films before (c) and after (d) bending.

The 5% PVDF-Bi<sub>2</sub>Te<sub>3</sub> nanowires resistance does not change significantly as a function of the bending cycle. From this, we believe the material is suitable for wearable flexible electronic applications as after 1000 bending cycles the film has not delaminated from the substrate. Comparing this to the drop-casted film we observe a much higher increase in resistance at least 4 times greater over the same number of bending cycles. This was despite the initial low concentration of PVDF in the screen-printed film, which was further reduced post-annealing. Additionally, the drop-casted film appears from Fig. 3.11d to have taken a higher degree of bending-related damage with parts of the film breaking off. This shows the unsuitability of the drop-casted films for flexible TE applications despite their much higher PFs. This shows the necessity of the PVDF in the composite to maintain film flexibility.

### 3.3 Single-leg flexible thermoelectric generator device and power output measurements

A prototype  $\text{Bi}_2\text{Te}_3$  nanowire single-leg FTEG device was fabricated from 5 films of 5 % PVDF- $\text{Bi}_2\text{Te}_3$  nanowires printed onto Kapton and annealed at 400 °C for 2 hr in an inert Ar atmosphere. The films had geometries of 20 mm x 5 mm x 0.006 mm and were connected in series using a silver pen (Chemtronics) with the silver contacts having a resistance of  $\sim 3 \Omega$ , as shown in Fig.3.12.



**Fig. 3.12-** Image of single-leg 5% PVDF- $\text{Bi}_2\text{Te}_3$  nanowire FTEG device.

The cold side was kept constant at 20° C while using a Peltier heater to increase the hot side, with a thermal camera used to attain an accurate temperature difference. The power output measurements are seen in Fig.3.13 while the images from the thermal camera are seen in Fig. 3.14.

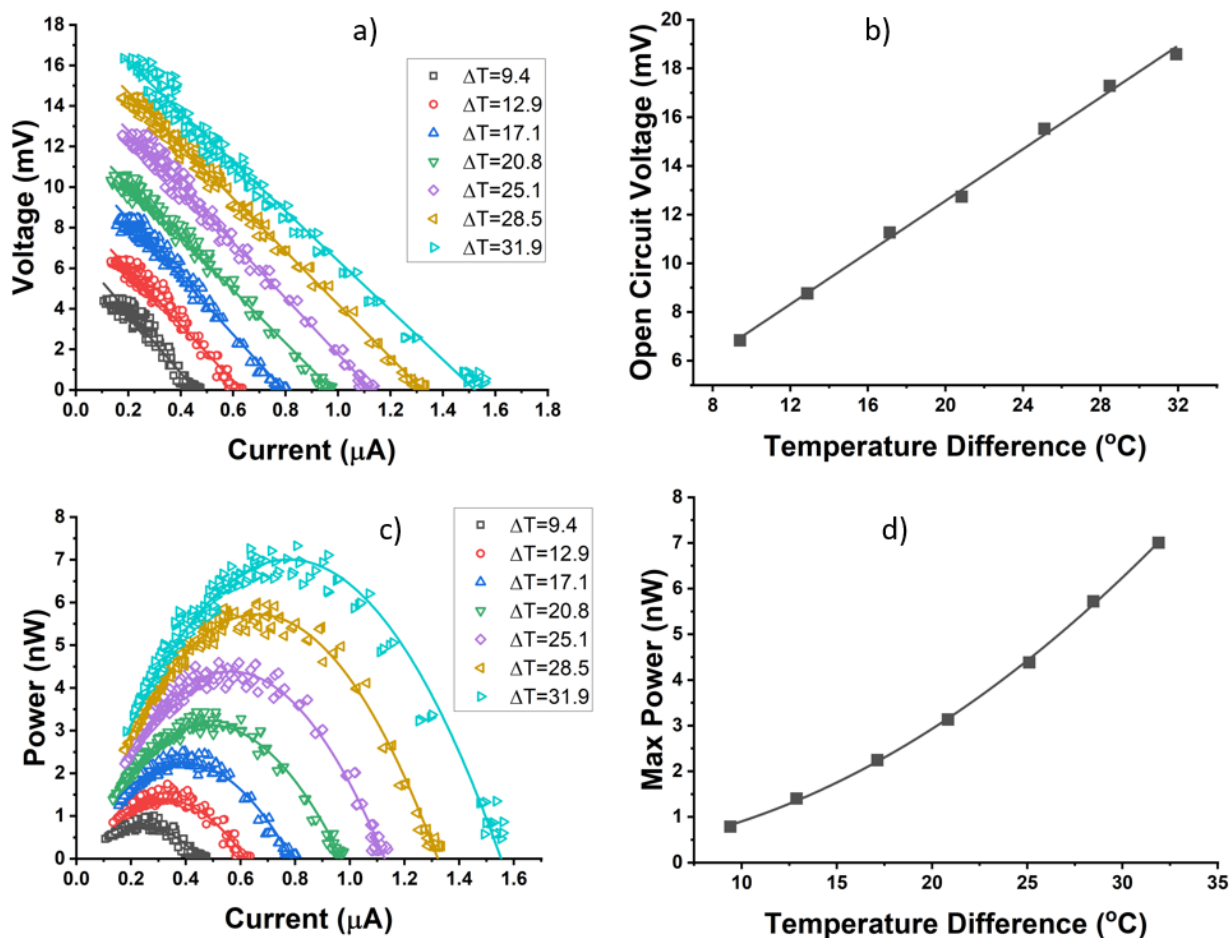


**Fig.3.13-** Graphs showing (a) the voltage vs current response for different temperature differences, (b) the open-circuit voltage with respect to the temperature difference, (c) the output power vs current and (d) the maximum output power with respect to the temperature difference of the single-leg 5% PVDF-Bi<sub>2</sub>Te<sub>3</sub> nanowire FTEG device.

The maximum power output reached was  $\sim 7$  nW for a thermal gradient of 31.9 K with the lowest thermal gradient of 9.4 K generating a power output of  $\sim 1$  nW. The open-circuit voltage at 31.9 K was  $\sim 19$  mV with the total Seebeck voltage per degree for the FTEG being 0.531 mV/K. This shows the material's potential in being used for an FTEG device with the ability to generate power at low-temperature gradients. However, the results are still subpar compared to the devices generated in the literature seen in Table 1.4. The main reason is the lower TE properties resulting from the films containing individual particles that cause the charge carriers to scatter between particle boundaries resulting in low mobility and low  $\sigma$  reducing the amount of current produced by the device. Another reason for this was the delay between the device fabrication and when the devices were measured. This could be seen through the average  $S$  when measured at the time of measuring the device power output  $S \sim -106 \mu\text{V}/\text{K}$  per leg while at the time of fabrication it was  $\sim -140 \mu\text{V}/\text{K}$ . We have seen in these samples that the  $S$  and  $\sigma$  decrease with exposure to oxygen. This is despite the device being stored in a vacuum desiccator in a nitrogen glovebox.

Furthermore, the silver contacts used were not ideal as can be seen in Fig.3.13 with sections being patchy due to the difficulties in depositing the silver ink onto the Kapton. In future, an all-screen-printed procedure in the fabrication of FTEGs is the most optimal path forward. Finally, the geometries of the films were not optimised for the generation of power and were chosen arbitrarily. This could be a good avenue for future work to computationally analyse more ideal geometry for the films.

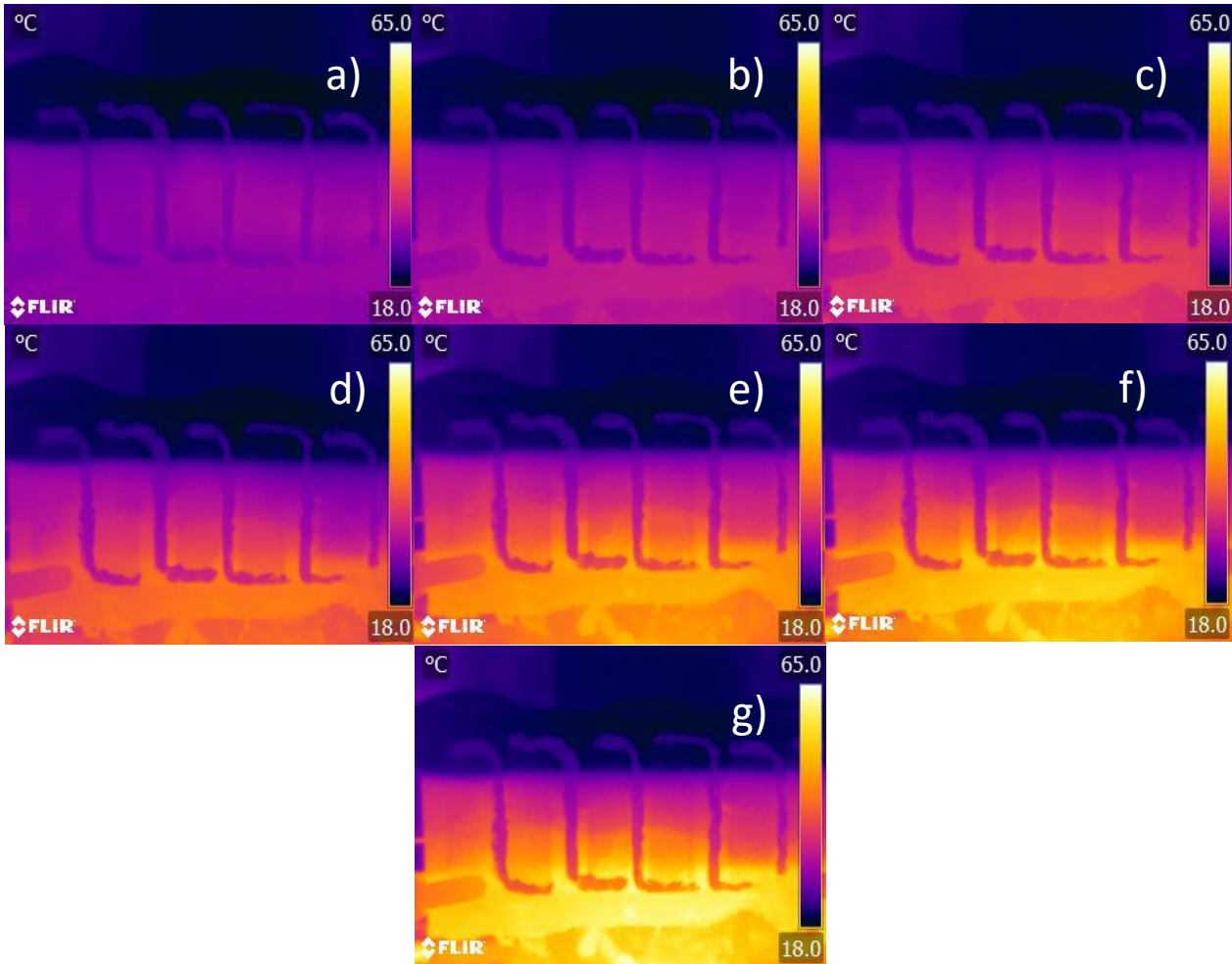


**Fig.3.14-** The thermal images are taken of the single-leg 5% PVDF-Bi<sub>2</sub>Te<sub>3</sub> nanowire FTEG device during measuring with a normalised temperature range with (a) 9.4 K, (b) 12.9 K, (c) 17.1 K,(d) 20.8 K, (e) 25.1 K, (f) 28.5 K and (g) 31.9 K.

### 3.4 Conclusions

In summary, we have synthesised  $\text{Bi}_2\text{Te}_3$  nanowires via PRS and have scaled up the reaction where we have observed changes in the nanowires' morphology. We observe wider and shorter nanowires when the reaction is scaled up however this does not seem to have affected the TE properties of the films once they are annealed. The main discovery has been the formation of n-type  $\text{Bi}_2\text{Te}_3$  INNs from annealed  $\text{Bi}_2\text{Te}_3$  nanowires with them achieving an  $S$  of  $-220 \pm 20 \mu\text{VK}^{-1}$  and a PF of  $180 \pm 20 \mu\text{Wm}^{-1}\text{K}^{-2}$  at 250 K. These INNs have thus far only been produced by annealing these nanowires at 400 °C for 2 hr in an inert Ar atmosphere in a tube furnace.

We have explored for the first seen in the literature the incorporation of PRS  $\text{Bi}_2\text{Te}_3$  nanowires into an NMP-PVDF solvent-binder paste formulation. The optimal annealing conditions for the PVDF- $\text{Bi}_2\text{Te}_3$  composite films were 400 °C for 2 hr in an inert Ar atmosphere. The concentration of PVDF in the screen-printed PVDF- $\text{Bi}_2\text{Te}_3$  nanowire composite films was then varied between 20 %, 10 % and 5 % and printed onto Kapton substrates. These films were then annealed at 400 °C for 2 hr in an inert Ar atmosphere resulting in 3 distinct morphologies. The first was the 20 % PVDF- $\text{Bi}_2\text{Te}_3$  nanowire composite films where the nanowires retained their pre-annealed structure. The TE properties for these films followed that of bulk  $\text{Bi}_2\text{Te}_3$  with their PFs increasing with temperature. This was due to the films having carrier concentrations in the highly doped semiconductor region between  $10^{19} \text{ cm}^{-3}$  and  $10^{20} \text{ cm}^{-3}$ . The second was the formation of INNs identified in some of the 10 % PVDF- $\text{Bi}_2\text{Te}_3$  composites after annealing. These INNs as seen in the annealed drop-casted films had an inverse relationship between their PFs and temperature. This inverse relationship was due to their higher charge carrier mobilities compensating for their lower carrier concentrations ( $10^{18} \text{ cm}^{-3}$ ) as their charge carrier mobilities would increase as temperature decreased causing  $\sigma$  to increase at lower temperatures. Meanwhile, their carrier concentrations decreased with temperature causing an increase in  $S$ . The 10 % PVDF- $\text{Bi}_2\text{Te}_3$  INN composites had the highest non-room temperature  $S$  and PF at  $-192 \pm 10 \mu\text{VK}^{-1}$  and a PF of  $36 \pm 7 \mu\text{Wm}^{-1}\text{K}^{-2}$  at 225 K. These INNs had a lower TE performance than their drop-casted counterparts as a result of being more porous from voids left from the burned off PVDF. The third morphology observed was a mix of the previous two seen in 10 % and 5 % PVDF- $\text{Bi}_2\text{Te}_3$  nanowire composite films. These had a flat PF in relation to temperature as both morphologies cancelled out the other.

## Chapter 3

The highest PF achieved at room temperature was for the 5 % PVDF-Bi<sub>2</sub>Te<sub>3</sub> nanowire composite films with a PF of  $37 \pm 8 \mu\text{Wm}^{-1}\text{K}^{-2}$  owing to its carrier concentrations in the highly doped semiconductor range while still maintaining an S of  $-140 \pm 10 \mu\text{VK}^{-1}$ . Unfortunately, by the time non-room temperature TE measured could be performed on the films they had severely oxidised with the oxygen concentration with respect to the Bi and Te more than doubling resulting in poor TE readings. As the room temperature PF was the highest achieved, 5 % was the standard PVDF concentration used in all successive screen-printed films.

We demonstrated that PVDF is a suitable binder for the screen-printing of flexible Bi<sub>2</sub>Te<sub>3</sub> nanowire films which provides a potential route toward the fabrication of flexible TE materials. We did this by performing a bending test of 1000 bending cycles at a bending radius of 10 mm where we observed lower bending-induced resistance in the screen-printed films on Kapton than in their drop-casted counterparts by a factor of 4.

Finally, 5 films of 5 % PVDF-Bi<sub>2</sub>Te<sub>3</sub> nanowires were screen-printed onto Kapton and annealed using the previously stated conditions. They were then connected in series via the use of a silver pen to form a single-leg FTEG device which was measured for temperature gradients between 9.4 K and 31.9 K. The lowest reading for 9.4 K resulted in a power output of  $\sim 1$  nW, while the maximum temperature gradient of 31.9 K allowed the FTEG to generate  $\sim 7$  nW with an open circuit voltage of  $\sim 19$  mV. This low power output is attributed to low  $\sigma$  due to the individualised nature of the films being a network of individual nanowires. To improve on the output power more research in future work should look to optimising the formation of 5 % PVDF-Bi<sub>2</sub>Te<sub>3</sub> INNs and fabricating FTEGs from them as well as using an all-screen-printed procedure for the FTEG fabrication. Further improvements to the performance could be made by altering the geometries of the films as the device had arbitrarily assigned geometries. This could be improved in the future with a computational study to observe more ideal geometries for heat to flow through the material to generate a higher power output.

## Chapter 4 Selenium alloying of polyol reflux synthesised Bismuth telluride selenide nanowires

We herein report the first screen-printed PVDF-Bi<sub>2</sub>Te<sub>3-x</sub>Se<sub>x</sub> nanowire composite films and compare them to their PVDF-Bi<sub>2</sub>Te<sub>3</sub> counterpart as discussed in the previous chapter. The alloying of Bi<sub>2</sub>Te<sub>3</sub> nanowires with Se was investigated as a potential route to improve the nanowires' TE performance. Based on the literature Bi<sub>2</sub>Te<sub>2.7</sub>Se<sub>0.3</sub> is the highest TE-performing alloy resulting from it having a higher *S* and low *κ* than Bi<sub>2</sub>Te<sub>3</sub> [28,80,100]. However, in the literature, there has not been any attempt at screen-printing flexible films of Bi<sub>2</sub>Te<sub>3-x</sub>Se<sub>x</sub> nanowires. This gap in the literature was addressed by incorporating a Se precursor into our Bi<sub>2</sub>Te<sub>3</sub> synthesis and screen-printing the resulting Bi<sub>2</sub>Te<sub>3-x</sub>Se<sub>x</sub> nanowires onto a flexible substrate.

### 4.1 Characterisation of Se alloyed nanowires

#### 4.1.1 One-step addition of Se and Bi precursor into the polyol reflux synthesis

A one-step addition process was investigated where the Se and Bi precursors were dissolved into a single solution of EG and added into the PRS reaction for Bi<sub>2</sub>Te<sub>3</sub> nanowires as described in section 2.11. To synthesise Bi<sub>2</sub>Te<sub>2.7</sub>Se<sub>0.3</sub> nanowires the quantities of the Bi, Te and Se precursors used in the PRS reaction had mass ratios of 40:54:6 respectively. These precursor concentrations were chosen as the target alloy only has a Se content of 6 % at the expense of the Te content. All other PRS reaction chemicals were kept constant with the Bi<sub>2</sub>Te<sub>3</sub> PRS in Chapter 3 to observe how the addition of the Se precursor would affect the reaction product. The resulting product was drop-casted to form thick films, which underwent microstructural analysis via SEM, EDX and GIXRD. The synthesis has been reproduced at least 3 times and a drop-casted film was fabricated for each synthesis to ensure the reproducibility of the PRS reaction. This revealed the drop-casted films to be made up of nanowires which had an average diameter of 150 ± 80 nm, with lengths that ranged from a few hundred nm up to several microns. Fig.4.1 shows the SEM images and EDX data of the Bi<sub>2</sub>Te<sub>3-x</sub>Se<sub>x</sub> nanowires.

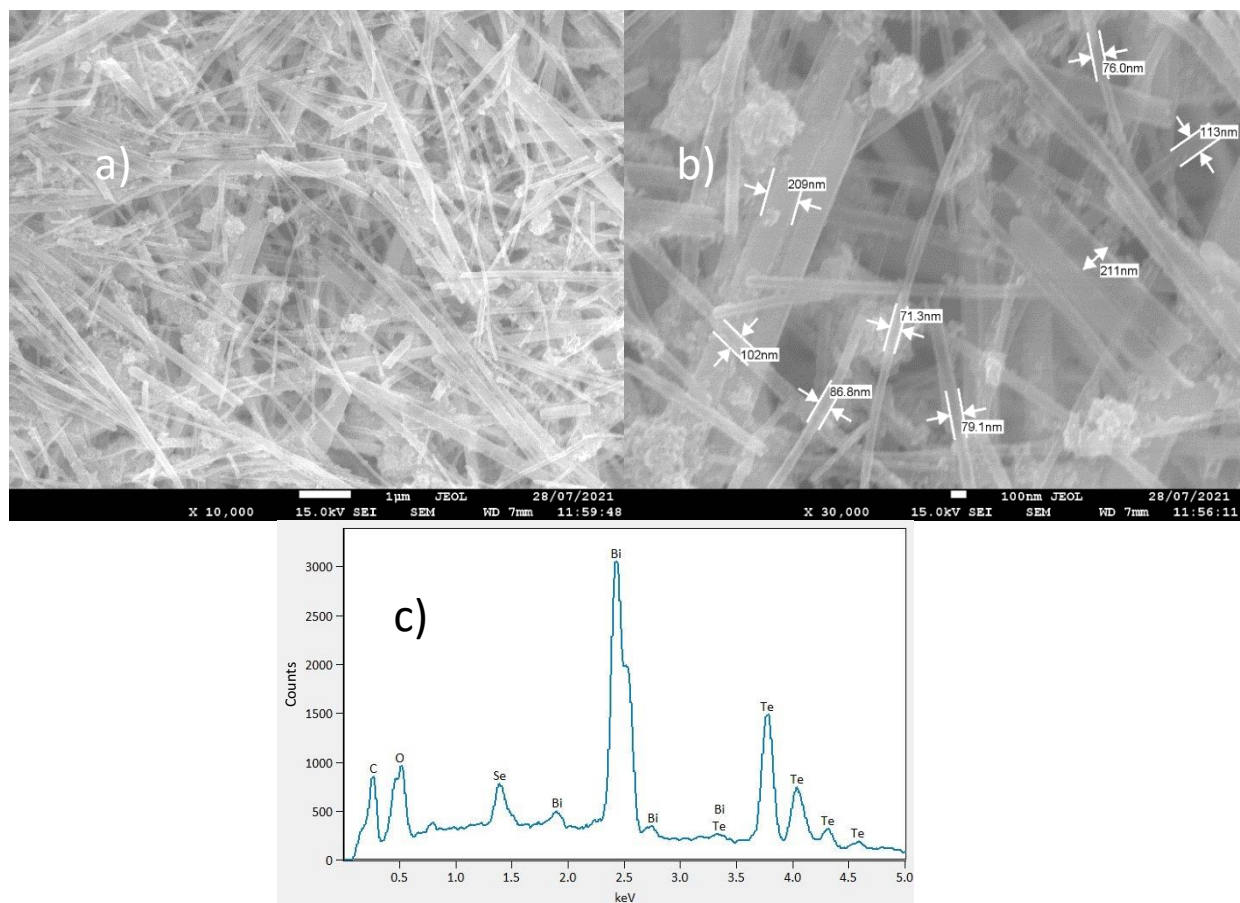


**Fig. 4.1-** SEM images (a) of a top-down view of  $\text{Bi}_2\text{Te}_{3-x}\text{Se}_x$  nanowires on a Si substrate, (b) showing the nanowire lengths and (c) EDX spectrum of the drop-casted PRS  $\text{Bi}_2\text{Te}_{3-x}\text{Se}_x$  nanowires film.

From the SEM images, it is clear that the incorporation of SeO in the reaction does not change the morphology of  $\text{Bi}_2\text{Te}_{3-x}\text{Se}_x$  nanowires. However, we observed fewer uniform diameters for the  $\text{Bi}_2\text{Te}_{3-x}\text{Se}_x$  nanowires compared to the  $\text{Bi}_2\text{Te}_3$  nanowires which had average diameters of  $60 \pm 20$  nm. The EDX data shows the atomic percentages for Bi:Te:Se as 37.2:52.2:10.7 respectively, which is close to the  $\text{Bi}_2\text{Te}_{2.5}\text{Se}_{0.5}$  alloy composition. The oxygen content of the  $\text{Bi}_2\text{Te}_{3-x}\text{Se}_x$  nanowires was 34 % with respect to the atomic percentages of Bi, Te and Se. This is within the 2 % uncertainty of the EDX detector when compared to the  $\text{Bi}_2\text{Te}_3$  nanowires' oxygen content of 32 % with respect to the atomic percentages of Bi and Te, indicating that the SeO is mostly reduced in the PRS reaction. GIXRD was also performed to ensure that the nanowires were indeed an alloy of  $\text{Bi}_2\text{Te}_{3-x}\text{Se}_x$ , as well as to see the preferred crystal lattice orientation of the nanowires.

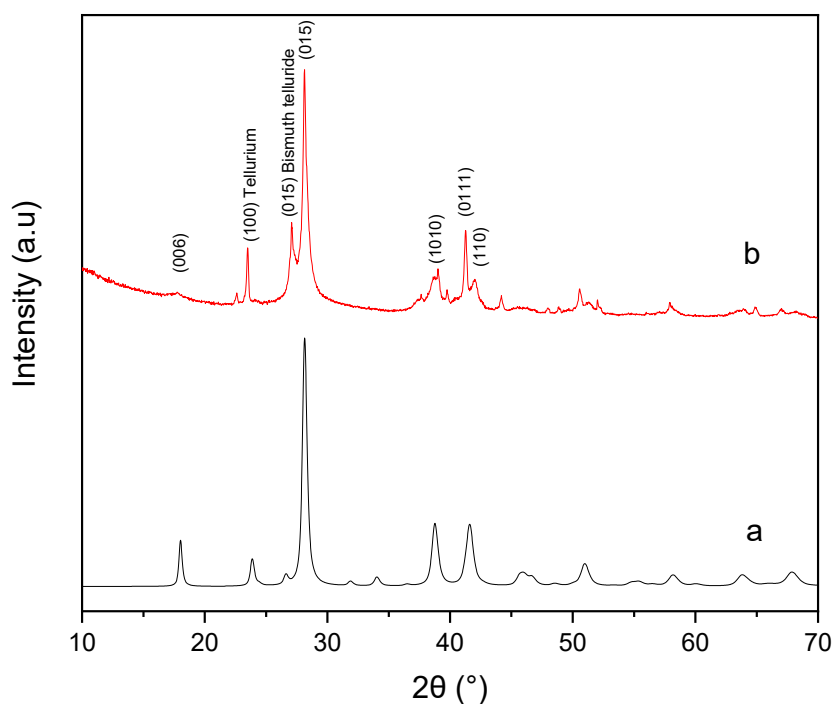


**Fig.4.2-** GIXRD diffraction patterns obtained for (a) reference XRD of Bismuth Selenide Telluride ( $\text{Bi}_2\text{SeTe}_2$ ) mineral from the International Centre of Diffraction Data (ICDD) database (PDF 01-089-2006) and (b) drop-casted film of PRS  $\text{Bi}_2\text{Te}_{3-x}\text{Se}_x$  nanowires on a Si substrate.

From the GIXRD we observe a preferred crystal lattice orientation of (0 1 5) with the pattern matching  $\text{Bi}_2\text{SeTe}_2$  despite the EDX atomic ratios being closer to  $\text{Bi}_2\text{Te}_{2.5}\text{Se}_{0.5}$ . Other peaks were indexed for the crystal lattice orientations of (1 0 0) for Te as well as (0 1 5) for  $\text{Bi}_2\text{Te}_3$ , indicating that there were still nanowires that had not fully incorporated the Se atoms into their crystal lattice. This could result from a competition between the Se and Bi atoms during the one-step addition of their precursors into the PRS reaction mixture.

When we compare the GIXRD spectrum of the drop-casted  $\text{Bi}_2\text{Te}_{3-x}\text{Se}_x$  nanowires to the drop-casted  $\text{Bi}_2\text{Te}_3$  nanowires in Fig. 4.3 we observe noticeable shifts in the (0 1 5) and (1 0 1 0) lattice orientations. We observe a shift from 27.8 ° for  $\text{Bi}_2\text{Te}_3$  to 28.1 ° for  $\text{Bi}_2\text{Te}_{3-x}\text{Se}_x$  for the (0 1 5) peak and a shift of 38.1 ° to 39.0 ° for the (1 0 1 0) peak. These shifts towards higher angles would indicate a contraction in the crystal lattice, which is a result of the  $\text{Te}^{(2)}$  sites being replaced with Se atoms which have a smaller atomic radius. As such we can be confident that some of the Se atoms have been incorporated into the crystal lattice, as similar peak shifts towards higher angles have also been identified in the literature [100–102].

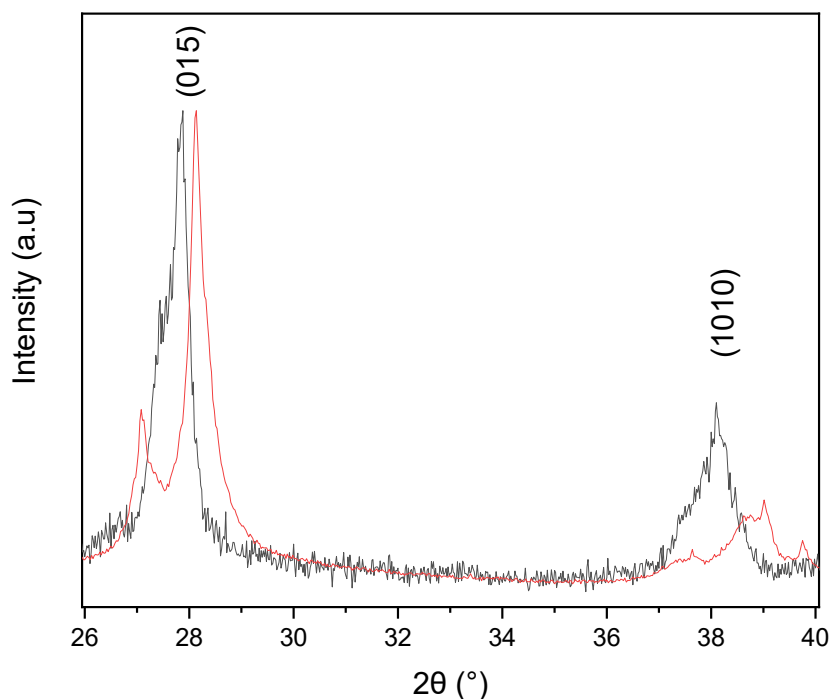


**Fig.4.3-** GIXRD diffraction patterns for the (black) drop-casted film of  $\text{Bi}_2\text{Te}_3$  nanowires on a Si substrate (red) for the drop-casted film of  $\text{Bi}_2\text{Te}_{3-x}\text{Se}_x$  nanowires between  $26^\circ$  and  $40^\circ$ .

#### 4.1.2 Two-step addition of Se and Bi precursor into the polyol reflux synthesis

A two-step addition approach was also used and is based on the work by Zhou et al <sup>[45]</sup>, the Se and Bi precursors were dissolved in separate 5 mL solutions of EG. The solution with the dissolved Se precursor was added to the PRS reaction 1 hr after the hydrazine hydrate and allowed to mix in the PRS reaction for an additional hour before the solution with the dissolved Bi precursor was added. As in the previous section, the resulting product was drop-casted to form thick films, which underwent microstructural analysis by SEM, EDX and GIXRD. The synthesis has been reproduced a minimum of 3 times and drop-casted films were fabricated for each synthesis to ensure the reproducibility of the PRS reaction.

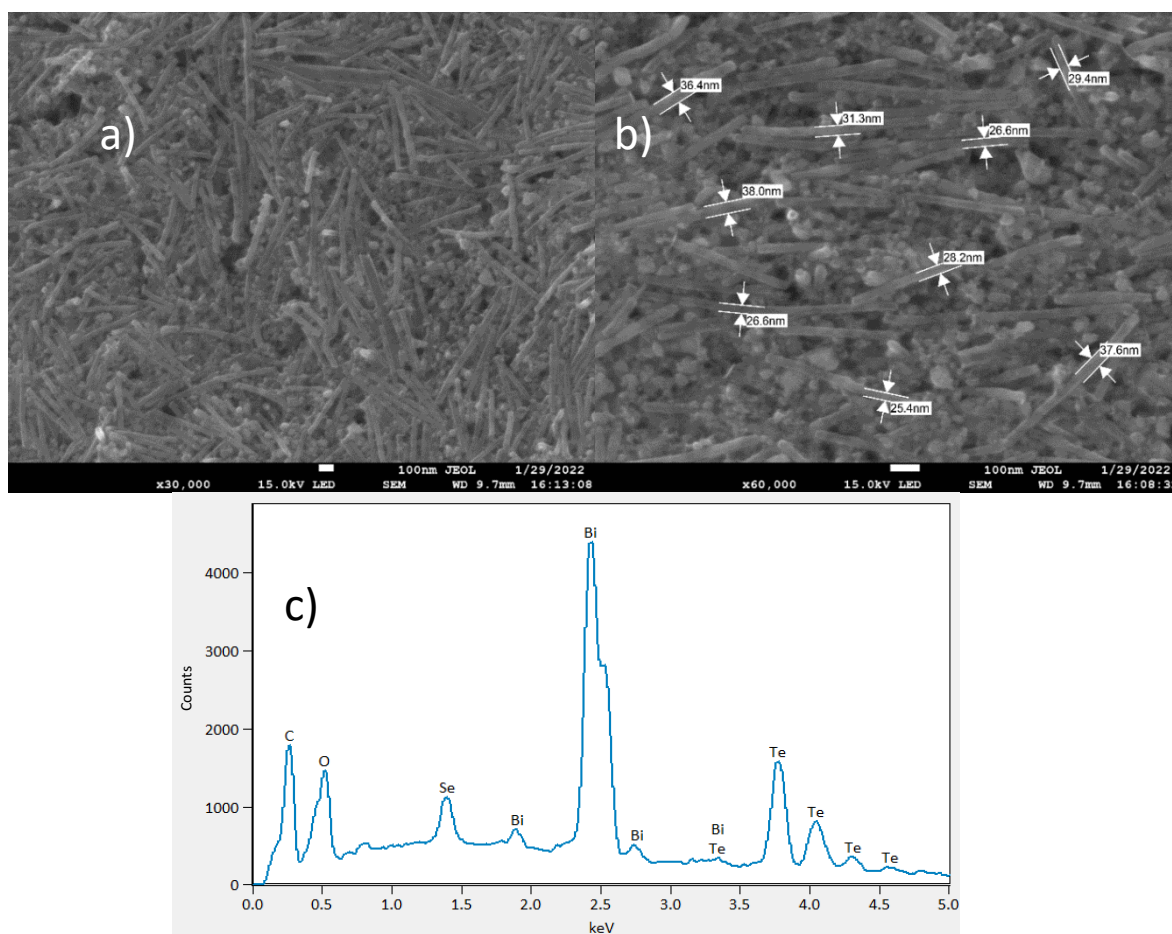


**Fig.4.4-** SEM images (a) of a top-down view of PRS  $\text{Bi}_2\text{Te}_{3-x}\text{Se}_x$  nanowires on a Si substrate, with (b) showing the nanowires lengths and (c) an EDX spectrum of the drop-casted PRS  $\text{Bi}_2\text{Te}_{3-x}\text{Se}_x$  nanowires film.

From the SEM images, it becomes clear that unlike in Fig. 3.1 and Fig. 4.1 the resulting nanowires from the two-step addition process are much thinner than the nanowires in those previous figures. The two main distinctions between the one-step and two-step addition processes is the point when the Se precursor is added to the PRS reaction and the duration of the  $\text{Bi}_2\text{Te}_{3-x}\text{Se}_x$  synthesis. We believe the thinning of the nanowires is a result of these differences. The average diameter of the nanowires was  $32 \pm 8$  nm, which is almost a fifth of the average diameter of the nanowires produced by the one-step addition process, and almost half the average diameter of the  $\text{Bi}_2\text{Te}_3$  nanowires. However, these  $\text{Bi}_2\text{Te}_{3-x}\text{Se}_x$  nanowires were 3x bigger than the  $\text{Bi}_2\text{Te}_{2.7}\text{Se}_{0.3}$  nanowires synthesised by Zhou et al <sup>[45]</sup>, this was due to them using a higher mass quantity of PVP growth directing agent. Additionally, when compared to the nanowires in the previous section these nanowires are more uniform as can be seen by the lower error in the average diameters. The EDX data shows the nanowires have atomic percentages of 39.6:53.5:6.9 for Bi:Te:Se respectively. These percentages are within the 2 % uncertainty of the EDX detector for that expected of  $\text{Bi}_2\text{Te}_{2.7}\text{Se}_{0.3}$ .

The nanowires' oxygen content was ~30 % with respect to the atomic percentages of Bi, Te and Se, which is 4 % lower than the nanowires produced by the one-step addition process. As the nanowires synthesised by both methods underwent the same oxygen-inducing cleaning process, the change in oxygen content is due to the extra time of the two-step addition process allowing more SeO to be reduced. Based on this we can reaffirm that the main source of oxygen in the EDX data is the result of the post-synthesis cleaning process with any residue precursors only slightly contributing to the oxygen content.

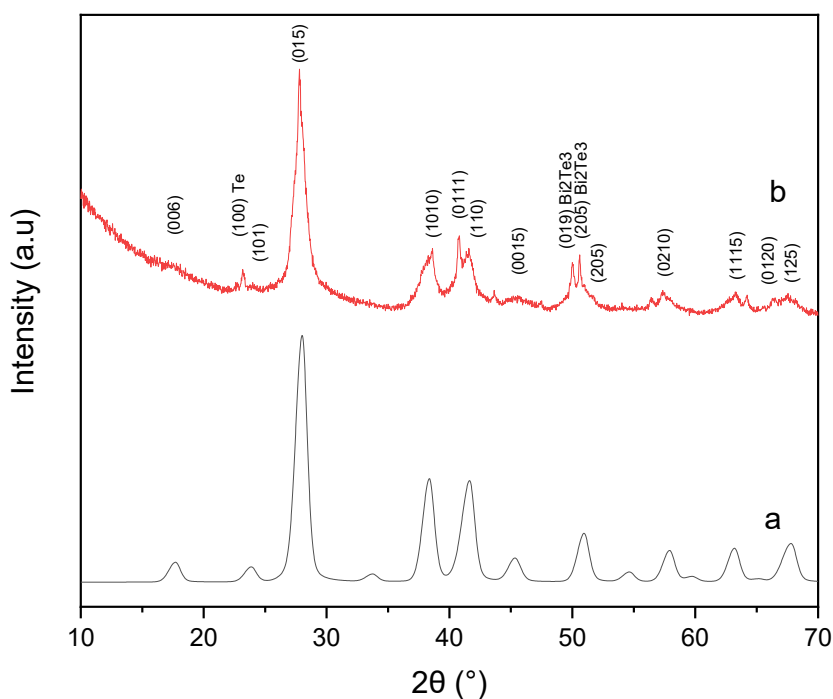


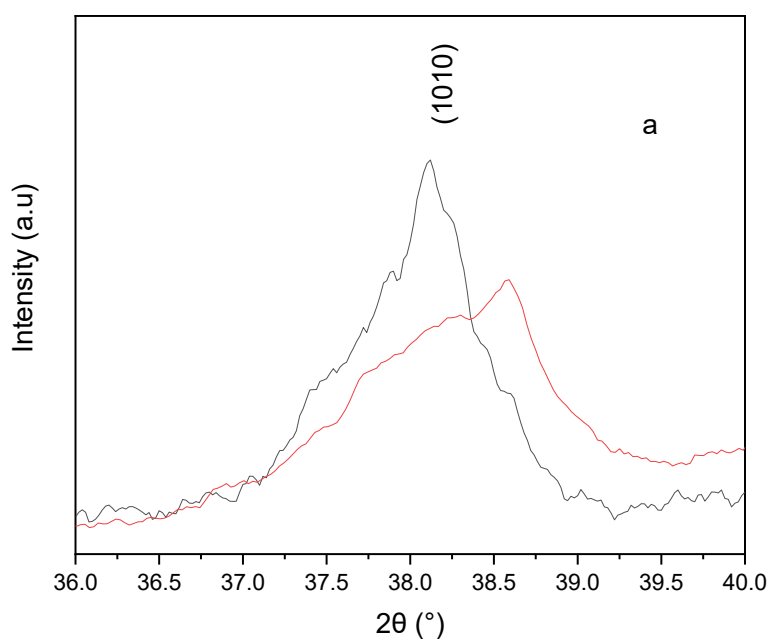
**Fig. 4.5-** GIXRD diffraction patterns obtained for (a) reference XRD of Bismuth Telluride Selenide ( $\text{Bi}_2\text{Te}_{2.5}\text{Se}_{0.5}$ ) mineral from the International Centre of Diffraction Data (ICDD) database (PDF 00-051-0643) and (b) drop-casted film of PRS  $\text{Bi}_2\text{Te}_{3-x}\text{Se}_x$  nanowires on a Si substrate.

From the GIXRD we observe a preferred crystal lattice orientation of (0 1 5) with the pattern matching  $\text{Bi}_2\text{Te}_{2.5}\text{Se}_{0.5}$  despite the EDX atomic percentages being closer to  $\text{Bi}_2\text{Te}_{2.7}\text{Se}_{0.3}$ . Other peaks were indexed for the crystal lattice orientations of (1 0 0) for Te as well as (0 1 9) and (2 0 5) for  $\text{Bi}_2\text{Te}_3$ , indicating that there were still nanowires that had not fully incorporated the Se atoms into their crystal lattice. This is despite the two-step addition process giving an extra 1 hr for the Se precursors to reduce and integrate into the Te nanowires. Based on the discrepancy between the EDX and GIXRD measurements, as well as GIXRD peaks indexed for Te and  $\text{Bi}_2\text{Te}_3$ , it would appear that the Se alloying process was not fully complete. We believe this is due to the Se atoms not being fully dispersed in the PRS reaction. As the EDX data shows the nanowires have the appropriate Bi:Te:Se atomic ratios to form  $\text{Bi}_2\text{Te}_{2.7}\text{Se}_{0.3}$ . While the data from the GIXRD would indicate there

were regions in the reaction that had higher concentrations of Se resulting in the synthesis of  $\text{Bi}_2\text{Te}_{2.5}\text{Se}_{0.5}$  nanowires, were as regions with low Se content remained as Te and  $\text{Bi}_2\text{Te}_3$  nanowires.

Higher reaction mixing speeds could be one avenue to improve the distribution of the Se atoms in the reaction. However, this was not safely feasible in our case due to the erratic bouncing of the magnetic stirrer in the RBF at speeds greater than 600 rpm. This erratic bouncing could potentially damage the RBF and leak the toxic reaction mixture.

We compared the GIXRD spectrum of the drop-casted  $\text{Bi}_2\text{Te}_{3-x}\text{Se}_x$  nanowires to the drop-casted  $\text{Bi}_2\text{Te}_3$  nanowires in Fig. 4.6, where we observe noticeable shifts in the (1 0 1 0), (1 1 1 5) and (1 2 5) lattice orientations. We observe a shift from  $38.1^\circ$  for  $\text{Bi}_2\text{Te}_3$  to  $38.6^\circ$  for  $\text{Bi}_2\text{Te}_{3-x}\text{Se}_x$  for the (1 0 1 0) peak, a shift of  $62.7^\circ$  to  $63.3^\circ$  for the (1 1 1 5) peak, and a shift of  $67.3^\circ$  to  $67.6^\circ$  for the (1 2 5) peak. The reduced shift of the lattice orientations for the two-step compared to the one-step addition process could be a result of the lower Se atomic concentration seen in the EDX data. Based on these peak shifts, and the EDX data as well as the change in morphologies of the nanowires seen in Fig. 4.4, we can conclude that the majority of the obtained nanowires are  $\text{Bi}_2\text{Te}_{2.5}\text{Se}_{0.5}$ .



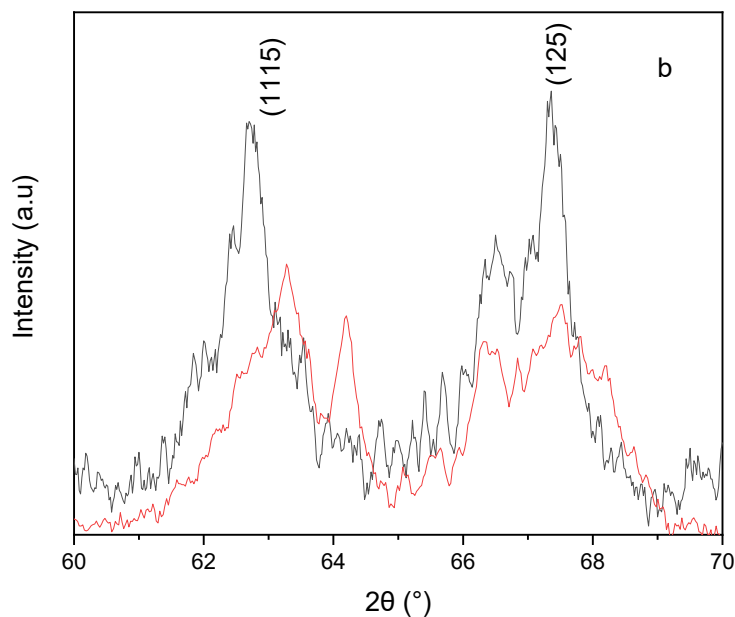


**Fig.4.6-** GIXRD diffraction patterns obtained for (black line) drop-casted film of Bi<sub>2</sub>Te<sub>3</sub> nanowires and (red line) drop-casted film of Bi<sub>2</sub>Te<sub>2.5</sub>Se<sub>0.5</sub> on a Si substrate for the range of (a) 36 ° - 40 ° and (b) 60 ° - 70 °.

As the challenges of fine-tuning the atomic compositions and crystal structure of the nanowires were too time-costly and potentially posed a safety risk, the two-step addition process was used to synthesise Bi<sub>2</sub>Te<sub>2.5</sub>Se<sub>0.5</sub> nanowires. These nanowires were formulated into TE pastes and screen-print onto flexible Kapton substrates where they were annealed to characterise and compare their material and TE properties to annealed screen-printed Bi<sub>2</sub>Te<sub>3</sub> nanowires.

## 4.2 Screen-printed PVDF-Bi<sub>2</sub>Te<sub>2.5</sub>Se<sub>0.5</sub> nanowire composite films

### 4.2.1 Morphological comparison between Bi<sub>2</sub>Te<sub>2.5</sub>Se<sub>0.5</sub> & Bi<sub>2</sub>Te<sub>3</sub> films

Using our paste formulation method as described in section 2.22 we used a PVDF binder concentration of 5 % to screen-print PVDF-Bi<sub>2</sub>Te<sub>2.5</sub>Se<sub>0.5</sub> nanowire films alongside PVDF-Bi<sub>2</sub>Te<sub>3</sub> nanowire films. Two samples were fabricated for each, one made from one print of Bi<sub>2</sub>Te<sub>2.5</sub>Se<sub>0.5</sub> and Bi<sub>2</sub>Te<sub>3</sub> and another with three printed layers stacked on one another. Fig. 4.7 shows the screen-printed films for one printing pass of PVDF-Bi<sub>2</sub>Te<sub>3</sub> and PVDF-Bi<sub>2</sub>Te<sub>2.5</sub>Se<sub>0.5</sub> nanowire films. The samples were annealed at 400 °C for 2 hr in an inert Ar atmosphere inside a tube furnace.

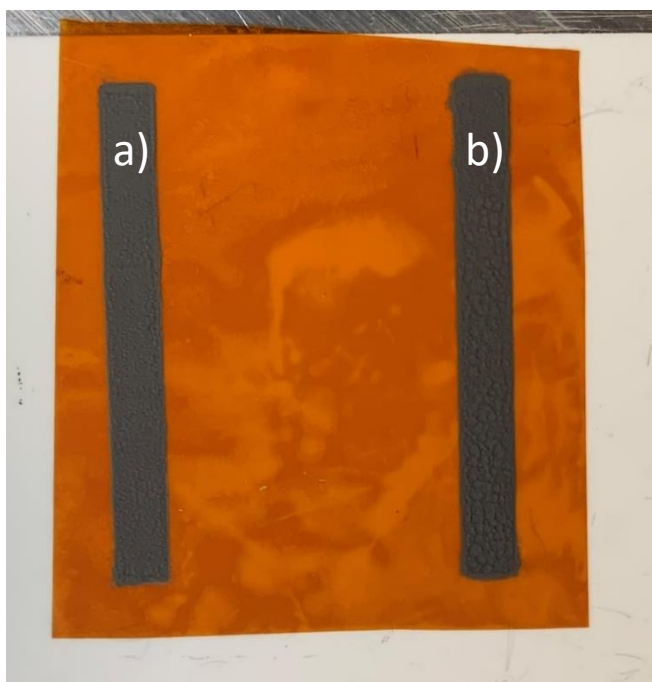


**Fig.4.7-** Photograph of single pass screen-printed (a) PVDF-Bi<sub>2</sub>Te<sub>3</sub> and (b) PVDF-Bi<sub>2</sub>Te<sub>2.5</sub>Se<sub>0.5</sub> nanowire films.

The annealed screen-printed films were investigated by SEM, EDX and GIXIRD. The SEM images as shown in Fig.4.8 reveal that the nanowire average diameters for both Bi<sub>2</sub>Te<sub>3</sub> and Bi<sub>2</sub>Te<sub>2.5</sub>Se<sub>0.5</sub> films had increased to  $100 \pm 20$  nm from their previous unannealed recorded diameters of  $60 \pm 20$  nm and  $32 \pm 8$  nm for Bi<sub>2</sub>Te<sub>3</sub> and Bi<sub>2</sub>Te<sub>2.5</sub>Se<sub>0.5</sub> respectively. Furthermore, the nanowires were also observed to have shortened lengths of only a few hundred nm causing them to appear nanorod-like in structure. The EDX data showed the presence of fluorine at <2 % for both films after annealing, while the oxygen content was ~24 % for the Bi<sub>2</sub>Te<sub>3</sub> and ~22 % for Bi<sub>2</sub>Te<sub>2.5</sub>Se<sub>0.5</sub> when compared to the Bi, Te and Se atomic percentages. The atomic percentages for the Bi<sub>2</sub>Te<sub>3</sub> nanowires were 38:62 for Bi and Te respectively. While for the Bi<sub>2</sub>Te<sub>2.5</sub>Se<sub>0.5</sub> nanowires the atomic percentages for Bi, Te and Se were 40.9:52.9:6.7. Compared to the drop-casted Bi<sub>2</sub>Te<sub>2.5</sub>Se<sub>0.5</sub> nanowires we observe an increase in Bi while the Te and Se content in the nanowires decreased, however, these changes are within the 2 % uncertainty of the EDX detector.

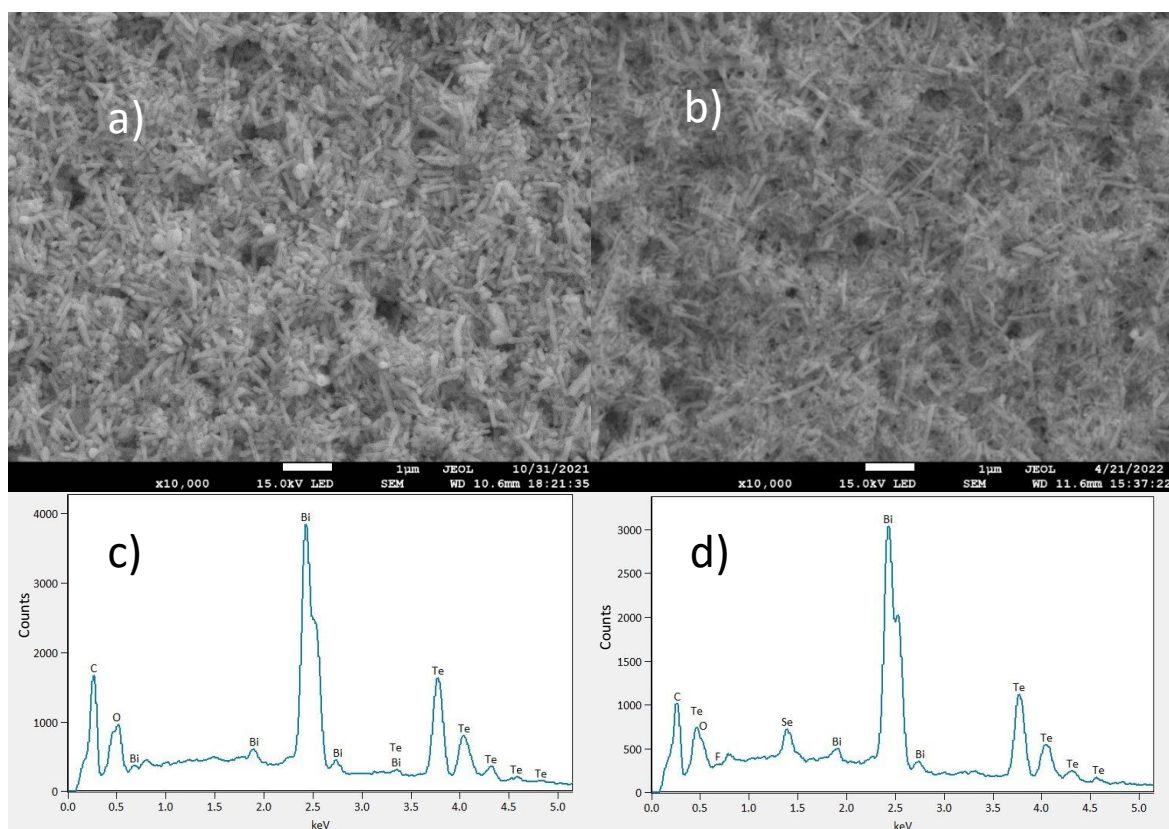
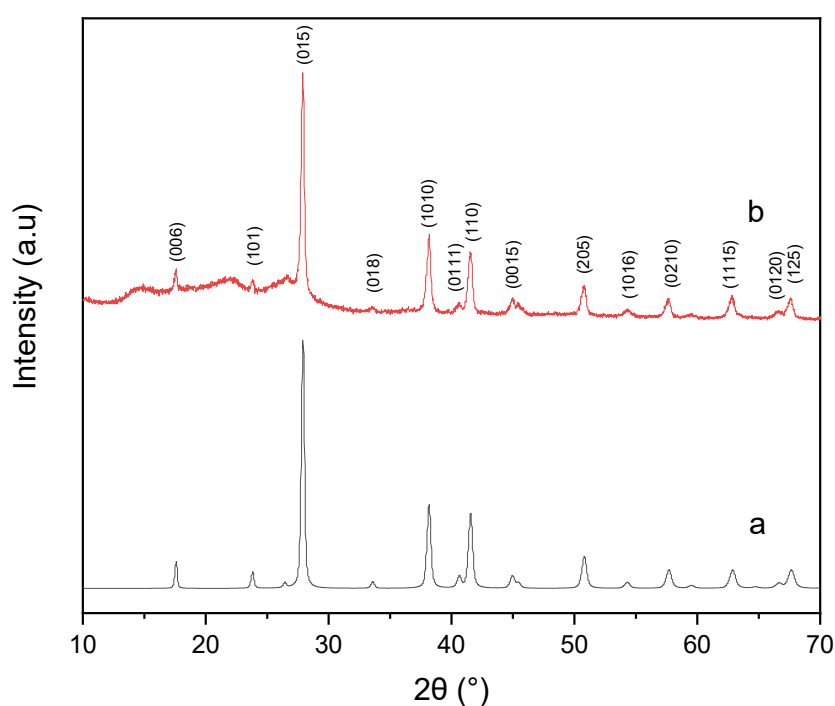


**Fig.4.8-** SEM images (a) of a top-down view of annealed PVDF-Bi<sub>2</sub>Te<sub>3</sub> and (b) annealed PVDF-Bi<sub>2</sub>Te<sub>2.5</sub>Se<sub>0.5</sub> and screen-printed films, with an EDX spectrum of the (c) annealed PVDF-Bi<sub>2</sub>Te<sub>3</sub> and (d) the annealed PVDF-Bi<sub>2</sub>Te<sub>2.5</sub>Se<sub>0.5</sub> films.

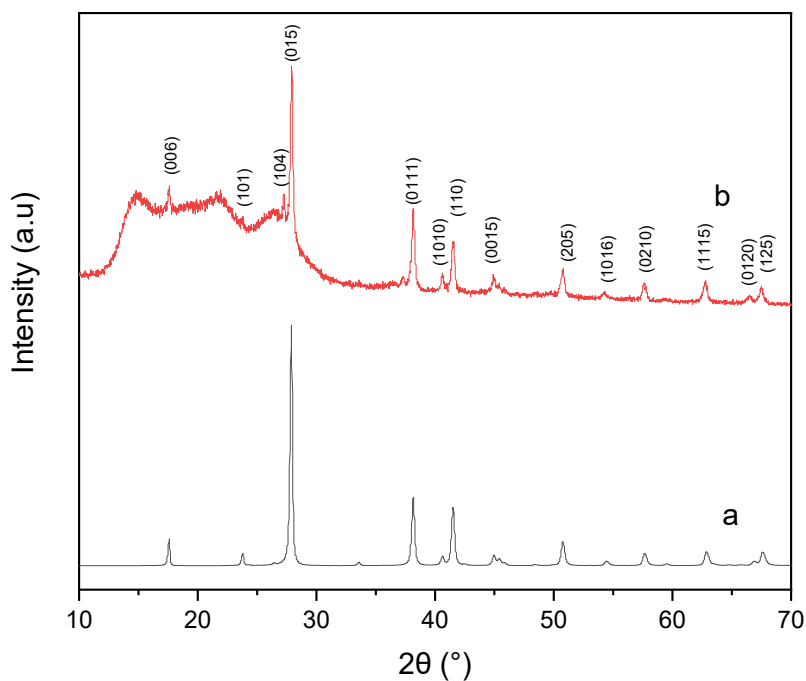
Using the GIXRD data of the annealed PVDF-Bi<sub>2</sub>Te<sub>3</sub> films we were able to index the films to Bi<sub>2</sub>Te<sub>3</sub>, while the PVDF-Bi<sub>2</sub>Te<sub>2.5</sub>Se<sub>0.5</sub> films were indexed to Bi<sub>2</sub>Te<sub>2.5</sub>Se<sub>0.5</sub> as can be seen in Fig.4.9 and Fig. 4.10. The GIXRD spectra show both alloys' have a preferential lattice orientation in the (0 1 5) phase, which carries on the trend that has been seen in the previous GIXRD spectrums. Both contain a broad shoulder between 10 ° and 25 ° with PVDF-Bi<sub>2</sub>Te<sub>3</sub> having a higher intensity. These broad shoulders can be associated with the Kapton substrate as seen in the literature [95–97].

When overlaying the spectra (seen in Fig. 4.11) for both Bi<sub>2</sub>Te<sub>3</sub> and Bi<sub>2</sub>Te<sub>2.5</sub>Se<sub>0.5</sub>, the peaks overlap with no noticeable shifts between 10 ° and 60 °. However, we identify shifts in the peaks between 66 ° and 69 ° for the (0 1 2 0) and (1 2 5) lattice orientations. We observe a shift of 66.5 ° to 66.7 ° for the (0 1 2 0) peak and a shift from 67.5 ° to 67.6 ° for the (1 2 5). As stated in section 4.1 these shifts are related to the contraction in the crystal lattice with the incorporation of smaller Se atoms replacing larger Te atoms. However, when comparing the GIXRD spectra (seen in Fig.4.12) for an annealed screen-printed PVDF-Bi<sub>2</sub>Te<sub>2.5</sub>Se<sub>0.5</sub> film with a drop-casted Bi<sub>2</sub>Te<sub>2.5</sub>Se<sub>0.5</sub> nanowire film we identify a shift towards lower angles for the (1 0 1 0) and (1 1 1 5) peaks. We observe a shift of 38.6 ° to 38.1 ° for the (1 0 1 0) peak and a shift from 63.2 ° to 62.8 ° for the (1 1 1 5) peak. The shift towards lower angles signifies an expansion in the crystal lattice.

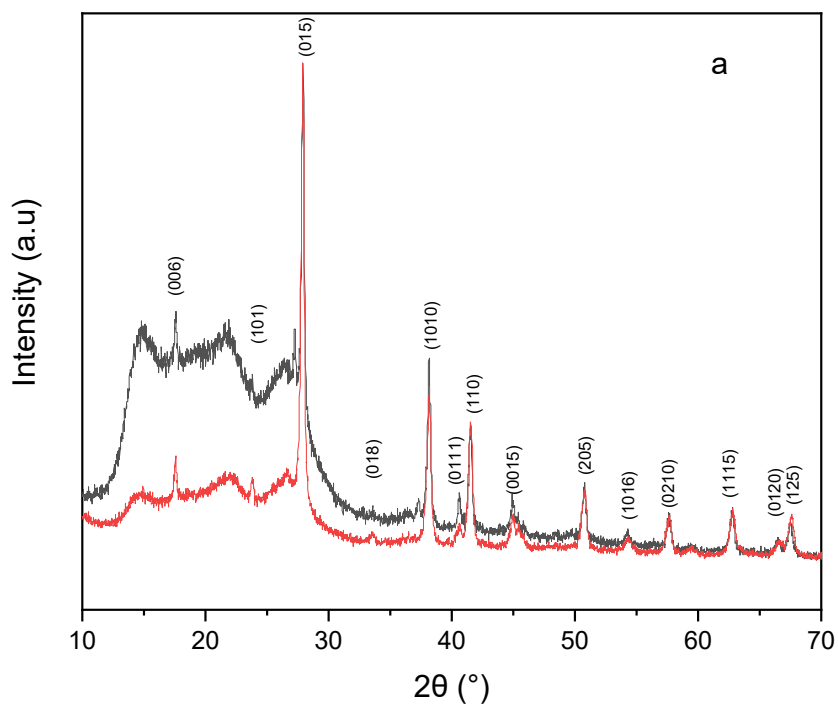
This shift in the crystal lattice is believed to be due to Bi antisite defects on Te and Se sites. Antisite defects can arise in the crystal structure of alloys when one chemical species of atoms occupies a site usually occupied by a different chemical species of atoms that exist in the alloy<sup>[103]</sup>. The reason we believe these are Bi antisite defects is that Bi has a larger atomic radius than Te or Se and the EDX data shows an increase in the Bi content at the expense of the Te and Se content<sup>[76]</sup>. These Bi antisite defect on Te and Se sites explains the reduced shift between the annealed screen-printed  $\text{Bi}_2\text{Te}_{2.5}\text{Se}_{0.5}$  compared to its  $\text{Bi}_2\text{Te}_3$  counterpart, as the Bi-related expansion in the crystal lattice would partly counter the lattice contraction from the Se incorporation. As stated by Kim et al<sup>[76]</sup> these Bi antisite defects are electron acceptor which could result in a lower charge carrier concentration of the annealed screen-printed PVDF- $\text{Bi}_2\text{Te}_{2.5}\text{Se}_{0.5}$  film.

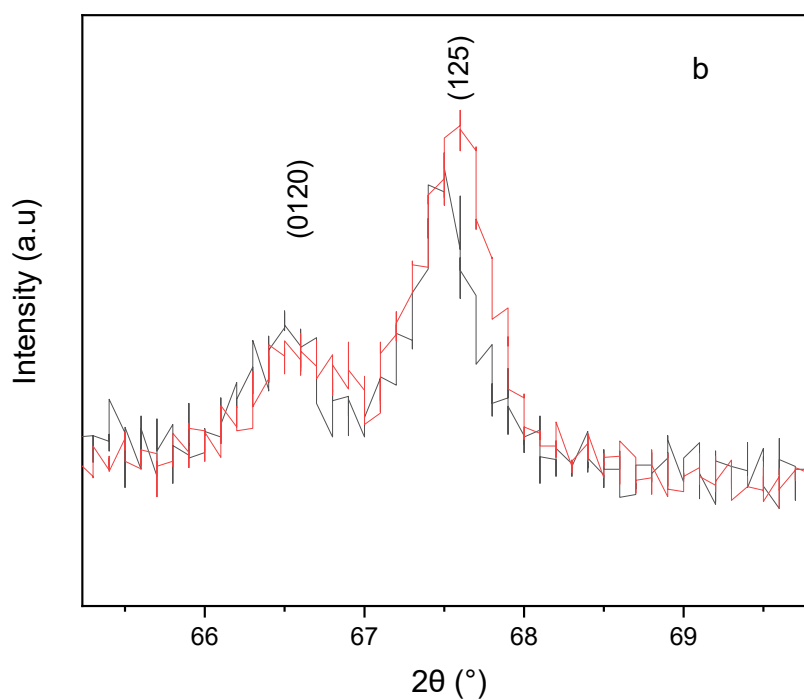


**Fig.4.9-** GIXRD diffraction patterns obtained for (a) reference XRD of Bismuth Telluride Selenide ( $\text{Bi}_2\text{Te}_{2.5}\text{Se}_{0.5}$ ) mineral from the International Centre of Diffraction Data (ICDD) database (PDF 00-051-0643) and (b) screen-printed PRS  $\text{Bi}_2\text{Te}_{2.5}\text{Se}_{0.5}$  nanowire film annealed at 400 °C for 2 hr in an Ar atmosphere on a Kapton substrate.

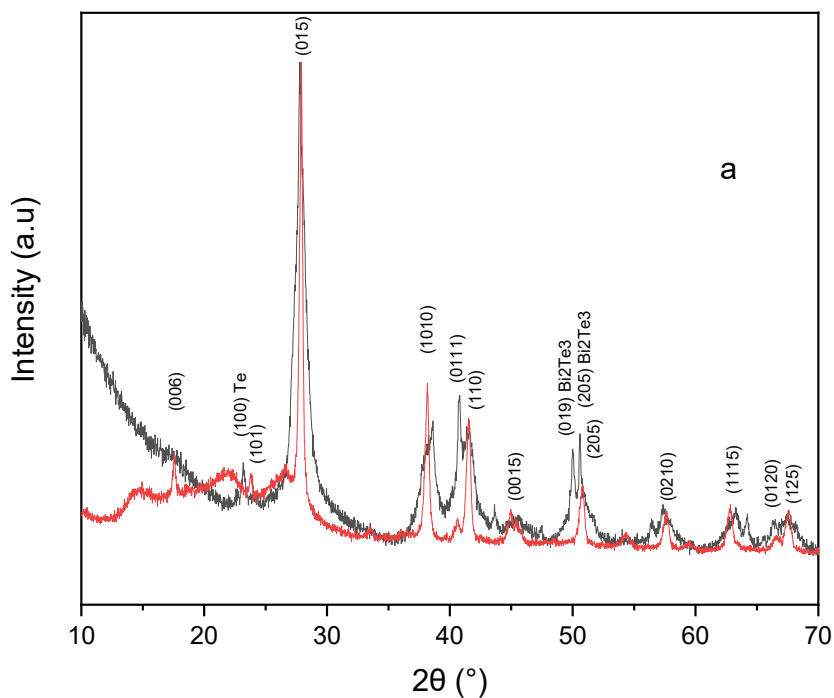


**Fig.4.10**-GIXRD diffraction patterns obtained for (a) reference XRD of tellurobismuthite ( $\text{Bi}_2\text{Te}_3$ ) mineral from the International Centre of Diffraction Data (ICDD) database (PDF 00-082-0358) (b) screen-printed PRS  $\text{Bi}_2\text{Te}_3$  nanowire film annealed at 400  $^\circ\text{C}$  for 2 hr in an Ar atmosphere on a Kapton substrate





**Fig. 4.11-** GIXRD diffraction patterns obtained for (black line) screen-printed Bi<sub>2</sub>Te<sub>3</sub> nanowires annealed in an inert Ar atmosphere and (red line) screen-printed PRS Bi<sub>2</sub>Te<sub>2.5</sub>Se<sub>0.5</sub> nanowire film annealed at 400 °C for 2 hr in an inert Ar atmosphere on a Kapton substrate for the range of (a) 10 °-70 ° and (b) zoomed in for 66 °-69 °.



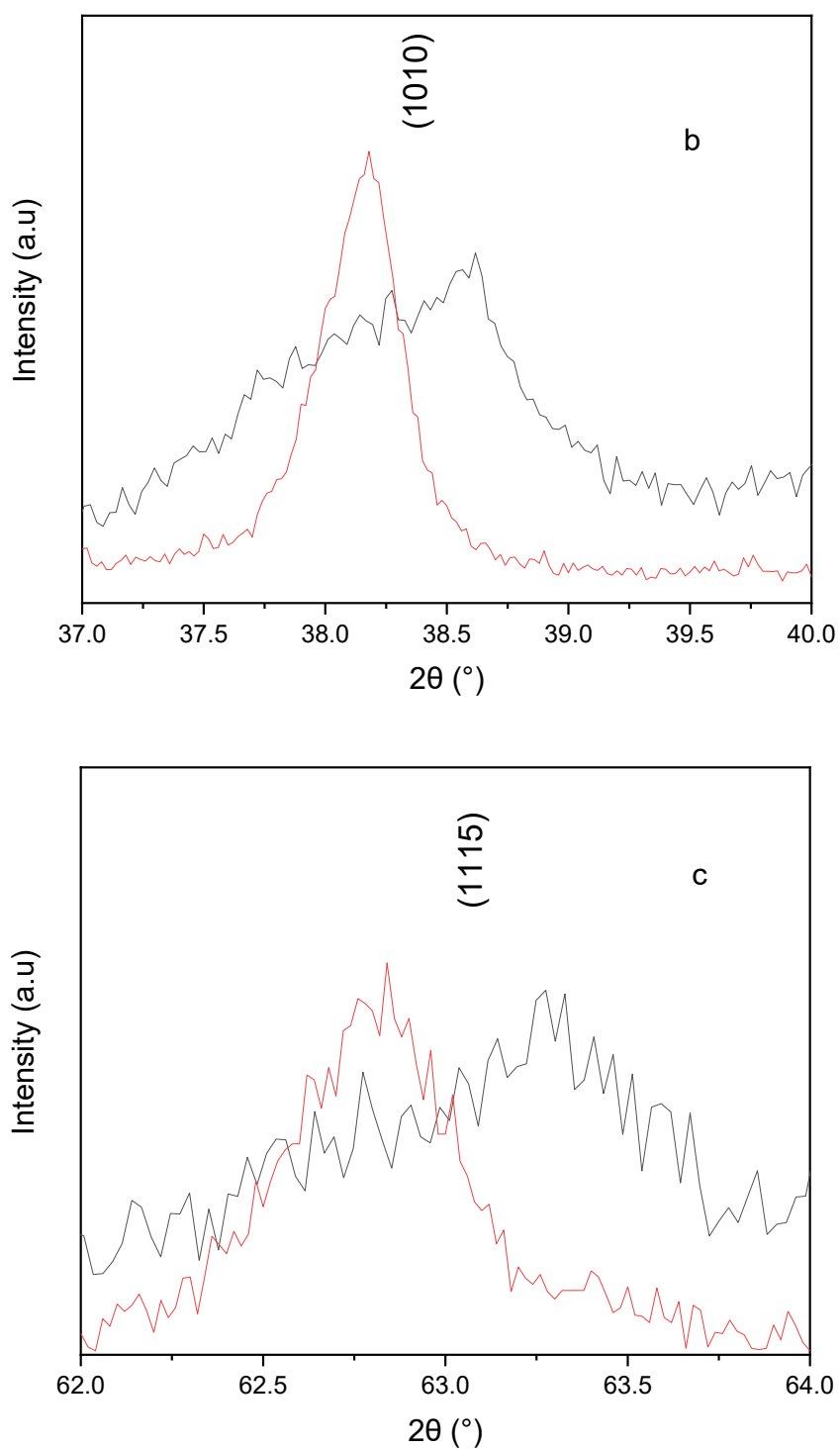


**Fig. 4.12-** GIXRD diffraction patterns obtained for (black line) drop-casted film of PRS  $\text{Bi}_2\text{Te}_{2.5}\text{Se}_{0.5}$  nanowires on Si substrate and (red line) screen-printed PRS  $\text{Bi}_2\text{Te}_{2.5}\text{Se}_{0.5}$  nanowire film annealed at 400 °C for 2 hr in an inert Ar atmosphere on a Kapton substrate for the range of (a) 10 °-70 °, (b) zoomed in for 37 °- 40 ° and (c) zoomed in for 62 °- 64 °.

#### 4.2.2 Thermoelectric analysis comparing post-annealed $\text{Bi}_2\text{Te}_{2.5}\text{Se}_{0.5}$ & $\text{Bi}_2\text{Te}_3$ films

Room temperature TE measurements of the annealed PVDF- $\text{Bi}_2\text{Te}_3$  and PVDF- $\text{Bi}_2\text{Te}_{2.5}\text{Se}_{0.5}$  films were carried out using the portable S probe shown in sections 2.411 and the Hall effect probe. The graphs of the TE measurements are seen in Fig. 4.13 and the Hall electrical properties are shown in Fig. 4.14. The PVDF- $\text{Bi}_2\text{Te}_3$  samples with one and three printing passes are denoted as BTP1 and BTP3 respectively. This is also the case for the PVDF- $\text{Bi}_2\text{Te}_{2.5}\text{Se}_{0.5}$  samples with one and three printing passes denoted as BTSP1 and BTSP3 respectively. It was observed that one of the annealed PVDF- $\text{Bi}_2\text{Te}_3$  films had formed INNs around the edges of the film. These INNs were also measured and compared to the other films in Fig. 4.13 and Fig.4.14 as BTP1-INNs. The samples' thicknesses were measured using a surface profilometer and were found to be  $5 \pm 2 \mu\text{m}$  for BTP1, BTP1-INNs and BTSP1. The high error in the films' thickness was due to the non-uniformity of these single print films. The thickness of the thicker films of BTP3 and BTSP3 was measured to be  $22 \pm 5 \mu\text{m}$  and  $28 \pm 7 \mu\text{m}$  respectively.

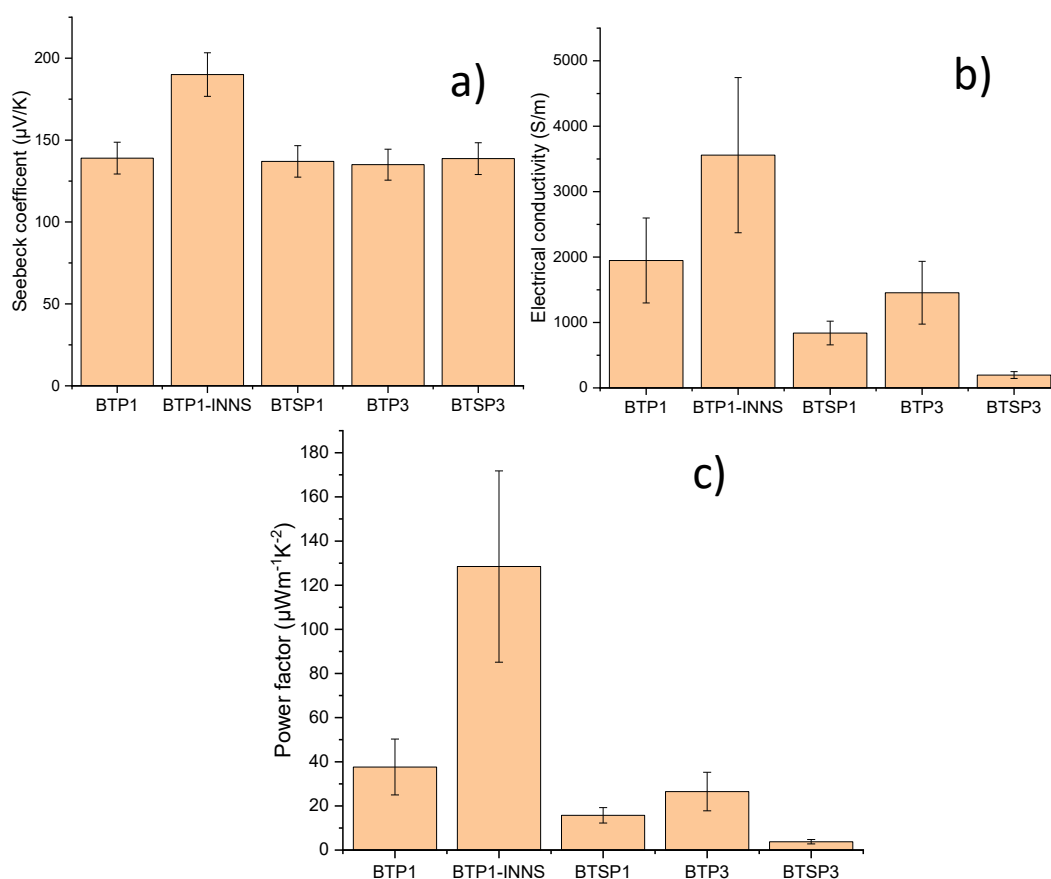


**Fig. 4.13-** Room temperature TE properties of (a) Seebeck coefficient, (b) electrical conductivity and (c) power factor for 1 printing pass and 3 printing pass films of PVDF- $\text{Bi}_2\text{Te}_3$  and PVDF- $\text{Bi}_2\text{Te}_{2.5}\text{Se}_{0.5}$  films annealed at  $400^\circ\text{C}$  for 2 hr in an inert Ar atmosphere. The uncertainty is based on the standard deviation of the results and the measured thickness of the films.

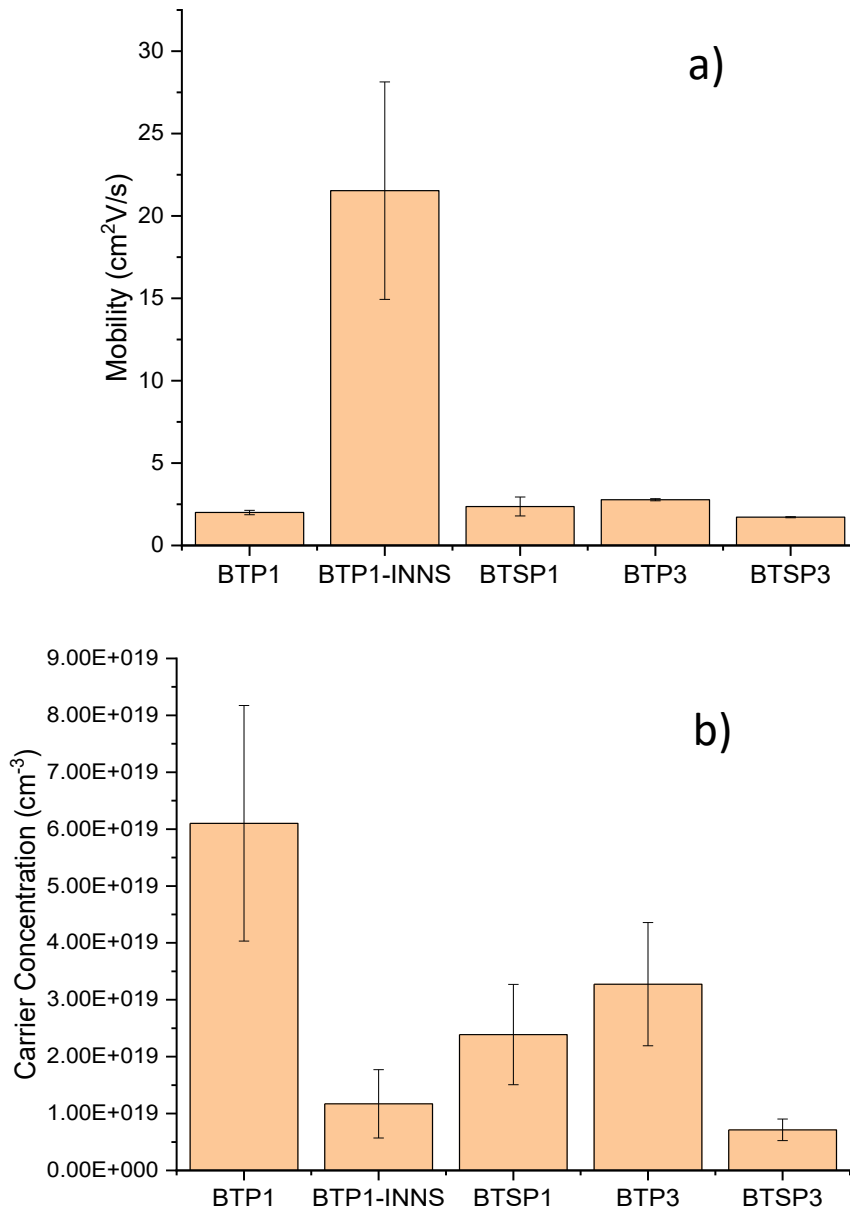


**Fig.4.14-** Room temperature (a) charge carrier mobility and (b) charge carrier concentration for 1 printing pass and 3 printing pass films of PVDF-Bi<sub>2</sub>Te<sub>3</sub> and PVDF-Bi<sub>2</sub>Te<sub>2.5</sub>Se<sub>0.5</sub> films annealed at 400 °C for 2 hr in an inert Ar atmosphere. The uncertainty is based on the standard deviation of the results and the measured thickness of the films.

From Fig.4.13 and Fig.4.14, the BTP1 sample was shown to be the highest performing film with an S of  $-140 \pm 10 \mu\text{VK}^{-1}$  and a PF of  $40 \pm 10 \mu\text{Wm}^{-1}\text{K}^{-2}$ , with only the BTP1-INNS having a higher TE performance of an S of  $-190 \pm 10 \mu\text{VK}^{-1}$  and a PF of  $130 \pm 40 \mu\text{Wm}^{-1}\text{K}^{-2}$ . We observe no change in the S between Se-alloyed and non-Se alloyed nanowires, with all the films excluding the INNS having an S of  $-140 \pm 10 \mu\text{VK}^{-1}$ . This is within the range of uncertainty of Zhou et al <sup>[45]</sup> Bi<sub>2</sub>Te<sub>2.7</sub>Se<sub>0.3</sub> nanowire pellet which obtained a room temperature S of  $-150 \mu\text{VK}^{-1}$ . The difference between the PVDF-Bi<sub>2</sub>Te<sub>3</sub> and PVDF-Bi<sub>2</sub>Te<sub>2.5</sub>Se<sub>0.5</sub> films' TE performance came down to  $\sigma$ .

The two factors that affected the samples' electrical properties were whether the film's nanowires were alloyed with Se and how many printing passes were used to fabricate the films. We note that the PVDF-Bi<sub>2</sub>Te<sub>2.5</sub>Se<sub>0.5</sub> film fabricated with 1 printing pass ( $5 \pm 2 \mu\text{m}$ ) had higher electrical properties than the PVDF-Bi<sub>2</sub>Te<sub>2.5</sub>Se<sub>0.5</sub> film printed with 3 printing passes ( $28 \pm 7 \mu\text{m}$ ). This was also observed for the PVDF-Bi<sub>2</sub>Te<sub>3</sub> films however the difference in electrical performance was within the range of uncertainty. The poor performance of the thicker films could be due to insufficient annealing which was also observed by Chen et al <sup>[53]</sup> for inkjet printed films of Bi<sub>2</sub>Te<sub>3</sub> nanowires. We observed higher carrier concentration from the PVDF-Bi<sub>2</sub>Te<sub>3</sub> films compared to their Se alloyed counterparts. This resulted in a lower  $\sigma$  for the PVDF-Bi<sub>2</sub>Te<sub>2.5</sub>Se<sub>0.5</sub> films, however, their lower carrier concentration was not significant enough to change the films' S. These samples have been reproduced 3 times and each time we still observe that the PVDF-Bi<sub>2</sub>Te<sub>3</sub> films have a higher TE performance than the PVDF-Bi<sub>2</sub>Te<sub>2.5</sub>Se<sub>0.5</sub> films due to the Se-alloyed films lower carrier concentration.

When comparing our findings with other polyol synthesised nanostructured Bi<sub>2</sub>Te<sub>2.5</sub>Se<sub>0.5</sub> in the literature, we similarly observe lower PFs as a result of lower  $\sigma$  for Bi<sub>2</sub>Te<sub>2.5</sub>Se<sub>0.5</sub> when compared to Bi<sub>2</sub>Te<sub>3</sub> <sup>[100,102]</sup>. Additionally, Hu et al <sup>[104]</sup> also noted a similar decrease in  $\sigma$  as the Se content increases for bulk Bi<sub>2</sub>Te<sub>3-x</sub>Se<sub>x</sub>. The lower carrier concentration causing the poor electrical performance of Bi<sub>2</sub>Te<sub>2.5</sub>Se<sub>0.5</sub> compared to Bi<sub>2</sub>Te<sub>3</sub> in our annealed screen-printed films and in the literature, is the result of Bi antisite defects in the Bi<sub>2</sub>Te<sub>2.5</sub>Se<sub>0.5</sub> crystal structure <sup>[100,104]</sup>. In the case of our annealed PVDF-Bi<sub>2</sub>Te<sub>2.5</sub>Se<sub>0.5</sub> films, due to the increase in the Bi content at the expense of the Te and Se content seen in the EDX data, as well as the shifts in the GIXRD peaks seen in Fig. 4.12 it is believed that Bi antisite defects were formed on Te and Se sites of the Bi<sub>2</sub>Te<sub>2.5</sub>Se<sub>0.5</sub> crystal structure. These Bi antisite defects provide hole charge carriers to the PVDF-Bi<sub>2</sub>Te<sub>2.5</sub>Se<sub>0.5</sub> films which lower their overall n-type carrier concentration <sup>[100,104]</sup>.

### 4.2.3 Bending analysis for screen-printed Bi<sub>2</sub>Te<sub>2.5</sub>Se<sub>0.5</sub> & Bi<sub>2</sub>Te<sub>3</sub> films

To evaluate whether the alloying of Se with the Bi<sub>2</sub>Te<sub>3</sub> nanowires had any changes to their flexibility, the same bending test as shown in section 3.33 was repeated for the Bi<sub>2</sub>Te<sub>2.5</sub>Se<sub>0.5</sub> nanowires. The sample experienced a bending test of over 1000 bending cycles at a bending radius of 10 mm, the results of which are shown in Fig.4.15. To account for the roughness of the fabric pocket of the bending apparatus the films are placed in a Kapton pocket. This is to prevent the films from being rubbed against the fabric which would cause an increase in resistance not due to the bending of the films. Finally, silver electrodes are deposited on both sides of the films to get accurate resistance readings without damaging the films with the measuring probes.

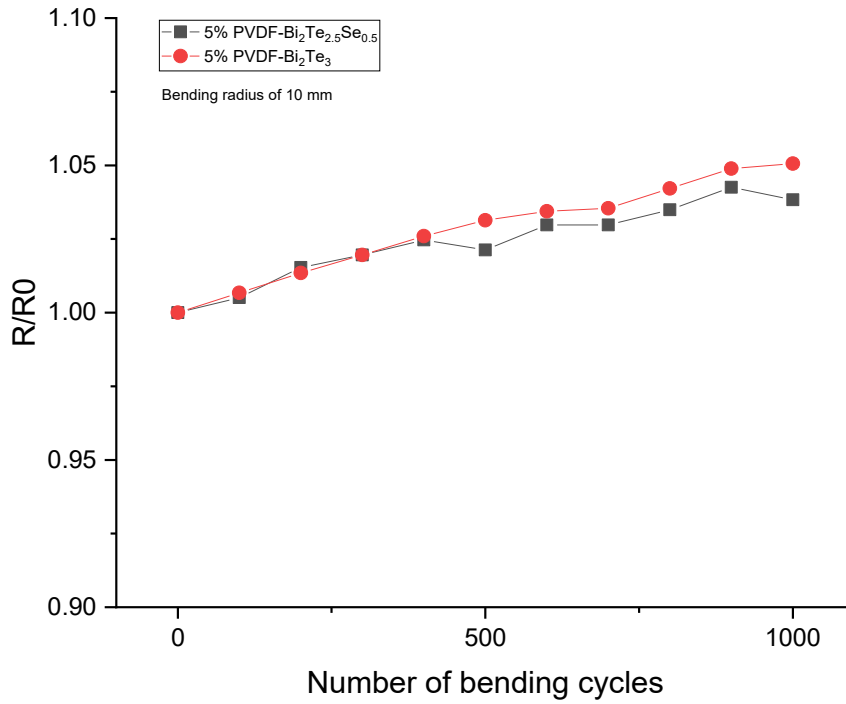


**Fig. 4.15-** The resistance normalized to the initial resistance of the single printing pass PVDF-Bi<sub>2</sub>Te<sub>3</sub> and PVDF-Bi<sub>2</sub>Te<sub>2.5</sub>Se<sub>0.5</sub> for 1000 bending cycles, with a bending radius of 10 mm.

From Fig.4.15 the PVDF-Bi<sub>2</sub>Te<sub>2.5</sub>Se<sub>0.5</sub> showed a slightly lower bending-induced resistance increase than the PVDF-Bi<sub>2</sub>Te<sub>3</sub>. Though the difference between the two is only 2 % with the film resistance after 1000 bending cycles increasing by 3 % and 5 % for the PVDF-Bi<sub>2</sub>Te<sub>2.5</sub>Se<sub>0.5</sub> and PVDF-Bi<sub>2</sub>Te<sub>3</sub> films respectively. These resistance increases are comparable with the literature for flexible printed Bi<sub>2</sub>Te<sub>3</sub>-based materials despite our smaller bending radius <sup>[53,64,75,105]</sup>. However, the difference in increased resistance is not significant enough to discern whether one film is more flexible than the other as such the PVDF-Bi<sub>2</sub>Te<sub>3</sub> film is considered the better n-type material for an FTEG due to its higher TE properties.

### 4.3 Conclusions

In summary, we synthesised  $\text{Bi}_2\text{Te}_{3-x}\text{Se}_x$  nanowires via PRS by modifying the previous  $\text{Bi}_2\text{Te}_3$  PRS reaction with the addition of SeO. Two different modifications to the PRS reaction were investigated. The first was a one-step addition of the Se and Bi precursors into the reaction. The second was a two-step addition method where the Se and Bi precursors were added to the reaction at separate times similar to what was seen by Zhou et al [45]. With the one-step addition process, we observed competition between the Se and Bi atoms to interact with the Te nanowires. While in the two-step addition process, we observe atomic percentages closer to the concentration of precursors in the reaction. This indicates that the extra time allowed the Se to interact with the Te nanowires. The morphology of the Se alloyed nanowires also changed depending on the addition process, as the one-step addition process produced nanowires with an average diameter of  $150 \pm 80$  nm, whereas the two-step addition process produced thinner nanowires that had an average diameter of  $32 \pm 8$  nm. The two-step addition nanowires had a fifth of the average diameter of the nanowires produced by the one-step addition process and almost half the average diameter of the  $\text{Bi}_2\text{Te}_3$  nanowires. Though when compared to  $\text{Bi}_2\text{Te}_{2.7}\text{Se}_{0.3}$  nanowires synthesised by Zhou et al [45] our nanowires were 3x bigger. This was due to them using a higher mass quantity of PVP growth directing agent used by Zhou et al [45]. Both batches had  $\text{Bi}_2\text{Te}_{3-x}\text{Se}_x$  crystal structures with the one-step addition method producing nanowires indexed to  $\text{Bi}_2\text{SeTe}_2$ , while the two-step addition produced nanowires that were indexed to  $\text{Bi}_2\text{Te}_{2.5}\text{Se}_{0.5}$ . When the GIXRD spectra for the different methods were compared to the GIXRD spectrum of the drop-casted  $\text{Bi}_2\text{Te}_3$  nanowires, we observed shifts towards higher angles in the lattice orientations. These shifts are a result of contractions in the crystal lattice which is explained as the  $\text{Te}^{(2)}$  sites being replaced with smaller Se atoms, with similar shifts seen in the literature [100–102]. However, we also observed peaks that were indexed to Te and  $\text{Bi}_2\text{Te}_3$  which highlights that this alloying was not fully complete during the reaction. This is believed to be due to the Se atoms not being fully dispersed in the PRS reaction, based on the alloy composition disparity in the EDX and GIXRD results. However, based on the results presented thus far, we can conclude that the majority of the synthesised nanowires are  $\text{Bi}_2\text{SeTe}_2$  and  $\text{Bi}_2\text{Te}_{2.5}\text{Se}_{0.5}$  for the one-step and two-step addition processes respectively.

For the first time seen in the literature,  $\text{Bi}_2\text{Te}_{2.5}\text{Se}_{0.5}$  nanowires were screen-printed to form a novel composite film with 5 % PVDF alongside  $\text{Bi}_2\text{Te}_3$  nanowires. The  $\text{Bi}_2\text{Te}_{2.5}\text{Se}_{0.5}$  nanowires were synthesised using the two-step addition process. Two sets of samples were printed one set with one printing pass and another with three printing passes. These screen-printed films were then annealed at 400 °C for 2 hr in an inert Ar atmosphere in a tube furnace. The films underwent microstructural analysis which revealed both  $\text{Bi}_2\text{Te}_{2.5}\text{Se}_{0.5}$  and  $\text{Bi}_2\text{Te}_3$  nanowires were nanorod-like in structure with average diameters of  $100 \pm 20$  nm.

The EDX spectrum showed the  $\text{Bi}_2\text{Te}_{2.5}\text{Se}_{0.5}$  film had atomic percentages of 40.9:52.9:6.7 between the Bi, Te and Se respectively. There was an increase in the Bi content for the post-annealed  $\text{Bi}_2\text{Te}_{2.5}\text{Se}_{0.5}$  films, however, this was within the uncertainty of the EDX detector. Using GIXRD the post-annealed  $\text{Bi}_2\text{Te}_{2.5}\text{Se}_{0.5}$  film was indexed to  $\text{Bi}_2\text{Te}_{2.5}\text{Se}_{0.5}$ . When the GIXRD spectra of both annealed screen-printed films were overlapped with one another, we observed peak shifts towards higher angles for the  $\text{Bi}_2\text{Te}_{2.5}\text{Se}_{0.5}$  film. This is in agreement with what was observed for the GIXRD spectra of the drop-casted nanowires. However, when the annealed screen-printed  $\text{Bi}_2\text{Te}_{2.5}\text{Se}_{0.5}$  film was compared to the drop-casted  $\text{Bi}_2\text{Te}_{2.5}\text{Se}_{0.5}$  film we observed peak shifts towards lower angles indicating that the crystal lattice had expanded. This is believed to be the result of Bi antisite defects on the Te and Se sites. This was based on the EDX data which showed an increased Bi content at the expense of the Te and Se content. Additionally, Bi has a larger atomic radius than Te or Se, with the occupation of Bi atoms on either Te or Se sites causing the expansion of the crystal lattice resulting in peak shifts towards lower angles.

The room temperature TE properties of the screen-printed films were measured using the portable S probe and the Hall probe. We observed a constant S of  $-140 \pm 10 \mu\text{VK}^{-1}$  for all films regardless of thickness and Se content. The only exception was for the case of  $\text{Bi}_2\text{Te}_3$  nanowires that formed INNs during the annealing process which had an S of  $-190 \pm 10 \mu\text{VK}^{-1}$  and a PF of  $130 \pm 40 \mu\text{Wm}^{-1}\text{K}^{-2}$ . The main differential was in the samples' electrical properties, as both 1 printing pass and 3 printing passes of  $\text{Bi}_2\text{Te}_3$  were higher than for the  $\text{Bi}_2\text{Te}_{2.5}\text{Se}_{0.5}$  resulting in lower PFs in the case of  $\text{Bi}_2\text{Te}_{2.5}\text{Se}_{0.5}$ . This is attributed to the lower carrier concentrations of the  $\text{Bi}_2\text{Te}_{2.5}\text{Se}_{0.5}$  films compared to the  $\text{Bi}_2\text{Te}_3$ . This has also been seen in the literature for bulk and nanostructured polyol synthesised  $\text{Bi}_2\text{Te}_{2.5}\text{Se}_{0.5}$  when compared to their non-Se alloyed counterpart<sup>[100,102,104]</sup>. These lower carrier concentrations have been associated with Bi antisite defects in the  $\text{Bi}_2\text{Te}_{2.5}\text{Se}_{0.5}$  crystal structure. In our results, these Bi antisite defects were identified by changes in the EDX and GIXRD data between the as-synthesised  $\text{Bi}_2\text{Te}_{2.5}\text{Se}_{0.5}$  nanowires and their annealed screen-printed counterparts. The Bi antisite defects formed on Te and Se sites, provide hole charge carriers to the  $\text{Bi}_2\text{Te}_{2.5}\text{Se}_{0.5}$  films which lower their overall n-type carrier concentration<sup>[100,104]</sup>.

The 1 printing pass annealed PVDF- $\text{Bi}_2\text{Te}_3$  and PVDF- $\text{Bi}_2\text{Te}_{2.5}\text{Se}_{0.5}$  films underwent a bending test of 1000 bending cycles at a bending radius of 10 mm. Both had increased resistances due to bending, with the resistance increasing by 3 % and 5 % for the PVDF- $\text{Bi}_2\text{Te}_{2.5}\text{Se}_{0.5}$  and PVDF- $\text{Bi}_2\text{Te}_3$  films respectively. These resistance increases are comparable with the literature for flexible printed  $\text{Bi}_2\text{Te}_3$ -based materials despite our smaller bending radius<sup>[53,64,75,105]</sup>. However, when comparing all the TE properties for both materials, as well as the extra work needed to alloy the nanowires, we believe it would be best to use 1 printing pass of  $\text{Bi}_2\text{Te}_3$  nanowire film for our n-type material in an FTEG device.

## Chapter 5 Screen-printed reflux synthesised Bismuth antimony telluride nanoplatelet films

Here we report the synthesis of PRS  $\text{Bi}_{0.4}\text{Sb}_{1.6}\text{Te}_3$  nanoplatelets and how they can be used to screen-print novel p-type composite films using an NMP-PVDF solvent-binder system. We also explore how to improve these screen-printed films' TE properties by incorporating Te nanorods as additives into the screen-printed films. Finally, a 3 thermocouple FTEG device on Kapton was fabricated using these films and our previously made n-type PVDF- $\text{Bi}_2\text{Te}_3$  printed composite films. We used this fabrication process to make the FTEG device as we have shown so far that it can produce TE films that can be used for flexible applications.

### 5.1 Characterisation analysis of drop-casted films polyol synthesised $\text{Bi}_{0.4}\text{Sb}_{1.6}\text{Te}_3$ nanoplatelets

#### 5.1.1 Material characterisation

The  $\text{Bi}_x\text{Sb}_{2-x}\text{Te}_3$  nanostructures synthesised using the method from section 2.12 were drop-casted onto Si substrates and examined using SEM, with images shown in Fig.5.1. The synthesis has been reproduced at least 3 times and a drop-casted film was fabricated for each synthesis to ensure the reproducibility of the PRS reaction. From the SEM images, the  $\text{Bi}_x\text{Sb}_{2-x}\text{Te}_3$  nanostructures were shown to have a nanoplatelet morphology with lengths between 100 nm and 350 nm as well as an average thickness of  $15 \pm 5$  nm. This was a quarter of the size of the average diameters of the  $\text{Bi}_2\text{Te}_3$  nanowires, as well as, more than half as thin as the average diameters of the  $\text{Bi}_2\text{Te}_{2.5}\text{Se}_{0.5}$  nanowires. The formation of 2D nanoplatelets in our reaction was due to the preference of the Sb atoms reacting with the Te nanowires in the EG system to form plate-like morphologies parallel to the *ab* plane of  $\text{Sb}_2\text{Te}_3$  nanocrystals [63].

The initial aim was to synthesise  $\text{Bi}_{0.5}\text{Sb}_{1.5}\text{Te}_3$  nanowires similar to Xu et al [36] and Chen et al [53]. However, this was not possible as the procedure developed in their reactions used a combination of hydrazine hydrate and anhydrous hydrazine as reducing agents [36,53]. Anhydrous hydrazine was used in synthesising  $\text{Bi}_{0.5}\text{Sb}_{1.5}\text{Te}_3$  nanowires as Yang et al [63] showed that the Sb ions ( $\text{Sb}^{3+}$ ) are difficult to reduce to elemental Sb using hydrazine hydrate in an EG system. To ensure the nanowire morphology the reaction durations must be kept as short as possible hence the use of aggressive reducing agents by Xu et al [36] and Chen et al [53].

However, the use of anhydrous hydrazine in our case was not possible, due to it being unavailable to be procured because of its extremely dangerous nature [58].

The chemical composition was measured by EDX for the drop-casted  $\text{Bi}_x\text{Sb}_{2-x}\text{Te}_3$  nanoplatelets and identified Bi, Sb and Te with average atomic percentages of 5:33:62 respectively. The atomic percentages correspond to an approximate alloy of composition  $\text{Bi}_{0.25}\text{Sb}_{1.65}\text{Te}_{3.1}$ . We observe a Bi deficiency compared to the molar concentration of the Bi precursor in the PRS reaction. From the molar concentration, we expected 10 % of the nanoplatelets to be made up of Bi, which is twice of what was observed in the EDX data. This is believed to be due to the competition between the Bi and Sb atoms interacting with the Te nanowires, similar to what was observed for the one-step addition process for  $\text{Bi}_2\text{Te}_{3-x}\text{Se}_x$  in section 4.111. The drop-casted nanoplatelets also had an average oxygen concentration of 30 % with respect to Bi, Sb and Te indicating the nanoplatelets were exposed to oxygen during the cleaning procedure.

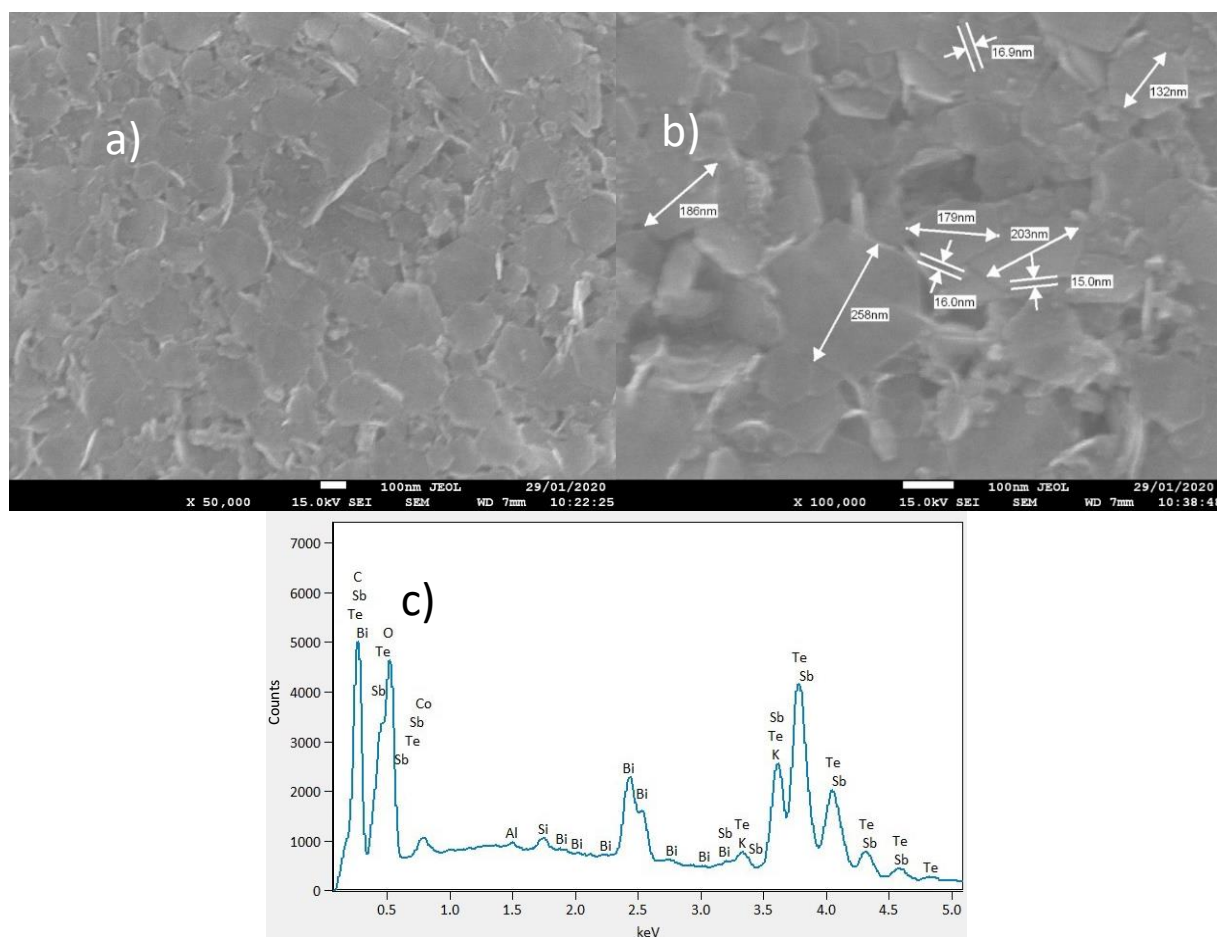


**Fig.5.1-** SEM images (a) of a top-down view of the drop-casted  $\text{Bi}_x\text{Sb}_{1-x}\text{Te}_3$  nanoplatelets on a Si substrate, with (b) showing the nanoplatelet's lengths and thicknesses. (c) EDX spectrum of the drop-casted nanoplatelets film.

The GIXRD data taken for the drop-casted nanoplatelets seen in Fig. 5.2 are indexed to the  $\text{Bi}_{0.4}\text{Sb}_{1.6}\text{Te}_3$  crystal structure. This is believed to be the result of the Bi deficiency observed in the EDX data. The most preferred crystal lattice orientation for the nanoplatelets was (0 1 5), which compares well with other synthesised  $\text{Bi}_x\text{Sb}_{2-x}\text{Te}_3$  nanoplatelets seen in the literature [62,106,107]. When we compared the GIXRD spectrum of the drop-casted  $\text{Bi}_{0.4}\text{Sb}_{1.6}\text{Te}_3$  nanoplatelets to the drop-casted  $\text{Bi}_2\text{Te}_3$  nanowires in Fig. 5.3 we observe noticeable shifts in the (0 1 5), (1 0 1 0) and (1 1 0) lattice orientations. We observe a shift from  $27.8^\circ$  to  $28.3^\circ$  for the (0 1 5) peak, a shift of  $38.1^\circ$  to  $38.7^\circ$  for the (1 0 1 0) peak and a shift from  $41.4^\circ$  to  $42.1^\circ$  for the (1 1 0) peak. These shifts to a higher angle would indicate a contraction in the crystal lattice, which is a result of the Bi sites being replaced with Sb atoms which have a smaller atomic radius. The significance of these shifts compared to the  $\text{Bi}_2\text{Te}_{3-x}\text{Se}_x$  nanowires in the previous chapter is due to a greater amount of replacement by the Sb as seen in the EDX data. Similar lattice orientation shifts toward higher angles have also been identified in the literature for  $\text{Bi}_x\text{Sb}_{2-x}\text{Te}_3$  nanoplatelets such as Zhang et al [62] who varied the Bi and Sb content to synthesise 8 different alloys of  $\text{Bi}_x\text{Sb}_{2-x}\text{Te}_3$  nanoplatelets.

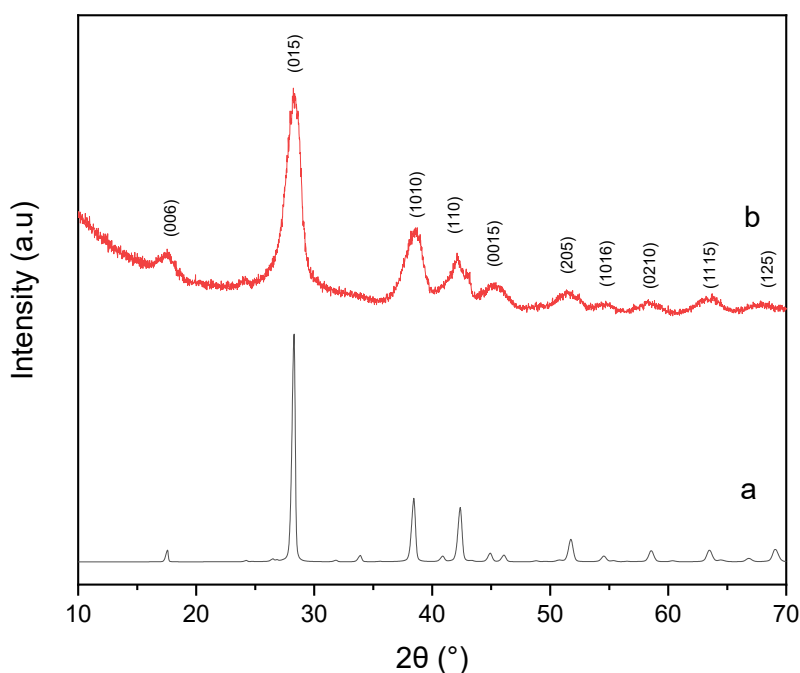


**Fig. 5.2-** GIXRD diffraction patterns obtained for (a) reference of Bismuth Antimony Telluride ( $\text{Bi}_{0.4}\text{Sb}_{1.6}\text{Te}_3$ ) mineral from ICDD database (PDF 01-072-1836) and (b) for the drop-casted film of  $\text{Bi}_{0.4}\text{Sb}_{1.6}\text{Te}_3$  nanoplatelets on a Si substrate.

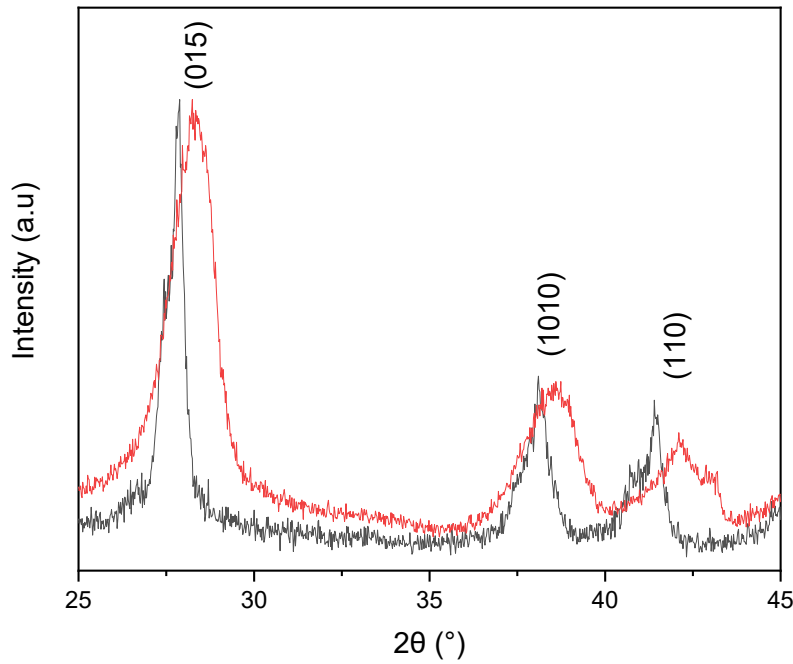


**Fig.5.3-** Comparison between the GIXRD diffraction patterns for the (black) drop-casted film of Bi<sub>2</sub>Te<sub>3</sub> nanowires and (red) for the drop-casted film of Bi<sub>0.4</sub>Sb<sub>1.6</sub>Te<sub>3</sub> nanoplatelets between 25 ° and 45 °.

**5.1.2 Thermoelectric analysis of drop-casted Bi<sub>0.4</sub>Sb<sub>1.6</sub>Te<sub>3</sub> nanoplatelet films**

The unannealed drop-casted Bi<sub>0.4</sub>Sb<sub>1.6</sub>Te<sub>3</sub> nanoplatelet films were conductive, unlike the unannealed drop-casted Bi<sub>2</sub>Te<sub>3</sub> nanowire films. As such room temperature S and Hall probe measurements were performed on the drop-casted films. The portable S probe showed the drop-casted films had a room temperature S of  $140 \pm 10 \mu\text{V K}^{-1}$ , which is within the range of uncertainty for the PRS Bi<sub>0.4</sub>Sb<sub>1.6</sub>Te<sub>3</sub> nanoplatelets synthesised by Zhang et al [62]. While the Hall probe showed an  $\sigma$  of  $8 \pm 2 \text{ S m}^{-1}$ , charge carrier mobility of  $5 \pm 1 \text{ cm}^2\text{V}^{-1}\text{s}^{-1}$  and a charge carrier concentration of  $2.8 \pm 0.7 \times 10^{18}$ . The positive S and carrier concentration show that the nanoplatelets have a p-type semiconductor behaviour. However, due to the low  $\sigma$  we observe PFs  $< 1 \mu\text{Wm}^{-1}\text{K}^{-2}$ . This is a result of the films containing individual particles that cause the charge carriers to scatter between particle boundaries. This lowers the films’ charge carrier mobility and overall  $\sigma$ . Additionally, the density of the drop-casted films is rather low with the films only being bound together by surface tension further reducing carrier mobility.

## 5.2 Characterisation analysis of Screen-printed PVDF-Bi<sub>0.4</sub>Sb<sub>1.6</sub>Te<sub>3</sub> nanoplatelets composite films

### 5.2.1 Characterisation analysis of scaled-up polyol synthesised Bi<sub>0.4</sub>Sb<sub>1.6</sub>Te<sub>3</sub> nanoplatelets

The PRS reaction was scaled up by a factor of 5 to increase the resulting product from 0.6 g to 3 g of Bi<sub>0.4</sub>Sb<sub>1.6</sub>Te<sub>3</sub> nanoplatelets. This was done to examine the scalability of this PRS reaction and observe any changes to the end product. Additionally, to screen-print these Bi<sub>0.4</sub>Sb<sub>1.6</sub>Te<sub>3</sub> nanoplatelets a higher mass quantity of them was needed to formulate enough paste for more than one print. The nanoplatelets were drop-casted onto Si and were examined by SEM as seen in Fig. 5.4. The synthesis has been reproduced at least 3 times and a drop-casted film was fabricated for each synthesis to ensure the reproducibility of the PRS reaction. The nanoplatelets were observed via SEM to have dimensions between 90 nm and 650 nm in length and thickness of 15 ± 5 nm. The main difference with the scaled-up nanoplatelets is a greater variation in their lengths as opposed to the previous synthesis with lengths ranging from 100 nm to 350 nm.

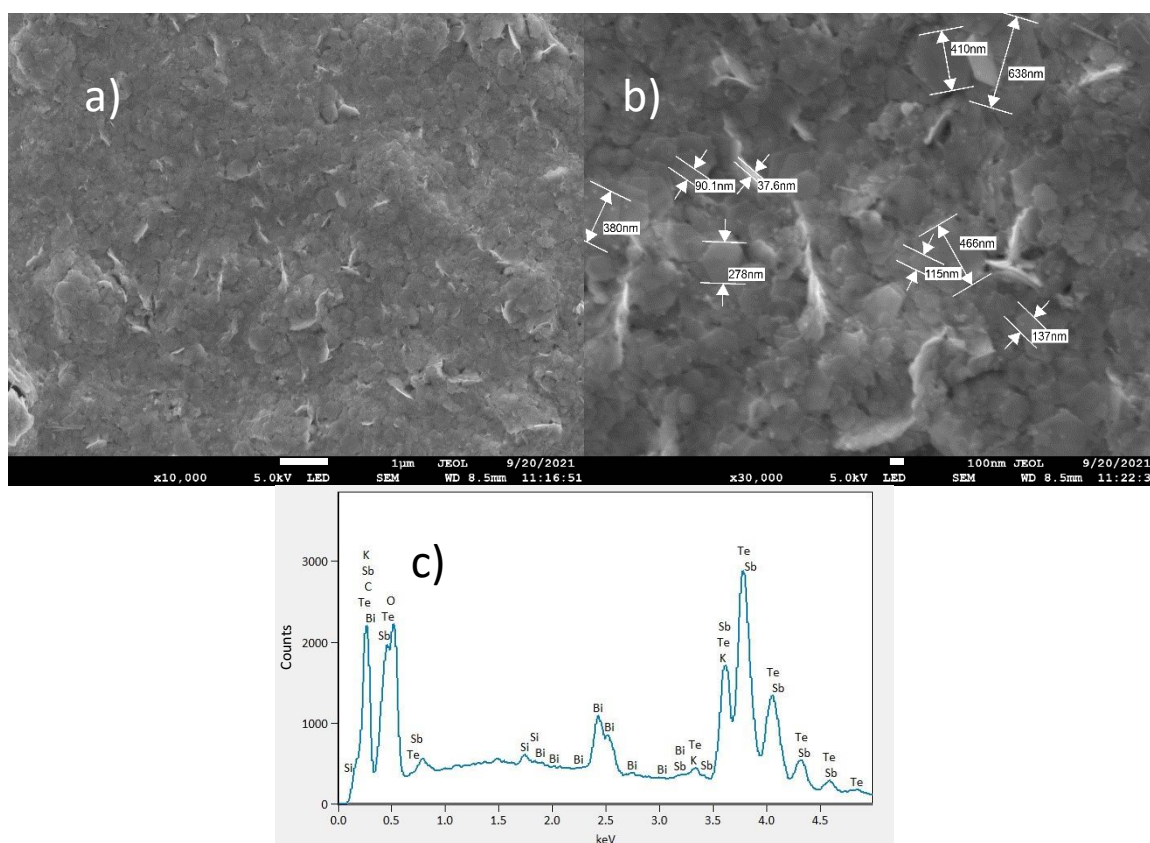


**Fig. 5.4-** SEM images (a) of a top-down view of scaled-up PRS Bi<sub>0.4</sub>Sb<sub>1.6</sub>Te<sub>3</sub> nanoplatelets on a Si substrate, with (b) showing the nanoplatelet's lengths and thicknesses. While (c) an EDX spectrum of the drop-casted PRS Bi<sub>0.4</sub>Sb<sub>1.6</sub>Te<sub>3</sub> nanoplatelets film.

We observed no changes in the nanoplatelets' atomic percentages, as the EDX spectrum showed atomic percentages of 5:33:62 for Bi, Sb and Te respectively. While oxygen content in the drop-casted films was 28 %, which is within the EDX detector error of 2 % when compared to the oxygen content of the nanoplatelets synthesised in section 5.1. This indicates that the scaled-up PRS reaction was able to successfully reduce the chemical precursors. The GIXRD data taken for the drop-casted nanoplatelets indexed them to  $\text{Bi}_{0.4}\text{Sb}_{1.6}\text{Te}_3$ , as seen in Fig. 5.5. This matches what was observed in the previous GIXRD spectrum in Fig. 5.2. Just as before we still observe (0 1 5) as the most preferred crystal lattice orientation for the nanoplatelets. From this, we observe the flexibility of the PRS process in scaling up the product masses with little change in the product in the case of  $\text{Bi}_{0.4}\text{Sb}_{1.6}\text{Te}_3$  nanoplatelets, based on the data presented in the SEM, EDX and GIXRD.

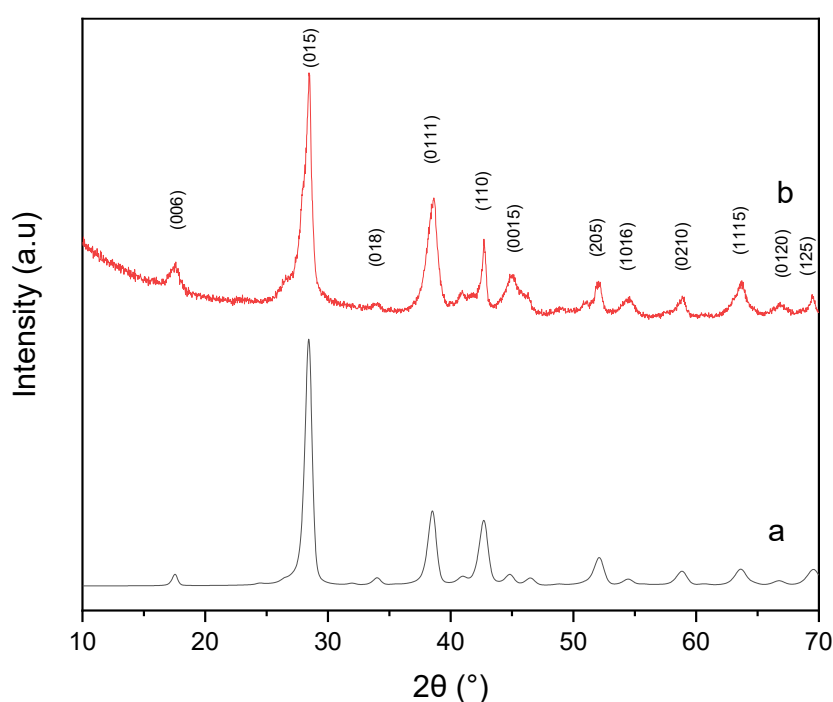


**Fig. 5.5-** GIXRD diffraction patterns obtained for (a) reference of Bismuth Antimony Telluride ( $\text{Bi}_{0.4}\text{Sb}_{1.6}\text{Te}_3$ ) mineral from ICDD database (PDF 01-072-1836) and (b) for the drop-casted film of scaled-up PRS  $\text{Bi}_{0.4}\text{Sb}_{1.6}\text{Te}_3$  nanoplatelets on a Si substrate.

The drop-casted films had their room temperature  $S$  measured using the portable  $S$  probe which showed an  $S$  of  $140 \pm 10 \mu\text{V K}^{-1}$  just as in the nanoplatelets in section 5.1, however, similar high resistance of the film as discussed in section 5.12 resulted in poor PF.

### 5.2.2 Screen-printed PVDF-Bi<sub>0.4</sub>Sb<sub>1.6</sub>Te<sub>3</sub> nanoplatelet films

The NMP-PVDF paste system was used to screen-print the Bi<sub>0.4</sub>Sb<sub>1.6</sub>Te<sub>3</sub> nanoplatelets, based on the ease of the paste formulation. Furthermore, the paste system has proven to reproducibly screen-print flexible Bi<sub>2</sub>Te<sub>3</sub> and Bi<sub>2</sub>Te<sub>2.5</sub>Se<sub>0.5</sub> nanowire films as shown by the bending tests in sections 3.23 and 4.23 respectively. Additionally, the same formulation process and paste system would simplify the FTEG fabrication process. Using the paste formulation from section 2.22 a PVDF-Bi<sub>0.4</sub>Sb<sub>1.6</sub>Te<sub>3</sub> nanoplatelets paste was developed with 5 % PVDF and screen-printed onto Kapton as shown in Fig. 5.6. Two films of 5 x 50 mm were printed with 1 printing pass and another with 4 printing passes. There was a drying step in a vacuum oven at 70 °C for 5 mins between each printing pass.

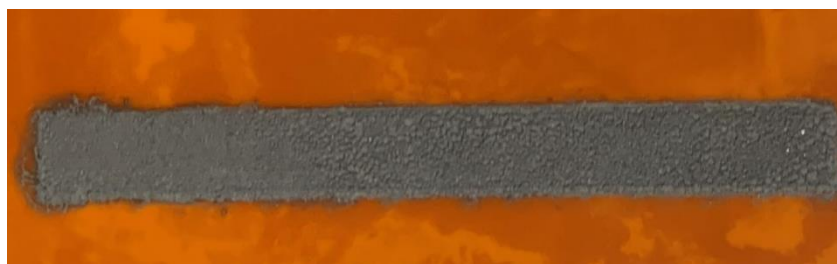


**Fig. 5.6-** Image of 5 x 50 mm PVDF-Bi<sub>0.4</sub>Sb<sub>1.6</sub>Te<sub>3</sub> nanoplatelet film for 4 printing pass.

During the characterisation of the pre-annealed films, it was noticed that the oxygen content had increased from 28 % to 45 %. This could result in lower TE performance of the post-annealed screen-printed films. It was believed this happened during bath sonication when the nanoplatelets were dispersing in NMP. The samples were annealed at 450 °C for 10 mins in an inert Ar atmosphere. This was done based on the results of Chen et al <sup>[53]</sup> who showed that these annealing conditions could result in higher TE properties for Bi<sub>0.5</sub>Sb<sub>1.5</sub>Te<sub>3</sub> nanowires, as opposed to using the 400 °C for 2 hr which had resulted in films with poor  $\sigma$ . The room temperature TE data is shown in Table 5.1.

**Table 5.1-** The TE properties of annealed PVDF-Bi<sub>0.4</sub>Sb<sub>1.6</sub>Te<sub>3</sub> nanoplatelets films on Kapton at room temperature. The Seebeck coefficient was taken with the portable Seebeck probe. The results are an average of multiple measurements with the error being the standard deviation of the average.

Printing pass	Film Thickness ( $\mu\text{m}$ )	Mobility ( $\text{cm}^2/\text{V}\cdot\text{s}$ )	Carrier concentration ( $\times 10^{19} \text{ cm}^{-3}$ )	Electrical conductivity (S/m)	Seebeck coefficient ( $\mu\text{V}/\text{K}$ )	Power factor ( $\mu\text{Wm}^{-1}\text{K}^{-2}$ )
1	$12 \pm 1$	$0.9 \pm 0.6$	$2 \pm 1$	$179.7 \pm 0.3$	$90 \pm 5$	$1.46 \pm 0.08$
4	$22 \pm 3$	$1 \pm 1$	$4 \pm 2$	$500 \pm 10$	$100 \pm 5$	$5.0 \pm 0.3$

We observe a higher PF for the thicker film as the extra printed layers would increase the coverage of the film and fill voids and pores left from the previous prints. We observe this when analysing these films with SEM seen in Fig.5.7. These films were also annealed at 400 °C for 2 hr in an inert Ar atmosphere where we observed poor PF  $< 1 \mu\text{Wm}^{-1}\text{K}^{-2}$  due to low  $\sigma$ , however, we still observed a greater PF for the thicker film compared to its thinner counterpart.

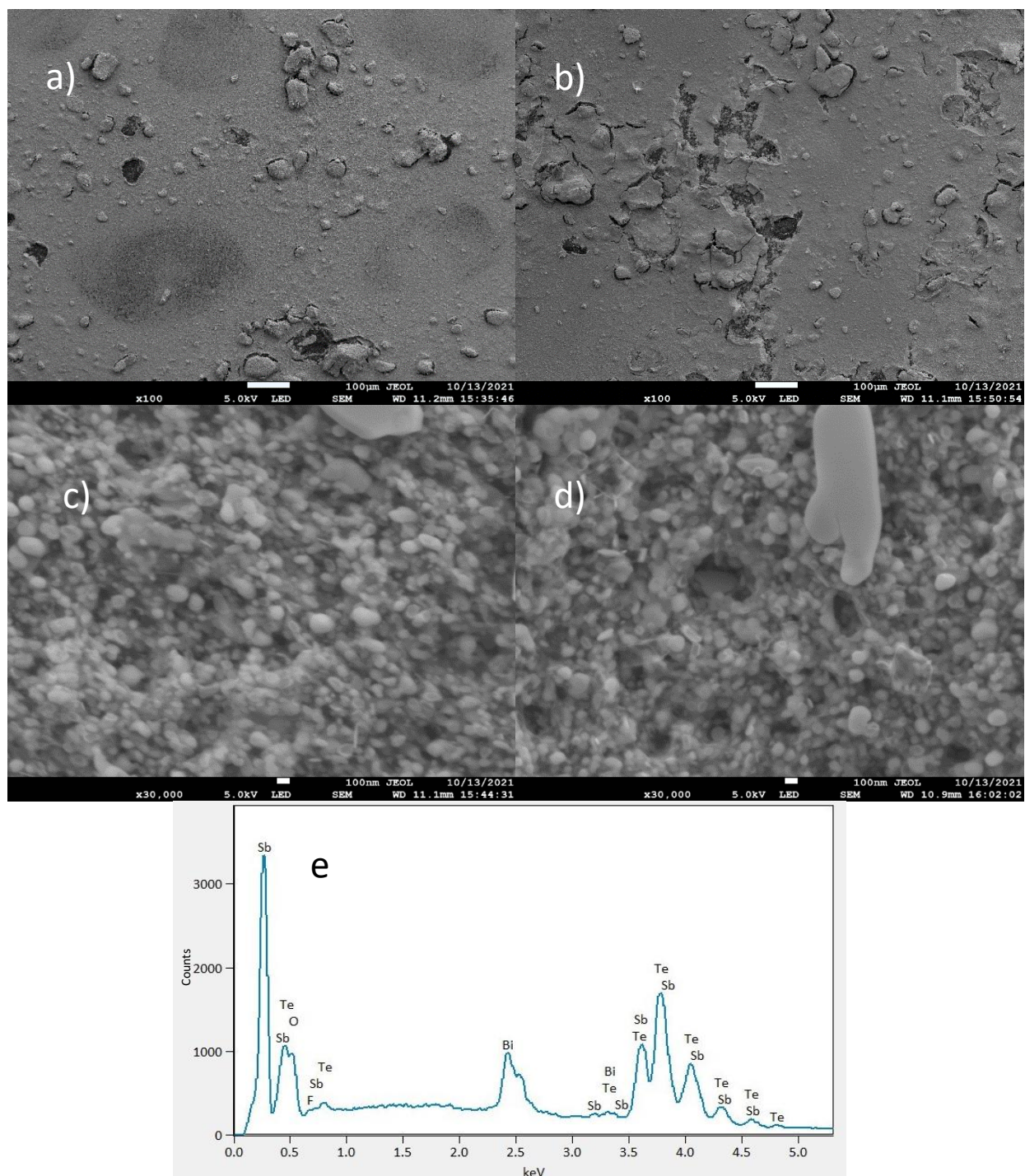


**Fig. 5.7-** SEM images of annealed PVDF-Bi<sub>0.4</sub>Sb<sub>1.6</sub>Te<sub>3</sub> nanoplatelet films at (a&b) low and (c&d) high magnifications. While (e) the EDX spectrum for an annealed PVDF-Bi<sub>0.4</sub>Sb<sub>1.6</sub>Te<sub>3</sub> nanoplatelet film of 1 printed pass.

From Fig 5.7a we observe regions of poor film coverage compared to Fig.5.7b which goes to explain the disparity in  $\sigma$  between the 1 printing pass and 4 printing passes screen-printed films. However, both films have poor PFs when compared to their  $\text{Bi}_2\text{Te}_3$  counterpart ( $37 \pm 8 \mu\text{Wm}^{-1}\text{K}^{-2}$  at room temperature), first from their low  $\sigma$  due to low mobility caused by junction resistance between the nanoparticles seen in Fig 5.7(c&d), and also their S which is lower than the drop-casted unannealed nanoplatelets. The post-annealing EDX spectra for both films showed similar ratios for the Bi, Sb and Te as before within the 2 % error of the EDX detector. The oxygen content was reduced from 45 % to 18 % and 12 % for the films fabricated from 1 printing pass and 4 printing passes respectively. Despite the oxygen content reduction during annealing, the damage from the paste formulation had already been done as shown with the poor PFs. When comparing the fluorine content before and after annealing, both films show a drop from  $\sim 28$  % to  $\sim 5$  % with respect to Bi, Sb and Te. However, we still observe some fluorine in the films revealing signs of residue PVDF which could also explain the low  $\sigma$ . Based on this data a longer annealing duration is needed, as such, we increased the duration from 10 mins to 1 hr.

To investigate whether the oxidation of the nanoplatelets was the result of them being dispersed in NMP by bath sonication, two dispersions of nanoplatelets were formulated using NMP and ethanol. These dispersions were drop-casted after 2 hr of bath sonication with the resulting films' oxygen content examined using EDX. We observed an oxygen content of  $\sim 45$  % for the NMP dispersion compared to the ethanol dispersion which had  $\sim 26$  %. This process was repeated for 3 synthesised batches of nanoplatelets with the same result within the 2 % error of the EDX detector. When the same dispersions were bath sonicated in an ice bath condition for the duration of sonication, the oxygen content for the NMP dispersed nanoplatelets was  $\sim 32$  % compared to the ethanol dispersed nanoplatelets which had  $\sim 27$  %. Repeated dispersions showed similar results indicating that temperature plays a role in the oxidation process of the nanoplatelets. It is believed that the increase in temperatures during bath sonication causes the NMP solvent to facilitate the interaction between oxygen atoms in the dispersion with the Sb atoms in the nanoplatelets. As there were no such oxygen increases seen with the  $\text{Bi}_2\text{Te}_3$  and  $\text{Bi}_2\text{Te}_{2.5}\text{Se}_{0.5}$  nanowires during the paste formulation process. Furthermore, due to the lack of literature on the topic more research should be placed to understand the specific chemical mechanisms for this oxidation process. To counter this oxidation two paths were devised, one route was to replace the NMP with DMSO which is another compatible solvent for PVDF seen in Appendix C. However, films printed with DMSO had poor adhesion at the current binder content while higher binder concentrations would reduce TE performance. Alternatively, we could limit the oxidation effect by sonicating in an ice bath and reducing the time between synthesis and printing.

### 5.3 Tellurium nanorod additive study

So far  $\text{Bi}_{0.4}\text{Sb}_{1.6}\text{Te}_3$  nanoplatelets have had a lower TE performance compared to the n-type  $\text{Bi}_2\text{Te}_3$  nanowires. To improve our screen-printable p-type composites' TE performance, we incorporated Te nanorods in the screen-printed PVDF- $\text{Bi}_{0.4}\text{Sb}_{1.6}\text{Te}_3$  nanoplatelet films. It has been observed in the literature that Te nanoparticles can act as TE performance-enhancing additives for other  $\text{Bi}_x\text{Sb}_{2-x}\text{Te}_3$  alloys [81,108,109]. Te nanorods were chosen as the additive for the ease and simplicity of their synthesis and their high S seen in the literature ( $S > 250 \mu\text{V K}^{-1}$ ) [67–70], which if incorporated into the screen-printed films could improve their TE performance via improvements in S.

#### 5.3.1 Characterisation analysis of drop-casted Tellurium nanorods

Te nanorods were synthesised using the process as described in section 2.13 and drop-casted onto Si substrate for microstructural analysis by SEM, EDX and GIXRD. The synthesis has been reproduced at least 3 times and a drop-casted film was fabricated for each synthesis to ensure the reproducibility of the PRS reaction. We observe in Fig. 5.8, 1D Te nanorods ranging in diameter from  $\sim 100$  nm to 200 nm with lengths between a few hundred nm and a few  $\mu\text{m}$ . Despite the lack of a growth directing agent in the PRS reaction, the formation of nanorods shows the 1D preferential growth of Te in the EG system as a result of Te's anisotropic crystal structure as stated by Yang et al [63]. The lack of uniformity in the dimensions of the nanorods is due to a lack of PVP in the PRS reaction. No PVP was used in the PRS to reduce the oxygen exposure to the Te nanorods while they precipitate out of the reaction mixture. Without a surfactant, the nanorods precipitate out of the reaction mixture without the aid of centrifugation. As such the nanorods can be retrieved from the reaction mixture in a dry nitrogen glovebox thus reducing their oxygen exposure.

The EDX spectrum in Fig.5.8 only revealed the presence of Te and oxygen showing that the nanorods had been completely washed off the chemicals used in the PRS. The EDX data for the drop-casted Te nanorod films showed an 80:20 split in the atomic percentages between the Te and oxygen content respectively. This would indicate that the nanorods were still exposed to oxygen despite them precipitating out of the reaction mixture in a dry nitrogen glovebox. GIXRD was also performed on the drop-casted Te nanorod film with the data, seen in Fig.5.9. The nanorods were indexed to Te with a polycrystalline structure which had a preferred lattice orientation at the (1 0 1) phase.

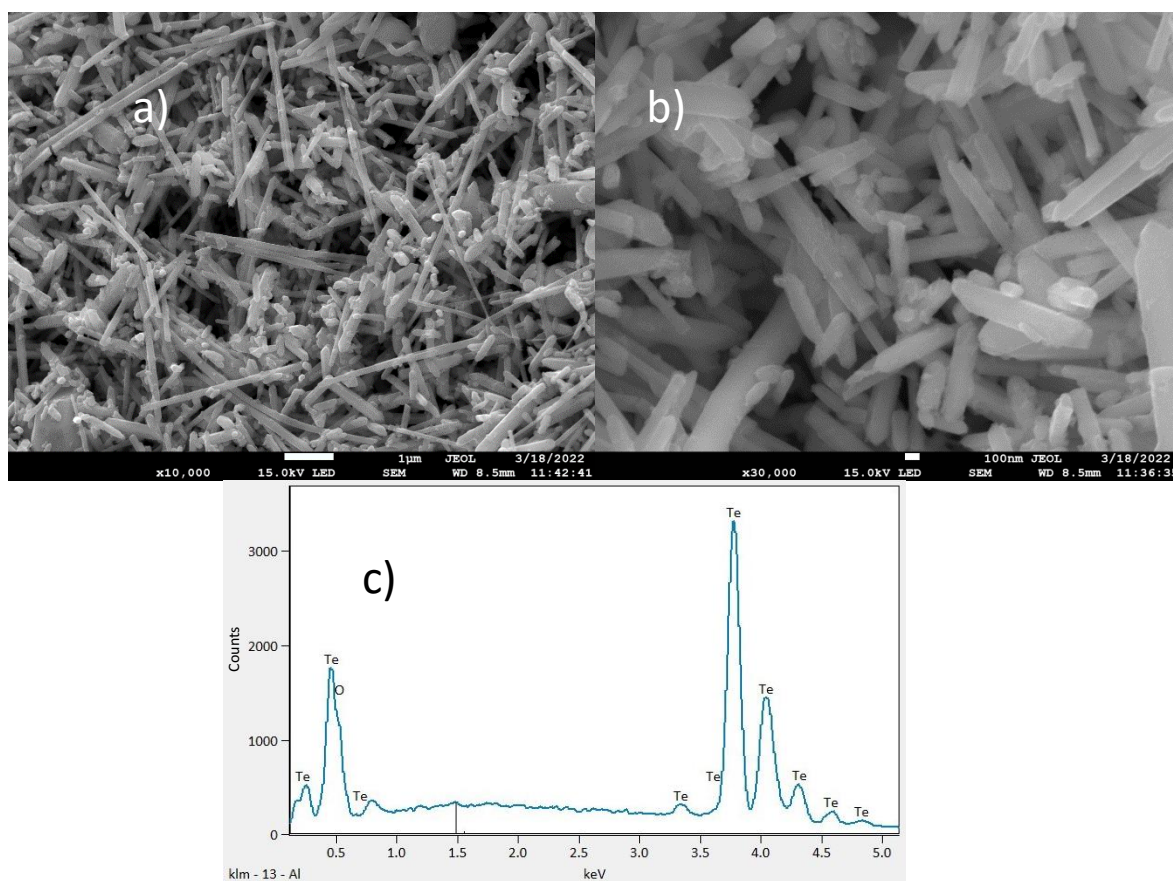


**Fig.5.8-** SEM images (a&b) of a top-down view of PRS Te nanorods on a Si substrate. While (c) an EDX spectrum of the drop-casted PRS Te nanorods film.

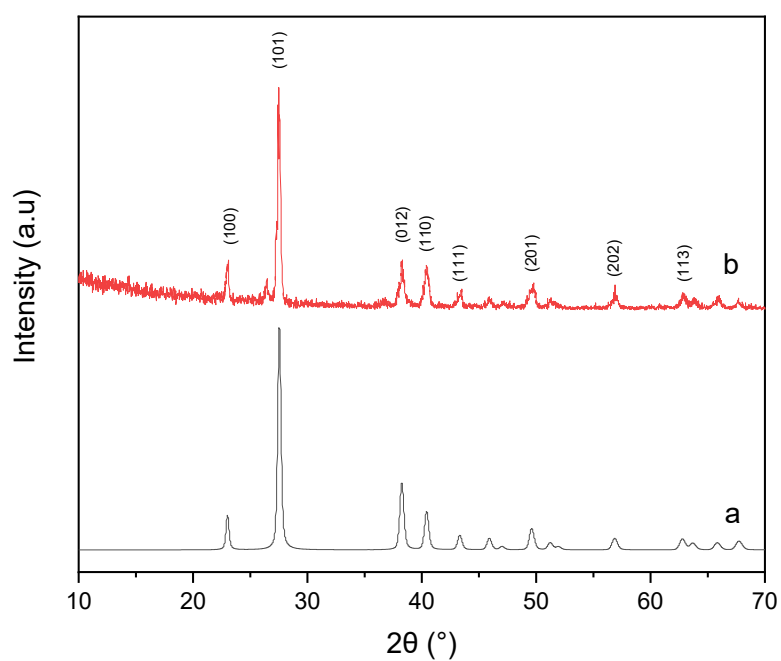


**Fig. 5.9-** GIXRD diffraction patterns obtained for (a) reference of Tellurium (Te) mineral from ICDD database (PDF 00-086-2268) and (b) for the drop-casted film of PRS Te nanorods on a Si substrate.

The drop-casted films had a low enough resistance ( $<50 \text{ K}\Omega$ ) where stable  $S$  measurements could be obtained. The drop-casted films had their room temperature  $S$  measured using the portable  $S$  probe shown in section 2.4.11 which showed an  $S$  of  $440 \pm 30 \mu\text{V K}^{-1}$ , which is in good agreement with the literature <sup>[67,68]</sup>. The samples' thickness was too non-uniform to obtain accurate Hall probe data, with the film thickness varying by  $\sim 50 \mu\text{m}$ . However, due to the high  $S$  and low relative resistance compared to the other TE nanomaterials studied in this project, it was believed that the Te nanorods could be a potential candidate for a screen-printable flexible p-type TE material.

### 5.3.2 Characterisation analysis of screen-printed Tellurium nanorods

A Te nanorod paste was formulated as described in section 2.22 with a 5 % PVDF binder. Two films were screen-printed onto Kapton, with a print gap of 0.4 mm. One film had two printing passes while the other had 4, with each print pass drying in a vacuum oven at  $70 \text{ }^\circ\text{C}$  for 5 mins seen in Fig. 5.10.

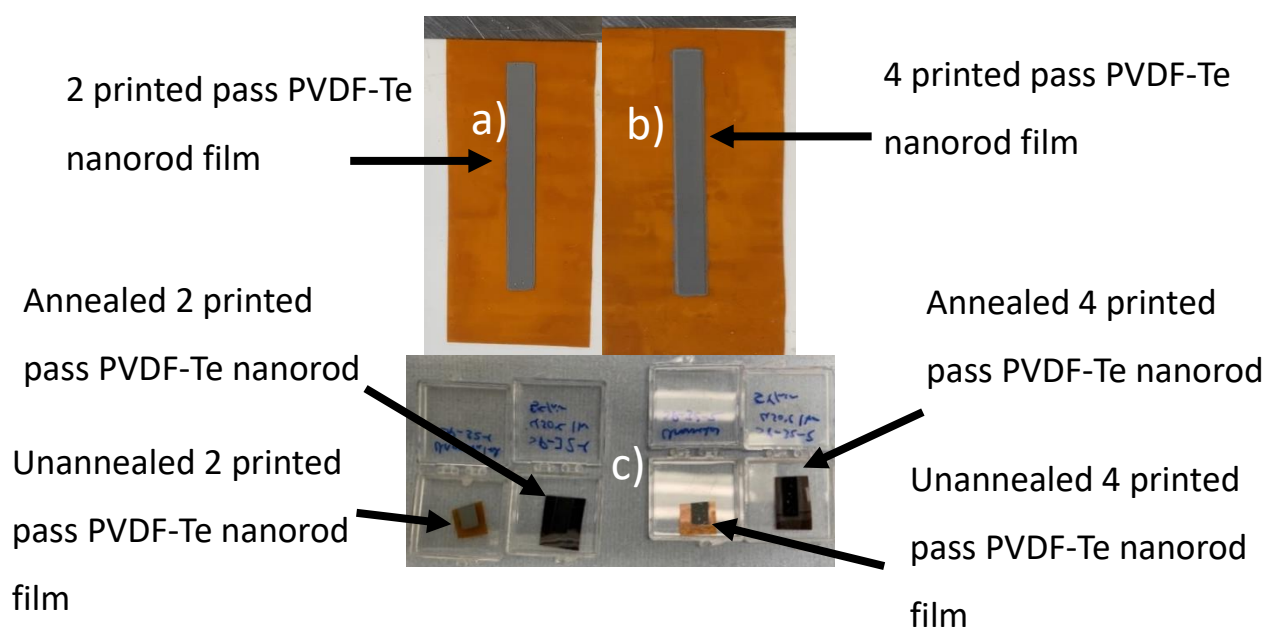


**Fig. 5.10-** Images of the (a) 2 and (b) 4 printed pass PVDF-Te nanorod films. While (c) shows the films before and after annealing at  $450 \text{ }^\circ\text{C}$  for 1 hr in an Ar inert atmosphere.

The films were measured with a surface profiler and had thicknesses of  $16 \pm 4 \mu\text{m}$  and  $55 \pm 2 \mu\text{m}$  for the 2 and 4 printing passes respectively. A section of the films was cut and annealed at the annealing conditions that the PVDF-Bi<sub>0.4</sub>Sb<sub>1.6</sub>Te<sub>3</sub> films would undergo at  $450 \text{ }^\circ\text{C}$  for 1 hr in an inert Ar atmosphere. However, the post-annealed films had resistances of  $\sim 10 \text{ M}\Omega$ , indicating the nanorods had been over-annealed. However, it was believed that the Te nanorods at low contents between 0 % and 20 % could still act as an additive to improve the overall TE performance of the screen-printed PVDF-Bi<sub>0.4</sub>Sb<sub>1.6</sub>Te<sub>3</sub>-Te films.

This was because at these low concentrations the increase in  $S$  due to the nanorods could offset the increase in film resistance. The unannealed PVDF-Te nanorod films were measured to obtain their TE properties at room temperature using the portable  $S$  probe and Hall probe, as seen in Table 5.2.

**Table 5.2-** The TE properties of annealed PVDF-Te nanorod films on Kapton at room temperature.

The Seebeck coefficient was taken with the portable  $S$  probe, while the electrical properties were measured with a Hall probe. The results are an average of multiple measurements with the error being the standard deviation of the average.

Printing passes	Film Thickness ( $\mu\text{m}$ )	Mobility ( $\text{cm}^2/\text{V s}$ )	Carrier concentration ( $\text{cm}^{-3}$ )	Electrical conductivity ( $\text{S m}^{-1}$ )	Seebeck coefficient ( $\mu\text{V K}^{-1}$ )	Power factor ( $\mu\text{Wm}^{-1}\text{K}^{-2}$ )
2	$16 \pm 4$	$2.7 \pm 0.5$	$3 \pm 1 \times 10^{17}$	$15 \pm 4$	$430 \pm 30$	$2.7 \pm 0.7$
4	$55 \pm 2$	$2 \pm 2$	$4 \pm 3 \times 10^{17}$	$7.1 \pm 0.3$	$440 \pm 30$	$1.4 \pm 0.3$

The data in Table 5.2 are in good agreement with the literature showcasing that despite the PVDF the screen-printed films can still act as a flexible TE material [68–70]. The high  $S$  seen confirms our belief that the Te nanorods could be used to improve the TE performance of the PVDF- $\text{Bi}_{0.4}\text{Sb}_{1.6}\text{Te}_3$  films via the enhancement of  $S$ . The PVDF-Te nanorod films were further investigated in Chapter 6 to see if the films could be integrated into fabrics to form E-textile compatible single-leg FTEGs.

### 5.3.3 Characterisation of screen-printed PVDF- $\text{Bi}_{0.4}\text{Sb}_{1.6}\text{Te}_3$ -Te films

Once the Te nanorods were characterised they were mixed into powders of  $\text{Bi}_{0.4}\text{Sb}_{1.6}\text{Te}_3$  nanoplatelets with the weight of the Te nanorods varying between 0 % and 20 % of the final weight of the screen-printable paste (excluding the NMP). Six pastes were formulated using the method described in section 2.22, using a 5 % PVDF binder concentration and containing Te nanorods that constitute 0 %, 4 %, 8 %, 12 %, 16 % and 20 % of the screen-printed films. The Te nanorod content was varied in steps of 4 % as both Madan et al [108] and Varghese et al [81] had shown that a Te nanoparticle content of 8 % in their  $\text{Bi}_{0.5}\text{Sb}_{1.5}\text{Te}_3$  and  $\text{Bi}_{0.4}\text{Sb}_{1.6}\text{Te}_3$  printed films respectively, achieved the highest improvement in TE performance. The results on how Te nanorod content can affect the screen-printed 5 % PVDF- $\text{Bi}_{0.4}\text{Sb}_{1.6}\text{Te}_3$  nanoplatelet composite films' TE properties are discussed below. These results are based on 3 runs of synthesising the nanomaterials, formulating the pastes and screen-printing the films to ensure the reproducibility of the results discussed below.

### 5.3.3.1 Material characterisation

The pastes were screen-printed onto Kapton with a print gap of 0.4 mm for a total of 4 printing passes. For each printed pass the wet deposit was dried in a vacuum oven at 70 °C for 5 mins. An example of the films is shown in Fig. 5.11 which shows the films containing 0 % and 8 % Te nanorods.

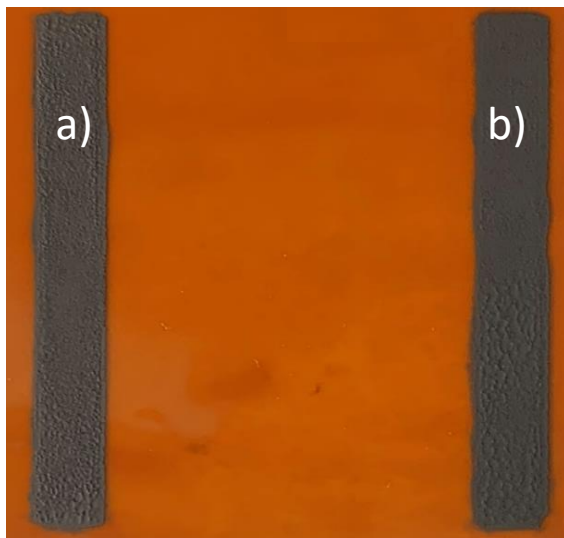


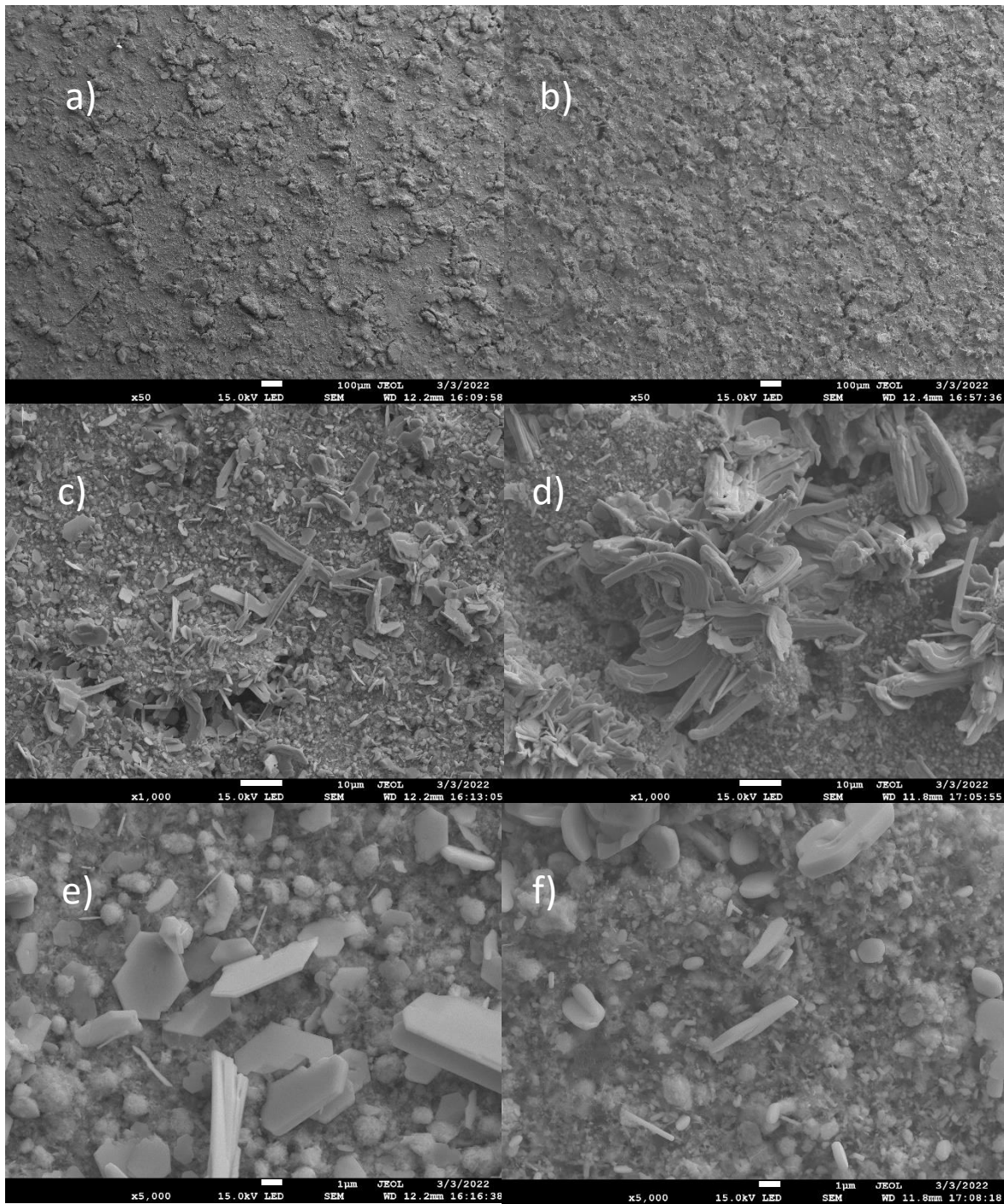
**Fig. 5.11-** Image of (a) PVDF-Bi<sub>0.4</sub>Sb<sub>1.6</sub>Te<sub>3</sub> nanoplatelets and (b) PVDF-Bi<sub>0.4</sub>Sb<sub>1.6</sub>Te<sub>3</sub> + 8 % Te.

After drying the films, they were measured with a surface profiler to obtain their thicknesses shown in Table 5.3. The films were cut into small strips of 15 x 5 mm and annealed at 450 °C for 1 hr in an inert Ar atmosphere. The resulting annealed films underwent microstructural analysis via SEM, EDX and GIXRD.

**Table 5.3-** The average thickness measurements for the PVDF-Bi<sub>0.4</sub>Sb<sub>1.6</sub>Te<sub>3</sub> nanoplatelets + Te nanorod films.

Percentage of Te nanorods in the film (%)	Film thickness (μm)
0	22 ± 3
4	32 ± 7
8	17 ± 7
12	35 ± 4
16	19 ± 7
20	27 ± 3

The nanorods were observed throughout all the screen-printed films before they were annealed with example SEM images shown in Appendix D. When viewing the post-annealed screen-printed films under low magnification they all appeared to have cracks as shown in Fig 5.12(a&b), resulting from heat-induced damage to the films during annealing. From the SEM images, we observe 3 types of morphologies irrespective of Te nanorod concentration in the screen-printed films. Initially, we observe cauliflower-like microstructures on the order of  $>10\ \mu\text{m}$  in size as shown in Fig 5.12(c&d). At higher magnifications, we observe the second type of smaller microstructures consisting of enlarged microplatelets  $<10\ \mu\text{m}$  in size seen in Fig 5.12(e&f). The third observed morphology was amorphous nanoparticles ranging between  $\sim 50\ \text{nm}$  to  $500\ \text{nm}$  in length which is believed to be the result of the nanoplatelets under annealing. These nanoparticles appear to agglomerate into clusters and are believed to be the first step in these nanoparticles merging to form microplatelets which seem to in turn coalesce into the larger cauliflower microstructures. The microplatelets and amorphous nanoparticles have been observed in the previous screen-printed films annealed at  $450\ ^\circ\text{C}$  for 10 mins seen in Fig 5.7, as such, we believe that the longer annealing durations allowed them to form these cauliflower microstructures. Further increases in the annealing duration are believed to lead to higher numbers of cauliflower microstructures, however, this may also result in further cracking of the films as seen in 5.12(a&b). Additionally, there is a potential for the films to become over-annealed as what was seen for the PVDF-Te nanorod films resulting in high film resistances. No Te nanorods were observed in the post-annealed screen-printed films. The lack of Te nanorods is believed to be a result of them merging with the  $\text{Bi}_{0.4}\text{Sb}_{1.6}\text{Te}_3$  microstructures as the melting point of bulk Te is  $445\ ^\circ\text{C}$  <sup>[110]</sup>.



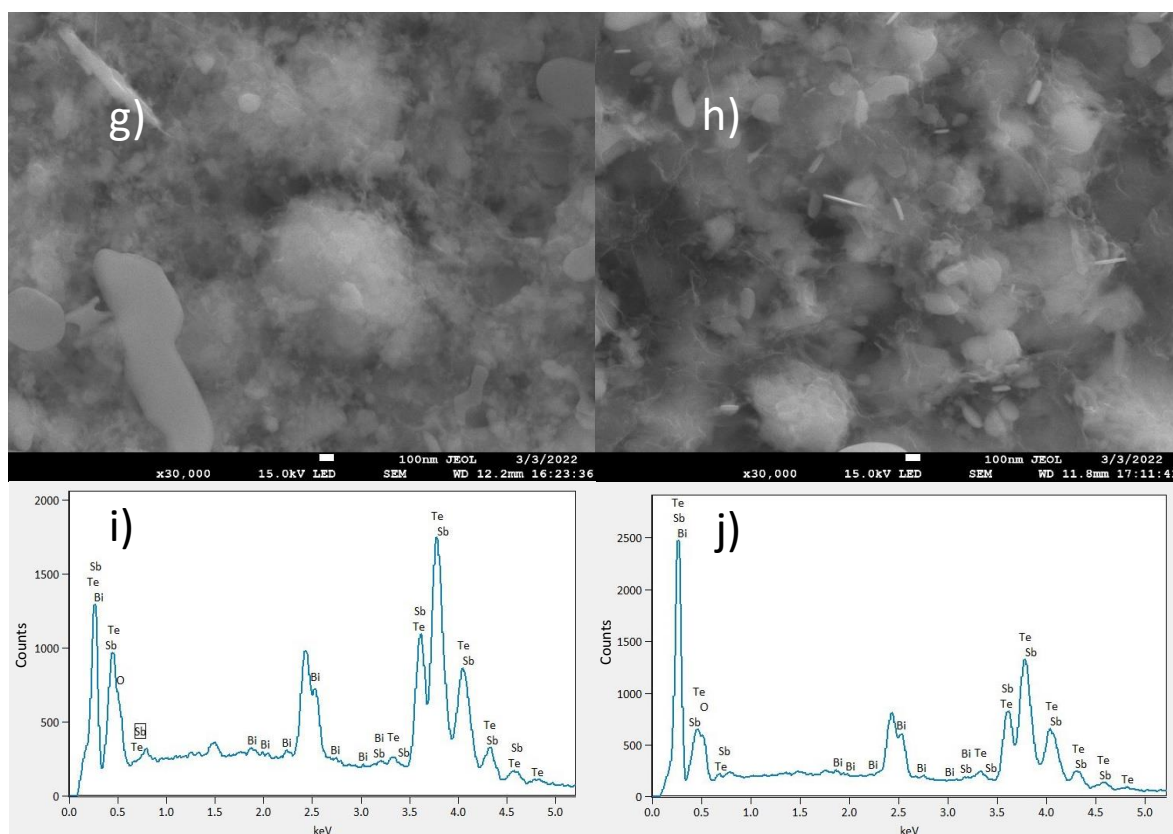


**Fig.5.12-** SEM images of PVDF-Bi<sub>0.4</sub>Sb<sub>1.6</sub>Te<sub>3</sub> nanorod film with 0 % (a,c,e & g) and 12 % (b,d,f & h) Te nanorods films annealed at 450 °C for 1 hr in an inert Ar atmosphere. While (i) the EDX spectrum for an annealed PVDF-Bi<sub>0.4</sub>Sb<sub>1.6</sub>Te<sub>3</sub> nanorod film with 0 % Te nanorods and (j) the EDX spectrum for the film with 12 % Te nanorods.

The EDX spectra for all annealed films revealed close to stoichiometric atomic percentages for Bi<sub>0.4</sub>Sb<sub>1.6</sub>Te<sub>3</sub> within the 2 % error of the EDX detector regardless of the Te nanorod content of the films. The only significant trend was a slight increase in Bi and a decrease in Te while Sb remained fairly consistent. The atomic percentages for Bi, Sb and Te were 7.68:32.6:59.88 and 9.98:32.275:58.7 for the 0 % and 20 % Te nanorod films respectively. This suggests that the Te nanorods were not only melted into the Bi<sub>0.4</sub>Sb<sub>1.6</sub>Te<sub>3</sub> microstructures but that excess Te in those microstructures was being burned off the films, due to the annealing temperature being higher than the melting point of bulk Te is 445 °C [81,110]. The oxygen content across the films ranged between 10 % and 15 % indicating that the Te nanorod content had little to no effect on the oxidation of the films. Additionally, there were no detectable fluorine signals for any of the post-annealed films, which comes down to the higher annealing duration used compared to the films in section 5.22.

The GIXRD spectra were measured for all the screen-printed films seen in Fig. 5.13. For the 0 %, 4 %, 8 % and 12 % Te nanorod films their GIXRD spectra observed a matching for the ICDD file for  $\text{Bi}_{0.4}\text{Sb}_{1.6}\text{Te}_3$  as was seen for the drop-casted nanoplatelets in Fig.5.5. We observe similar spectrums with the (0 1 5) lattice orientation being the most prominent for the films. However, shifts in the peak position were observed towards lower angles for the 4 %, 8 % and most notably for the 12 % films compared to the 0 % film seen in Fig. 5.14. For the 12 % film, the most notable shift was for the lattice orientation (0 1 5) from  $28.36^\circ$  in the 0 % to  $27.74^\circ$ . We observe similar shifts to lower angles of  $\sim 0.5^\circ$  for all lattice orientations of the 12 % film. This would indicate the crystal lattice parameters have expanded as the sublimed Te is replaced with larger Bi atoms as supported by the trend in the EDX data. However, this shift is not seen with the 16 % and 20 % films where their lattice orientations are associated with the ICDD model for  $(\text{Bi}_{0.5}\text{Sb}_{0.5})_4\text{Te}_3$ . It is believed that the replacement of Te atoms with Bi atoms reached a critical point where the crystal structure of the films was no longer  $\text{Bi}_{0.4}\text{Sb}_{1.6}\text{Te}_3$ . This idea is further supported by the observation of a peak indexed to the Bi lattice orientation (1 0 4) for the 20 % film's GIXRD spectrum. Suggesting that in some areas of the film the replacement was high enough that metallic Bi could form. Notably, we observe a peak for the lattice orientation of (1 0 1) for Te, believed to be from the surviving Te nanorods as the (1 0 1) were the nanorods preferred lattice orientation. The peak was only observed at these higher concentrations which suggests the films had enough Te nanorods that survived the annealing step. This is despite no Te nanorods being observed for any of the films under SEM.

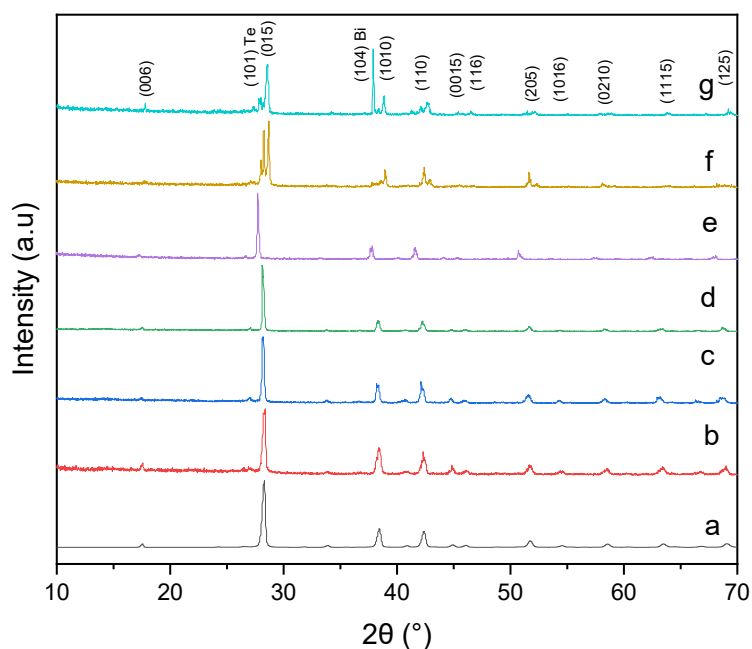


**Fig.5.13-** GIXRD diffraction patterns obtained for (a) reference of Bismuth Antimony Telluride ( $\text{Bi}_{0.4}\text{Sb}_{1.6}\text{Te}_3$ ) mineral from ICDD database (PDF 01-072-1836) and (b) PVDF- $\text{Bi}_{0.4}\text{Sb}_{1.6}\text{Te}_3$  nanoplatelet containing (b) 0 %, (c) 4 %, (d) 8 %, (e) 12 %, (f) 16 % and (g) 20 % Te nanorods films annealed at  $450^\circ\text{C}$  for 1 hr in an inert Ar atmosphere.

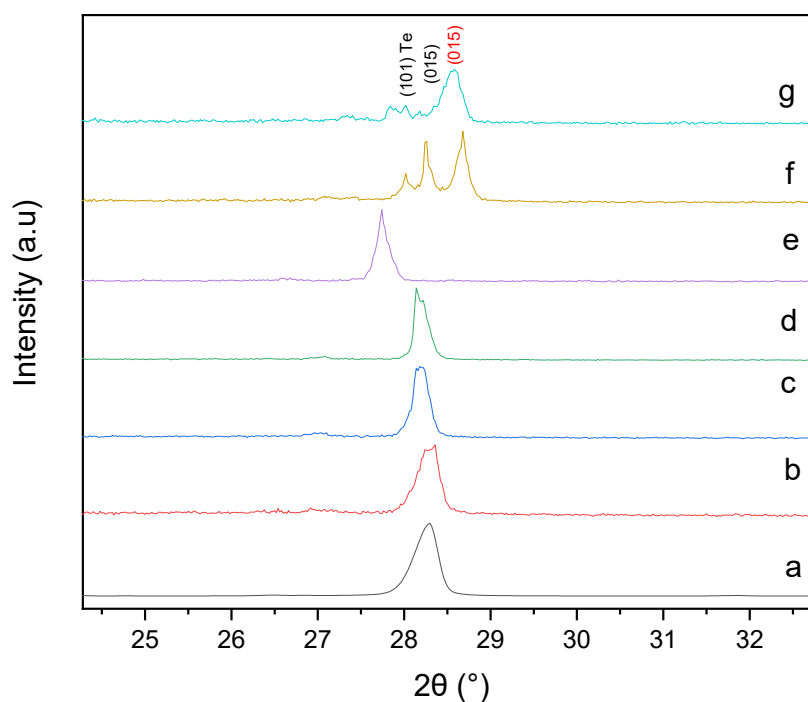


**Fig. 5.14-** GIXRD diffraction patterns obtained between 24 ° and 33 ° for (a) reference of Bismuth Antimony Telluride ( $\text{Bi}_{0.4}\text{Sb}_{1.6}\text{Te}_3$ ) mineral from ICDD database (PDF 01-072-1836) and (b) 5% PVDF- $\text{Bi}_{0.4}\text{Sb}_{1.6}\text{Te}_3$  nanoplatelet containing (b) 0 %, (c) 4 %, (d) 8 %, (e) 12 %, (f) 16 % and (g) 20 % Te nanorods films annealed at 450 °C for 1 hr in an inert Ar atmosphere. With the lattice orientations identified for (1 0 1) for Te ICDD database (PDF 00-086-2268), (0 1 5)  $\text{Bi}_{0.4}\text{Sb}_{1.6}\text{Te}_3$  ICDD database (PDF 01-072-1836) and in red the (0 1 5) ( $\text{Bi}_{0.5}\text{Sb}_{0.5}$ ) $_4\text{Te}_3$  ICDD database (PDF 01-072-1838).

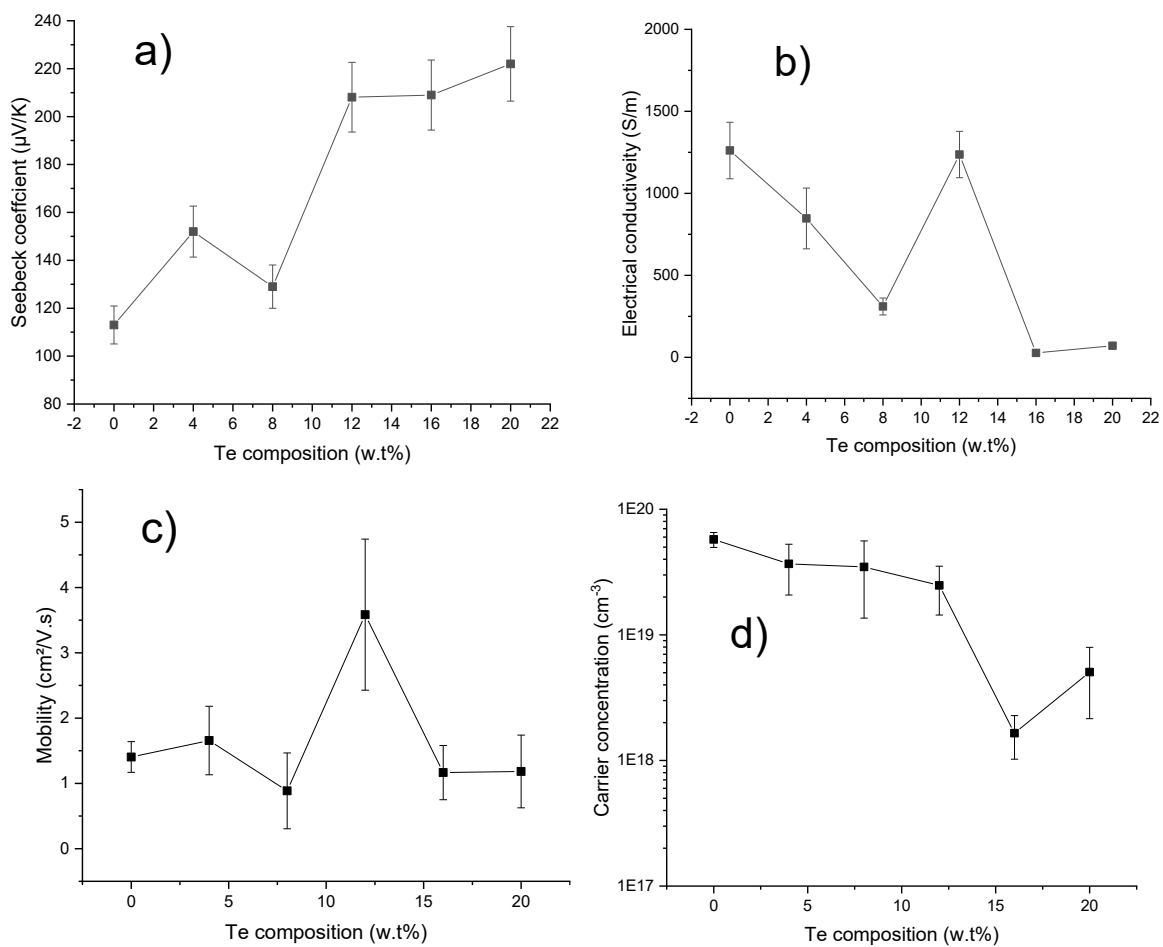
From the EDX and GIXRD data, we can state that just as with the annealed screen-printed  $\text{Bi}_2\text{Te}_{2.5}\text{Se}_{0.5}$  nanowires in section 4.2, there are also Bi antisite defects in the crystal structure of the screen-printed PVDF- $\text{Bi}_{0.4}\text{Sb}_{1.6}\text{Te}_3$ -Te films. This is based on the EDX data with an increasing Bi content replacing Te and the peak shifts towards lower angles indicating that the larger Bi atoms are occupying the sites of smaller Te atoms in the crystal structure. These Bi antisite defects would suggest higher carrier concentrations as well as a potential decrease in  $S$  for the screen-printed films.

The average crystal grain sizes for the films were calculated using the Scherrer equation seen in equation 2.2, with the exceptions of the 16 % and 20 % films, due to the high errors associated with obtaining their peaks' full width at half maximum. We observe an expansion in the average grain sizes from  $24 \pm 2$  nm,  $27 \pm 5$  nm,  $30 \pm 6$  nm and  $33 \pm 4$  nm for the 0 %, 4 %, 8 % and 12 % films respectively. However, as the increase in the average grain size was within the range of uncertainty for the 4 % and 8 % films, we can only confidently state that the 12 % film has larger average grain sizes than the 0 % film.

This grain size expansion was also observed in the literature for ball-milled  $\text{Bi}_{0.4}\text{Sb}_{1.6}\text{Te}_3$  with 8 % Te additives by Varghese et al [81]. This was explained as the extra Te liquifying due to its lower melting point thereby acting as a grain coalescing agent and interface for the  $\text{Bi}_{0.4}\text{Sb}_{1.6}\text{Te}_3$  particles [81].

### 5.3.3.2 Thermoelectric characterisation

The screen-printed PVDF- $\text{Bi}_{0.4}\text{Sb}_{1.6}\text{Te}_3$  nanoplatelet + Te nanorod films had their room temperature TE properties measured as shown in Fig. 5.15 using the portable S probe and the Hall effect probe.



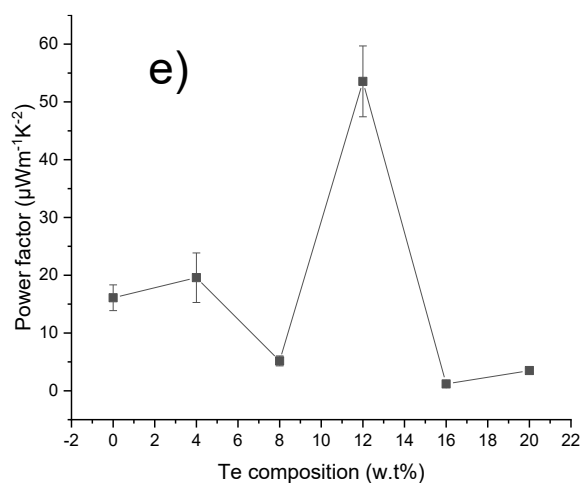


**Fig. 5.15-** Room temperature TE properties of (a) Seebeck coefficient, (b) electrical conductivity, (c) charge carrier mobility, (d)  $\log_{10}$  scale charge carrier concentration and (e) power factor for  $\text{Bi}_{0.4}\text{Sb}_{1.6}\text{Te}_3$  nanoplattlet + Te nanorod films annealed at 450 °C for 1 hr in an inert Ar atmosphere. The uncertainty is based on the standard deviation of the results and the measured thickness of the films.

From the room temperature TE data in Fig.5.15, we observe a positive  $S$  and charge carrier concentration confirming the p-type nature of the films. The initial  $S$  for a 0 % film is within the same range as the PRS  $\text{Bi}_{0.4}\text{Sb}_{1.6}\text{Te}_3$  nanoplattlets of Zhang et al <sup>[62]</sup>. With an increase in the Te nanorods content, we note an improvement in  $S$  from  $113 \pm 8 \mu\text{V K}^{-1}$  to  $220 \pm 20 \mu\text{V K}^{-1}$  for the 0 % and 20 % film respectively. Our  $S$  results are also in line with the findings from Maden et al <sup>[108]</sup> for Te nanoparticle additives in dispenser printed  $\text{Bi}_{0.5}\text{Sb}_{1.5}\text{Te}_3$  films annealed at 250 °C for 12 hr. In their work, they observed an increase from  $180 \mu\text{V K}^{-1}$  to  $280 \mu\text{V K}^{-1}$  for films with 0 % and 10 % Te nanoparticle content respectively <sup>[108]</sup>. Where our results differ from the literature is we note a decline in  $\sigma$  when increasing the percentage of Te nanorods except for the 12 % films. This reduction in  $\sigma$  is explained by a fall in the films' charge carrier concentrations which is most obvious for the 16 % and 20 % films with carrier concentrations  $<10^{19} \text{ cm}^{-3}$  and  $\sigma$  of  $30 \pm 10 \text{ S m}^{-1}$  and  $70 \pm 10 \text{ S m}^{-1}$  respectively. This decreasing trend in carrier concentration is also observed by Maden et al <sup>[108]</sup> and in our case is the result of the Te nanorod's lower carrier concentrations seen in Table 5.2. As such we observe the stronger suppression of the carrier concentrations by the Te nanorods than the increase in hole charge carriers provided by the Bi antisite defects in the screen-printed films. Interestingly the charge carrier mobility of the films stays within the range between  $0.5 \text{ cm}^2/\text{V s}$  and  $1.5 \text{ cm}^2/\text{V s}$  except for the 12 % film which has a charge carrier mobility of  $3.6 \pm 1.2 \text{ cm}^2/\text{V s}$ .

The highest PF observed was for the 12 % films which when compared to the 0 % films had a higher PF by a factor of >3.3x from  $16 \pm 2 \mu\text{Wm}^{-1}\text{K}^{-2}$  to  $54 \pm 6 \mu\text{Wm}^{-1}\text{K}^{-2}$ . However, the other films had a lower PF than the 0 % film except for the 4 % films. Unfortunately, the 0 % film's PF is within the error range of the 4 % film's PF of  $20 \pm 4 \mu\text{Wm}^{-1}\text{K}^{-2}$ . The main factor for the 12 % film's higher PF was its higher charge carrier mobility while maintaining a high S which can be attributed to its larger average grain size of  $33 \pm 4 \text{ nm}$  compared to the 0 % film's  $24 \pm 2 \text{ nm}$ . The larger average grain sizes reduce the number of grain boundaries that could scatter the charge carriers. As such we observe 12 % to be the ideal concentration of Te nanorods in the PVDF-Bi<sub>0.4</sub>Sb<sub>1.6</sub>Te<sub>3</sub> nanoplatelet films.

However, despite the >3.3x improvement in the PF, our films are still subpar to the bulk and other printed films in the literature seen in Tables 1.2 and 1.4 [60,76,81,108]. This is a result of the films containing individual particles that cause the charge carriers to scatter between particle boundaries. This lowers the films' charge carrier mobility and overall  $\sigma$ . The main improvement seen in the literature appears to be due to grain coalescing of the Te nanoparticles acting as an interface layer between Bi<sub>0.5</sub>Sb<sub>1.5</sub>Te<sub>3</sub> grains improving charge carrier mobility and  $\sigma$  of the films [81,108]. This does not seem to be the case with our films with the exception being the 12 % film. This could be due to the size of the Te nanorods being too large to fully liquefy during the annealing duration to act as a grain coalescing agent compared to the Te nanoparticles obtained by ball milling. One potential route to alleviate this could be to use a higher annealing duration to achieve the same liquefaction. Another route could be to synthesise small Te nanorods. The 12 % film was a novel screen-printable composite film between Bi<sub>0.4</sub>Sb<sub>1.6</sub>Te<sub>3</sub> nanoplatelets and Te nanorods which was the highest performing p-type material produced and will be used in the FTEG device seen in section 5.4.

### 5.3.3.3 Flexibility characterisation

The annealed screen-printed PVDF-Bi<sub>0.4</sub>Sb<sub>1.6</sub>Te<sub>3</sub>+12 % Te nanorod film underwent the same bending test as seen with the Bi<sub>2</sub>Te<sub>3</sub> and Bi<sub>2</sub>Te<sub>2.5</sub>Se<sub>0.5</sub> nanowires in the previous chapters. The screen-printed film on Kapton experienced a bending test of 1000 bending cycles at a bending radius of 10 mm, the results of which are shown in Fig.5.16. To account for the roughness of the fabric pocket of the bending apparatus the films are placed in a Kapton pocket, with silver electrodes deposited on both sides of the films to get accurate resistance readings without damaging the films.

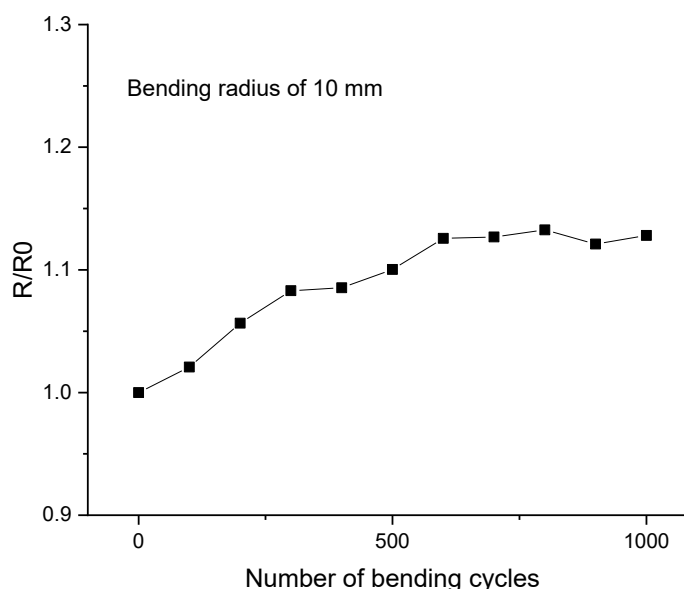


**Fig. 5.16-** The resistance normalized to the initial resistance of the single printing pass PVDF-Bi<sub>0.4</sub>Sb<sub>1.6</sub>Te<sub>3</sub>+12 % Te nanorod film on Kapton for 1000 bending cycles, with a bending radius of 10 mm.

The film observed a bending-related resistance increase of 12 %, which is higher than the PVDF-Bi<sub>2</sub>Te<sub>3</sub> film's resistance increase of 5 % under the same conditions. The main reason for this disparity is due to the difference in thicknesses, as the p-type film has a thickness of  $35 \pm 3 \mu\text{m}$  compared to the n-type Bi<sub>2</sub>Te<sub>3</sub> film's  $5 \pm 2 \mu\text{m}$ . As stated by Orril et al <sup>[51]</sup>, screen-printed films can be prone to cracking and delamination when their film thickness is greater than 20  $\mu\text{m}$ . However, the PVDF-Bi<sub>0.4</sub>Sb<sub>1.6</sub>Te<sub>3</sub>+12 % Te nanorod film rate of resistance increase stabilises past 600 bending cycles, which coupled with the lack of film delamination during the bending test shows its potential compatibility for flexible applications.

#### 5.4 Device fabrication and power output measurements

Two FTEGs were fabricated with the first being a single-leg device made of one single-leg p-type PVDF-Bi<sub>0.4</sub>Sb<sub>1.6</sub>Te<sub>3</sub> nanoplatelets + 12 % Te nanorod film and another with three thermocouples of p-type PVDF-Bi<sub>0.4</sub>Sb<sub>1.6</sub>Te<sub>3</sub> nanoplatelet + 12 % Te nanorod films and n-type PVDF-Bi<sub>2</sub>Te<sub>3</sub> nanowire films. The films were screen-printed onto Kapton and annealed at 450 °C for 1 hr in an inert Ar atmosphere and then connected with a silver metal contact using a silver pen (Chemtronics). The cold side was kept constant at 20° C while using a Peltier heater to increase the hot side, with a thermal camera used to attain an accurate temperature difference.

### 5.4.1 Single-leg flexible thermoelectric generator device

The single-leg device as shown in Fig. 5.17 had geometries of 20 mm x 5 mm x 0.028 mm and had its power output measured for temperature differences between 10 K and 90 K, however, using a thermal camera the max temperature difference achieved was 46.4 K. Silver contacts were deposited on the film to fabricate the device with the contacts' resistance being  $\sim 3 \Omega$ .



**Fig.5.17-** Image of single-leg PVDF-Bi<sub>0.4</sub>Sb<sub>1.6</sub>Te<sub>3</sub> nanoplatelet + 12 % Te nanorod FTEG device.

Despite only one film being measured the power output data seen in Fig. 5.18 shows a maximum voltage and power output for a temperature difference of 46.4 K was 11 mV and 20 nW. When comparing this device to the previous single-leg Bi<sub>2</sub>Te<sub>3</sub> device in section 3.5, at similar temperature differences of 27.6 K to 28.5 K for the Bi<sub>0.4</sub>Sb<sub>1.6</sub>Te<sub>3</sub> and Bi<sub>2</sub>Te<sub>3</sub> devices respectively, we observe a higher power output of 7 nW for the Bi<sub>0.4</sub>Sb<sub>1.6</sub>Te<sub>3</sub> compared to the 6 nW of the Bi<sub>2</sub>Te<sub>3</sub> device. This is despite the Bi<sub>2</sub>Te<sub>3</sub> device containing 5 films compared to this device's 1. The higher power output observed is due to the film's higher PF of  $54 \mu\text{Wm}^{-1}\text{K}^{-2}$  compared to the Bi<sub>2</sub>Te<sub>3</sub> PF of  $37 \mu\text{Wm}^{-1}\text{K}^{-2}$ . The thermal camera images for the different temperature gradient are shown in Fig. 5.19.

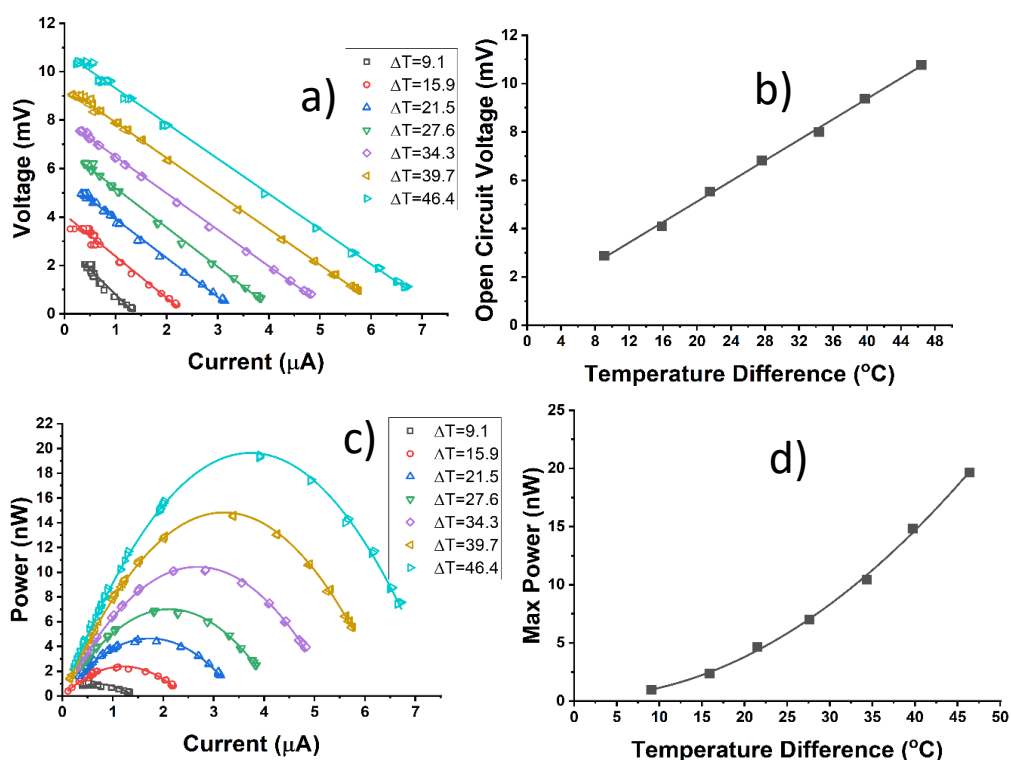


**Fig.5.18-** Graphs show (a) the voltage vs current response for different temperature differences, (b) the open-circuit voltage with respect to the temperature difference, (c) the output power vs current and (d) the maximum output power with respect to the temperature difference of the single-leg 5% PVDF- $\text{Bi}_{0.4}\text{Sb}_{1.6}\text{Te}_3$  nanoplatelet + 12 % Te nanorod FTEG device.

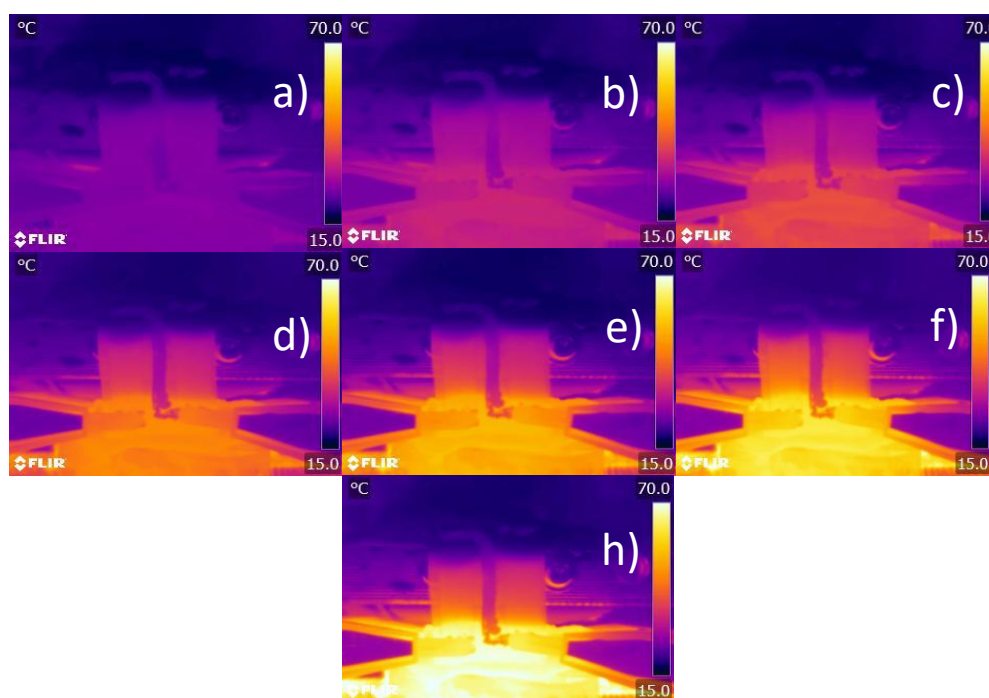


**Fig.5.19-** The thermal images are taken of the single-leg PVDF-  $\text{Bi}_{0.4}\text{Sb}_{1.6}\text{Te}_3$  nanoplatelet + 12 % Te nanorod FTEG device during measuring with a normalised temperature range of (a) 9.1 K, (b) 15.9 K, (c) 21.1 K, (d) 27.6 K, (e) 34.3 K, (f) 39.7 K and (g) 46.4 K.

5.4.2 P-N thermocouple flexible thermoelectric generator device

The three thermocouples FTEG had geometries of 20 mm x 5 mm x 0.028 mm and 20 mm x 5 mm x 0.005 mm for the p-type and n-type legs respectively with Fig. 5.20 showing an image of the FTEG device. As with the previous single-leg device the silver contacts had a resistance of ~3 Ω.

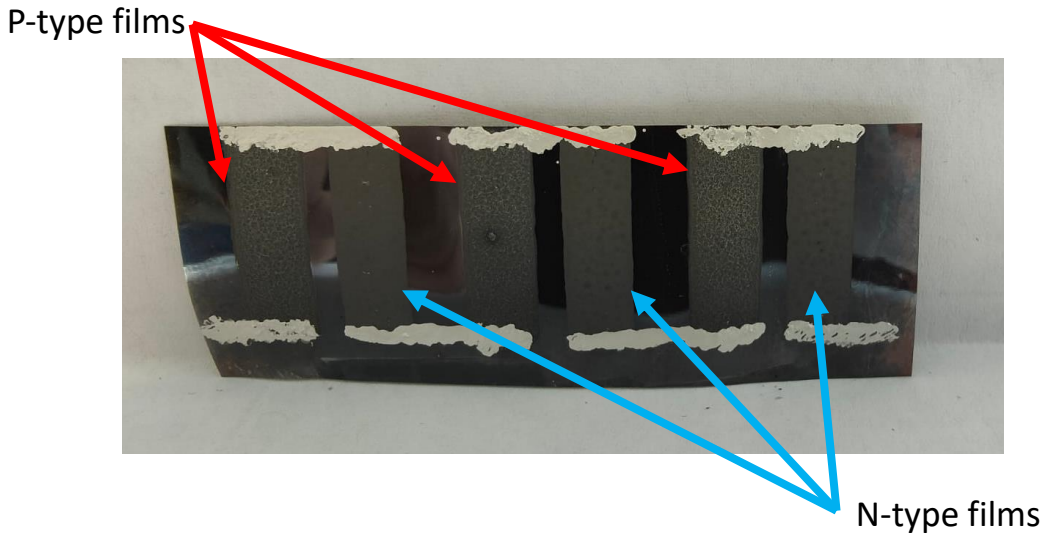
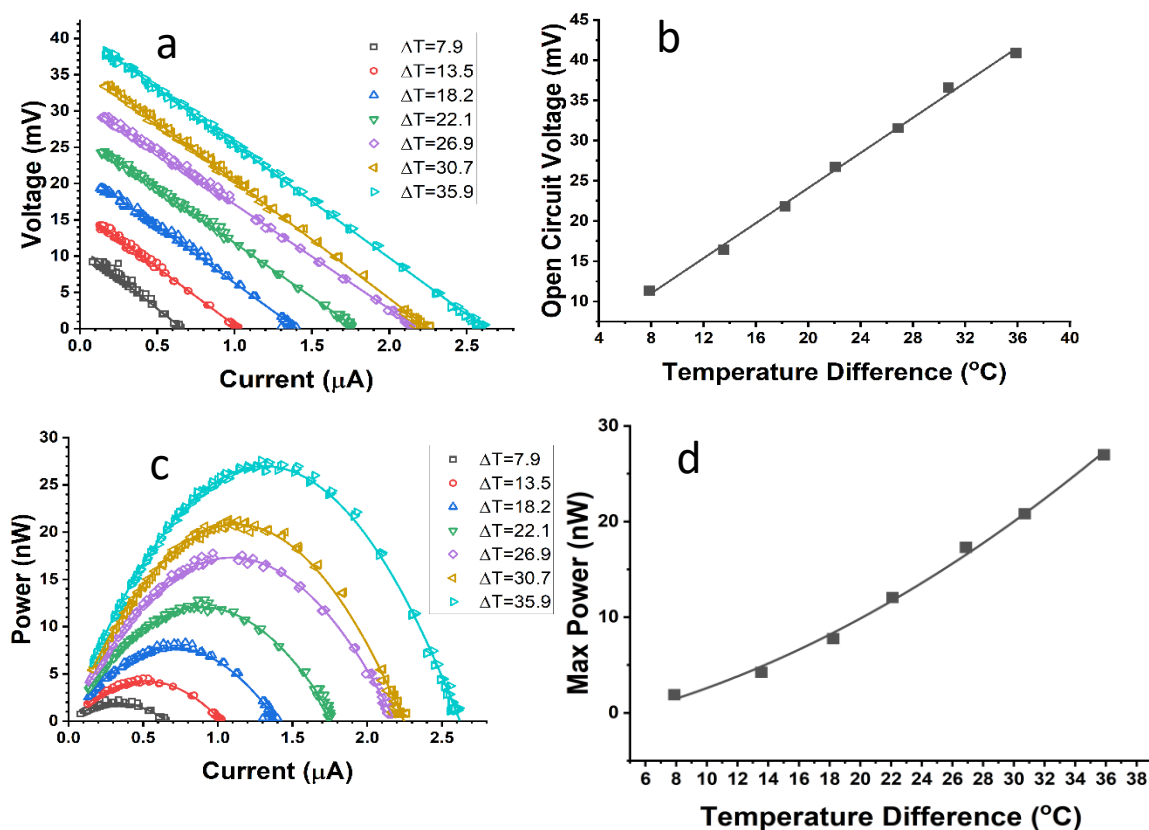


Fig.5.20- Image of a 3 thermocouple FTEG device on Kapton made of p-type PVDF-Bi<sub>0.4</sub>Sb<sub>1.6</sub>Te<sub>3</sub> nanoplatelet + 12 % Te nanorod films and n-type PVDF-Bi<sub>2</sub>Te<sub>3</sub> nanowire films. The thermocouples are connected via silver metal contacts.

The power output data with respect to the temperature difference is shown in Fig. 5.21. The FTEG's power output was measured for temperature differences between 10 K and 90 K, however, using a thermal camera the max temperature difference achieved was 35.9 K with thermal camera images taken for each measurement shown in Fig. 5.22. We observe a maximum voltage and power output for a temperature difference of 35.9 K was 40 mV and 27 nW. However, this power output seems to be too low given that for a similar thermal gradient of 34.3 K a single p-type leg can achieve 10 nW. With this in mind, 3 p-type legs connected by a metal contact should achieve ~30 nW. One factor could be the non-optimal annealing conditions at 450 °C for 1 hr used for the n-type Bi<sub>2</sub>Te<sub>3</sub> nanowires, which can be seen in Appendix A for 20 % PVDF-Bi<sub>2</sub>Te<sub>3</sub> nanowire films resulting in a low PF. Additionally, delays between device fabrication and when the device was measured resulted in the partial oxidation of the device causing an increase in device resistance and lowering of the power output as seen with the single-leg Bi<sub>2</sub>Te<sub>3</sub> device. Furthermore, the silver contacts used were not ideal as can be seen in Fig. 5.20 with patches in the contacts due to the difficulties in depositing the silver ink onto the Kapton. As such our 3 thermocouple FTEG falls short of devices seen in the literature [74,75,77,80].



**Fig. 5.21-** Graphs show (a) the voltage vs current response for different temperature differences, (b) the open-circuit voltage with respect to the temperature difference, (c) the output power vs current and (d) the maximum output power with respect to the temperature difference of a 3 thermocouple FTEG device on Kapton.

To improve the FTEG power output in the future the silver ink used here needs to be replaced with a screen-printable paste. As such the geometries of the films need to be chosen with regard to optimal heat flow through the device for the generation of power and not chosen arbitrarily. This could be a good avenue for future work to computationally analyse more ideal geometry for the films. Finally, the annealing process needs to be modified so that the Te nanorod additives can liquefy in the p-type film while allowing for the formation of INNs in the n-type would improve TE performance and increase power output.

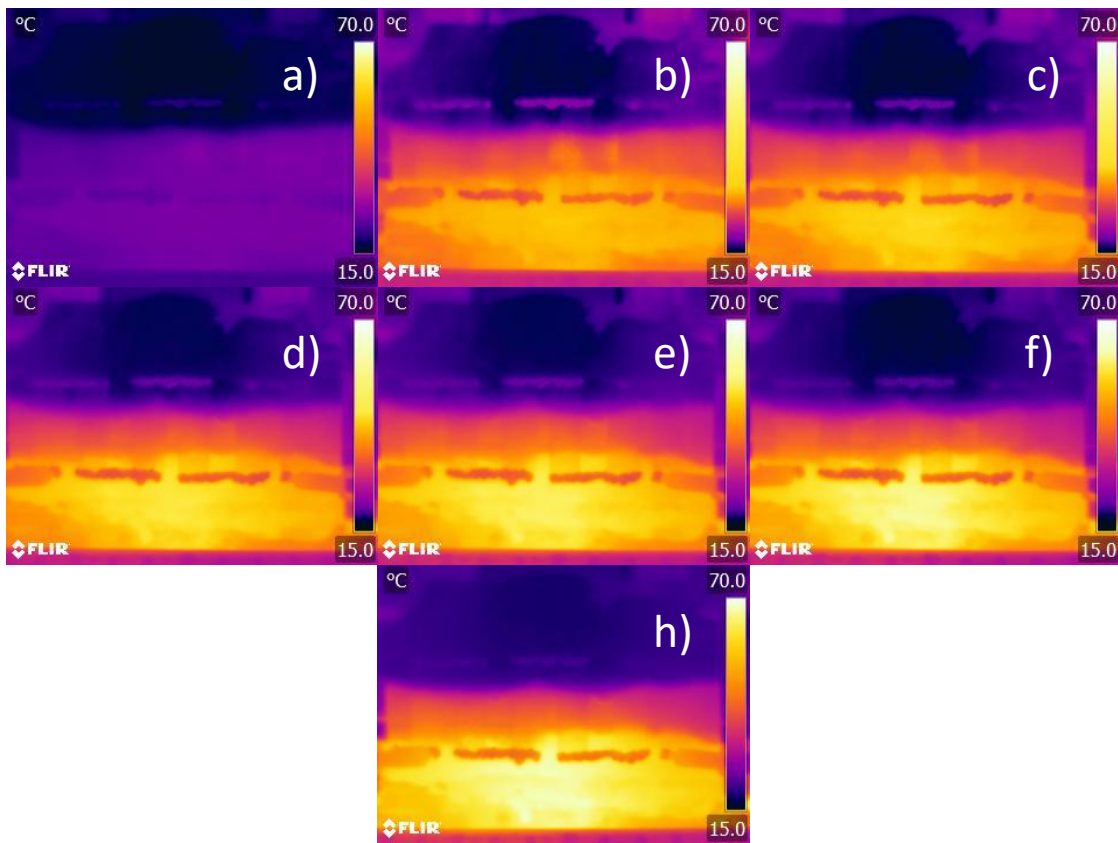


**Fig. 5.22-** The thermal images are taken of the 3 thermocouple FTEG device on Kapton during measuring with a normalised temperature range of (a) 7.9 K, (b) 13.5 K, (c) 18.2 K, (d) 22.1 K, (e) 26.9 K, (f) 30.7 K and (g) 35.9 K.

## 5.5 Conclusions

In summary, we have synthesised p-type  $\text{Bi}_{0.4}\text{Sb}_{1.6}\text{Te}_3$  nanoplatelets via PRS instead of  $\text{Bi}_{0.5}\text{Sb}_{1.5}\text{Te}_3$  nanowires seen in the literature for similar reactions. This was a result of replacing the reducing agent anhydrous hydrazine with hydrazine hydrate in the PRS reaction due to the unavailability of anhydrous hydrazine as a result of its dangerous nature [36,53]. The nanoplatelets had lengths between 100 nm and 350 nm as well as a thickness of  $15 \pm 5$  nm. Drop-casted films of these nanoplatelets were deposited onto glass substrates to measure their TE properties. Unlike the  $\text{Bi}_2\text{Te}_3$  nanowires, the films were conducive enough for TE measurements where we observe a room temperature  $S$  of  $\sim 140 \pm 10 \mu\text{V K}^{-1}$  [60]. However, due to the films' poor electrical properties, the PFs were  $< 1 \mu\text{Wm}^{-1}\text{K}^{-2}$ .

The PRS reaction for the nanoplatelets was scaled up by a factor of 5 to have enough nanoplatelets to formulate screen-printable pastes, as well as examine the scalability of this PRS reaction. Scaling up the PRS procedure showed no noticeable changes in the nanoplatelets' crystal structure or atomic composition. The only observed change was that the nanoplatelet lengths were more varied between 90 nm and 650 nm. Drop-casted films of these nanoplatelets still had room temperature  $S$  of  $\sim 140 \pm 10 \mu\text{V K}^{-1}$ , showcasing the flexibility of the PRS method. The  $\text{Bi}_{0.4}\text{Sb}_{1.6}\text{Te}_3$  nanoplatelets were formulated into a paste containing 5 % PVDF while NMP was used as the solvent and screen-printed onto Kapton. Two films were produced with 1 and 4 printing passes with a drying step of 5 mins in a vacuum oven at  $70^\circ\text{C}$  for 5 mins between each printing pass. The films were annealed at  $450^\circ\text{C}$  for 10 mins in an Ar inert atmosphere as Chen et al [53] showed that these annealing parameters could improve the TE properties of  $\text{Bi}_{0.5}\text{Sb}_{1.5}\text{Te}_3$  nanowires compared to  $400^\circ\text{C}$  for 2 hr used for  $\text{Bi}_2\text{Te}_3$  nanowires. However, the films' PFs were  $1.46 \pm 0.08 \mu\text{Wm}^{-1}\text{K}^{-2}$  and  $5.0 \pm 0.3 \mu\text{Wm}^{-1}\text{K}^{-2}$  for the 1 and 4 print passes respectively. These low PFs were the result of the oxidation effect caused when the nanoplatelets are bath sonicated in NMP at above room temperature. To reduce this effect the pastes were sonicated in an ice bath and the sonication times were reduced.

Once all the paste formulation process was optimised for the p-type nanoplatelets we embarked on our study to improve these screen-printed PVDF-Bi<sub>0.4</sub>Sb<sub>1.6</sub>Te<sub>3</sub> nanoplatelet films with Te additives. As these Te additives have improved the TE performance in the literature for printed ball-milled Bi<sub>0.4</sub>Sb<sub>1.6</sub>Te<sub>3</sub> and Bi<sub>0.5</sub>Sb<sub>1.5</sub>Te<sub>3</sub> films under different annealing conditions [81,108,109]. In our case, we synthesised Te nanorod additives for the ease and simplicity of their synthesis and their high *S* seen in the literature (*S* > 250 μV K<sup>-1</sup>) [67–70], which if incorporated into the screen-printed films could improve their TE performance via improvements in *S*. These nanorods' diameters ranged between ~100 nm and 200 nm with lengths between a few hundred nm and a few μm. The Te nanorods had a room temperature *S* of 440 ± 10 μV K<sup>-1</sup> which is in good agreement with the literature [67,68]. They were then formulated into screen-printable pastes with a 5 % PVDF binder and screen-printed onto Kapton and obtained the highest non-annealed film PF of 2.7 ± 0.7 μWm<sup>-1</sup>K<sup>-2</sup>. This makes the Te nanorods suitable to be screen-printed onto fabrics, as they do not need to be annealed at high temperatures to act as energy harvesters, which is explored further in Chapter 6. The screen-printed PVDF-Te nanorod films were annealed at 450 °C for 1 hr in an inert Ar atmosphere, which caused the films to degrade with resistances > 10 MΩ.

A novel Te nanorod additive study was conducted, whereby Te nanorods were incorporated into the Bi<sub>0.4</sub>Sb<sub>1.6</sub>Te<sub>3</sub> nanoplatelet pastes, with the Te nanorod content ranging from 0 % to 20 % in steps of 4 % with respect to the Bi<sub>0.4</sub>Sb<sub>1.6</sub>Te<sub>3</sub> nanoplatelet content in the pastes. These films were screen-printed with 4 printing passes each onto Kapton with a drying step of 5 mins in a vacuum oven at 70 °C between each printing pass, after which they were annealed at 450 °C for 1 hr in an inert Ar atmosphere. The post-annealed films regardless of Te nanorod concentration showed 3 distinct morphologies, we observe cauliflower-like microstructures on the order of >10 μm in size, followed by smaller microplatelets <10 μm in size and amorphous nanoparticles ranging between ~50 nm and 500 nm in length. The larger microstructures were due to the agglomeration of the nanoplatelets and nanorods during the annealing process. In the EDX data for the screen-printed films, we observed an increase of the Bi from 7.68 % to 9.98 % and a decrease in Te from 59.88 % to 58.7 %, while Sb was fairly consistent (~32 %) as the Te nanorod content increased in the screen-printed films. While the crystal structure between 0 % and 12 % were indexed for the Bi<sub>0.4</sub>Sb<sub>1.6</sub>Te<sub>3</sub>, however, there were notable shifts in the (0 1 5) peak with the 12 % films observed to have the greatest shift for all the peaks on average 0.5 ° to lower angles. Based on the EDX and GIXRD data it was believed that just as in the annealed screen-printed Bi<sub>2</sub>Te<sub>2.5</sub>Se<sub>0.5</sub> nanowires in section 4.2, there were also Bi antisite defects in the crystal structure of the screen-printed PVDF-Bi<sub>0.4</sub>Sb<sub>1.6</sub>Te<sub>3</sub>-Te films. When calculating these films' average crystal grain size we observe an expansion from 24 ± 2 nm to 33 ± 4 nm from the 0 % to 12 % films respectively.

Similar grain size expansions were also observed in the literature and explained as the extra Te liquifying due to its lower melting point thereby acting as a grain coalescing agent and interface for the  $\text{Bi}_{0.4}\text{Sb}_{1.6}\text{Te}_3$  particles <sup>[81]</sup>. Meanwhile, the 16 % and 20 % films were indexed to  $(\text{Bi}_{0.5}\text{Sb}_{0.5})_4\text{Te}_3$  and had observed peaks in elemental Bi and Te. This was believed to be due to the increase in Bi content in the films' atomic composition allowing for the formation of metallic Bi in some areas of the films. While the separate elemental Te peak is due to a sufficient amount of Te nanorods surviving the annealing process.

The room temperature TE properties were obtained for the films where we observe a > 3.3x improvement in the PF from  $16 \pm 2 \mu\text{Wm}^{-1}\text{K}^{-2}$  to  $54 \pm 6 \mu\text{Wm}^{-1}\text{K}^{-2}$  for the 0 % and 12 % films respectively. This improvement was observed due to a near doubling of S as the films went from an S of  $113 \pm 8 \mu\text{V K}^{-1}$  to  $220 \pm 20 \mu\text{V K}^{-1}$  for the 0 % and 20 % films respectively. However, this increase in S was coupled with a decrease in  $\sigma$  for all films except for the 12 % films which maintained its  $\sigma$  by increasing carrier mobility, which was associated with the expansion in the grain size noted in the GIXRD data. However, the PFs of the screen-printed films are still below that of the literature <sup>[60,76,81,108]</sup>. Similar to the  $\text{Bi}_2\text{Te}_3$  screen-printed films the PVDF binder still negatively affects the TE performance as when the PVDF is burnt off it results in voids in the films. Additionally, the films unlike the  $\text{Bi}_2\text{Te}_3$  INNs contain individual particles that cause the charge carriers to scatter between particle boundaries. These factors lower the film's carrier mobility and overall  $\sigma$ . To improve the PF performance we suggest using smaller Te nanorods to achieve to increase the Te liquefaction during annealing as the grain coalescing resulting from this appears to be the main route to improving the carrier mobility and  $\sigma$  of the films <sup>[81,108]</sup>.

A flexibility study was performed on the post-annealed PVDF- $\text{Bi}_{0.4}\text{Sb}_{1.6}\text{Te}_3$  nanoplatelet + 12 % Te nanorod film. The film was bent at a bending radius of 10 mm for 1000 bending cycles, where we observe an increase of 12 % in the film's resistance due to bending damage which is higher than what was observed for the n-type screen-printed films. However, this is due to those n-type films' lower thicknesses of  $5 \pm 2 \mu\text{m}$  compared to this p-type film's  $35 \pm 3 \mu\text{m}$ . The p-type film maintains its structure and the low bending resistance shows its compatibility for flexible applications.

## Chapter 5

Two devices were fabricated, one FTEG with three thermocouples of p-type PVDF-Bi<sub>0.4</sub>Sb<sub>1.6</sub>Te<sub>3</sub> nanoplatelet + 12 % Te nanorod films and n-type PVDF-Bi<sub>2</sub>Te<sub>3</sub> nanowire films, while the other was a single-leg p-type device. The films were screen-printed onto Kapton and annealed at 450 °C for 1 hr in an inert Ar atmosphere and then connected with a silver metal contact using a silver pen (Chemtronics). The devices experienced a thermal gradient using two Peltier cells with a heat sink keep at a constant temperature of 20 °C with a heat source between 30 °C and 90 °C. However, using a thermal camera we observe different thermal gradients for each device. For the single-leg p-type device, we observe at a thermal gradient of 46.4 K a maximum voltage and power output of 11 mV and 20 nW. While the three thermocouple FTEG device experienced a maximum temperature difference, voltage and power output of 35.9 K, 40 mV and 27 nW. However, this power output falls short of other devices in the literature <sup>[74,75,77,80]</sup>. This can be put down to non-optimal annealing conditions for the n-type film while the delays from device fabrication to measuring resulted in partial oxidation of the device reducing its performance. To improve device performance more ideal annealing parameters must be investigated to achieve INN formation in the n-type film and Te liquefaction in the p-type film. As well as optimising the geometries of the TE legs for better heat flow through the device to achieve higher power outputs, as the devices here used arbitrary geometries.

## **Chapter 6 Screen-printed Tellurium-Polyvinylidene fluoride composite-based flexible thermoelectric generators for E-textiles**

We explore the effects of scaling up the Te nanorod PRS reaction to achieve higher mass quantities of Te nanorods to formulate novel screen-printable pastes using the NMP-PVDF solvent-binder system. As has been shown in the previous chapter these PVDF-Te nanorod composites are compatible with fabrics as they do not need to be annealed at high temperatures to be electrically conductive enough to act as energy harvesters. For the first time seen in the literature, we fabricate a single-leg p-type FTEG device on a polyurethane-based interface layer on polyester-cotton, based on our novel screen-printable PVDF-Te nanorod composite films.

### **6.1 Scaled-up polyol reflux synthesis of Tellurium nanorods**

The Te nanorods PRS was scaled-up by a factor of 5 with a portion of the resulting product being drop-casted on a Si substrate to undergo microstructural analysis by SEM, EDX and GIXRD. The synthesis has been reproduced at least 3 times and a drop-casted film was fabricated for each synthesis to ensure the reproducibility of the PRS reaction. The SEM seen in Fig. 6.1 showed similar nanorod geometries as in section 5.31, where we observed nanorods ranging in diameter from ~100 nm to 200 nm with lengths between a few hundred nm and a few  $\mu\text{m}$ . However, the SEM also revealed other nanostructures with a dice-shaped morphology which as shown in Fig.6.1 seem to have nanorods growing out of them. This would indicate that these dice-shaped nanostructures are the seed particles formed from nanocrystal aggregation during the growth step of the PRS reaction explained in section 1.5. This second dice-shaped morphology is visible in the scaled-up nanorods as opposed to the nanorods in section 5.31, as more time needs to be given to fully convert all the seed particles to nanorods and achieve the same product. This was also the case in previous scaled-up batches such as with the  $\text{Bi}_2\text{Te}_3$  nanowires in section 3.21. The EDX spectrum for the drop-casted films showed an 80:20 split between Te and oxygen. This shows that the scaling-up of the PRS did not affect the reduction reaction of the PRS as these atomic percentages were also observed for the Te nanorods in section 5.31.

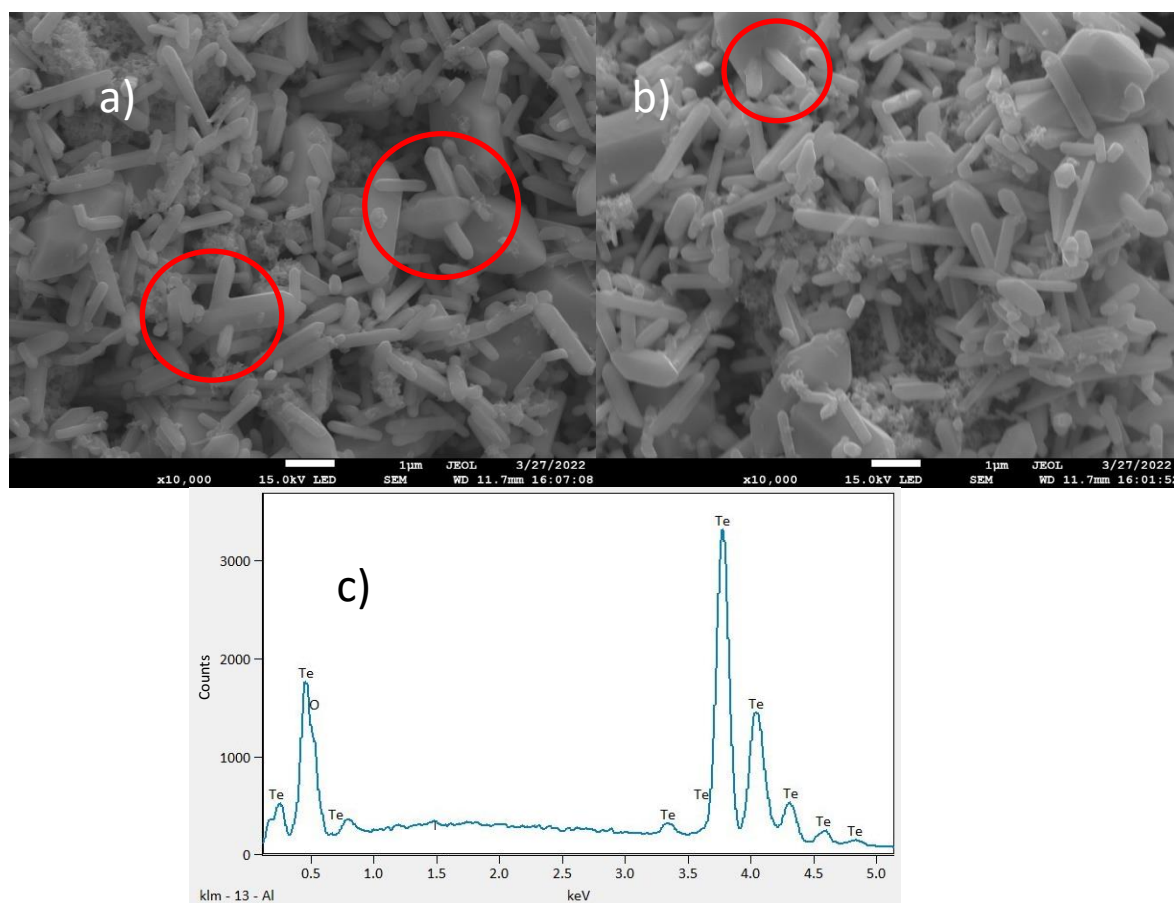


**Fig. 6.1-** SEM images (a&b) of a top-down view of scaled-up Te nanorods on a Si substrate, with red circles indicating areas where the nanorods are growing out of the dice-shaped nanoparticles. While (c) an EDX spectrum of the drop-casted scaled-up Te nanorods film.

GIXRD was also performed on the drop-casted scaled-up Te nanorod films with the data, seen in Fig.6.2, with the spectrum compared to the GIXRD spectrum of the Te nanorods from section 5.31. The scaled-up Te nanorods matched two Te reference materials in the ICDD database. The first set of peaks matches the previous IDCC Te reference (PDF 00-086-2268) with the second set matching another Te reference (PDF 00-085-0554). The first set can be attributed to the nanorods while the second set is to the dice-shaped nanostructures. In the case of both nanostructures, the preferred lattice orientation was the (1 0 1). The only difference between the Te references is the lattice cell parameters with the reference matching the nanorods having parameters of 4.457 Å, 4.457 Å and 5.929 Å, while the Te reference for the dice-shaped nanostructures had 4.411 Å, 4.411 Å and 5.934 Å. The lattice cell parameter difference is most likely related to the different shapes of the two nanostructures.

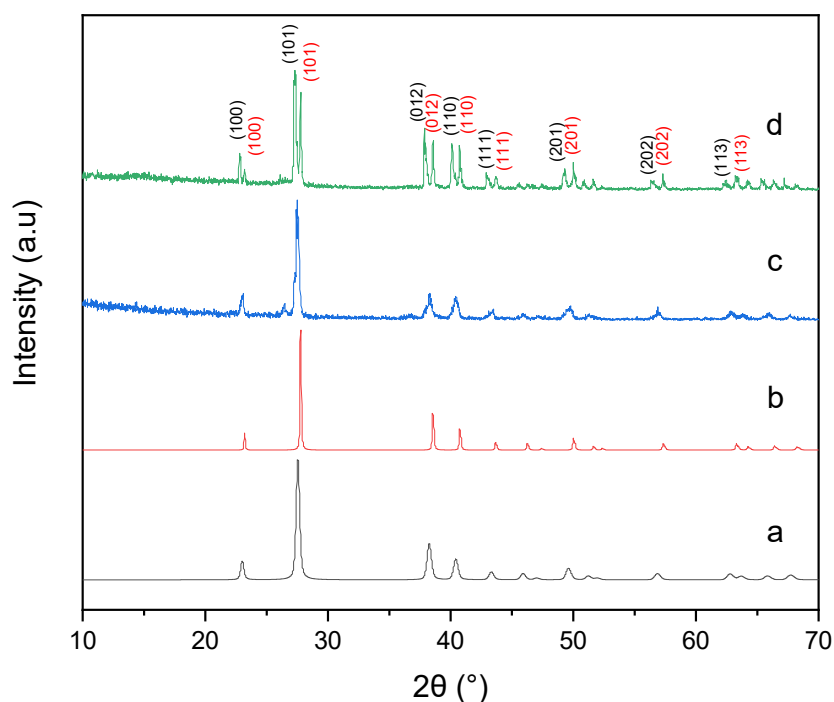


**Fig.6.2-** GIXRD diffraction patterns obtained for reference of Tellurium (Te) mineral from ICDD database (a) (PDF 00-086-2268) and (b) (PDF 00-085-0554). With the black and red indexes associated for (a) and (b) respectively. As well as the drop-casted films on Si substrates for (c) PRS Te nanorods and (d) the scaled-up PRS Te nanorods.

The drop-casted films had their room temperature  $S$  measured using the portable  $S$  probe shown in section 2.411 which showed an  $S$  of  $540 \pm 40 \mu\text{V K}^{-1}$ . Compared to the Te nanorods in section 5.31 we observe an increase in the  $S$  of  $100 \mu\text{V K}^{-1}$ . Additionally, the  $S$  recorded for these scaled-up Te nanorods is higher than what has been seen so far in the literature<sup>[67,68]</sup>. This increase in  $S$  appears to be due to the additional morphology in the drop-casted films as that appears to be the sole difference between the sets of Te nanorods. However, the films' thickness was too non-uniform to obtain accurate Hall probe data, with the film thickness varying by  $\sim 50 \mu\text{m}$ .

## 6.2 Bending analysis of Screen-printed Tellurium-Polyvinylidene fluoride composite

The scaled-up Te nanorods were screen-printed using the method described in section 2.22 with a 5 % PVDF binder on to polyurethane-based interface layer on polyester-cotton. The screen-printed films were deposited in 4 printing passes with a drying step in the vacuum oven for 5 mins at  $70^\circ\text{C}$  between each printing pass. The thickness of the screen-printed films was measured from cross-sectional SEM images as  $90 \pm 20 \mu\text{m}$ .

One screen-printed 5 % PVDF-Te nanorod film underwent the same bending test as seen in the previous chapters. The screen-printed film on Kapton experienced a bending test of 1000 bending cycles at a bending radius of 10 mm, the results of which are shown in Fig.6.3. To account for the roughness of the fabric pocket of the bending apparatus the films are placed in a Kapton pocket, with silver electrodes deposited on both sides of the films to get accurate resistance readings without damaging the films.

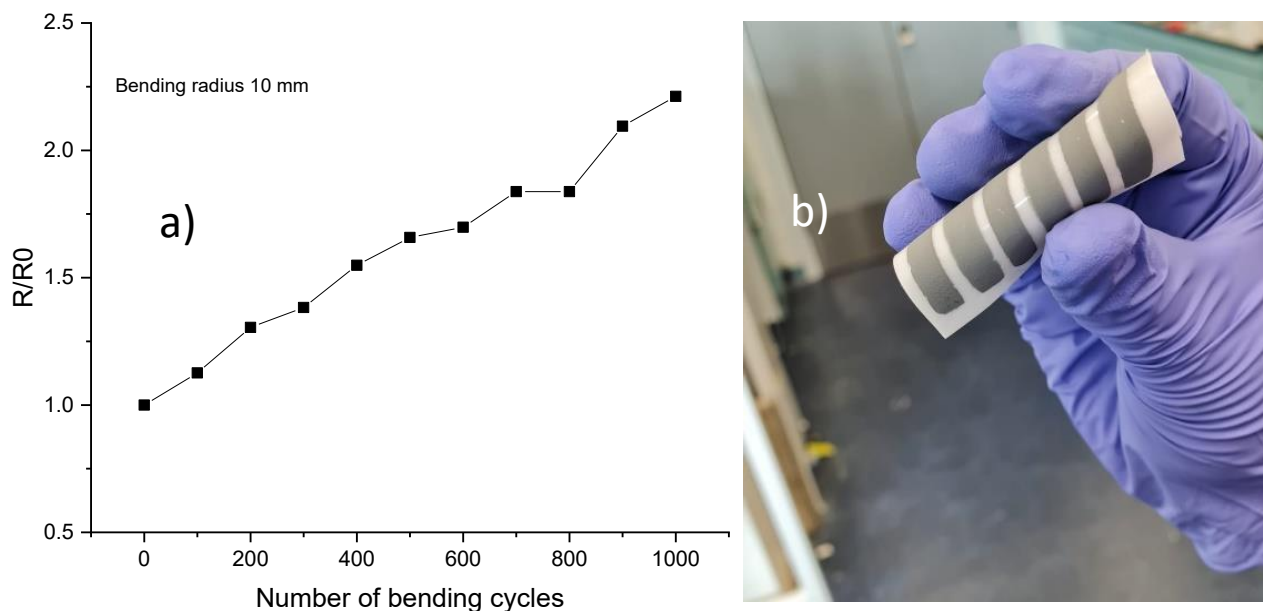


**Fig.6.3-** The (a) resistance normalized to the initial resistance of the single printing pass PVDF- Te nanorod film on polyurethane-based interface layer on polyester-cotton for 1000 bending cycles, with a bending radius of 10 mm and (b) photograph insert of curved composite PVDF-Te nanorod film.

The film showed a higher bending-related resistance increase after 1000 bending cycles, with the resistance increasing by a factor of 2.25 compared to the previous screen-printed films with 5 % PVDF. This is due to the lower thicknesses of the  $\text{Bi}_2\text{Te}_3$  ( $5 \pm 2 \mu\text{m}$ ) and  $\text{Bi}_{0.4}\text{Sb}_{1.6}\text{Te}_3 + 12\% \text{Te}$  nanorod films ( $35 \pm 3 \mu\text{m}$ ) compared to the PVDF-Te nanorod composite ( $90 \pm 20 \mu\text{m}$ ). Despite the higher bending-related resistance, the composite maintains its structure and does not delaminate when bent showing its potential for flexible applications.

### 6.3 Device fabrication and power output measurements

A p-type single-leg FTEG device was fabricated using 5 composite films of PVDF-Te nanorods on a polyurethane-based interface layer on a polyester-cotton substrate as shown in Fig. 6.4. The films had geometries of 20 mm x 5 mm x 0.09 mm and were connected with a silver metal contact using a silver pen (Chemtronics), with the silver contacts having a resistance  $\sim 3 \Omega$ . The cold side was kept constant at 20° C while using a Peltier heater to increase the hot side, with a thermal camera used to attain an accurate temperature difference.

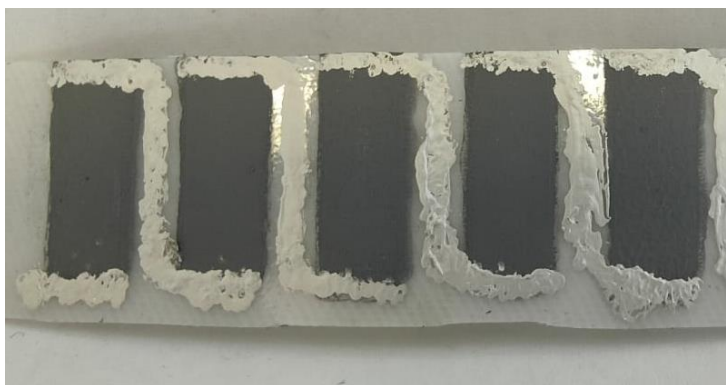


**Fig. 6.4-** Image of the single-leg p-type PVDF-Te nanorod FTEG device.

Our prototype FTEG device was measured by applying a thermal gradient from 8 K to 29.8 K with the power output data shown in Fig. 6.5 with the thermal images for each measurement in Fig.6.6. The maximum voltage and power output for a temperature difference of 29.8 K was 95 mV and 50 nW. In comparison to the other FTEG devices fabricated so far, this device was the best performing with the additional benefit of not needing to be annealed, which makes it compatible with E-textile applications. This higher performance can be attributed to the Te nanorod's higher  $S$  compared to the  $\text{Bi}_2\text{Te}_3$  and the  $\text{Bi}_{0.4}\text{Sb}_{1.6}\text{Te}_3$  as highlighted by the maximum voltage. When taking the voltage per degree per film we see that each film was generating  $\sim 625 \mu\text{V K}^{-1}$ , which was higher than the composite's recorded  $S$  of  $540 \pm 40 \mu\text{V K}^{-1}$ . This higher voltage has allowed our device to generate more power when factoring in the thermal gradient and number of TE legs than other more efficient nanocomposites in the literature using Te nanorods <sup>[73,111]</sup>. However, due to oxygen exposure, the resulting performance is much lower than expected as the resistance across the device had increased from  $\sim 10 \text{ K}\Omega$  to  $\sim 60 \text{ K}\Omega$  between the time it was fabricated to when the device's power output was measured. This increase in resistance was due to the Te nanorods oxidising before the device could be measured and lowering its overall performance. Despite these issues, the prototype demonstrates the potential of incorporating screen-printed PVDF-Te nanorod composite-based FTEG devices into E-textile applications.

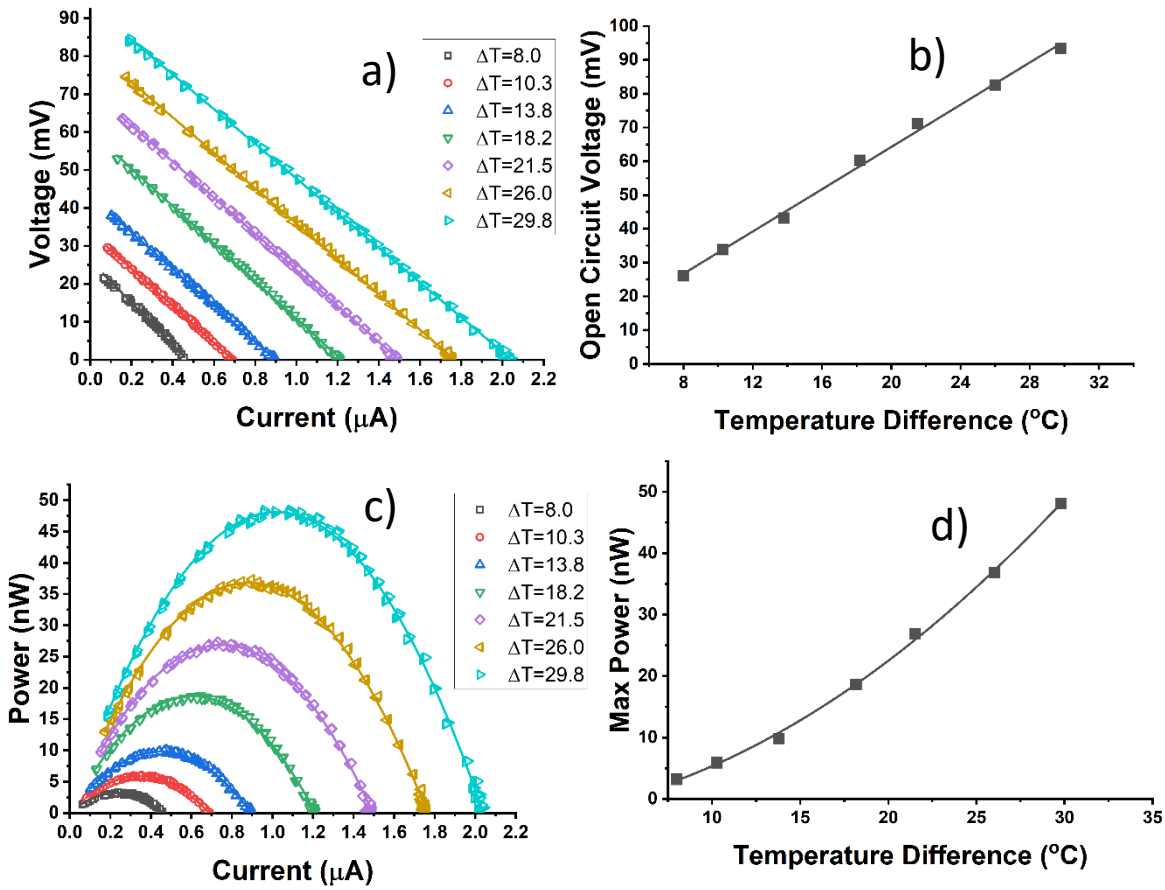


**Fig.6.5-** Graphs showing (a) the voltage vs current response for different temperature differences, (b) the open-circuit voltage with respect to the temperature difference, (c) the output power vs current and (d) the maximum output power with respect to the temperature difference of a single-leg PVDF-Te nanorod FTEG device.

To improve the FTEG device an additional screen-printable sealant layer needs to be applied to the composite films to reduce oxygen exposure to the films and improve device power output stability. Different concentrations of PVDF could be observed to see if the film's adhesion to the substrate can be improved without sacrificing power output. Additionally, the literature has shown that the use of incorporating conductive polymers into the composite films can be an avenue for higher device performance [68,69,71,73]. To improve the scalability of the FTEG fabrication process the silver ink used in Fig.6.4 needs to be replaced with a screen-printable paste so that the FTEG can be fabricated in a fully screen-printable process. Additional work needs to be done to find more optimal electrodes for the composite films. Finally, the geometries of the films were not optimised for power output and were chosen arbitrarily. More ideal geometries could yield better performances and could be a good avenue for future work to use computationally analyse to find more ideal geometry for the composite films.

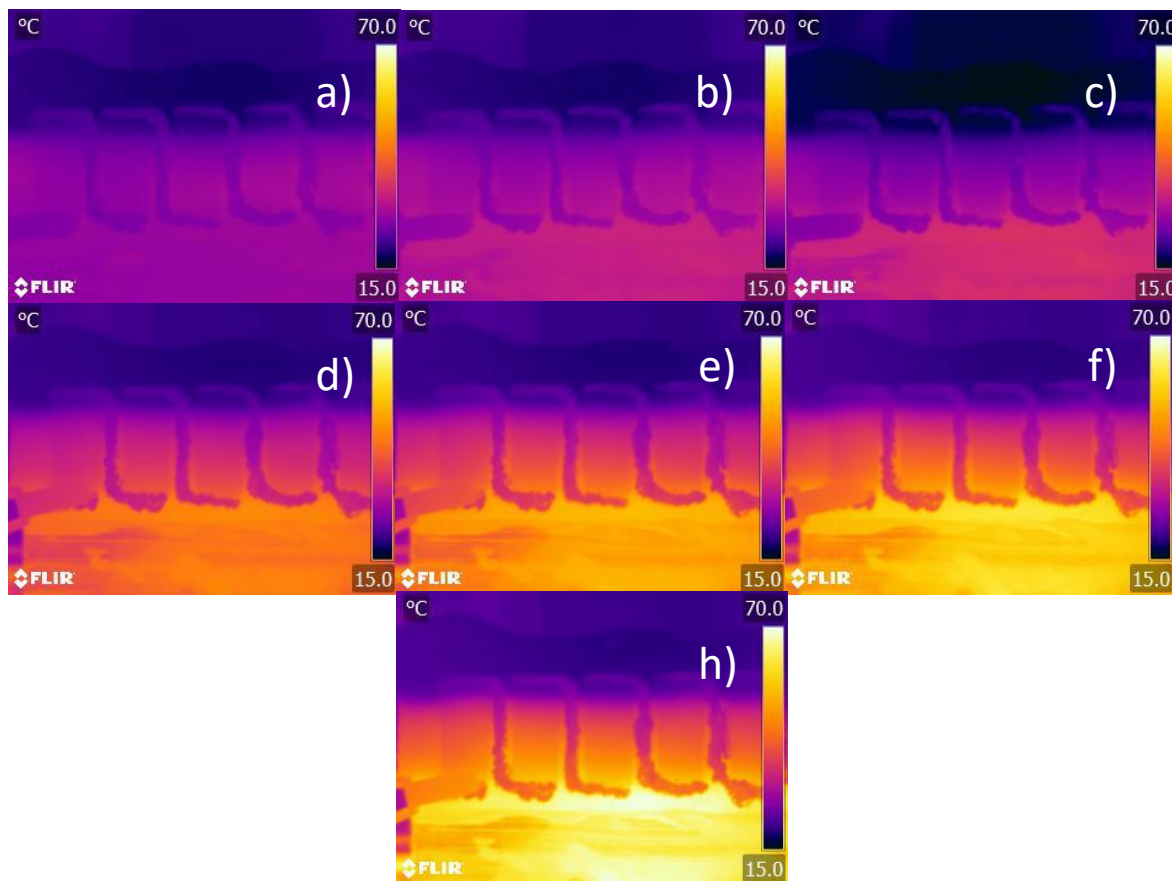


**Fig.6.6-** The thermal images are taken of the single-leg PVDF-Te nanorod FTEG device during measuring with a normalised temperature range of (a) 8.0 K, (b) 10.3 K, (c) 13.8 K, (d) 18.2 K, (e) 21.5 K, (f) 26.0 K and (g) 29.8 K.

## 6.4 Conclusions

In summary, we demonstrate for the first time a screen-printable prototype single-leg p-type PVDF-Te nanorod-based FTEG device that is compatible with textiles. We did this by successfully scaling up the PRS reaction for the Te nanorods which led to an insight into the growth mechanism of the nanorods. We observe Te nanorods growing out of dice-shaped seed nanostructures indicating that during the growth step of the PRS reaction, the Te nanocrystals agglomerate into these dice-shaped seeds and then due to the reaction conditions the Te nanorods grow out of them until all the Te atoms are used.

The Te nanorods were screen-printed with 5 % PVDF using the NMP-PVDF solvent-binder paste formulation, onto a polyurethane-based interface layer on a polyester-cotton substrate. The resulting composite films were formed from 4 printing passes with a drying step between each pass, giving them a thickness of  $90 \pm 20 \mu\text{m}$ . The films underwent a bending test of 1000 bending cycles at a bending radius of 10 mm. This caused a bending-induced resistance in the film resulting in the film resistance increasing by a factor of 2.25 times compared to before the bending test. This was much higher than previous films due to the PVDF-Te nanorod films thickness of  $90 \pm 20 \mu\text{m}$  compared to the  $5 \pm 2 \mu\text{m}$  and  $35 \pm 3 \mu\text{m}$  of the  $\text{Bi}_2\text{Te}_3$  nanowires and  $\text{Bi}_{0.4}\text{Sb}_{1.6}\text{Te}_3$  nanoplatelets respectively. Despite the higher bending resistance the composite did not delaminate highlighting its potential use in flexible applications.

Our prototype single-leg p-type FTEG device was fabricated from 5 films of PVDF-Te nanorods with geometries of  $20 \text{ mm} \times 5 \text{ mm} \times 0.09 \text{ mm}$  and electrically connected with silver metal contacts. These nanocomposite films unlike the previous  $\text{Bi}_2\text{Te}_3$  nanowires and  $\text{Bi}_{0.4}\text{Sb}_{1.6}\text{Te}_3$  nanoplatelets are not required to be annealed to achieve measurable power outputs. We observe the highest power output of 50 nW for a thermal gradient of 29.8 K for this FTEG device on a fabric highlighting a potential application in E-textiles. This higher power output was due to the high S achieved by the composite films with the device's voltage per degree per film being  $\sim 625 \mu\text{V K}^{-1}$ . The FTEG device was expected to perform better than observed, however, this was not the case due to the films being oxidised between device fabrication and measuring the device's power output as seen by the six-fold increase in the resistance across the device during that time. To improve the FTEG device an additional sealant layer needs to be applied to the composite films to reduce oxygen exposure to the films and improve device power output stability. As well as parameterising the geometrics of the films to achieve higher power outputs.

## Chapter 7 Conclusions and Future work

TEGs have been shown to be a unique energy harvesting technology that could be used to harvest human body heat to power a variety of recently developed low-power-consuming sensors, displays, communication and other IoT devices [1–5]. However, so far they have been limited to niche applications due to their low efficiency as well as their bulk and rigid nature [7–9,112–114]. However, their general future outlook shows promise with incremental improvements in TE performance allowing for greater energy harvesting applications such as for industrial waste heat recovery. This can be seen in the literature with nanostructured  $\text{Bi}_2\text{Te}_3$ -based nanomaterials at temperatures between 300 K and 450 K reaching a peak ZT of  $\sim 1.5$ , surpassing the current commercial TEGs. Meanwhile, at temperatures between 750 K and 900 K, Bromine-doped Tin selenide has been measured ZT  $\sim 2.7$  [26]. Additionally, printable FTEGs will most certainly play a role in powering wearable IoT devices with the current literature demonstrating devices capable of generating power at the  $\mu\text{W}$  level at thermal gradients as low as 20 K [74,75]. To fully realise this future where TEGs play a greater role in powering wearable devices the remaining gaps in the TE literature such as material flexibility and scalably manufacturing device need to be filled. In this thesis, we aimed to expand the applicable uses of TEGs by improving their flexibility while using scalable methods suitable for industry. Screen-printable polyol synthesised  $\text{Bi}_2\text{Te}_3$ -based nanomaterials and PVDF-Te nanorod composites were presented as a potential route for FTEG devices to expand the applications of TEGs as a power source for E-textile systems and other IoT devices.

### 7.1 Summary of results

We examine using PRS to synthesise  $\text{Bi}_2\text{Te}_3$  nanowires, which after a thorough cleaning process were drop-casted onto Au-coated Si substrates and observed by SEM to have diameters of  $60 \pm 20$  nm, with lengths that ranged from 0.4  $\mu\text{m}$  up to 5  $\mu\text{m}$ . These nanowires' preferred lattice orientation was (0 1 5) and were too resistive to measure any TE properties. It was found that the optimal annealing temperature for these nanowires was 400 °C for 2 hr in an inert Ar atmosphere. The post-annealed drop-casted nanowires were observed to have formed n-type  $\text{Bi}_2\text{Te}_3$  INNs. These INNs achieved a maximum S of  $-220 \pm 20 \mu\text{VK}^{-1}$  and a PF of  $180 \pm 20 \mu\text{Wm}^{-1}\text{K}^{-2}$  at 250 K. The  $\text{Bi}_2\text{Te}_3$  nanowires were then formulated into a novel paste using NMP as the solvent and PVDF as the binding agent. The PRS reaction was scaled-up to ensure enough  $\text{Bi}_2\text{Te}_3$  nanowires to vary the concentration of PVDF binder in the paste formulation. We observe wider and shorter nanowires with an average diameter of  $90 \pm 20$  nm and lengths of between 0.4 and 3  $\mu\text{m}$  when the reaction was scaled-up, however, this does not seem to have a tangible effect on the TE properties of the nanowires once they are annealed.

The binder concentration varied between 5 %, 10 % and 20 % PVDF with the screen-printed PVDF- $\text{Bi}_2\text{Te}_3$  nanowire films annealed at 400 °C for 2 hr in an inert Ar atmosphere. We observed 3 distinct morphologies with the 20 % PVDF films maintaining their nanowire structure, the 10 % and 5 % films having both INNs and nanowires with some 10 % PVDF films having fully formed INNs. The highest non-room temperature S and PF at  $-192 \pm 10 \mu\text{V K}^{-1}$  and a PF of  $36 \pm 7 \mu\text{Wm}^{-1}\text{K}^{-2}$  at 225 K for the screen-printed INNs. The lower PF between the screen-printed INNs versus the drop-casted INNs is due to them being more porous from voids left by the burned-off PVDF. Meanwhile the highest room temperature PF was  $37 \pm 8 \mu\text{Wm}^{-1}\text{K}^{-2}$  for the 5 % PVDF films. We observed a linear, flat and inverse relationship between the PF and temperature for the nanowire, INN and nanowire and fully formed INN morphology respectively.

The linear relationship between PF and temperature for the nanowire morphology as they have a charge carrier concentration in the highly doped semiconductor range while the INNs have it at a lower carrier concentration with their PF being dominated by their S. Meanwhile, the films with both morphologies have a flat relationship between PF and temperature as both morphologies cancel out the other. Due to the higher PF, 5 % was chosen as the optimal binder content for the screen-printed films. A bending test of 1000 bending cycles at a bending radius of 10 mm was performed where we observe lower bending-induced resistance in the screen-printed films on Kapton than in their drop-casted counterparts by a factor of 4. Finally, a single-leg n-type prototype FTEG device was fabricated with 5 films of screen-printed  $\text{Bi}_2\text{Te}_3$  nanowires on Kapton which was connected with silver metal contacts and obtained a maximum voltage and power output at a thermal gradient of 31.9 K of  $\sim 19$  mV and  $\sim 7$  nW respectively.

Steps were taken to improve the TE properties of the  $\text{Bi}_2\text{Te}_3$  nanowires by alloying them with Se. This alloying process occurred during the PRS reaction as the nanowires were being synthesised. A Se precursor was added to the PRS reaction before the Bi precursor with the resulting nanowires having a thinner average diameter than the  $\text{Bi}_2\text{Te}_3$  nanowires of  $32 \pm 8$  nm. The nanowires' GIXRD matched to a  $\text{Bi}_2\text{Te}_{2.5}\text{Se}_{0.5}$  crystal structure with a preferred lattice orientation of (0 1 5). These nanowires were formulated into pastes and screen-printed onto Kapton alongside  $\text{Bi}_2\text{Te}_3$  nanowires, with 1 and 3 printing passes for each material to observe how the materials' film thickness affects their TE properties. These screen-printed films had 5 % PVDF and were annealed at 400 °C for 2 hr in an inert Ar atmosphere. The  $\text{Bi}_2\text{Te}_3$  nanowires were shown to have higher room temperature TE properties than the  $\text{Bi}_2\text{Te}_{2.5}\text{Se}_{0.5}$  nanowires. In both materials, the thinner films were shown to have a higher PF than the thicker films. Both materials had an S of  $-140 \pm 10 \mu\text{VK}^{-1}$ , however, the  $\text{Bi}_2\text{Te}_{2.5}\text{Se}_{0.5}$  had a lower  $\sigma$  which was due to an observed lower carrier concentration. This lower carrier concentration was believed to be due to Bi antisite defects formed on Te and Se sites in the  $\text{Bi}_2\text{Te}_{2.5}\text{Se}_{0.5}$  crystal structure.

These Bi antisite defects were identified from the GIXRD peak shifts between the annealed screen-printed  $\text{Bi}_2\text{Te}_{2.5}\text{Se}_{0.5}$  nanowires and their unannealed drop-casted counterpart. As well as an EDX data showing an increase in the Bi content at the expense of the Te and Se content after annealing. These Bi antisite defects provided hole charge carriers to the films lowering their overall n-type carrier concentration as seen in the literature for the same alloy compositions <sup>[100,102,104]</sup>. Both films underwent a bending test of 1000 bending cycles at a bending radius of 10 mm. Both had increased resistances due to bending, however, there was a noticeable 2 % difference in favour of the  $\text{Bi}_2\text{Te}_{2.5}\text{Se}_{0.5}$ . Both films were flexible enough to be used in an FTEG device. However, when comparing all the TE properties for both materials as well as extra work needed to alloy the nanowires, we believe it would be best to use 1 printing pass of  $\text{Bi}_2\text{Te}_3$  nanowires for our n-type material in an FTEG device.

Post-annealing a portion of the thin  $\text{Bi}_2\text{Te}_3$  nanowires screen-printed film had formed INNs which had an  $S$  of  $-190 \pm 10 \mu\text{VK}^{-1}$  and a PF of  $130 \pm 40 \mu\text{Wm}^{-1}\text{K}^{-2}$ . This was notably higher than the PF seen for the INNs screen-printed with 10 % PVDF and is due to the fewer PVDF-induced voids forming from the PVDF being burnt off. This further highlights the need to better understand the INN formation process and whether such INNs could be formed from other  $\text{Bi}_2\text{Te}_3$ -based nanowires, as well as, how this would affect such INNs' TE performance, which could be the study of future work.

We then used PRS to synthesised p-type  $\text{Bi}_{0.4}\text{Sb}_{1.6}\text{Te}_3$  nanoplatelets instead of nanowires seen in the literature for similar reactions, as a result of replacing the reducing agent anhydrous hydrazine with hydrazine hydrate in the PRS reaction <sup>[36,53]</sup>. The nanoplatelets were observed to have lengths between 100 nm and 350 nm as well as a thickness of  $15 \pm 5$  nm. The nanoplatelets had preferred lattice orientations of (0 1 5) and unlike the nanowires were conductive enough to obtain a room temperature  $S$  of  $\sim 140 \pm 10 \mu\text{V K}^{-1}$ , however, due to the films' poor electrical properties, the PF was  $< 1 \mu\text{Wm}^{-1}\text{K}^{-2}$ . The PRS reaction for the nanoplatelets was scaled up by a factor of 5 with no noticeable changes in the nanoplatelets' crystal structure or atomic composition. The only change was the more varied nanoplatelet lengths between 90 nm and 650 nm. The drop-casted films of these nanoplatelets still have a room temperature  $S$  of  $\sim 140 \pm 10 \mu\text{V K}^{-1}$ , showcasing the scalability of the PRS method. The nanoplatelets were formulated into pastes using the same method as with the  $\text{Bi}_2\text{Te}_3$  with 5 % PVDF. Two films were produced with 1 and 4 printing passes and annealed at 450 °C for 10 mins in an inert Ar atmosphere as Chen et al <sup>[53]</sup> showed that these annealing parameters could improve the  $\text{Bi}_{0.5}\text{Sb}_{1.5}\text{Te}_3$  TE properties compared to 400 °C for 2 hr used for  $\text{Bi}_2\text{Te}_3$  nanowires. However, the films' PFs were  $1.46 \pm 0.08 \mu\text{Wm}^{-1}\text{K}^{-2}$  and  $5.0 \pm 0.3 \mu\text{Wm}^{-1}\text{K}^{-2}$  for the 1 and 4 print passes respectively. These low PFs were the result of an oxidation effect caused when the nanoplatelets were bath sonicated in NMP at above room temperature.

This was mitigated in further paste formulations by ice bath sonicating the pastes and ensuring the temperature remained below room temperature. A novel Te nanorod additive study was conducted with the  $\text{Bi}_{0.4}\text{Sb}_{1.6}\text{Te}_3$  nanoplatelet films by ranging the concentration of the Te nanorods screen-printed films from 0 % to 20 % in steps of 4 %. The films were then annealed at 450 °C for 1 hr in an inert Ar atmosphere. The films regardless of Te nanorod concentration showed the sample 3 distinct morphologies, we observe cauliflower-like microstructures on the order of  $>10\ \mu\text{m}$  in size, followed by smaller microplatelets  $<10\ \mu\text{m}$  in size and amorphous nanoparticles ranging between  $\sim 50\ \text{nm}$  and  $500\ \text{nm}$  in length. The room temperature TE properties were obtained for the films where we observe an improvement by a factor of 3.3 times in the PF from  $16 \pm 2\ \mu\text{Wm}^{-1}\text{K}^{-2}$  to  $54 \pm 6\ \mu\text{Wm}^{-1}\text{K}^{-2}$  for the 0 % and 12 % films respectively.

This improvement was observed due to a near doubling of  $S$  as the films went from an  $S$  of  $113 \pm 8\ \mu\text{V K}^{-1}$  to  $220 \pm 20\ \mu\text{V K}^{-1}$  for the 0 % and 20 % films respectively. However, this increase in  $S$  was coupled with a decrease in  $\sigma$  for all films except for the 12 % films which maintained their  $\sigma$  by having higher carrier mobility, which was associated with the expansion in the grain size from  $24 \pm 2\ \text{nm}$  to  $33 \pm 4\ \text{nm}$  for the 0 % to 12 % films respectively. The increase in the grain size was due to the Te nanorods liquifying and acting as a grain coalescing agent and interface for the nanoplatelets [81]. The same bending test was conducted on the annealed PVDF- $\text{Bi}_{0.4}\text{Sb}_{1.6}\text{Te}_3$  nanoplatelet + 12 % Te nanorod film where we observe an increase of 12 % in the film's resistance due to bending damage, which is higher than what was observed for the n-type screen-printed films. This increase in bending-induced damage was due to the p-type film being thicker than the previously measured n-type films. The p-type film maintains its structure and the low bending resistance shows its compatibility for flexible applications. An FTEG with three thermocouples of p-type PVDF- $\text{Bi}_{0.4}\text{Sb}_{1.6}\text{Te}_3$  nanoplatelet + 12 % Te nanorod films and n-type PVDF- $\text{Bi}_2\text{Te}_3$  nanowire films was screen-printed onto Kapton. The TE legs were electrically connected via a silver metal contact. The FTEG device experienced a maximum temperature difference, voltage and power output of 35.9 K, 40 mV and 27 nW. However, this power output falls short of other devices in the literature [74,75,77,80]. This can be put down to non-optimal annealing conditions for the n-type film while the delays from device fabrication to measuring resulted in partial oxidation of the device reducing its performance.

Based on the results from this work we have met our objective of identifying and proving PRS as a viable synthesis route for the scalable production of  $\text{Bi}_2\text{Te}_3$ -based nanomaterials as shown by the reaction's ability to be scaled up. However, as seen in the characterisation of these nanomaterials such scaling-up needs to alter the duration of the PRS to achieve the same product. Though the changes in the nanowire morphology as observed so far have not affected the overall TE performance.

Concerning the overall aim of this project, the discovery of the INNs has been the most notable result, as their high TE performance at low temperatures makes them an ideal material to be integrated into an FTEG device for arctic clothing. However, more work still needs to be done to fully understand the formation mechanism of these INNs as shown by the disparity between screen-printed and drop-casted INNs. Additionally, thought must be put into how to achieve INNs and how best to integrate them into clothing that would otherwise not stand to the high annealing temperatures in the INN formation process. Finally, we can conclude from the data presented here that the NMP-PVDF can act as a viable paste formulation for the scalable screen-printing of flexible Bi<sub>2</sub>Te<sub>3</sub>-based nanostructured films as seen by the low resistance increases from the bending study. However, as high annealing temperatures are needed for these films to act as FTEGs, it would not be possible to print these materials directly onto fabrics without printing them onto Kapton and integrating the Kapton into clothing.

This would run into the same complex issue of integrating the devices individually onto an article of clothing as seen in Leonov et al <sup>[5]</sup>, however, these devices would solve the issue of user comfort by being lightweight and flexible and as such more of them could be integrated into the E-textile system. Additionally, though the NMP-PVDF can produce flexible films this comes at the cost of the films' TE performance due to PVDF-induced voids. To reduce the effect of voids on film performance further investigations into post-printing processes need to be conducted in tandem with how best to integrate these materials into fabrics.

Finally, the Te nanorods were shown to be conducive enough to obtain TE measurements after screen-printing them with the PVDF binder while maintaining a high room temperature  $S$  of  $440 \pm 10 \mu\text{V K}^{-1}$ . They were then formulated into screen-printable pastes with a 5 % PVDF binder and screen-printed onto Kapton and obtained the highest room temperature PF for a non-annealed film of  $2.7 \pm 0.7 \mu\text{Wm}^{-1}\text{K}^{-2}$ . The Te nanorod PRS reactions were scaled-up by a factor of 5, where it was discovered that the nanorods grew out of dice-shaped seed nanostructures. This gave us an insight into the growth step of the PRS reaction where the Te nanocrystals agglomerate into these dice-shaped seeds and then due to the reaction conditions the Te nanorods grow out of them until all the Te atoms in the seed nanoparticles were used. These scaled-up Te nanorods had a room temperature  $S$  of  $540 \pm 40 \mu\text{V K}^{-1}$ , this increase in  $S$  is associated with this extra dice-shaped morphology. Composite films of PVDF-Te nanorods were screen-printed onto a polyurethane-based interface layer on a polyester-cotton substrate. The same bending test as performed previously was conducted causing a bending-induced resistance in the film which increase the film resistance by 2.25 times compared to before the bending test. This was much higher than previous films due to the composite film's thickness of  $90 \pm 20 \mu\text{m}$  compared to the  $5 \pm 2 \mu\text{m}$  and  $35 \pm 3 \mu\text{m}$  of the Bi<sub>2</sub>Te<sub>3</sub> nanowires and Bi<sub>0.4</sub>Sb<sub>1.6</sub>Te<sub>3</sub> nanoplatelets respectively.

This shows the limit to the adhesive properties of the PVDF binder though the binder concentrations used were to maximise TE performance and INN formation for annealed  $\text{Bi}_2\text{Te}_3$  nanowires. So far it is yet to be seen how detrimental a higher PVDF content will be for these composites' TE performance when compared to enhancing the composites' flexibility. Despite the higher bending resistance, the composite did not delaminate highlighting its potential use in flexible applications. The composite films on the polyurethane-based interface were electrically connected with silver metal contacts and fashioned into a prototype single-leg p-type FTEG device with 5 legs and geometries of 20 mm x 5 mm x 0.09 mm. The highest voltage and power output for the E-textile compatible FTEG device was 95 mV and 50 nW respectively for a thermal gradient of 29.8 K. This higher power output compared to the previous devices was due to the high  $S$  achieved by the composite films with the device's voltage per degree per film being  $\sim 625 \mu\text{V/K}$ .

The FTEG device was expected to perform better than observed, however, this was not the case due to the films being oxidised. This caused a six-fold increase in the resistance across the device between when the device was fabricated to just before the device's power output was measured. This shows that post-fabrication sealing layers need to be added to such devices to extend their operational lifetimes.

## 7.2 Future work

The PRS reactions in both n-type and p-type cases can be re-examined to find reactions that can achieve the same product without the use of highly toxic substances such as hydrazine hydrate. As well as investigating whether it is possible to achieve  $\text{Bi}_{0.5}\text{Sb}_{1.5}\text{Te}_3$  nanowires using PRS without the need for anhydrous hydrazine. This can be done by exploring the full reach of the EG reduction reaction on the precursor chemicals as well as other less harmful reducing agents such as ascorbic acid.

Further work would need to be carried out to better optimise the annealing conditions for the screen-printed films of  $\text{Bi}_2\text{Te}_3$  nanowires and the  $\text{Bi}_{0.4}\text{Sb}_{1.6}\text{Te}_3$  nanoplatelets. The annealing conditions need to allow for the formation of INNs in the  $\text{Bi}_2\text{Te}_3$  nanowire films, while also enabling the complete liquefaction of the Te nanorod additives in the  $\text{Bi}_{0.4}\text{Sb}_{1.6}\text{Te}_3$  nanoplatelet films. We have already examined that 5 % PVDF is ideal for these nanomaterials. However, other polymer-based binding agents should be examined to observe if they can improve over the PVDF in film flexibility as well as not hinder the TE properties of the composite films. Additionally, the NMP solvent should be replaced due to its toxic nature, with another greener solvent.

Additionally, in the case of  $\text{Bi}_2\text{Te}_3$  INNs, an annealing study should be conducted to investigate whether it is possible to form  $\text{Bi}_2\text{Te}_3$  INNs as a powder which could then be formulated into a conductive TE screen-printable paste. Additionally, post-printing processes such as the mechanical compression of the screen-printed films should be investigated to reduce the number of voids in these films and densify them to improve TE performance.

To extend the work presented in the thesis an additional study into the controlling of the Se alloying of  $\text{Bi}_2\text{Te}_3$  nanowires needs to be looked into as we were not able to achieve the ideal alloy of  $\text{Bi}_2\text{Te}_{2.7}\text{Se}_{0.3}$  for the nanowires. As well only one particular alloy was investigated so for these nanowires other alloys could achieve higher TE performances over the  $\text{Bi}_2\text{Te}_3$  nanowires. Additionally, an annealing study should be conducted to observe if these Se alloyed nanowires can form INNs.

For the further development of the FTEGs, a study into a screen-printable electrode material should take place to identify a material with optimal electronic properties for both n-type and p-type materials, while also being flexible. Additionally, a computational study could be advantageous in discovering geometric parameters more suited to the flow of heat in the device to maximise power output.

Finally, for the PVDF-Te nanorod composite more work on understanding the TE behaviour of the dice-shaped seed nanoparticles could be an avenue for increasing  $S$  further than what has already been achieved. This can be done by taking samples out of the mixture during the PRS to better understand the synthesis process of these Te nanorods. Additionally, a study into annealing the Te nanorods as a powder before formulating the paste could result in improving the composite TE performance. For the FTEG device, further work to improve the power output can be achieved by incorporating different conductive polymers such as poly (3,4-ethylene dioxythiophene) polystyrene sulfonate (PEDOT:PSS) or polyaniline (PANI) into the composite films to improve their electrical properties and film flexibility.



## Appendix A [Optimising post-printing annealing process for screen-printed 20 % PVDF-Bi<sub>2</sub>Te<sub>3</sub> nanowire films]

Initial screen-printed composite films were made using the paste formulation method of section 2.21. The as-printed films were made from 20 % PVDF and 80 % Bi<sub>2</sub>Te<sub>3</sub> nanowires and were printed onto polyester-cotton and Kapton with a print gap of 0.5 mm for one print as shown in Fig.A.1:

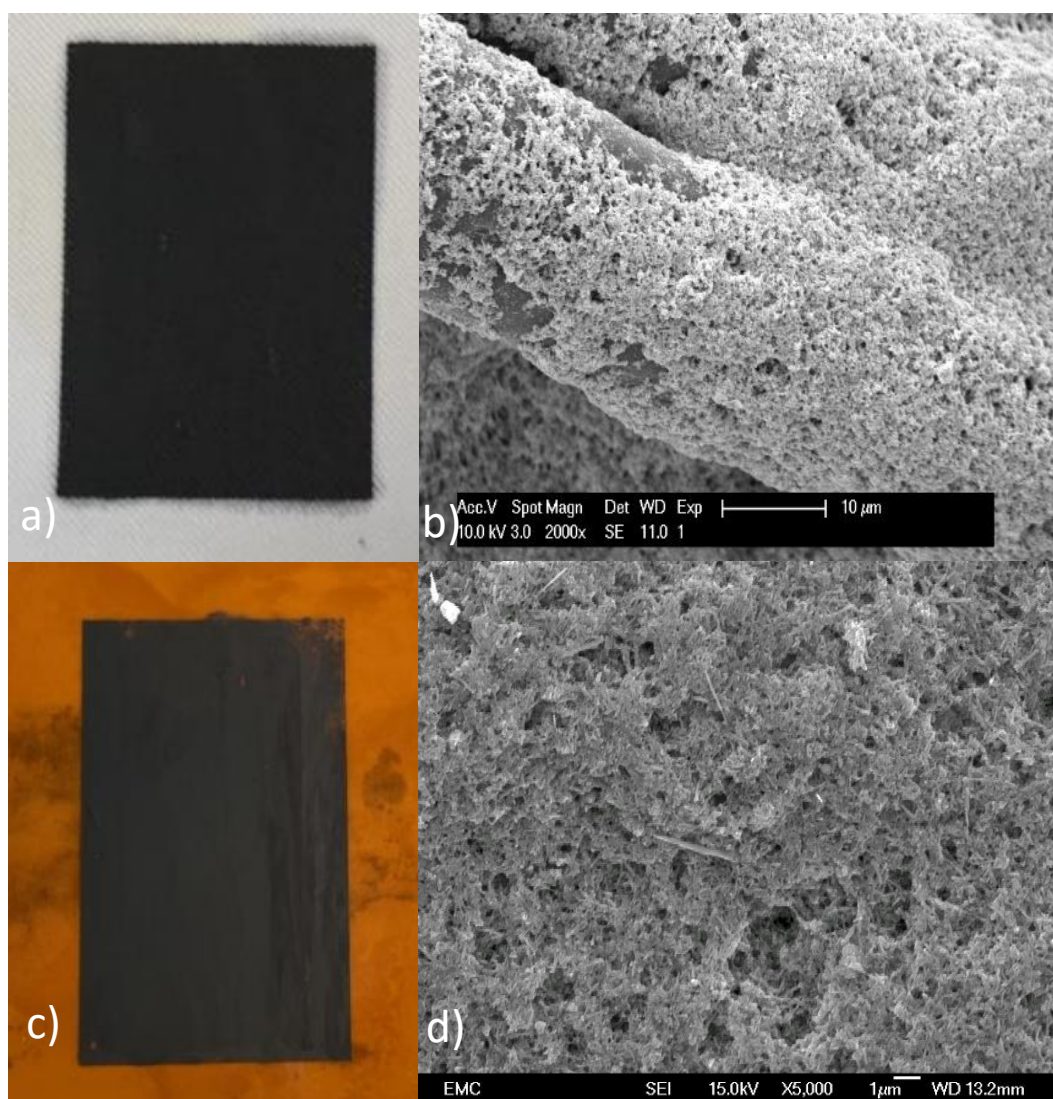


**Fig.A.1-** Photograph (a) of screen-printed 20% PVDF-Bi<sub>2</sub>Te<sub>3</sub> nanowire film on polyester cotton ~200 μm with (b) an SEM image of one of the polyester-cotton fibres coated by the composite and (c) an image of the screen-printed 20% PVDF-Bi<sub>2</sub>Te<sub>3</sub> nanowire film on a Kapton substrate with (d) an SEM image of the Bi<sub>2</sub>Te<sub>3</sub> nanowire film on a Kapton annealed at 300 °C for 1 hr in an inert Ar atmosphere.

## Appendix A

The films were dried at 140 °C for 1 hr, however, the films were not conductive due to the high concentration of PVDF and needed to be annealed. The initial composite film of PVDF-Bi<sub>2</sub>Te<sub>3</sub> (20/80) on Kapton was annealed at 200, 250 and 300 °C for 1 hr in an inert Ar atmosphere in a tube furnace.

The resulting films visually and via SEM looked identical to Fig.A.1(c&d). EDX also shows a ~38:62 split for Bi and Te atomic ratios respectively, which is within the error of the detector for stoichiometric Bi<sub>2</sub>Te<sub>3</sub>. The slight decrease in Bi content compared to section 3.1 is due to the decrease in Bi precursor from 1.07 g to 1 g. Additionally, we observed as the annealing temperature increased, the oxygen content of the films decreased from 20 % to 13 % with respect to Bi and Te. While the fluorine representing the PVDF increased from 35% to 47% with respect to Bi and Te. This would indicate a burning off of oxide species on the nanowires, while the increase in the fluorine could be due to improper mixing of the binder during paste formulation and that more rigorous mixing is needed instead of using a magnetic stirrer bar to mix the two materials. As such further paste formulations used the method described in section 2.22.

Interestingly the annealed films' GIXRD as shown in Fig.A.2 showed a broad peak between 20 ° and 25 ° with the peak intensity decreasing at higher annealing temperatures. This shoulder was not seen in Fig.3.2 or Fig.3.4 and is thus attributed to the breaking down of the PVDF crystal structure before it would get burned off at higher temperatures. The GIXRD data confirms the Bi<sub>2</sub>Te<sub>3</sub> structure with the (0 1 5) orientation being the most pronounced as in the other GIXRD graphs. Due to a reduction in the amount of Bi precursor used in the PRS reaction, we do not observe the sharp peak seen in Fig. 3.4.

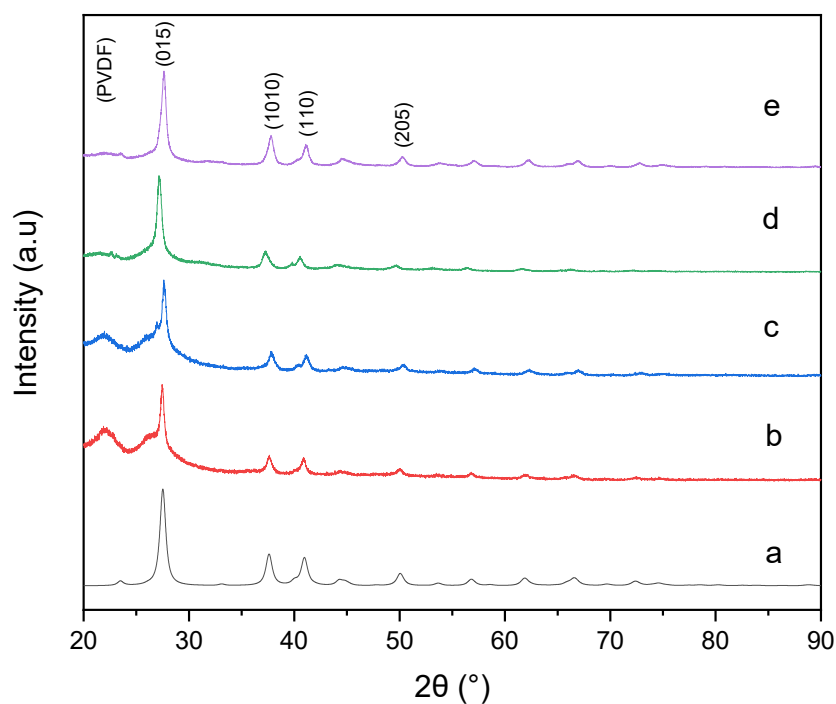


**Fig.A.2-** GIXRD diffraction patterns obtained for (a) reference XRD of tellurobismuthite ( $\text{Bi}_2\text{Te}_3$ ) mineral from International Centre of Diffraction Data (ICDD) database (PDF 01-082-0358) (b) unannealed screen-printed 20% PVDF- $\text{Bi}_2\text{Te}_3$  nanowires, (c) screen-printed  $\text{Bi}_2\text{Te}_3$  nanowires annealed in an inert Ar atmosphere at (c) 200  $^\circ\text{C}$ , (d) 250  $^\circ\text{C}$  and (e) 300  $^\circ\text{C}$  for 1 hr.

To confirm when the PVDF would break down and burn a thermogravimetric analysis (TGA) measurement was taken in an inert nitrogen environment and is shown in Fig.A.3:

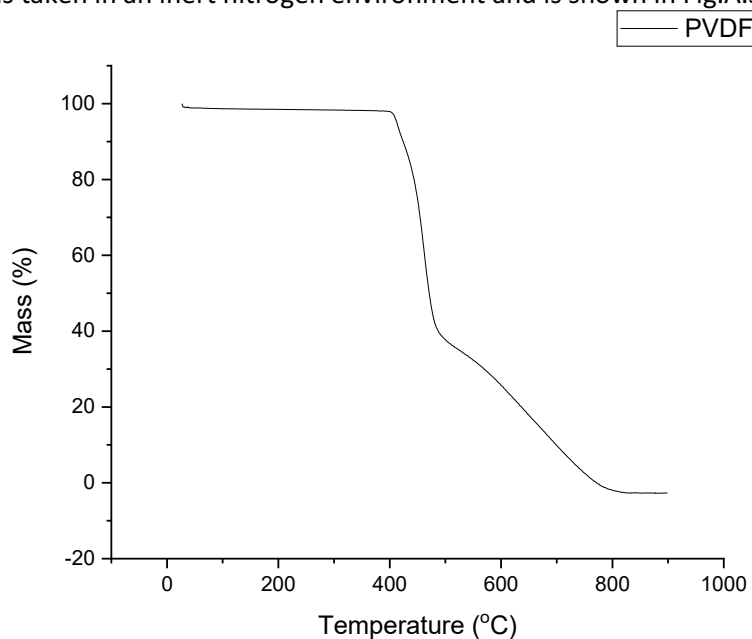


**Fig.A.3-** TGA of PVDF powder from the range of 30  $^\circ\text{C}$  to 900  $^\circ\text{C}$  in a nitrogen inert environment.

## Appendix A

The TGA shows the reduction of PVDF mass between 400 °C and 500 °C, this can be used as an indication of the PVDF starting to burn off. However, there is a 0.5 % drop in mass between 300 °C and 400 °C which could support the PVDF starting to break down as seen in the GIXRD data in Fig. A.2.

Only the film annealed at 300 °C was conductive enough to have its TE properties measured. As such the PVDF-Bi<sub>2</sub>Te<sub>3</sub> nanowire film on Kapton was also annealed at 300 °C for a duration of 4 hr to observe how the annealing duration could affect the film's TE properties. There was no morphological or crystal structure change with the main distinction between the films being that the oxygen had increased from 13 % to 16 % and the fluorine decreased from 47 % to 26 %. The longer duration did result in a higher TE performance as shown in Table A.1.

**Table A.1-** The TE properties of annealed Bi<sub>2</sub>Te<sub>3</sub> films on Kapton at room temperature. The Seebeck coefficient was measured with the portable Seebeck probe. The results are an average of multiple measurements with the error being the standard deviation of the average for the Hall probe results and the 7 % error of the portable Seebeck probe.

Annealing time (hr)	Mobility (cm <sup>2</sup> /V.s)	Carrier concentration (cm <sup>-3</sup> )	Electrical conductivity (S/m)	Seebeck coefficient (μV/K)	Power factor (μWm <sup>-1</sup> K <sup>-2</sup> )
1	0.5 ± 0.4	-1.0 ± 1 × 10 <sup>19</sup>	59.1 ± 0.1	-140 ± 10	1.15 ± 0.08
4	5 ± 2	-3.0 ± 1 × 10 <sup>18</sup>	172.0 ± 0.4	-127 ± 9	2.8 ± 0.2

Using the paste formulation method of section 2.22 films were screen-printed onto silicon (Si) and silicon dioxide/silicon (SiO<sub>2</sub>/Si) wafer pieces as seen in Fig. A.4. The change in the substrate was to allow the films to be annealed at higher temperatures (>300 °C).



**Fig.A.4-** Image of 20% PVDF-Bi<sub>2</sub>Te<sub>3</sub> films printed onto (left) SiO<sub>2</sub>/Si and (right) Si wafer pieces.

The films were annealed from 300 to 500 °C in steps of 50 °C for 1 hr in the tube furnace in an inert Ar atmosphere. The EDX data of the films showed an approximate 40:60 split of the atomic ratios for Bi and Te respectively for all the films except for the film annealed at 500 °C which had a 45:55 split for Bi and Te respectively. The fluorine content in the films decreased with respect to the Bi and Te atomic ratios from 25.7 % to 0 %. The GIXRD data shown in Fig. A.5 reveal a preferential orientation of (0 1 5) phase for  $\text{Bi}_2\text{Te}_3$  with no broad shoulder as was seen in Fig. A.2.

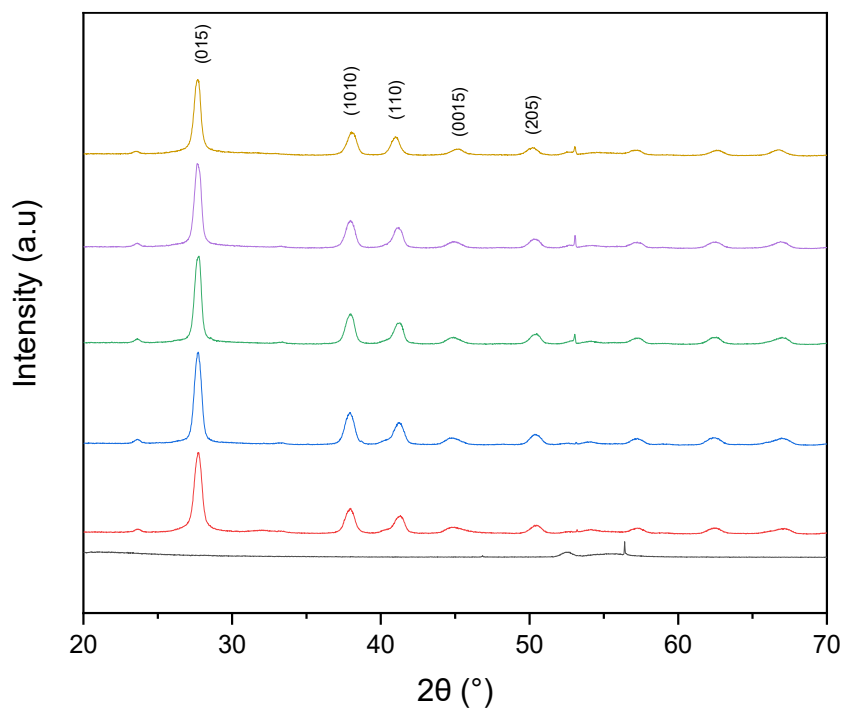


**Fig.A.5-** GIXRD diffraction patterns obtained for (a) the  $\text{SiO}_2/\text{Si}$  substrate, (b) reference XRD of tellurobismuthite ( $\text{Bi}_2\text{Te}_3$ ) mineral from International Centre of Diffraction Data (ICDD) database (PDF 01-082-0358), screen-printed 20% PVDF- $\text{Bi}_2\text{Te}_3$  nanowires annealed in an inert Ar atmosphere at (c) 300 °C, (d) 350 °C, (e) 400 °C, (f) 450 °C and (g) 500 °C for 1 hr.

The annealed screen-printed films TE data at room temperature was measured as shown in Table A.2. Two additional films on Si and  $\text{SiO}_2$  were annealed at the annealing conditions of Chen et al <sup>[57]</sup> with inert Ar replacing their FGA environment.

**Table A.2-** The TE properties of annealed 20% PVDF-Bi<sub>2</sub>Te<sub>3</sub> films on Si and SiO<sub>2</sub>/Si at room temperature. The Seebeck coefficient was measured with the portable Seebeck probe. The results are an average of multiple measurements with the error being the standard deviation of the average for the Hall probe results and the 7 % error of the portable Seebeck probe.

Annealing temperature (°C)	Annealing duration (hr)	Substrate	Mobility (cm <sup>2</sup> /V.s)	Carrier concentration (cm <sup>-3</sup> )	Electrical conductivity (S/m)	Seebeck coefficient (μV/K)	Power factor (μWm <sup>-1</sup> K <sup>-2</sup> )
300	1	SiO <sub>2</sub>	0.5 ± 0.5	-1 ± 1 × 10 <sup>19</sup>	30 ± 20	-104 ± 8	0.3 ± 0.2
350	1	SiO <sub>2</sub>	0.7 ± 0.5	-9 ± 1 × 10 <sup>19</sup>	500 ± 200	-80 ± 6	3 ± 1
400	1	SiO <sub>2</sub>	0.5 ± 0.5	-3 ± 4 × 10 <sup>20</sup>	300 ± 30	-85 ± 6	2.2 ± 0.3
450	1	SiO <sub>2</sub>	0.8 ± 0.7	-5 ± 4 × 10 <sup>19</sup>	300 ± 100	-81 ± 6	2 ± 0.7
500	1	SiO <sub>2</sub>	1 ± 1	-2 ± 3 × 10 <sup>20</sup>	400 ± 300	-67 ± 5	2 ± 1
400	2	SiO <sub>2</sub>	2.71 ± 0.02	-7.00 ± 0.05 × 10 <sup>18</sup>	298.21 ± 0.04	-132 ± 9	5.2 ± 0.4
400	2	Si	1.6 ± 0.5	-3.0 ± 0.5 × 10 <sup>19</sup>	700 ± 100	-119 ± 8	10 ± 2

The TE data show that the most ideal annealing temperature for the PVDF-Bi<sub>2</sub>Te<sub>3</sub> nanowire films is 400 °C for 2 hr in an inert Ar atmosphere. This is due to higher annealing temperatures reducing the thermopower of the films while too low a temperature causes the films to be too resistive with PFs < 2 μWm<sup>-1</sup>K<sup>-2</sup>. Additionally, from Fig 3.9 the annealing temperature is also a temperature where the PVDF binder can be mostly burned off and improve the Bi<sub>2</sub>Te<sub>3</sub> nanowires TE properties as shown in table 3.2 and in the literature from Chen et al <sup>[57]</sup>.

## Appendix B [Screen-printing annealed Bi<sub>2</sub>Te<sub>3</sub> nanowire powders]

As a result of the high annealing temperature needed to obtain a reasonable TE performance from the screen-printed Bi<sub>2</sub>Te<sub>3</sub> nanowire films, it was not possible to incorporate the films into E-textiles. However, a potential procedure was conceived that could allow for Bi<sub>2</sub>Te<sub>3</sub> nanowire films to be printed onto fabrics without any post-printing annealing. Instead of annealing the Bi<sub>2</sub>Te<sub>3</sub> nanowires after screen-printing, the nanowires would be annealed before formulating the paste. The powder as-synthesised was poured into a crucible and placed in the same tube furnace as previously used at 400 °C for 2 hr in an inert Ar atmosphere, Fig. B.1 shows the resulting morphology and powder post-annealing.

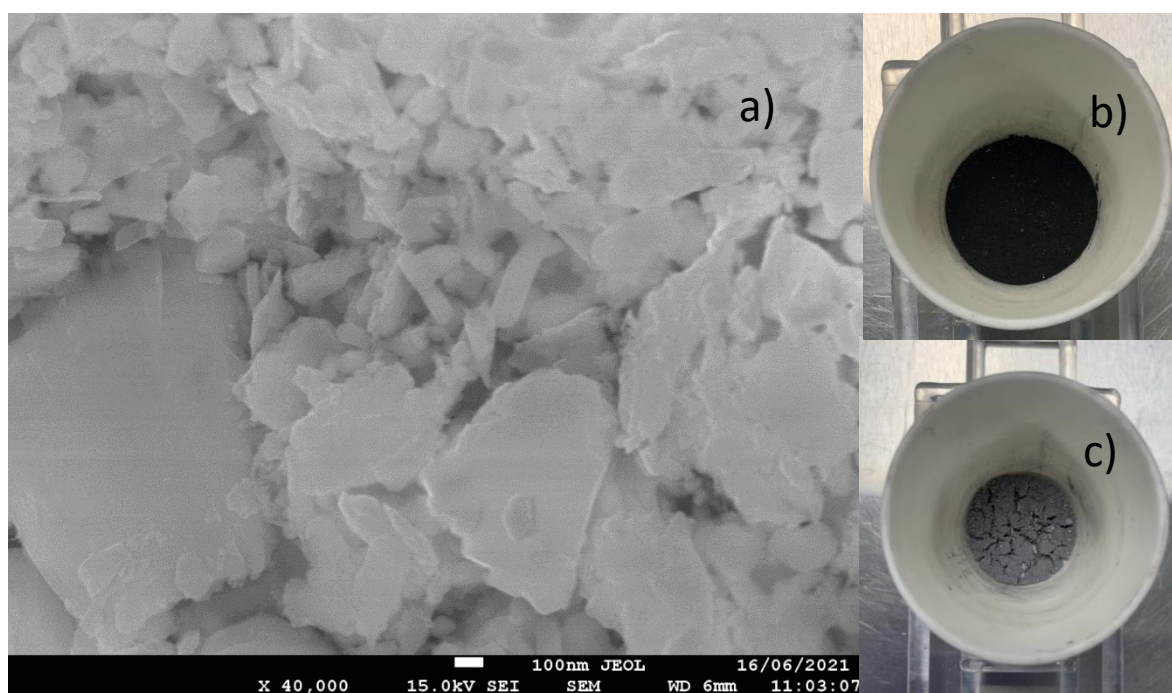


**Fig.B.1-** An (a) SEM image of drop-casted annealed Bi<sub>2</sub>Te<sub>3</sub> nanowires on a Si substrate. Images of the nanowire powder before (b) and after (c) annealing at 400 °C for 2 hr in an inert Ar atmosphere.

As seen in Fig.B.1 the Bi<sub>2</sub>Te<sub>3</sub> loses its 1D nanowire structure seen in Fig. 3.1, this is also visually seen with the black powder turning grey indicating a reduction in the scatter point in the powder which is seen in the SEM image with amorphous particles. What potentially occurred was the nanowires deformed/broken down from the higher annealing and agglomerated together to form these amorphous particles. This is due to the higher surface area of the powder compared to the films both drop-casted and screen-printed, causing the individual particles to be greater affected by the annealing.

The EDX data for these annealed  $\text{Bi}_2\text{Te}_3$  particles showed a close stoichiometric ratio of  $\sim 39:61$  for Bi:Te respectively, with the oxygen content at  $\sim 26\%$  with respect to Bi and Te. Unfortunately, the drop-casted film for this annealed powder was too resistive to obtain accurate TE measurements, which is blamed on poor charge carriers' mobility, as the carriers would lose energy jumping from one particle to the next. Though with more research a viable  $\text{Bi}_2\text{Te}_3$  powder with 1D nanostructures could be obtained in theory, though this is believed to be best saved for future work.

As the annealed powders were too resistive to formulate a paste with, another alternative route was examined. This procedure took the wet powder after the cleaning stage and dispersed it into ethanol and drop-casted the whole dispersion over a wide enough substrate. The dispersion was drop-casted onto 8 microscope glass slides (76 mm x 26 mm) and annealed at  $400\text{ }^\circ\text{C}$  for 2 hr in an inert Ar atmosphere as seen in Fig.B.2.

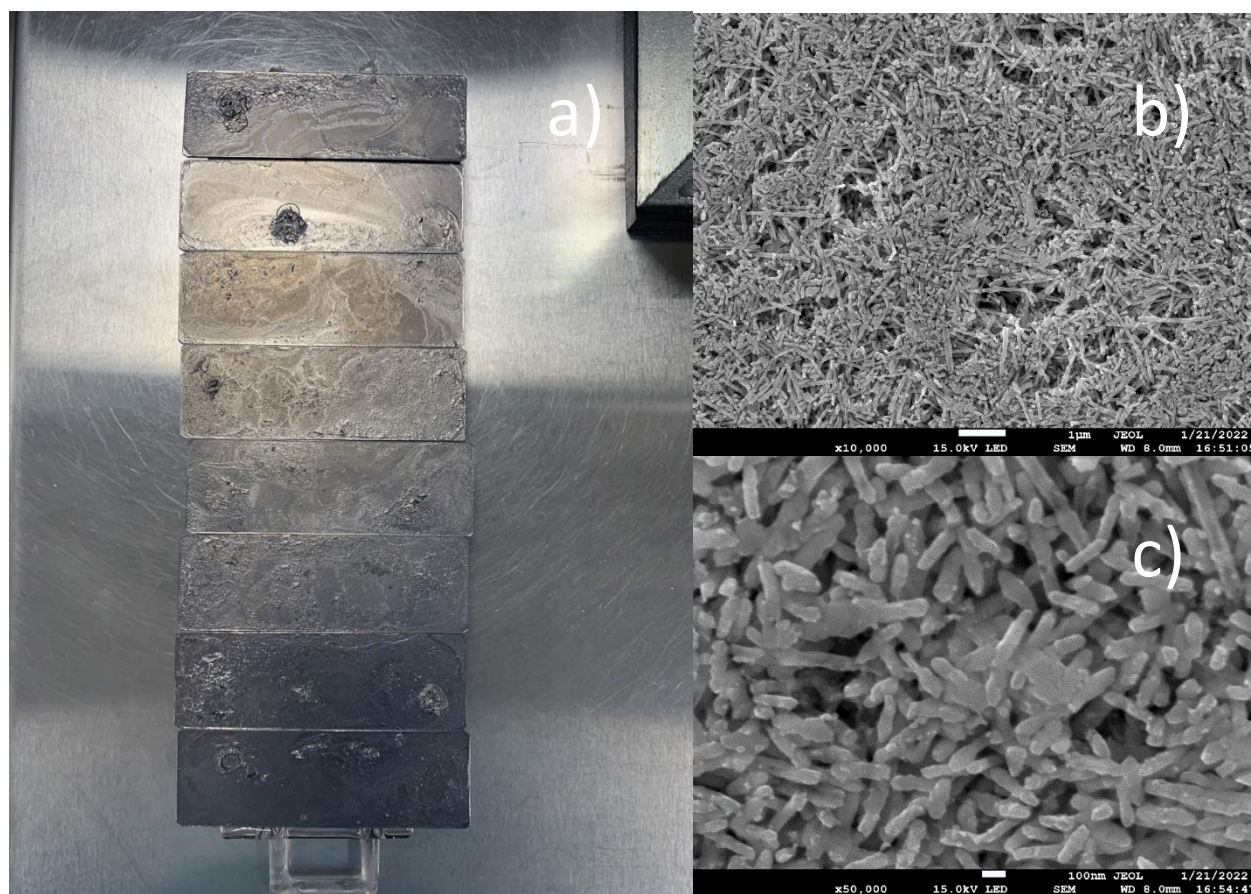


**Fig.B.2-** Image (a) of annealed drop-casted  $\text{Bi}_2\text{Te}_3$  nanowire films, with (b-c) SEM images.

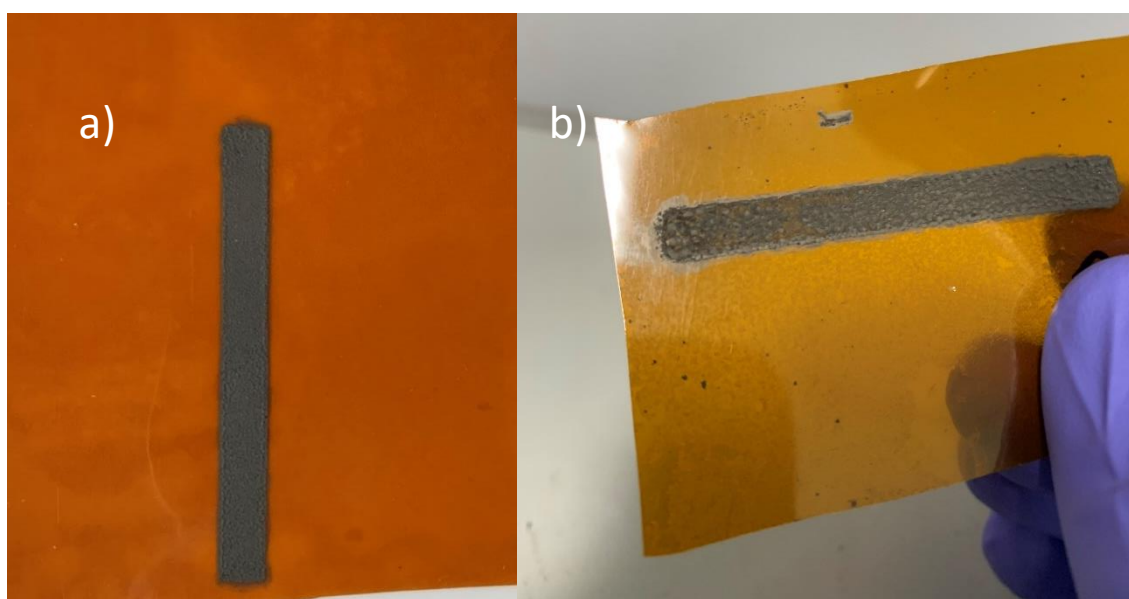
The annealed  $\text{Bi}_2\text{Te}_3$  nanowire films had a room temperature  $S$  ranging from  $-80 \pm 6\text{ }\mu\text{V/K}$  for thicker sections of the film to  $-180 \pm 10\text{ }\mu\text{V/K}$  for thinner parts. Though most of the films had an  $S$  of  $-80\text{ }\mu\text{V/K}$  and were much thicker than the drop-casted films used to get the initial variable temperature measurements in Fig.3.5.

From the SEM images as seen in Fig.B.2b and Fig.B.2c the nanowires retain their 1D structure though some do appear to be shorter with some having melted together similar to what is seen with INNs which could explain the high S for some parts of the films.

The annealed Bi<sub>2</sub>Te<sub>3</sub> nanowires were then scraped off the glass substrates and formulated into a paste as described in section 2.23 and printed onto a Kapton substrate. However, the TE properties of these screen-printed films of annealed Bi<sub>2</sub>Te<sub>3</sub> nanowires with 5% PVDF had a PF < 0.01  $\mu\text{Wm}^{-1}\text{K}^{-2}$  at room temperature due to a very low  $\sigma$  < 1 S/m, while S remained moderate at  $-85 \pm 6 \mu\text{V/K}$ . This is too low to be considered to be used in E-textiles. The poor performance is believed to be due to the drop-casted films being too thick to properly anneal the nanowires resulting in the low S and  $\sigma$ . More work needs to be placed into finding the optimal thickness and annealing conditions to obtain a drop-casted film of Bi<sub>2</sub>Te<sub>3</sub> nanowires that can overcome the resistive properties of the PVDF when both materials are screen-printed together in a composite film.

## Appendix C [Screen-printed $\text{Bi}_{0.4}\text{Sb}_{1.6}\text{Te}_3$ nanoplatelets using a DMSO-PVDF paste formulation]

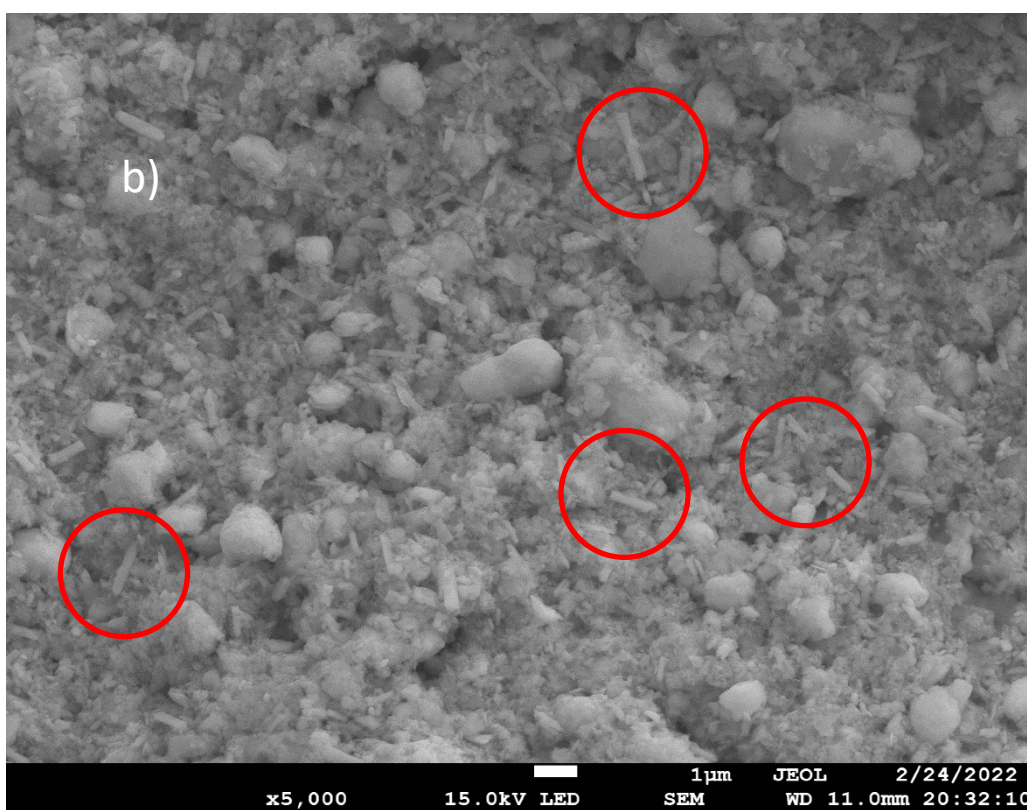
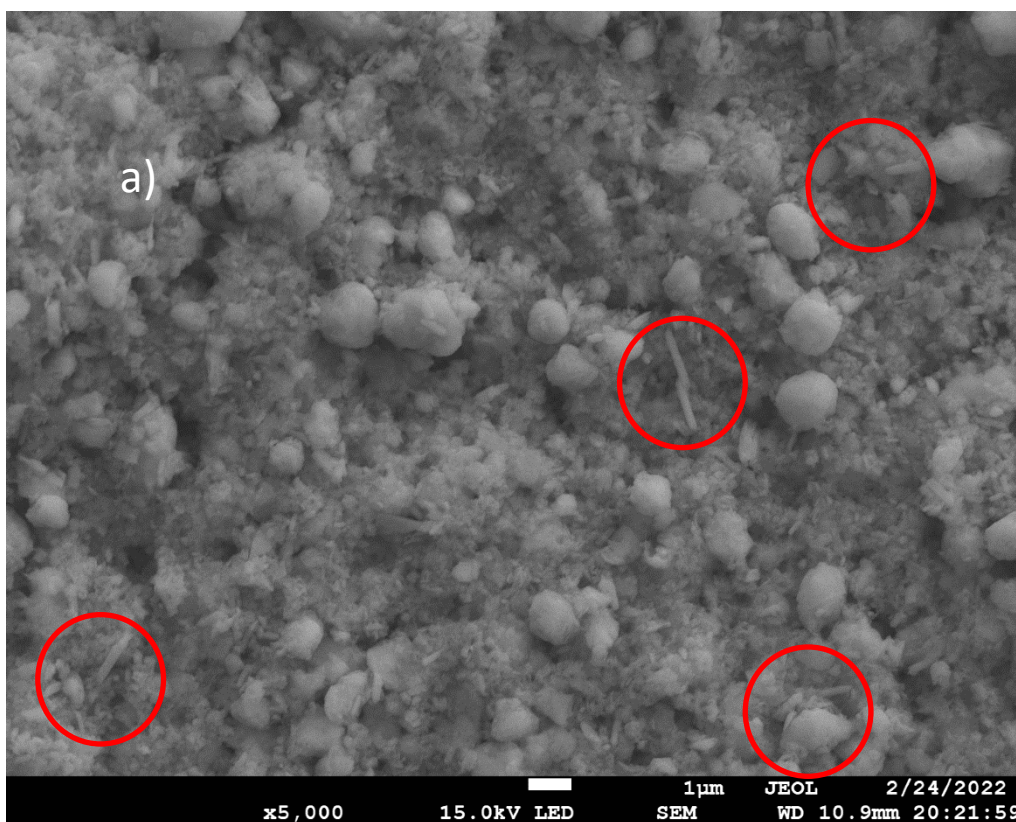
To avoid the oxidation of the  $\text{Bi}_{0.4}\text{Sb}_{1.6}\text{Te}_3$  nanoplatelets NMP was replaced with DMSO and a paste was formulated as described in sections 2.22 and 2.23. A PVDF- $\text{Bi}_{0.4}\text{Sb}_{1.6}\text{Te}_3$  nanoplatelet film was printed with 2 printing passes with a drying step between each pass of 15 mins in a vacuum oven at 70 °C. However, the film delaminated and broke up once the Kapton substrate had been peeled off the alumina plate, Fig. C.1 shows the film after the Kapton had peeled off.



**Fig.C.1-** Images of the screen-printed PVDF- $\text{Bi}_{0.4}\text{Sb}_{1.6}\text{Te}_3$  nanoplatelet film before (a) and after (b) the Kapton substrate had been peeled off the alumina plate.

The poor film adhesion to the Kapton could be explained by the hygroscopic nature of DMSO, causing the paste to absorb water molecules in the surrounding environment. As the PVDF binder isn't water soluble<sup>[115]</sup> it could have caused partial precipitation of the binder in the paste reducing the actual percentage of binder being printed. A lower PVDF concentration would explain the poor film adhesion, however, resolving this by increasing the PVDF concentration in the paste has been shown to be detrimental to TE performance as seen for the n-type  $\text{Bi}_2\text{Te}_3$ . As such it was decided to keep NMP as the paste solvent, although the time the nanoplatelets are in the paste would be reduced to 5 hr. The 5 hr is the minimum time needed for the pastes to be speed mixed and have two rounds of 2 hr bath sonication. Additionally, the pastes would be ice bath sonicated to potential heat-induced oxidation in the NMP.

**Appendix D [SEM images of screen-printed 5 % PVDF-  
 $\text{Bi}_{0.4}\text{Sb}_{1.6}\text{Te}_3$ + Te nanorods]**



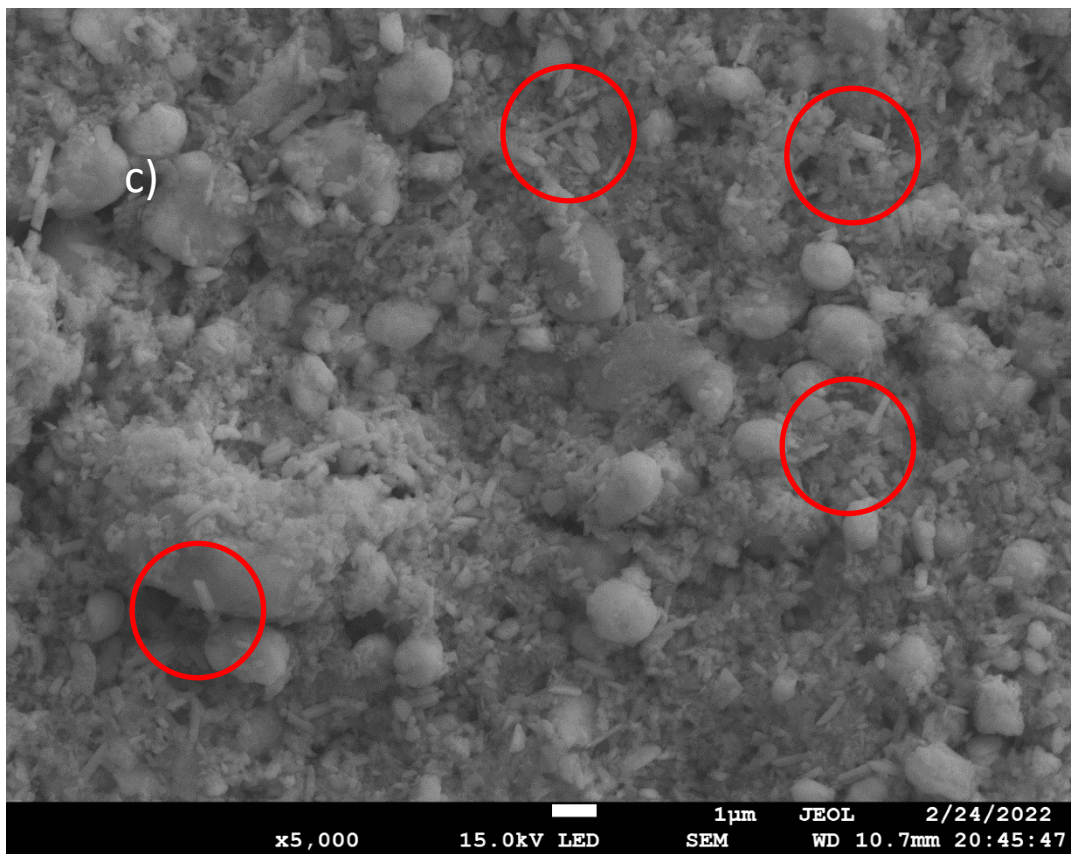


**Fig.D.1-** SEM images of PVDF-Bi<sub>0.4</sub>Sb<sub>1.6</sub>Te<sub>3</sub> nanoplatelet with a Te nanorod content of (a) 4 %, (b) 8 % and (c) 12 %.

## Appendix E [Viscosity measurements]

Repeat viscosity measurements were conducted on a sample of the 5 % PVDF-Bi<sub>2</sub>Te<sub>3</sub> nanowire paste with a viscometer, the results shown in Fig.E.1. The sheering of the paste by the measurement probe of the viscometer resulted in an observed decrease in the viscosity of the paste. This indicates that the paste has a thixotropic nature which allows the paste to be screen-printable.

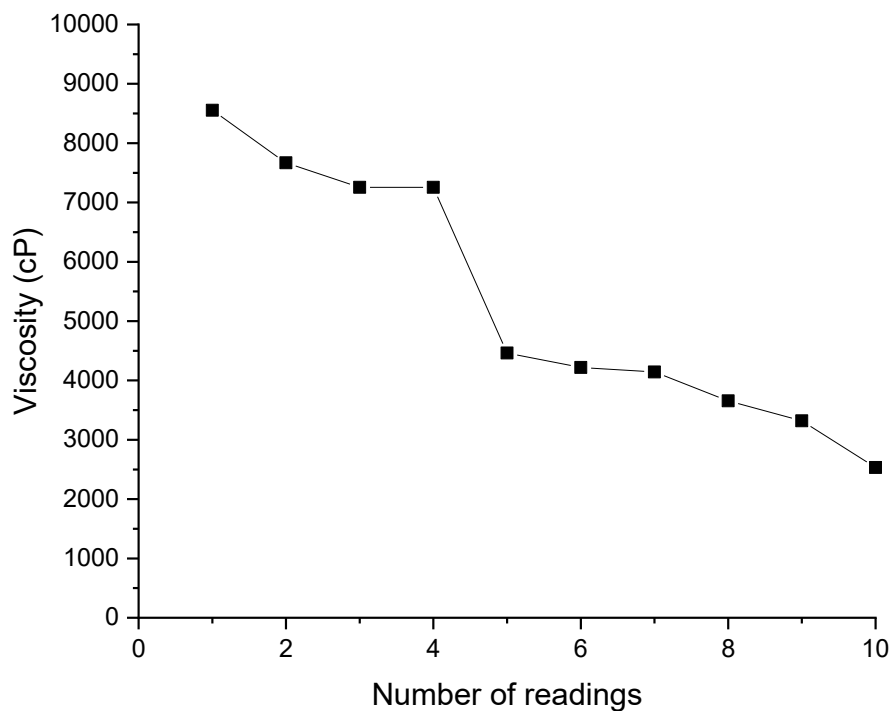


**Fig.E.1-** Graph of the viscosity of the 5 % PVDF-Bi<sub>2</sub>Te<sub>3</sub> nanowire paste with respect to the number of readings taken.



## List of References

- 1 Z. Wang, V. Leonov, P. Fiorini and C. Van Hoof, *Sensors Actuators, A Phys.*, 2009, **156**, 95–102.
- 2 J. S. Heo, J. Eom, Y. H. Kim and S. K. Park, *Small*, 2018, **14**, 1–16.
- 3 G. Rong, Y. Zheng and M. Sawan, *Sensors*, 2021, **21**, 1–23.
- 4 A. Nozariasbmarz, H. Collins, K. Dsouza, M. H. Polash, M. Hosseini, M. Hyland, J. Liu, A. Malhotra, F. M. Ortiz, F. Mohaddes, V. P. Ramesh, Y. Sargolzaeiaval, N. Snouwaert, M. C. Öztürk and D. Vashae, *Appl. Energy*, 2020, **258**, 114069.
- 5 V. Leonov and R. J. M. Vullers, *J. Renew. Sustain. Energy*, 2009, **1**, 062701.
- 6 I. Stark, *Proc. - Wirel. Heal. 2011, WH'11*, 2011, 5–6.
- 7 A. R. M. Siddique, S. Mahmud and B. Van Heyst, *Renew. Sustain. Energy Rev.*, 2017, **73**, 730–744.
- 8 M. B. Ali Bashir, M. Mohamad, S. B. M. Said, M. F. M. Sabri, M. Hamid Elsheikh, M. Haji Hassan and D. A. Shnawah, *Renew. Sustain. Energy Rev.*, 2013, **30**, 337–355.
- 9 A. Shakouri, *Annu. Rev. Mater. Res.*, 2011, **41**, 399–431.
- 10 J. H. Bahk, H. Fang, K. Yazawa and A. Shakouri, *J. Mater. Chem. C*, 2015, **3**, 10362–10374.
- 11 G. J. Snyder and E. S. Toberer, 2008, **7**, 105–114.
- 12 G. Chhatrasal and K. K. Kamal, *Prog. Mater. Sci.*, 2016, **83**, 330–382.
- 13 M. . Vederniko and E. . Iordanishvili, 1998, 37–42.
- 14 A. DASGUPTA, NANDITA DASGUPTA, *Semiconductor Devices: Modelling and Technology*, PHI Learning, 2004.
- 15 A. J. Naylor, 2014.
- 16 L. I. Berger, *Semiconductor materials*, CRC-Press, 1997.
- 17 R. K. Rajput, *Basic Electrical And Electronics Engineering (PTU, Jalandhar)*, Laxmi

## List of References

- Publications Pvt Limited, 2006.
- 18 F. D. Rosi, *Solid State Electron.*, 1968, **11**, 833–868.
- 19 M. Martín-González, O. Caballero-Calero and P. Díaz-Chao, *Renew. Sustain. Energy Rev.*, 2013, **24**, 288–305.
- 20 J. Na, Y. Kim, T. Park, C. Park and E. Kim, *ACS Appl. Mater. Interfaces*, 2016, **8**, 32392–32400.
- 21 S. Bäßler, T. Böhnert, J. Gooth, C. Schumacher, E. Pippel and K. Nielsch, *Nanotechnology*, , DOI:10.1088/0957-4484/24/49/495402.
- 22 C. T. Hong, Y. H. Kang, J. Ryu, S. Y. Cho and K. S. Jang, *J. Mater. Chem. A*, 2015, **3**, 21428–21433.
- 23 H. L.D. and D. M.S., *Sci. Comput.*, 1993, **47**, 8–11.
- 24 S. L. Shinde and J. Goela, *High Thermal Conductivity Materials*, Springer US.
- 25 C. B. Vining, *Nat. Mater.*, 2009, **8**, 83–85.
- 26 D. Beretta, N. Neophytou, J. M. Hodges, M. G. Kanatzidis, D. Narducci, M. Martin-Gonzalez, M. Beekman, B. Balke, G. Cerretti, W. Tremel, A. Zevalkink, A. I. Hofmann, C. Müller, B. Dörling, M. Campoy-Quiles and M. Caironi, *Mater. Sci. Eng. R Reports*, 2019, **138**, 210–255.
- 27 I. T. Witting, T. C. Chasapis, F. Ricci, M. Peters, N. A. Heinz, G. Hautier and G. J. Snyder, *Adv. Electron. Mater.*, 2019, 5.
- 28 I. T. Witting, F. Ricci, T. C. Chasapis, G. Hautier and G. J. Snyder, *Research*, 2020, **2020**, 1–15.
- 29 M. R. Burton, University of Southampton, 2017.
- 30 G. Chen and A. Shakouri, *J. Heat Transfer*, 2002, **124**, 242–252.
- 31 H. L.D. and D. M.S., *Phys. Rev. B*, 1993, **47**, 12727–12731.
- 32 R. Chen, J. Lee, W. Lee and D. Li, *Chem. Rev.*, 2019, 119, 9260–9302.
- 33 J. Mao, Z. Liu and Z. Ren, *npj Quantum Mater.*, 2016, 1.
- 34 J. P. Heremans, V. Jovovic, E. S. Toberer, A. Saramat, K. Kurosaki, A. Charoenphakdee, S.

- Yamanaka and G. J. Snyder, *Science (80-. )*, 2008, **321**, 1457–1461.
- 35 G. Zhang, B. Kirk, L. A. Jauregui, H. Yang, X. Xu, Y. P. Chen and Y. Wu, *Nano Lett.*, 2012, **12**, 56–60.
- 36 B. Xu, M. T. Agne, T. Feng, T. C. Chasapis, X. Ruan, Y. Zhou, H. Zheng, J. H. Bahk, M. G. Kanatzidis, G. J. Snyder and Y. Wu, *Adv. Mater.*, , DOI:10.1002/adma.201605140.
- 37 R. Venkatasubramanian, T. Colpitts, E. Watko, M. Lamvik and N. El-Masry, *J. Cryst. Growth*, 1997, **170**, 817–821.
- 38 O. Eibl, K. Nielsch, N. Peranio and F. Völklein, *Thermoelectric Bi<sub>2</sub>Te<sub>3</sub> Nanomaterials*, 2015.
- 39 F. Fievet, S. Ammar-Merah, R. Brayner, F. Chau, M. Giraud, F. Mammeri, J. Peron, J. Y. Piquemal, L. Sicard and G. Viau, *Chem. Soc. Rev.*, 2018, **47**, 5187–5233.
- 40 S. Ammar and F. Fiévet, *Nanomaterials*, 2020, **10**, 1–8.
- 41 F. Bensebaa, in *Nanoparticle technologies: from lab to market*, Academic Press, 2012, vol. 19, pp. 85–146.
- 42 Y. Xia, Y. Xiong, B. Lim and S. E. Skrabalak, *Angew. Chemie - Int. Ed.*, 2009, **48**, 60–103.
- 43 V. K. LaMer and R. H. Dinegar, *J. Am. Chem. Soc.*, 1950, **72**, 4847.
- 44 T. H. Yang, Y. Shi, A. Janssen and Y. Xia, *Angew. Chemie - Int. Ed.*, 2020, **59**, 15378–15401.
- 45 C. Zhou, C. Dun, K. Wang, X. Zhang, Z. Shi, G. Liu, C. A. Hewitt, G. Qiao and D. L. Carroll, *Nano Energy*, 2016, **30**, 709–716.
- 46 D. Deganello, in *Organic Light-Emitting Diodes (OLEDs): Materials, Devices and Applications*, 2013.
- 47 J. F. Steffe, *Rheological Methods in Food Process Engineering*, Freeman Press, 1996.
- 48 J. Riley, *Advances in Electrochemical Science and Engineering*, 2000, vol. 493.
- 49 M. Shirai and H. Okamura, *Polym. Int.*, 2016, **65**, 362–370.
- 50 Z. Cao, University of Southampton, 2014.
- 51 M. Orril and S. LeBlanc, *J. Appl. Polym. Sci.*, , DOI:10.1002/app.44456.

## List of References

- 52 E. Koukharenko, S. A. Boden, N. P. Sessions, N. Frety, I. Nandhakumar and N. M. White, *J. Mater. Sci. Mater. Electron.*, 2018, **29**, 3423–3436.
- 53 B. Chen, M. Kruse, B. Xu, R. Tutika, W. Zheng, M. D. Bartlett, Y. Wu and J. C. Claussen, *Nanoscale*, 2019, **11**, 5222–5230.
- 54 Y. Yang, Z. H. Lin, T. Hou, F. Zhang and Z. L. Wang, *Nano Res.*, 2012, **5**, 888–895.
- 55 I. Domnez Noyan, G. Gadea, M. Salleras, M. Pacios, C. Calaza, A. Stranz, M. Dolcet, A. Morata, A. Tarancon and L. Fonseca, *Nano Energy*, 2019, **57**, 492–499.
- 56 K. Wang, H. W. Liang, W. T. Yao and S. H. Yu, *J. Mater. Chem.*, 2011, **21**, 15057–15062.
- 57 B. Chen, S. R. Das, W. Zheng, B. Zhu, B. Xu, S. Hong, C. Sun, X. Wang, Y. Wu and J. C. Claussen, *Adv. Electron. Mater.*, , DOI:10.1002/aelm.201600524.
- 58 J. K. Niemeier and D. P. Kjell, *Org. Process Res. Dev.*, 2013, **17**, 1580–1590.
- 59 L. D. Zhao, B. P. Zhang, W. S. Liu and J. F. Li, *J. Appl. Phys.*, , DOI:10.1063/1.3063694.
- 60 B. Poudel, Q. Hao, Y. Ma, Y. Lan, A. Minnich, B. Yu, X. Yan, D. Wang, A. Muto, D. Vashaee, X. Chen, J. Liu, M. S. Dresselhaus, G. Chen and Z. Ren, *Science (80-. )*, 2008, **320**, 634–638.
- 61 W. Thongkham, C. Lertsatitthanakorn, K. Jiramitmongkon, K. Tantisantisom, T. Boonkoom, M. Jitpukdee, K. Sinthiptharakoon, A. Klamchuen, M. Liangruksa and P. Khanchaitit, *ACS Appl. Mater. Interfaces*, 2019, **11**, 6624–6633.
- 62 C. Zhang, Z. Peng, Z. Li, L. Yu, K. A. Khor and Q. Xiong, *Nano Energy*, 2015, **15**, 688–696.
- 63 H. Q. Yang, L. Miao, C. Y. Liu, C. Li, S. Honda, Y. Iwamoto, R. Huang and S. Tanemura, *ACS Appl. Mater. Interfaces*, 2015, **7**, 14263–14271.
- 64 C. Hollar, Z. Lin, M. Kongara, T. Varghese, C. Karthik, J. Schimpf, J. Eixenberger, P. H. Davis, Y. Wu, X. Duan, Y. Zhang and D. Estrada, *Adv. Mater. Technol.*, 2020, **5**, 1–8.
- 65 N. S. Chauhan, S. V. Pyrlin, O. I. Lebedev, L. S. A. Marques, M. M. D. Ramos, T. Maiti, K. Kovnir, B. A. Korgel and Y. V. Kolen'Ko, *J. Phys. Chem. C*, 2021, **125**, 20184–20194.
- 66 C. Ou, A. L. Sangle, A. Datta, Q. Jing, T. Busolo, T. Chalklen, V. Narayan and S. Kar-Narayan, *ACS Appl. Mater. Interfaces*, 2018, **10**, 19580–19587.
- 67 C. Dun, C. A. Hewitt, H. Huang, D. S. Montgomery, J. Xu and D. L. Carroll, *Phys. Chem.*

- Chem. Phys.*, 2015, **17**, 8591–8595.
- 68 K. C. See, J. P. Feser, C. E. Chen, A. Majumdar, J. J. Urban and R. A. Segalman, *Nano Lett.*, 2010, **10**, 4664–4667.
- 69 S. K. Yee, N. E. Coates, A. Majumdar, J. J. Urban and R. A. Segalman, *Phys. Chem. Chem. Phys.*, 2013, **15**, 4024–4032.
- 70 S. Ma, K. Anderson, L. Guo, A. Yousuf, E. C. Ellingsworth, C. Vajner, H. T. Wang and G. Szulczewski, *Appl. Phys. Lett.*, , DOI:10.1063/1.4893740.
- 71 Y. Wang, S. M. Zhang and Y. Deng, *J. Mater. Chem. A*, 2016, **4**, 3554–3559.
- 72 W. Wang, C. Li, X. Li, Y. Jia, F. Jiang, C. Liu, R. Tan and J. Xu, *Thin Solid Films*, 2018, **654**, 23–29.
- 73 Q. Meng, Q. Jiang, K. Cai and L. Chen, *Org. Electron.*, 2019, **64**, 79–85.
- 74 Z. Cao, M. J. Tudor, R. N. Torah and S. P. Beeby, *IEEE Trans. Electron Devices*, 2016, **63**, 4024–4030.
- 75 S. J. Kim, J. H. We and B. J. Cho, *Energy Environ. Sci.*, 2014, **7**, 1959–1965.
- 76 S. J. Kim, H. Choi, Y. Kim, J. H. We, J. S. Shin, H. E. Lee, M. W. Oh, K. J. Lee and B. J. Cho, *Nano Energy*, 2017, **31**, 258–263.
- 77 Z. Cao, E. Koukharenko, M. J. Tudor, R. N. Torah and S. P. Beeby, *Sensors Actuators, A Phys.*, 2016, **238**, 196–206.
- 78 J. H. We, S. J. Kim, G. S. Kim and B. J. Cho, *J. Alloys Compd.*, 2013, **552**, 107–110.
- 79 T. Varghese, C. Hollar, J. Richardson, N. Kempf, C. Han, P. Gamarachchi, D. Estrada, R. J. Mehta and Y. Zhang, *Sci. Rep.*, 2016, **6**, 6–11.
- 80 S. Shin, R. Kumar, J. W. Roh, D. S. Ko, H. S. Kim, S. Il Kim, L. Yin, S. M. Schlossberg, S. Cui, J. M. You, S. Kwon, J. Zheng, J. Wang and R. Chen, *Sci. Rep.*, 2017, **7**, 1–9.
- 81 T. Varghese, C. Dun, N. Kempf, M. Saeidi-Javash, C. Karthik, J. Richardson, C. Hollar, D. Estrada and Y. Zhang, *Adv. Funct. Mater.*, 2020, **30**, 1–8.
- 82 T. Torfs, V. Leonov, C. Van Hoof and B. Gyselinckx, *Proc. IEEE Sensors*, 2006, 427–430.

## List of References

- 83 V. Leonov, T. Torfs, P. Fiorini and C. Van Hoof, *IEEE Sens. J.*, 2007, **7**, 650–656.
- 84 T. Torfs, V. Leonov, R. F. Yazicioglu, P. Merken, C. Van Hoof, R. J. M. Vullers and B. Gyselinckx, *Proc. IEEE Sensors*, 2008, 1269–1272.
- 85 S. Zhu, Z. Fan, B. Feng, R. Shi, Z. Jiang, Y. Peng, J. Gao, L. Miao and K. Koumoto, *Energies*, 2022, **15**, 1–27.
- 86 Z. Niu and Y. Li, *Chem. Mater.*, 2014, **26**, 72–83.
- 87 A. Gören, J. Mendes, H. M. Rodrigues, R. E. Sousa, J. Oliveira, L. Hilliou, C. M. Costa, M. M. Silva and S. Lanceros-Méndez, *J. Power Sources*, 2016, **334**, 65–77.
- 88 C. Luo, Y. Zhang, X. Zeng, Y. Zeng and Y. Wang, *J. Colloid Interface Sci.*, 2005, **288**, 444–448.
- 89 L. Reimer, *Scanning electron microscopy: physics of image formation and microanalysis*, 2013.
- 90 J. I. Goldstein, D. E. Newbury, J. . Michael, N. . Ritchie, J. H. . Scott and D. . Joy, *Scanning electron microscopy and X-ray microanalysis*, 2017.
- 91 A. . Garratt-Reed and D. . Bell, *Energy dispersive X-ray analysis in the electron microscope*, 2003.
- 92 G. . Hornyak, H. . Tibbals, J. Dutta and J. . Moore, *Introduction to nanoscience and nanotechnology.*, 2008.
- 93 A. Amin, R. Huang, D. W. Newbrook, V. Sethi, S. P. Beeby and I. S. Nandhakumar, *J. Phys. Energy*, , DOI:10.1088/2515-7655/ac572e.
- 94 H. Morkoc, *Handbook of Nitride Semiconductors and Devices, Electronic and Optical Processes in Nitrides*, 2009.
- 95 S. T. Bergold, F. Goetz-Neunhoeffler and J. Neubauer, *Cem. Concr. Res.*, 2013, **53**, 119–126.
- 96 A. F. Abdulrahman, S. M. Ahmed, N. M. Ahmed and M. A. Almessiere, *AIP Conf. Proc.*, , DOI:10.1063/1.4998358.
- 97 J. Su and A. C. Lua, *J. Memb. Sci.*, 2007, **305**, 263–270.
- 98 K. Chatterjee, M. Mitra, K. Kargupta, S. Ganguly and D. Banerjee, *Nanotechnology*, , DOI:10.1088/0957-4484/24/21/215703.

- 99 F. et al. Jiao, C. Di, Y. Sun, P. Sheng, W. Xu and D. Zhu, *Philos. Trans. R. Soc. A*.
- 100 M. Hong, T. C. Chasapis, Z. G. Chen, L. Yang, M. G. Kanatzidis, G. J. Snyder and J. Zou, *ACS Nano*, 2016, **10**, 4719–4727.
- 101 A. M. Adam, A. El-Khouly, E. Lilov, S. Ebrahim, Y. Keshkh, M. Soliman, E. M. El Maghraby, V. Kovalyo and P. Petkov, *Mater. Chem. Phys.*, 2019, **224**, 264–270.
- 102 C. Bauer, I. Veremchuk, C. Kunze, A. Benad, V. M. Dzhagan, D. Haubold, D. Pohl, G. Schierning, K. Nielsch, V. Lesnyak and A. Eychmüller, *Small Sci.*, 2021, **1**, 2000021.
- 103 R. J. Tilley, *Defects in Solids*, John Wiley & Sons, 2008.
- 104 L. Hu, T. Zhu, X. Liu and X. Zhao, *Adv. Funct. Mater.*, 2014, **24**, 5211–5218.
- 105 J. H. We, S. J. Kim and B. J. Cho, *Energy*, 2014, **73**, 506–512.
- 106 M. Scheele, N. Oeschler, I. Veremchuk, K. G. Reinsberg, A. M. Kreuziger, A. Kornowski, J. Broekaert, C. Klinke and H. Weller, *ACS Nano*, 2010, **4**, 4283–4291.
- 107 C. J. Liu, G. J. Liu, Y. L. Liu and L. R. Chen, *AIP Conf. Proc.*, 2012, **1449**, 103–106.
- 108 D. Madan, Z. Wang, A. Chen, P. K. Wright and J. W. Evans, *ACS Appl. Mater. Interfaces*, 2013, **5**, 11872–11876.
- 109 D. Madan, Z. Wang, P. K. Wright and J. W. Evans, *Appl. Energy*, 2015, **156**, 587–592.
- 110 A. S. Epstein, H. Fritzsche and K. Lark-Horovitz, *Phys. Rev.*, 1957, **107**, 412–419.
- 111 Q. Meng, K. Cai, Y. Du and L. Chen, *J. Alloys Compd.*, 2019, **778**, 163–169.
- 112 R. Vaillon, O. Dupré, R. B. Cal and M. Calaf, *Sci. Rep.*, 2018, **8**, 1–9.
- 113 D. Champier, *Energy Convers. Manag.*, 2017, **140**, 167–181.
- 114 M. D. A. Albert, K. O. Bennett, C. A. Adams and J. G. Gluyas, *Renew. Sustain. Energy Rev.*, , DOI:10.1016/j.rser.2022.112230.
- 115 J. E. Marshall, A. Zhenova, S. Roberts, T. Petchey, P. Zhu, C. E. J. Dancer, C. R. McElroy, E. Kendrick and V. Goodship, *Polymers (Basel)*, 2021, **13**, 1–31.



